Advanced optical laser diagnostics for oxy-fuel biomass combustion

Vom Fachbereich Maschinenbau
an der Technischen Universität Darmstadt

zur Erlangung des akademischen Grades eines
Doktors der Ingenieurwissenschaften (Dr.-Ing.)
genehmigte

Dissertation

von

Henrik Schneider, M.Sc.

aus Lich

Berichterstatter:	Prof. Dr. rer. nat. habil. Andreas Dreizler
Mitberichterstatter:	Prof. Dr.-Ing. Reinhold Kneer
Tag der Einreichung:	05.12.2023
Tag der mündlichen Prüfung:	23.01.2024

Darmstadt 2024
D17

Henrik Schneider:
Advanced optical laser diagnostics for oxy-fuel biomass combustion

Darmstadt, Technische Universität Darmstadt

Tag der mündlichen Prüfung: 23.01.2024
Jahr der Veröffentlichung auf TUprints: 2024

URN: urn:nbn:de:tuda-tuprints-286208
URI: https://tuprints.ulb.tu-darmstadt.de/id/eprint/28620

Erklärung

Hiermit erkläre ich, dass ich die vorliegende Arbeit, abgesehen von den in ihr ausdrücklich genannten Hilfen, selbständig verfasst habe.

Darmstadt, 05.12.2023

Henrik Schneider

Danksagung

Die vorliegende Dissertation ist das Ergebnis meiner Tätigkeit als wissenschaftlicher Mitarbeiter am Fachgebiet Reaktive Strömungen und Messtechnik (RSM) der Technischen Universität Darmstadt. Ich blicke auf schöne fünfeinhalb Jahre zurück, die von einer Vielzahl an Personen begleitet wurden und ohne deren Unterstützung diese Arbeit so nicht möglich gewesen wäre.

Ganz besonders möchte ich mich bei meinem Doktorvater Prof. Andreas Dreizler bedanken. Danke für die Möglichkeit einer Promotion an deinem Fachgebiet und die großartige Unterstützung über die gesamte Promotionszeit. Ich schätze sehr, dass man bei dir zu jederzeit ein offenes Ohr gefunden hat und du stets zu helfen wusstest.

Weiterhin möchte ich mich bei Prof. Dr.-Ing. Reinhold Kneer vom Lehrstuhl für Wärme- und Stoffübertragung der RWTH Aachen bedanken für die Übernahme des Korreferats meiner Dissertation und die langjährige Arbeit als Sprecher des SFB/TRR 129 Oxyflame innerhalb welches diese Arbeit entstand.

Die tägliche Arbeit im Labor und im Büro wäre undenkbar ohne das tolle kollektive Miteinander am RSM. Hier möchte ich mich insbesondere bei meinem Arbeitsgruppenleiter Dr. Benjamin Böhm und bei meinen Kollegen Janik Hebel, Christopher Geschwindner, Pascal Johe, Matthias Bonarens, Dr. Hendrik Nicolai, Dr. Johannes Emmert, Dr. Max Greifenstein, Dr. Florian Zentgraf und Dr. Tao Li bedanken. Hervorheben möchte ich an dieser Stelle Janik Hebel, danke für die großartige Unterstützung im Labor bei vielen Messkampagnen, die zu dieser Arbeit geführt haben. Auch möchte ich Dr. Steven Wagner und Dr. Luigi Biondo danken für die schöne Zusammenarbeit im Bereich der Lehre, die mir immer viel Spaß gemacht hat.

Im Laufe dieser Arbeit wurden mehrere Untersuchungen zusammen mit anderen Instituten durchgeführt. Hier möchte ich Dr. Christian Meißner, Evaggelos Sidiropoulos, Jonas Hölzer und Prof. Thomas Seeger des Lehrstuhls Technische Thermodynamik von der Universität Siegen und Sarah Valentiner, Dr. Nikita Vorobiev und Dr. Martin Schiemann vom Lehrstuhl für Energieanlagen und Energieprozesstechnik der Ruhr-Universität Bochum danken.

Ohne die tatkräftige Unterstützung unseres Sekretariats, Marion Müller und Angela Berger, unserer Werkstatt, Roland Berntheisel, Dirk Feldmann, Sebastian Feuerbach und Mathias Felter, und unserer IT, Hardy Hamel, Janik Hebel und Robin Schultheis, wäre die Forschung am RSM nicht möglich. Vielen Dank! Zudem gilt mein Dank Andreas Ludwig, der bei vielen Problemen im Labor und an den Lasersystemen stets zu helfen wusste.

Zu dieser Dissertation und meiner Arbeit am RSM haben eine Vielzahl von Studenten im Rahmen von Bachelor- und Masterarbeiten und als Hiwis beigetragen. Hier möchte ich mich insbesondere bei Philipp Jonas, Lucas Gebauer, Pascal Steffens, Tim Heckmann, Lukas Biesalski, Janik Hebel, Christoph Möller und Lars Marolt bedanken und freue mich darüber mit einigen von euch inzwischen als Kollegen zusammenzuarbeiten.

Einen ganz besonderen Dank möchte ich an meine Frau Janina und meinen Sohn Kilian sowie an meine Eltern Andrea und Harald Schneider richten. Meinen Eltern danke ich für die Unterstützung während meines Studium und meiner Promotion und dafür, dass ihr immer für mich da wart. Janina, ich danke dir für die inzwischen mehr als 10 schönen Jahre, die wir schon gemeinsam erleben und insbesondere dafür, dass du mich beim Schreiben dieser Arbeit jederzeit liebevoll unterstützt hast. Kilian, jedes Kinderlachen von dir hat mir während des Schreibens ein Lächeln ins Gesicht gezaubert und mir geholfen diese Arbeit zu beenden. Danke!

Darmstadt, Dezember 2023
Henrik Schneider

Abstract

Biomass energy with carbon capture and storage (BECCS) is a key technology for removing CO_2 from the atmosphere and is an essential part of climate scenarios to prevent large temperature increases caused by the anthropogenic climate change. Combustion of pulverized biomass in an oxy-fuel atmosphere consisting mainly of CO_2, O_2, and H_2O is a promising approach for subsequent efficient carbon capture and storage (CCS). The changed combustion atmosphere under oxy-fuel conditions results in significant changes in combustion behavior and flame stability. Although oxy-fuel combustion has been widely studied in the recent decades, the fundamentals of the complex fluid-mechanical, particle-dynamical and chemical processes and their interactions in the combustion of pulverized solid fuels are not fully understood.

In this thesis, a solid fuel combustor (SFC) has been investigated that operates gas-assisted solid fuel flames in the power range up to 70 kW_{th}. The SFC stabilizes a swirl flame and exhibits important characteristics of modern combustors while providing large optical access. The focus of several studies is on the near-burner region where the flame is stabilized and several important combustion processes such as particle heating, volatile release, volatile combustion, onset of char combustion, and particle-fluid mixing take place.

Multi-parameter studies using advanced optical laser diagnostics were performed to improve our understanding of pulverized solid fuel combustion under oxy-fuel conditions. The advanced optical laser diagnostics applied allow in-situ measurements of flow and scalar fields with high spatial and temporal resolution while being non-invasive or minimally invasive.

Flow dynamics and particle temperatures in the near-burner region are analyzed to support our understanding of flame stabilization, burnout behavior, and burnout rate. The flow field, fluid-particle mixing, particle trajectories, and gas and particle residence times are investigated using particle image velocimetry (PIV) and high-speed particle tracking velocimetry (PTV). Particle temperatures at different stages of the combustion are evaluated using two-color pyrometry.

The influence of oxygen concentration and solid fuel type on the combustion process of fuel particles and the effects on flame stabilization and pollutant formation are analyzed. Flame stabilization is investigated using information on CH* chemiluminescence, gas flow velocities, particle velocities, and gas temperatures determined by CH* chemiluminescence imaging, a two-phase PIV/PTV approach, and tomographic absorption spectroscopy (TAS). The combustion process of biomass particles and the formation of pollutants are analyzed using qualitative soot and polycyclic aromatic hydrocarbon (PAH) measurement data, obtained using a quasi-simultaneous laser-induced fluorescence/laser-induced incandescence (LIF/LII) configuration, in combination with information on the flow field and gas temperature distribution.

A novel O_2-CO_2-coherent anti-Stokes Raman spectroscopy (CARS) approach is developed, experimentally validated, and successfully applied to pulverized oxy-fuel biomass combustion to study the thermochemical state at different flame positions within the combustion process. These investigations are the first CARS measurements in particle-laden reactive flows beyond demonstration. Using the O_2-CO_2-CARS setup, radial gas temperature and mole fraction profiles of O_2 and CO_2 are determined and analyzed for different oxygen concentrations in oxy-fuel conditions.

The results presented provide novel insights into the solid fuel combustion process under oxy-fuel atmospheres that go beyond the state of research and provide a unique comprehensive data set for validation of numerical simulations.

Kurzfassung

Bioenergie mit CO_2-Abscheidung und -Speicherung (BECCS) ist eine Schlüsseltechnologie zur CO_2 Reduktion in der Atmosphäre und ein wesentlicher Bestandteil von Szenarien zur Verhinderung eines starken Temperaturanstiegs aufgrund des anthropogenen Klimawandels. Die Verbrennung von staubförmiger Biomasse in einer Oxy-Fuel Atmosphäre, die hauptsächlich aus CO_2, O_2 und H_2O besteht, ist ein vielversprechender Ansatz für eine anschließende effiziente CO_2-Abscheidung und -Speicherung (CCS). Die veränderten Bedingungen in der Oxy-Fuel Atmosphäre führen zu erheblichen Unterschieden im Verbrennungsprozess und bei der Flammenstabilität. Obwohl an der Oxy-Fuel Verbrennung in den letzten Jahrzehnten viel geforscht wurde, sind die Grundlagen der komplexen strömungsmechanischen, partikeldynamischen und chemischen Prozesse und ihre Wechselwirkungen bei der Verbrennung von staubförmigen Festbrennstoffen nicht vollständig verstanden.

In dieser Arbeit wurde eine Brennkammer (SFC) untersucht, in der gasunterstützte Staubflammen mit thermischen Leistungen bis zu 70 kW_{th} betrieben wurden. Der SFC stabilisiert eine Drallflamme und besitzt wichtige Eigenschaften moderner Brenner, bei gleichzeitig guter optischer Zugänglichkeit. Der Fokus der Untersuchungen liegt auf dem brennernahen Bereich, in dem die Flamme stabilisiert wird und mehrere wichtige Verbrennungsprozesse wie die Partikelaufheizung, die Ausgasung und Verbrennung von Volatilen, der Beginn des Koksabbrands und die Vermischung von Partikel- und Gasphase stattfinden.

Multi-Parameter-Studien mit optischer Laserdiagnostik wurden durchgeführt, um unser Verständnis der Verbrennung staubförmiger Brennstoffe unter Oxy-Fuel Bedingungen zu verbessern. Die optische Laserdiagnostik ermöglicht in-situ-Messungen von Strömungs- und Skalarfeldern mit hoher räumlicher und zeitlicher Auflösung, während der Prozess dabei nicht oder nur wenig beeinflusst wird.

Die Strömungsdynamik und Partikeltemperaturen im brennernahen Bereich wurden analysiert, um unser Verständnis der Flammenstabilisierung, des Ausbrandverhaltens und der Ausbrandrate zu erweitern. Das Strömungsfeld, die Vermischung von Partikel- und Gasphase, Partikeltrajektorien sowie Gas- und Partikelverweilzeiten wurden mit Hilfe der Particle Image Velocimetry (PIV) und Particle Tracking Velocimetry (PTV) untersucht. Partikeltemperaturen wurden zu verschiedenen Zeitpunkten während der Verbrennung mit einem Zweifarben-Pyrometer gemessen und analysiert.

Der Einfluss der Sauerstoffkonzentration und des Brennstofftyps auf den Verbrennungsprozess, die Flammenstabilisierung und die Schadstoffbildung wurden untersucht. Die Flammenstabilisierung wurde auf Basis von CH* Chemilumineszenz, Strömungsfeldern, Partikelgeschwindigkeiten und Gastemperaturen analysiert, die mithilfe von CH* Chemilumineszenzmessungen, einem Zwei-Phasen-PIV/PTV-Ansatz und tomographischer Absorptionsspektroskopie (TAS) gemessen wurden. Der Verbrennungsprozess und die Schadstoffbildung wurden anhand von Strömungsfeldern und Temperaturverteilungen in Kombination mit qualitativen Messdaten von Ruß und polyzyklischen aromatischen Kohlenwasserstoffen (PAH) analysiert, die mit einem quasi-simultanen Laser-induzierten Fluoreszenz/ Laser-induzierten Inkandeszenz (LIF/LII)-Aufbau bestimmt wurden.

Ein Ansatz für die kohärente-Anti-Stokes-Raman-Spektroskopie (CARS) basierend auf O_2 und CO_2 wurde entwickelt, experimentell validiert und erfolgreich auf die Oxy-Fuel Verbrennung von Biomasse angewendet, um den thermochemischen Zustand zu unterschiedlichen Zeitpunkten innerhalb des Verbrennungsprozesses zu untersuchen. Diese Untersuchungen sind die ersten CARS-Messungen in partikelbeladenen reaktiven Strömungen, die über eine Demonstration hinausgehen. Unter Verwendung des O_2-CO_2-CARS-Aufbaus wurden radiale Profile der Gastemperatur und der O_2-/CO_2-Molenbrüche bestimmt und für verschiedene Sauerstoffkonzentrationen unter Oxy-Fuel Bedingungen analysiert.

Die vorgestellten Ergebnisse bieten neue Einblicke in den Verbrennungsprozess fester Brennstoffe unter Oxy-Fuel Bedingungen, die über den Stand der Forschung hinausgehen, und einen einzigartigen umfassenden Datensatz zur Validierung numerischer Simulationen.

Contents

List of Figures

List of Tables

Nomenclature

Lower-case Latin letters		Unit
a	Minor axis diameter of ellipsoid	m
b	Major axis diameter of ellipsoid	m
b	Offset	-
c_p	Specific heat capacity at constant pressure	J/(kg K)
d	Diameter	m
f	Focal length	m
g	Body force	m/s^2
h	Height	m
h	Specific enthalpy	kJ/kg
k	Wave vector	1/m
l	Length	m
m	Mass	kg
p	Pressure	N/m^2
q	Energy source term	W/m^3
r	Radius	m
t	Time	s
u	Velocity	m/s

Upper-case Latin letters		Unit
$\mathscr{L}$	Characteristic length	m
$\mathscr{U}$	Characteristic velocity	m/s
Da	Damköhler number	-
Re	Reynolds number	-
St	Stokes number	-
S	Swirl number	-
D	Diffusion coefficient	m^2/s
G	Momentum flux	Ns/m^2
I	Identity matrix	-
I	Signal intensity	W/m^2
K	Amplitude	-
N	Number	-
R	Characteristic radius	m
S	Line strength	-
S	Spin	-
T	Temperature	K
T	Total Time	s
V	Volume	m^3
x	Mole fraction	-
Y	Mass fraction	-

Lower-case Greek letters		Unit
$\alpha, \beta, \gamma, \delta$	Angles	rad
α	Absorbance	1/m
χ	Susceptibility	cm3/(erg amagat)
ϵ	Spectral emissivity	-
ϵ	Turbulent dissipation rate	m^2/s^3
η	Dynamic viscosity	kg/(ms)
η	Quantum efficiency	-
γ	Regularization parameter	-
κ	Spectral absorption coefficient	m^2/mol
λ	Oxidizer-to-fuel ratio	-
λ	Thermal conductivity	W/(mK)
λ	Wavelength	m
μ	Dynamic viscosity	kg/(ms)
ν	Frequency	1/s
ν	Kinematic viscosity	m^2/s
ν', ν''	Stoichiometric coefficients	-
ω	Chemical source term	$kg/(m^3 s)$
ω	Frequency	Hz
ϕ	Fraction	-
ϕ	Stoichiometric ratio	-
ρ	Density	kg/m^3
σ_A	Absorption cross section	cm^2/molecule
τ	Characteristic timescale	s

Upper-case Greek letters		Unit
Γ	Transition line width	m
Ω	Observed angle	rad
Φ	Line shape function	-
Φ_F	Fluorescence quantum yield	-

Indices and Superscripts	
0	Integral scale
α	Species
η	Kolmogorov scale
0	Initial
1, 2, 3	Integer index
ad	Adiabatic
AS	Absorption spectroscopy
A	Absorption
CARS	Coherent anti-Stokes Raman spectroscopy
chem	Chemical
fuel	Fuel

F	Fluorescence
f	Flow
LIF	Laser-induced fluorescence
L	Laser
max	Maximal
min	Minimal
NR	Non-resonant
ox	Oxidator
phys	Physical
P	Phosphorescence
p	Particle
R	Resonant
shift	Shift
sub	Sublimation
total	Total
TPT	Thermographic phosphor thermometry
TR	Thermal radiation
θ	Tangential
h	Energy
j	Transition
m	Mass
n	Internuclear
R	Radiation
s	Slip
t	Turbulent
u	Momentum
v	Volume
x	Axial

Physical constants		**Value**
ϵ_0	Permittivity of the free space	$8.854 \cdot 10^{-12}\,\mathrm{F/m}$
c	Speed of light	$299\,792\,458\,\mathrm{m/s}$
h	Planck's constant	$6.626 \cdot 10^{-34}\,\mathrm{Js}$
k_B	Boltzmann's constant	$1.3806 \cdot 10^{-23}\,\mathrm{J/K}$

Abbreviations

AFT	Adiabatic flame temperature
BBDL	Broadband dye laser
BECCS	Biomass energy with carbon capture and storage
BW	Beech wood
CARS	Coherent anti-Stokes Raman spectroscopy
CCD	Charge-coupled device
CCS	Carbon capture and storage

CCU	Carbon capture and usage
CL	Chemiluminescence
CMOS	Complementary metal-oxide-semiconductor
CRC	Collaborative Research Center
CRIEPIE	Central Research Institute of Electric Power Industry
CTF	Contrast transfer function
DEHS	Di-ethyl-hexyl-sebacate
DP-CARS	Dual-pump CARS
ECD	Equivalent circular diameter
FOV	Field of view
FWHM	Full width at half maximum
HHR	Heat release rate
HHV	Higher heating value
IQR	Interquartile ranges
IR	Infrared
IRO	Intensified relay optics
IRZ	Inner recirculation zone
ISC	Intersystem crossing
LDA	Laser Doppler anemometry
LDV	Laser Doppler velocimetry
LES	Large-eddy simulation
LHAT	Linear hyperspectral absorption tomography
LHV	Lower heating value
LIF	Laser-induced fluorescence
LII	Laser-induced incandescence
LOHC	Liquid organic hydrogen carriers
LRS	Linear regression of the sum
MFC	Mass flow controller
ND	Neutral density
NIR	Near-infrared
ORZ	Outer recirculation zone
PAH	Polycyclic aromatic hydrocarbon
PCC	Pulverized coal combustion
PDF	Probability density function
PIV	Particle image velocimetry
PLIF	Planar laser-induced fluorescence
PMT	Photomultiplier tube
PTV	Particle tracking velocimetry
RET	Rotational energy transfer
RL	Rhenish lignite
RMS	Root mean square
RSM	Institute of Reactive Flows and Diagnostics
SCOT	Stereoscopic camera system for optical thermography
SFC	Solid fuel combustor
TAS	Tomographic absorption spectroscopy
TDLAS	Tunable diode laser absorption spectroscopy

TiRe-LII	Time-resolved LII
TPT	Thermographic phosphor thermometry
TRR	Transregio
TTS	Institute of Engineering Thermodynamics
TU	Technical university
UV	Ultra-violet
VET	Vibrational energy transfer
WIDECARS	Width-increased dual-pump enhanced CARS
WS	Walnut shell
YAG	Yttrium aluminum garnet

1 Introduction

1.1 Motivation

The anthropogenic climate change is leading to a steady rise in global temperature, which has reached about 1.2 °C above pre-industrial (1850-1900) levels in 2023 [17, p. 155]. The main driver of temperature rise is the large amount of greenhouse gases emitted into the atmosphere. The most important greenhouse gases are carbon dioxide (CO_2), methane (CH_4), nitrous oxide (N_2O), halogenated gases, volatile organic compounds, and carbon monoxide (CO) which trap heat in the Earth's atmosphere and cause the average surface temperature to rise. Of these, CO_2 has the greatest impact on the Earth's radiative balance, accounting for approximately 70% of the increase in global temperature [18, p. 713].

In 2015, at the United Nations Climate Change Conference (COP21) in Paris, 196 parties agreed to hold "the increase in the global average temperature to well below 2 °C above pre-industrial levels" and pursue "efforts to limit the temperature increase to 1.5 °C above pre-industrial levels" in order to "significantly reduce the risks and impacts of climate change" [19]. To achieve this goal, net emissions of greenhouse gases must reach zero within the next few decades, and even CO_2 must be removed from the atmosphere due to its long residence time.

Today, about 80% of total energy demand is still met by fossil fuels [17, p. 105], which emit large amounts of CO_2 into the atmosphere when burned. The power sector alone is responsible for 42% of the total fossil CO_2 emissions in 2022 [20, p. 9], not including CO_2 emissions from land management. To reduce CO_2 emissions from energy production, a transition of the world's fossil-based economy to one based on renewable energy sources is urgently needed and underway.

Renewable energy sources, which include solar, wind (onshore and offshore), hydro, geothermal, and biomass, offer CO_2 neutral energy production. Combustion of hydrogen produced by electrolysis from renewable electricity and combustion of fossil fuels combined with carbon capture and storage (CCS) are additional technologies to prevent CO_2 emissions into the atmosphere. While some renewable energy sources, such as solar and wind, suffer from short- and long-term fluctuations, biomass, hydrogen, or fossil fuel combustion with CCS can provide large amounts of electricity and heat regardless of seasonal and weather conditions.

The combination of bioenergy conversion processes with CCS technologies has the ability to provide large amounts of electricity and heat while removing the CO_2 from the atmosphere consumed during the growth of the feedstock. Biomass energy with carbon capture and storage (BECCS) is a key technology for CO_2 removal and is an essential part of climate scenarios to achieve the goals of the Paris agreement [18, p. 698].

The global potential of biomass is approximated by various studies that consider the inextricable link between biomass for energy, water consumption, food production, and land-use. Today, biomass provides about 10% of the global energy and there is a potential to increase the energy production from biomass by a factor of 2 to 5 based on the various studies [21, 22].

In this thesis the term BECCS is used exclusively for biomass combustion with CCS, following the definition of Gough et al. [23], while biomass conversion to biofuel by gasification and liquefaction is excluded.

CCS technologies transport CO_2 streams to long-term storages in underground geological formations such as depleted oil and gas fields or saline aquifers (porous and permeable reservoir rocks that contain saline fluid in the pore spaces between the rock grains). In 2023, the annual capture capacity of commercial CCS facilities is 49 Mt [24, p. 11], equivalent to 0.13% of the global energy-related CO_2 emissions in 2022 [20, p. 5]. Taking into account the CCS facilities under construction and in development (storage capacity for 312 Mt CO_2 per year [24, p. 11]), CO_2 capture capacity will increase sharply in the future while energy-related CO_2 emissions will peak before 2030 and start to decline [17, p. 101].

For high CCS process efficiency, the CO_2 stream must be separated from other gases prior to storage. In BECCS, there are several ways to produce high purity CO_2 streams, including pre-combustion capture, post-combustion capture, oxy-fuel combustion, and chemical looping [25]. Each of these technologies results in a penalty to the overall efficiency of the power plant.

In pre-combustion capture, biomass is exposed to a steam of air or oxygen at high temperature and pressure to produce syngas, a mixture of CO and H_2. The syngas is further reacted with steam (water-gas shift reaction) to form CO_2 and H_2, from which CO_2 is separated and H_2 is used as fuel. This technique is advantageous for integrated gasification combined cycle (IGCC) power plants.

Post-combustion methods capture CO_2 from flue gases based on chemical absorption, physical separation, membrane separation, or cryogenic methods. Chemical solvents in the form of amine solvents show the highest efficiencies [26]. This technology can be applied to existing power plants.

In oxy-fuel combustion, biomass is burned in an atmosphere consisting of CO_2, O_2, and H_2O. This is achieved by recirculating large amounts of flue gas into the combustion chamber and adding pure oxygen and fuel. The oxygen is first separated from the air by a cryogenic air separation unit. The flue gas consists mainly of CO_2 and water, which can be easily condensed. This technique can also be retrofitted to existing power plants, although the modifications are larger compared to post-combustion methods.

Chemical looping technology uses a dual fluidized bed system that significantly changes the design of conventional combustors. A metallic oxygen carrier is used to transport oxygen from the air reactor to the fuel reactor where the metal oxide is reduced by a hydrocarbon fuel. The reduced metal is transported back to the air reactor where it is oxidized again. With this technique, the flue gas consists primarily of CO_2 and water, similar to oxy-fuel combustion.

A comparison of the techniques that can be applied to existing power plants for BECCS, pre-combustion capture, post-combustion capture, and oxy-fuel combustion, showed slight advantages in plant efficiency for pulverized fuel combustion power plants operating with oxy-fuel combustion. However, the overall efficiency for oxy-fuel power plants is about 8% lower than for conventional pulverized fuel power plants [26, 27].

The changed combustion atmosphere under oxy-fuel conditions results in significant changes in combustion behavior and flame stability. For effective and reliable design of large-scale oxy-fuel combustion systems, a deep understanding of the relevant chemical and physical processes involved is required. Here, further research is needed and motivates this thesis.

1.2 Current state of research

Oxy-fuel combustion was first proposed in 1982 by Abraham et al. [28] in the context of enhanced oil recovery. Since then, various research groups and consortia have investigated combustion phenomena, conducted pilot-scale studies, and designed demonstration plants. Most studies have focused on

oxy-fuel combustion with coal, while research on biomass combustion under oxy-fuel conditions has become more prominent in recent years.

The state of research has been summarized in several review articles. Wall et al. [25] described the state of research and technology development with a focus on the differences between oxy-fuel combustion and conventional air combustion necessary for boiler retrofits. A comprehensive overview of recent developments in pilot plants and demonstration projects was also provided. The review article by Toftegaard et al. [29] on oxy-fuel combustion of solid fuels highlighted the possible advantages and challenges associated with retrofitting coal-fired power plants and described the possibilities when designing oxy-fuel power plants from scratch. It also summarized work on the process fundamentals of oxy-fuel combustion with a focus on flue gas composition and residual products. Scheffknecht et al. [30] summarized the fundamentals of the oxy-fuel coal combustion process and included modeling of pulverized fuel oxy-fuel combustion and oxy-fuel combustion in circulating fluidized beds. The article by Chen et al. [31] reviewed experimental and numerical studies on the fundamentals of oxy-fuel coal combustion and described the effects of elevated pressures on oxy-fuel coal combustion. Stanger et al. [32] presented an overview of state-of-the-art oxy-fuel applications in pulverized coal combustors, circulating fluidized beds and gas turbine based power plants.

The review articles identified the need for further research in oxy-fuel combustion, including oxy-fuel system design, fundamentals, modeling, numerical simulations, and large-scale demonstrations [25, 29–32]. This thesis addresses the fundamentals of oxy-fuel combustion with the experimental application of advanced optical laser diagnostics. In order to provide the current state of research with respect to the topic of this thesis, the application of optical laser diagnostics to solid fuel combustion is summarized based on the different experimental scales:

- Single and group particle combustion
- Gas-assisted pulverized fuel combustion
- Self-sustained pulverized fuel combustion

Since the application of optical laser diagnostics to oxy-fuel combustion for larger experimental scales is sparse, important experiments on conventional solid fuel combustion are included.

1.2.1 Single and group particle combustion

Single particle combustion studies of micrometer-sized coal or biomass particles are performed to determine ignition delay times and the kinetics of volatile and char combustion, and to reveal differences between combustion in oxy-fuel and air environments. The experiments are conducted in generic systems with well-known boundary conditions that allow the study of the particle combustion process and the physio-chemical interactions between the particle and gas phase with high spatial resolution. In addition, these generic systems allow the analysis of dependencies by variation of single parameters. In group particle combustion experiments, the effect of particle-particle interactions on the combustion process is investigated.

In particular, the research groups of Levendis [33–39], Schiemann [40–43], Shaddix and Molina [44–46], and Böhm and Dreizler [43, 47, 48] conducted various investigations of single and group particle combustion under oxy-fuel conditions.

Laboratory experiments have been performed using test rigs that achieve particle heating rates close to realistic conditions in the order of 10^4 K/s or higher. The studies used drop tube furnaces [33–39, 49–51] or flat flame burners such as the Hencken burner [44–46, 52–54], the McKenna burner [40–42, 55, 56], or the laminar flow reactor [43, 47, 48]. Drop tube furnaces generally heat a fluid flow electrically to 1600 K and solid fuel particles are introduced into the hot flow. Flat flame burners

provide a hot flue gas atmosphere with an adjustable gas mixture into which particles are injected and observed. Further details on the different reactor types are given in [58].

Various optical and laser diagnostics are used to study the combustion process. With low and high speed imaging of single and group particles, the effects of solid fuel type, atmosphere, or particle size on volatile and char combustion times have been studied [34–39, 44–47, 49–56]. Two- or three-color pyrometry has been used to determine particle temperatures within the combustion process [33, 35–43, 50, 51, 53, 55]. High resolution experimental setups were applied to determine particle sizes at different stages of combustion [41, 42, 47, 48]. Laser-induced fluorescence (LIF) of OH was used to define particle ignition [47, 48].

The main results of the single and group particle combustion studies can be summarized as follows:

- The ignition delay time increases when N_2 is replaced by CO_2 due to the 1.7 times higher volumetric heat capacity of CO_2 compared to N_2 [33, 35, 37, 44, 45, 49, 50, 53, 56]. In contrast, Farazi et al. [57] showed in a numerical study that the increase in ignition delay time is related to the depletion of radicals reacting with the abundant CO_2 of the oxy-fuel atmosphere, and that the increased heat capacity can be neglected.
- In the case of similar initial gas-mixture temperatures of oxy-fuel and air combustion atmospheres, faster release of volatiles and ignition under oxy-fuel conditions is observed due to a lower temperature drop in the vicinity of the particle [47].
- Similar particle temperatures during combustion were observed for air and oxy-fuel combustion with an increased oxygen concentration to 30 vol.% to 35 vol.% [33, 37–39, 51].
- Higher oxygen concentrations in the hot gas mixture decrease volatile burn-out times [44, 47, 52] and increase particle surface temperatures due to higher reactivity [33, 35].
- The volatile combustion time is extended in oxy-fuel combustion compared to air combustion due to the lower oxygen diffusivity in CO_2 compared to N_2 [45].
- Lower particle temperatures are observed for particles burning in a group compared to single particle combustion [43].
- Increasing the particle number density in group combustion first leads to a reduction of the ignition delay time until an optimum is reached and increases for higher particle loads [46, 58].

1.2.2 Gas-assisted pulverized fuel combustion

Investigation on gas-assisted pulverized fuel combustion with optical and laser diagnostics include various burner configurations in the range between 5 kW_{th} and 40 kW_{th}. Gas-assistance is required to ignite the solid fuel particles due to the lack of thermal radiation from hot walls caused by the design for good optical access. The studies focused primarily on near-nozzle phenomena and complete solid fuel conversion was not achieved. Multi-parameter investigations were performed in order to improve the understanding of solid fuel combustion.

Studies in this category have been carried out by Balusamy [59, 60] in the research group of Hochgreb, by the Japanese 'Central Research Institute of Electric Power Industry' (CRIEPI) [61–66], by a Korean research group around Sung, Moon, and Li, [67–72] and by Becker [73–75] in the research group of Dreizler.

CRIEPI [61–66] focused on the investigation of a gas-assisted turbulent jet pulverized coal flame with a thermal power in the order of 5 kW_{th}. Studies were conducted in air only. A shadow Doppler particle analyzer was used to determine the velocity and shape of non-spherical coal particles along with a two-color pyrometer to estimate particle temperatures [61, 63]. It was observed that small particles

decrease in size with increasing distance from the burner due to char combustion while large particles increase in size due to particle swelling during devolatilization [63]. The velocity magnitudes of different particle sizes were similar in the central jet region, while they differed in the outer shear layers. Simultaneous measurements of OH planar laser-induced fluorescence (OH−PLIF) and Mie scattering were performed to investigate the spatial relationships of combustion reaction zones and pulverized coal particles [61, 62]. The investigations showed different combustion phenomena with increasing distance from the burner due to mixing of the cold coal particle jet and the hot methane pilot flame [62]. Soot formation was studied by applying laser-induced incandescence (LII) in combination with Mie scattering and OH−PLIF [64], time-resolved LII (TiRe-LII) [65], and a simultaneous approach of LII, Mie scattering, and LIF of polycyclic aromatic hydrocarbons (PAHs) [66]. Their results showed enhanced soot formation when particles were located in regions of high temperature and low oxygen concentration [64] and increasing soot volume fractions and primary soot particle diameters for higher residence times [65]. A sequential appearance of coal particles, PAHs, and soot in the radial direction, implying longer residence times necessary for soot formation, was observed [66].

Studies by Sung et al. [67, 70, 71], Moon et al. [68, 69] and Li et al. [72] focused on a gas-assisted coaxial jet burner [67–69] and a gas-assisted dual swirl pulverized coal combustion burner [70–72]. The burners were operated in the thermal power range between 5 kW_{th} and 10 kW_{th} and only air conditions were investigated. Chemiluminescence imaging of CH* showed higher heating rates for small coal particles and a dependence of particle size and volatile matter content on combustion time [67]. The different combustion characteristics of low rank coals and biomass were investigated using high-speed imaging, two-color pyrometry, and CH* chemiluminescence. It was observed that the addition of biomass to coal combustion improved ignition and promoted reactivity [68]. Based on CH* chemiluminescence images, three zones, preheating, volatile matter reaction, and char reaction, could be identified [69]. PIV measurements, two-color pyrometry, and chemiluminescence imaging of CH* and OH* were performed to elucidate the effect of swirl number on combustion. For high swirl conditions, a larger inner recirculation zone (IRZ) is formed and lower temperatures were observed [70, 71]. Variation of coal particles size showed a decrease in IRZ size, temperature, and OH* intensity with increasing particle size [72].

Balusamy et al. [59, 60] studied a gas-assisted pulverized coal burner under air and oxy-fuel operation conditions at approximately 20 kW_{th}. Flow field measurements were performed using laser Doppler velocimetry (LDV) and particle image velocimetry (PIV) techniques to prove the applicability of these diagnostics to particle-laden reacting flows [59]. Simultaneous Mie scattering and OH−PLIF measurements in combination with LII and LDV techniques were used to study the reaction zone under different particle loads and varying operation conditions. The results showed instantaneous devolatilization of particles upon crossing the flame interface and increasing velocities due to thermal expansion with increasing O_2 content [60].

Becker [73–75] has designed an optically accessible combustion chamber that operates gas-assisted swirl flames in air and oxy-fuel conditions up to 40 kW_{th}. The burner exhibits important characteristics of a state-of-the-art combustor, including a quarl connecting the nozzle and combustion chamber. Flame stabilization is investigated by stereoscopic PIV, OH-PLIF and broadband chemiluminescence. Stabilization in the form of a diffusion flame near the nozzle was observed, while further downstream premixed combustion regimes were suspected [73]. An approach to simultaneously measure flow and particle velocities was developed and slip velocities were calculated for non-reactive conditions [74]. This approach was then applied to reactive conditions and additional PAH-LIF measurements were performed. Regions of intense pyrolysis were identified and mechanisms of flame stabilization were investigated [75].

1.2.3 Self-sustained pulverized fuel combustion

Optical and laser diagnostic studies on self-sustaining pulverized fuel combustion have been performed on combustors ranging from 40 kW_{th} to 1 MW_{th}. Typically, optical access is small in these combustors, limiting measurements to certain regions of the combustion process. It should be noted that the gap towards oxy-fuel pilot plants such as the 'Schwarze Pumpe' [76] (30 MW_{th}) or pulverized coal power plants (> 1 GW_{el}) is still large.

Several studies using optical and laser diagnostics on self-sustained solid fuel combustion under air and oxy-fuel conditions were performed in the research group of Kneer at the RWTH Aachen (Germany) [77–88] and at the Brigham Young University from Utah (USA) [89–92]. Recently, a 1 MW_{th} oxy-fuel research combustion chamber was put into operation at the Technical University of Darmstadt (Germany) [16], where optical and laser diagnostics can be applied. In addition, several demonstration studies on the possibility of Coherent anti-Stokes Raman spectroscopy (CARS) measurements in pulverized coal combustion have been performed [93–96]

The test facility at RWTH Aachen operates a down-fired combustion chamber that is 4 m long and has a diameter of 400 mm. Swirl flames up to 120 kW_{th} can be stabilized. Optical access is provided by three ports at one level and the burner can be moved vertically to measure at different levels. A special burner design has been developed to stabilize oxy-fuel flames with low oxygen concentrations down to 21 vol.% [77, 78]. Flame stability for air and oxy-fuel combustion was determined by LDV measurements and OH* chemiluminescence imaging. A close relationship between the momentum flow through the burner and the flame shape was observed [79] and flame structures and characteristics were identified [80]. LDV and PIV measurements were compared with respect to performance in particle-laden reacting flows [82]. Flame and particle radiative properties were investigated using a non-intrusive narrow-angle optical system and an intrusive cold-background optical probe. Particle temperatures and relative radiant fluxes were evaluated by comparison with the Planck blackbody radiation function. A strong impact of oxidant composition on flame radiation and measured temperatures was found [83]. The effects of oxidant O_2 concentration on the flow field were studied using LDV, narrow-band chemiluminescence imaging, and cold-background optical probe. Oxygen concentrations within the oxy-fuel atmosphere were varied between 23 vol.% and 33 vol.%. Increased velocities in the the main vortex were observed for higher oxygen concentrations, while the size of the IRZ became smaller. This effect was attributed to the modified swirl due to the higher expansion of the product gases in oxy-fuel combustion with high oxygen concentrations [84]. Similar flame structures were observed while the local flame intensity was increased at higher oxygen levels. In addition, a linear increase in particle temperatures with increasing oxygen concentration was found [85]. An analysis of flow patterns between air and oxy-fuel combustion at 25 vol.% O_2 concentration showed that the flame length is primarily controlled by the effective swirl intensity and that the flow inlet conditions control the position of the peak combustion intensity [86]. A comparison between coal (lignite) and torrefied biomass combustion was made using LDV and an ellipsoidal radiometer to measure flow fields and radiative heat fluxes. Similar overall combustion characteristics were observed, while radiative heat fluxes were higher for torrefied biomass combustion [87]. The effect of methane assistance on pulverized biomass combustion was investigated by varying the proportion of methane to the thermal output between 0% and 50%. LDV and narrow-band flame imaging were performed and showed a significant influence of methane assistance on ignition, flow field, and flame shape leading to flame stabilization closer to the burner [88].

The Controlled Profile Reactor is a combustion facility in the thermal power range between 200 kW_{th} and 400 kW_{th} and is operated at Brigham Young University. The combustor is down-fired, stabilizes swirling pulverized coal flames, and has a chamber with a length of 2.4 m and an inner diameter of 800 mm. Optical access is provided by multiple optical ports at different chamber heights. Tree et al. [90] summarized several investigations that were primarily performed with intrusive measurement probes to measure gas species, gas temperature, particle velocity, particle size, and particle number

density. Optical diagnostics included two-color pyrometry to determine particle cloud temperature profiles and a radiation probe to quantify flame intensity. In addition, CARS measurements were performed to measure gas temperatures [89]. The results showed that heat transfer is dominated by radiation from particles and that particle size influences many aspects of the combustion process such as particle trajectories, dispersion, devolatilization and burnout. They emphasized that significant advances in the understanding and prediction of pulverized combustion have been achieved through the integrated approach of extensive measurements and modeling efforts. The effects of swirl intensities were evaluated using laser Doppler anemometry (LDA). The results showed the establishment of an IRZ for swirl numbers above 0.5 [91, 92].

1.3 Aim and structure of this work

This thesis addresses the complex fluid-mechanical, particle-dynamical and chemical processes and their interactions in the combustion of pulverized solid fuels under oxy-fuel conditions. The current state of research has shown that multi-parameter studies are valuable to improve our understanding of pulverized solid fuel combustion. While many studies have focused on single and group particle combustion, investigations of complex, more application-oriented configurations under oxy-fuel conditions are sparse. In addition, most of the research has been conducted with different coals, while the application of pulverized biomass for BECCS technology is promising. To improve our understanding, optical laser diagnostics are applied to the oxy-fuel combustion chamber designed by Becker [73] which have the possibility to measure flow and scalar fields in-situ with high spatial and temporal resolution while being non-invasive or minimal invasive.

The aims of this thesis can be summarized as follows:

1. Improve our understanding of the combustion of pulverized solid fuels under oxy-fuel conditions, with a focus on biomass combustion. This requires the analysis of a comprehensive data set of flow and scalar fields to investigate the intricate interplay between complex fluid mechanical, particle-dynamical, and chemical processes.
2. Develop, improve, and apply various advanced optical laser diagnostics to pulverized solid fuel combustion in oxy-fuel atmospheres to create a comprehensive data set.
3. Creation of a large experimental database for validation of numerical simulations and model improvements. This is important for the development of a physics-based, efficient simulation method for effective and reliable design of large-scale oxy-fuel combustion systems in the future.

This thesis is divided into 7 chapters.

In Chapter 2, fundamental aspects of solid fuel combustion are outlined, including fluid dynamics, single-phase and multiphase reactive flows, solid fuel composition, combustion process of solid fuels, and oxy-fuel combustion. The basic principles of the optical laser diagnostics used in this thesis are presented.

Chapter 3 describes the solid fuel combustor (SFC) used for the investigations in this thesis, including modifications from the design by Becker [73], operation conditions, and employed solid fuels. Thermal boundary conditions are provided by thermocouple and thermographic phosphor thermometry (TPT) measurements.

In Chapter 4, a comprehensive investigation of the flow dynamics and temperatures of solid fuel particles is performed to support our understanding of flame stabilization, burnout behavior, and burnout rate. To provide an insight into particle conditions at different stages of the combustion process, various optical laser diagnostics are used. Gas phase velocities are determined using PIV in combination

with a particle separation algorithm. Trajectories of large solid fuel particles are evaluated in a two-dimensional plane using a combined high-speed PIV/PTV approach. Particle temperatures and sizes are measured using two-color pyrometry.

Chapter 5 provides an analysis of the influence of oxygen concentration on oxy-fuel combustion in the near-nozzle region. Effects on flame stabilization, pollutant formation and the combustion process of biomass particles are investigated. A large data set is measured, including CH* chemiluminescence imaging, gas and solid phase flow velocities, gas temperatures, and qualitative soot measurements, including visualization of PAH occurrence as soot precursors.

In Chapter 6, a study of thermochemical states in single-phase and gas-assisted pulverized biomass combustion under oxy-fuel and air atmospheres is presented. The laser diagnostic of coherent anti-Stokes Raman spectroscopy (CARS) is extended to the simultaneous measurement of O_2 and CO_2 with CARS. The novel O_2-CO_2-CARS approach is thoroughly quantified in terms of accuracy and precision and subsequently applied to single-phase and gas-assisted pulverized biomass combustion.

Chapter 7 summarizes the presented results and findings. In addition, remaining open questions for further research from the author's perspective are outlined.

2 Fundamentals

In this chapter, the fundamentals that form the basis of the research conducted in this thesis are described, providing a solid groundwork for a comprehensive understanding of the subsequent analyses and findings. The first two sections cover fundamental aspects of the research object, while the third section summarizes the basic principles underlying the optical laser diagnostics that are applied to the research object in this thesis.

The fundamental aspects of the research object are divided into fluid dynamics and combustion, and solid fuel combustion. The section fluid dynamics and combustion deals with the phenomenological fundamentals in turbulent flows, swirling flows, single-phase reactive flows and multiphase reactive flows by introducing important definitions and characteristic numbers. The section on solid fuel combustion is more application-orientated and deals with the composition and properties of solid fuels and the combustion process of solid fuels. Additionally, an introduction to oxy-fuel combustion and its changes to conventional combustion under air is provided.

The section on optical laser diagnostics covers measurement techniques that enable the in-situ and minimal-invasive determination of flow, scalar fields, particle properties, and pollution formation with high spatial and temporal resolution. The basic principles of the optical laser diagnostics applied within this thesis are discussed, including chemiluminescence imaging (CL), particle image and particle tracking velocimetry (PIV/PTV), laser-induced fluorescence (LIF), thermographic phosphor thermometry (TPT), coherent anti-Stokes Raman spectroscopy (CARS), absorption spectroscopy, pyrometry, and laser-induced incandescence (LII). Details on the specific application of these optical laser diagnostics are provided in the methods sections of chapters 3.3 to 6.

In the following, a brief overview is given and references are provided for more specific details.

2.1 Fluid dynamics and combustion

2.1.1 Turbulent flows

Turbulent flows are an important part of fluid dynamics and omnipresent in nature, engineering, and industrial applications. Turbulent flows are characterized by their inherent complexity, marked by chaotic and random fluctuations in fluid velocity and pressure. Considerable research efforts have been made in the field of turbulent flows. In the following, a brief introduction into the basics of turbulent flows is given, mostly inspired by the seminar book of Pope [97]. The description provided below is collected from these sources and others, as indicated.

Reynolds number In general, flows can be divided into laminar and turbulent flows. While laminar flows exhibit a smooth, orderly flow of fluid, turbulent flows show a chaotic, unpredictable movement of fluid. Turbulent flows have the characteristic to mix and transport fluids very effectively, making this type of flow favorable for combustion applications. The dimensionless quantity to predict the type of flow is the Reynolds number Re, which compares inertial forces to viscous forces in the flow. The Reynolds number Re is defined as:

$$\mathrm{Re} = \frac{\mathscr{U}\,\mathscr{L}}{\nu} \tag{2.1}$$

Here, $\mathscr{U}$ and $\mathscr{L}$ are characteristic velocity and length scales of the flow, and ν is the kinematic viscosity of the flow. As Re becomes large enough, the transition from laminar to turbulent flow occurs.

Mathematical description Mathematically, fluid flows, including turbulent flows, of Newtonian fluids can be fully described by the continuity and Navier-Stokes equations, which ensure the conservation of mass and momentum:

$$\frac{\partial \rho}{\partial t} + \nabla \cdot (\rho \mathbf{u}) = 0 \tag{2.2}$$

$$\frac{\partial (\rho \mathbf{u})}{\partial t} + (\rho \mathbf{u} \cdot \nabla)\mathbf{u} = -\nabla p + \nabla \cdot \boldsymbol{\tau} + \rho \mathbf{g} \tag{2.3}$$

t, ρ, $\mathbf{u}$, p and $\mathbf{g}$ designate time, density, flow velocity, pressure and body force, respectively. $\boldsymbol{\tau}$ represents the viscous stress tensor and is calculated for a Newtonian fluid as follows:

$$\tau = \mu\left((\nabla \mathbf{u} + (\nabla \mathbf{u})^t) - \frac{2}{3}(\nabla \cdot \mathbf{u})\mathbf{I} \right) \tag{2.4}$$

In Equation (2.4), μ represents the dynamic viscosity and $\mathbf{I}$ is the identity matrix.

Statistical description of turbulence As described before, turbulent flows exhibit a random nature. This contrasts the classical mechanics embodied in the Navier-Stokes equations, revealing a deterministic motion. The random nature of turbulent flows arise from unavoidable perturbations in initial conditions, boundary conditions and material properties and the acute sensitivity of the turbulent flow to such perturbations. To better predict turbulence, a statistical description is introduced by dividing the velocity into a mean velocity $\bar{u}$ and fluctuation of the velocity u', also known as the Reynolds decomposition:

$$u = \bar{u} + u' \tag{2.5}$$

A statistically full description of the velocity distribution at a certain location over time can be achieved with the probability density function (PDF). In practice, mostly the first and second-order moments of the PDF are used, representing the mean velocity and the variance. The square root of the variance is the standard deviation, also known as the RMS (root mean square) value. The denotation of the RMS value is commonly used in the scientific community in the field of solid fuel combustion and is therefore used in this thesis. The first and second-order moments of the PDF over the time period T are calculated as follows:

$$\bar{u} = \frac{1}{T}\int_0^T u(t)dt \tag{2.6}$$

$$u_{\mathrm{rms}} = \sqrt{\overline{u'^2}} = \sqrt{\frac{1}{T}\int_0^T (u(t) - \bar{u})^2 dt} \tag{2.7}$$

The mean velocity $\bar{u}$ as well as RMS values u_{rms} are typical quantities that can be measured in experiments, as outlined in Section 2.3.2.

Turbulent scales A further feature to consider when performing experiments on turbulent flows are the scales of turbulence. Turbulent flows exhibit a wide range of scales that span from the largest coherent structures defined by the flow boundaries to the smallest turbulent eddies, which are an intrinsic feature of the flow. The large eddies contain most of the kinetic energy and are responsible for the dominant motions of the flow. They can be described by the integral length and time scales: l_0 and t_0. l_0 is typically in the order of the characteristic length scale $\mathscr{L}$ of the flow and the integral time scale is defined as $t_0 = l_0/u_0$, where u_0 represents the velocity magnitude of the large eddies in the flow. The integral time scale t_0 describes the time span in which velocity fluctuations are correlated for a distinct location.

The large eddies transfer their kinetic energy to smaller eddies through a process described as the energy cascade. Thereby the transfer of energy occurs as larger eddies break down into smaller ones. The energy cascade continues until it reaches the smallest scales of turbulence, known as the Kolmogorov scales. At this point, the kinetic energy is dissipated into thermal energy due to the effects of fluid viscosity. The Kolmogorov scales, Kolmogorov length scale l_η, Kolmogorov velocity scale u_η and Kolmogorov time scale t_η, are determined by the kinematic viscosity ν and the turbulent dissipation rate ϵ:

$$l_\eta = \left(\frac{\nu^3}{\epsilon}\right)^{1/4} \tag{2.8}$$

$$u_\eta = (\nu\epsilon)^{1/4} \tag{2.9}$$

$$t_\eta = \left(\frac{\nu}{\epsilon}\right)^{1/2} \tag{2.10}$$

With the definition of the turbulent Reynolds number $Re_t = u_0 l_0/\nu$, the Kolmogorov scales can be expressed as a function of the turbulent Reynolds number and the relation between turbulence intensity and smallest scales within the flow become obvious:

$$l_\eta = l_0 Re_t^{-3/4} \tag{2.11}$$

$$u_\eta = u_0 Re_t^{-1/4} \tag{2.12}$$

$$t_\eta = t_0 Re_t^{-1/2} \tag{2.13}$$

For experiments the knowledge about the Kolmogorov scales is of great importance as it can be compared against optical and time resolution. If the resolution in the experiments is larger than the Kolmogorov scales an experiment-related filtering happens.

2.1.2 Swirling flows

Swirling flows represent a special configuration of turbulent flows and are of great relevance within combustion chambers, as explored in this thesis. The creation of swirling flows leads to an efficient mixing of reactants and substantially support flame stabilization. Additionally, process control and adjustment are achievable through modulation of swirl intensity. This section provides a fundamental overview of swirling flows based on the work of Beér and Chigier [98].

Swirl number The introduction of swirl to a fluid flow induces radial and axial pressure gradients, subsequently impacting the flow field. Under significant swirl, the amplified negative axial pressure gradient leads to a reversed flow along the axis, establishing an inner recirculation zone (IRZ). A measure for the swirl intensity is the swirl number S which is defined as the ratio of the axial flux of tangential momentum G_θ to the axial flux of axial momentum G_x times a characteristic radius R [98, p. 106 f.]. The swirl number S is further modified by Sheen et al. [99] for a radial-type swirl generator as:

$$S = \frac{G_\theta}{R \cdot G_x} = \frac{\int_0^\infty u_x u_\theta r^2 dr}{R \cdot \int_0^\infty u_x^2 r dr}, \tag{2.14}$$

where u_x, u_t and r represents the axial and tangential velocities and the radius, respectively. While G_θ and G_x are constant for unconfined swirling flows, they will not remain constant for confined flows due to the effects of the confined boundary [99].

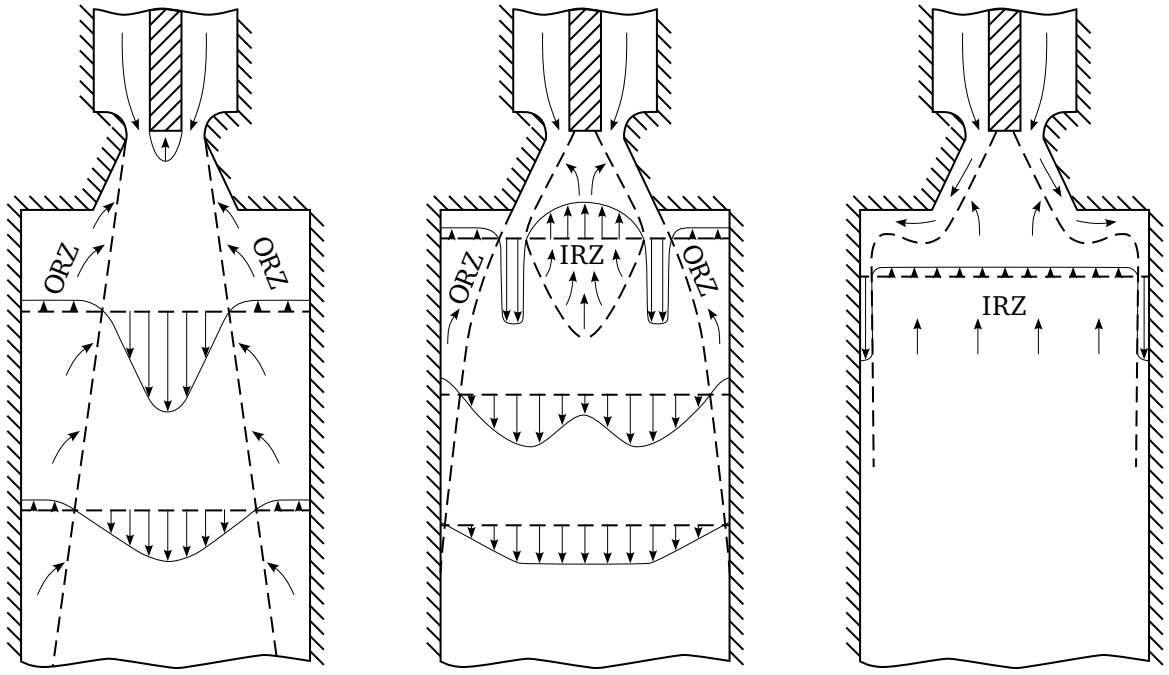

Figure 2.1: Basic flow types observed for swirling jets and flames issuing from divergent nozzles. Illustration adapted from [98, p. 125].

Flow types of swirling flows Depending on the value of the swirl number, Leuckel [100] classified three basic flow types based on experimental investigations of swirling jets and flames issuing from divergent nozzles. The different flow types are illustrated in Figure 2.1. In this configuration, two modifications were incorporated into the design compared to simple axial swirled jets, which can enhance swirl stabilization if designed accordingly. The introduction of a central bluff body creates a recirculation zone in the wake of the bluff body, even without the presence of any swirl. This phenomenon occurs as the inflow velocities reach a magnitude that induces a large enough negative pressure gradient downstream the bluff body to cause separation of the boundary layers. Additionally, a divergent nozzle extension, also referred to as a quarl, is incorporated. The quarl serves to expand the radial

separation between the peaks of the axial and tangential velocities by increasing the opening to the combustion chamber and the flow direction away from the center. Simultaneously, the reverse mass flow rate within the configuration is enhanced [98, p. 124].

Flow type A in Figure 2.1 is characterized by a weak swirl, resulting in a flow pattern similar to that of a non-swirling jet. In this configuration, the comparable small IRZ solely arises due to the presence of the bluff body. With a medium or high degree of swirl, flow type B is established. Here, the flow remains stably attached to the walls of the quarl, enclosing a much larger IRZ. This flow type is particularly advantageous for combustors, as it facilitates flame stabilization with ignition close to the nozzle exit. Within flow type B, the size of the IRZ is positively correlated with the swirl number [98, p. 126 f.]. From the outside fluid is drawn into the flow and given an enclosed chamber, an outer recirculation zone (ORZ) is formed. Flow type C represents the radial wall jet, which occurs at even higher swirl numbers. This flow pattern is strongly influenced by both the inlet conditions and the geometry of the divergent nozzle. In flow type C, the flow is directed towards the walls, resulting in the prominent presence of a very large IRZ at the center.

Notably, the design exerts a substantial influence on the resultant flow type and the extent of the IRZ, in addition to the influence of the swirl number itself. As previously mentioned, the inclusion of bluff bodies and divergent nozzle extensions can enhance swirl stabilization. Moreover, downstream elements, like exit constructions, can exert a substantial influence on the resulting flow patterns [101].

Creation of swirling flows Various designs can be employed to generate swirling flows. Boushaki [102] classifies these approaches into three distinct categories:

(i) Fins or adjustable propellers that tangentially deflect the axial flow

(ii) Rotating mechanical devices which generate a rotational movement to the fluid passing between them

(iii) Tangential injection of parts or all fluid quantity into a main duct

The combustion chamber examined in this thesis employs swirl generation of type (iii). In this configuration, swirl intensity is modulated by adjusting the ratio of tangentially injected flow to axially injected flow, all without the inclusion of any moving components. This constant and non-moving design proves highly advantageous for numerical simulations.

2.1.3 Single-phase reactive flows

Single-phase reactive flows combine the two fundamental research areas of fluid dynamics and combustion science. The fundamentals of fluid dynamics, as discussed in preceding sections, remain applicable for reactive flows, while combustion adds additional complexity. Single-phase reactive flows encompass the transport and chemical conversion of species within a single, homogeneous fluid phase, which is mostly gaseous, as exemplified by the methane flame employed in this study to assist solid fuel combustion. Classical descriptions for combustion fundamentals are provided by Glassman et al. [103] and Warnatz et al. [104]. A well-structured introduction to turbulent reacting flows is given by Cant and Mastorakos [105]. This section summarizes important fundamentals from these sources.

Mathematical description In addition to the continuity (Equation (2.2)) and Navier-Stokes (Equation (2.3)) equations, the set of governing equations for reactive flows is extended by the energy and species conservation equations:

$$\frac{\partial(\rho h)}{\partial t} + \nabla \cdot (\rho \mathbf{u} h) = \frac{\partial p}{\partial t} + \nabla \cdot (\mathbf{u} p) + \nabla \cdot (\lambda \nabla T) + \nabla \cdot \left(\rho D \sum_{\alpha=1}^{N} h_\alpha \nabla Y_\alpha \right) + q_\mathrm{R} \tag{2.15}$$

$$\frac{\partial(\rho Y_\alpha)}{\partial t} + \nabla \cdot (\rho \mathbf{u} Y_\alpha) = \nabla \cdot (\rho D \nabla Y_\alpha) + \omega_\alpha \tag{2.16}$$

The energy conservation is formulated in terms of specific enthalpy h, neglecting viscous heating and acoustic interactions. In Equations (2.15) and (2.16), λ represents thermal conductivity, T the temperature, D the diffusion coefficient, Y_α the mass fraction of species α, h_α the specific enthalpy, q_R the radiation source term, and ω_α the chemical source term. For the species conservation Fick's law of diffusion is employed and an equal diffusion coefficient D for all species is assumed. The gas mixture consists of N species, consequently the species conservation equation has to be solved for N-1 species.

The chemical source term ω_α can be described as the net rate of production and consumption of species α. In chemical reactions, mass is neither created nor destroyed, leading to $\sum_{\alpha=1}^{N} \omega_\alpha = 0$. The species and elementary chemical reactions considered are contingent on the particular system under investigation and are consolidated into a chemical mechanism. An example of a well-established chemical mechanism for natural gas combustion is the GRI 3.0 mechanism [106], which encompasses 53 species and 325 reactions. Given the significance of hydrocarbon combustion within this thesis, Equation (2.17) represents the global chemical reaction for hydrocarbons. However, to describe the combustion of hydrocarbons satisfactorily necessitates the incorporation of numerous elementary reactions.

$$\nu'_{\mathrm{C_xH_y}}\,\mathrm{C}_x\mathrm{H}_y + \nu'_{\mathrm{O_2}}\,\mathrm{O_2} \longrightarrow \nu''_{\mathrm{CO_2}}\,\mathrm{CO_2} + \nu''_{\mathrm{H_2O}}\,\mathrm{H_2O} \tag{2.17}$$

The parameters ν' and ν'' represent the stoichiometric coefficients of the reactants and products, respectively. When the reactants are entirely consumed and only the products CO_2 and H_2O are present, the combustion process is described as stoichiometric.

Stoichometric ratio The dimensionless parameter to quantify the relative amount of fuel and oxidizer in a combustion mixture compared to the stoichiometrically ideal ratio required for complete combustion is the equivalence ratio ϕ or its reciprocal value λ, which is used in this thesis. λ is defined as the ratio of the stoichiometric fuel-to-oxidizer ratio required for complete combustion to the actual fuel-to-oxidizer ratio:

$$\lambda = \frac{1}{\phi} = \frac{(Y_\mathrm{fuel}/Y_\mathrm{ox})_\mathrm{st}}{(Y_\mathrm{fuel}/Y_\mathrm{ox})} \tag{2.18}$$

The value $\lambda = 1$ indicates stoichiometric conditions, while values of $\lambda < 1$ represent a fuel-rich mixture and values $\lambda > 1$ indicate a fuel-lean mixture.

Adiabatic flame temperature The conversion of reactants to products is typically an exothermic process in combustion meaning that energy is released. This results in a temperature increase of the gas mixture. The highest achievable temperature for the gas mixture is the adiabatic flame temperature T_{ad}, where heat losses to the surroundings are neglected. T_{ad} can be calculated iteratively using Equation (2.19) [104, p. 51]. This equation is derived from the first law of thermodynamics, which requires equal specific enthalpy for reactants and products in a closed adiabatic system under constant pressure.

$$\sum_{\alpha=1}^{N} h_{\alpha}^{(\mathrm{product})} = \sum_{\alpha=1}^{N} \left(h_{\alpha}^{(\mathrm{reactant})} + \int_{T_0}^{T_{\mathrm{ad}}} c_{p,\alpha} dT \right) \tag{2.19}$$

T_0 is the temperature of the gas mixture before combustion and c_p is the heat capacity.

Turbulent flame types Depending on the supply of fuel and oxidizer to the flame, two primary flame types can be categorized: premixed flames and non-premixed flames. In premixed flames, the fuel and oxidizer are mixed before the combustion process. In contrast, non-premixed flames are characterized by simultaneous mixing and combustion, meaning that fuel and oxidizer are introduced separately and mix within the combustion zone. In solid fuel combustion, typically non-premixed or partially premixed flames, which are outside of the flammability limits, are present due to safety reasons. Hence, non-premixed flames are discussed in more detail here.

Within non-premixed flames, the mixing of reactants and the chemical reaction rate are the dominant processes for fuel conversion. The mixing of fuel and oxidizer depends on the molecular transport, which is significantly amplified by turbulence. The chemical reaction rate is a function of the local gas mixture, the local temperature and pressure. To quantify the ratio between the physical timescale of mixing τ_{phys} and the chemical timescale τ_{chem}, the non-dimensional Damköhler number Da is employed:

$$\mathrm{Da} = \frac{\tau_{\mathrm{phys}}}{\tau_{\mathrm{chem}}} \tag{2.20}$$

For turbulent combustion of hydrocarbon fuels at atmospheric conditions, the chemistry is generally much faster than the mixing, leading to $\mathrm{Da} \gg 1$. The reaction zone is typically thin and wrinkled due to turbulence and consists of regions with varying mixtures of fuel and oxidizer. In contrast, the chemistry of pollutant formation or consumption is much slower and physical and chemical timescales are in the same order of magnitude [105, p. 9].

2.1.4 Multiphase reactive flows

Multiphase reactive flows extend the single-phase reactive flows discussed in the previous section towards two or more distinct phases (e.g., gas, liquid, solid), which coexist and interact. These phases may exist in various combinations, such as gas-liquid, liquid-liquid, or gas-liquid-solid, and they can exhibit complex behaviors, including mixing, separation, dispersion, transfer of mass, momentum, and heat and phase transitions. In pulverized combustion systems regarded in this thesis, the gas-solid interaction plays an important role and will be discussed in more detail in this section. The fundamentals are summarized based on Michaelides et al. [107] and Balachandar and Eaton [108] with a focus on particle-fluid and particle-particle interactions. In addition, the process of solid fuel combustion is discussed in detail in Section 2.2.

Mathematical description For gas-solid multiphase reactive flows all phases need to be described, including their interactions. The gas phase is described by the continuity, the Navier-Stokes, and the energy and species conservation equations, as shown in the previous sections. In turbulent multiphase reactive flows, particularly in scenarios involving particle-laden flows such as pulverized solid fuel combustion, the Lagrangian point-particle approach is widely used [108]. This approach does not fully resolve the particles' boundary layers and instead describe their cumulative behavior based on the equation of motion to track the position and employing the mass, momentum, and energy conservation equations for the particles. At the gas-solid interface mass, momentum, and heat transfer have to be considered. This can be covered for the gas phase by source terms for mass S_m, momentum S_u, energy S_h, and species S_{Y_α}, which are added to the right side of the Equations (2.2), (2.3), (2.15), and (2.16), respectively. The coupling of the solid phase can be implemented through the gas phase quantities required in the particle equations [109].

Here, no general equations for the mathematical description of the solid phase and the gas-solid interface are provided. The formulation of these equations heavily depend on the situation as described by Michaelides et al. [107, p. 18 ff.] and Balachandar and Eaton [108]. Formulations for solid fuel combustion are derived for example by Farmand et al. [110] for single and group particle combustion and by Nicolai [111] for solid fuel combustion at laboratory scale.

Flow regimes One critical parameter that determines the particle-fluid and particle-particle interactions in the governing equations is the overall flow regime. Depending on the volume fraction ϕ_v and mass fraction ϕ_m of the solid phase, the flow regime can be divided into dilute and dense flows.

$$\phi_\mathrm{v} = \frac{V_\mathrm{p}}{V} \tag{2.21}$$

$$\phi_\mathrm{m} = \frac{V_\mathrm{p}\rho_\mathrm{p}}{V\rho} = \frac{m_\mathrm{p}}{m} \tag{2.22}$$

V_p, ρ_p and m_p represent the volume, the density and mass of the particle phase, while V, ρ and m are the total values, respectively. According to Elghobashi [112], dilute flows are characterized by $\phi_\mathrm{v} < 10^{-3}$, while dense flows exhibit $\phi_\mathrm{v} > 10^{-3}$ for small particles that follow the flow instantaneously. This separation slightly shifts to lower volume fractions for larger particles and flows with higher Reynolds number.

In very dilute flows ($\phi_\mathrm{v} < 10^{-6}$) particles are influenced by the turbulent flow, while the influence in the opposite direction can be neglected (one-way coupling). With increasing ϕ_v the back influence of the particles onto the turbulent flow becomes evident (two-way coupling). For dense flows also particle-particle interactions have to be considered (four-way coupling) in the governing equations.

In practical applications, the solid phase is neither distributed homogeneously in space nor time and often all flow regimes occur simultaneously within solid fuel combustion. This results from the design of the particle feeding system and additionally due to preferential concentration of particles caused by turbulence [113].

Stokes number To characterize the behavior of solid particles suspended in a fluid flow, the dimensionless Stokes number St is introduced. It quantifies the relative importance of inertial forces to viscous forces acting on the particles by calculating the ratio of the momentum timescale of the particle τ_p to the characteristic timescale of the flow τ_f:

$$\mathrm{St} = \frac{\tau_\mathrm{p}}{\tau_\mathrm{f}} \tag{2.23}$$

For τ_f two different definitions can be found in literature. Within this thesis τ_f is defined as the ratio of the characteristic velocity u_0 to the characteristic length of the flow l_0: $\tau_\mathrm{f} = u_0/l_0$. However, also the Kolmogorov time scale t_η (Equation (2.13)) is often used as τ_f. When assuming a spherical particle with the particle diameter d_p, τ_p is calculated as [107, p. 5]:

$$\tau_\mathrm{p} = \frac{d_\mathrm{p}^2 \rho_\mathrm{p}}{18\mu} \tag{2.24}$$

For $\mathrm{St} \ll 1$ the particle responds to changes in the flow instantaneously and follows the flow streamlines closely, while for $\mathrm{St} \gg 1$ particles detach from the flow and exhibit little influence by turbulent vortices. For $\mathrm{St} \approx 1$ particle and fluid timescales are in the same order and particles respond strongly to turbulent vortices, possibly leading to preferential concentrations [113]. For gas velocity measurement techniques relying on tracer particles, $\mathrm{St} < 0.1$ should be achieved for the tracer particles to have an accuracy error below 1% [114, p. 289].

Particle Reynolds number As described before, particles featuring a large enough Stokes number St, detach from the surrounding fluid flow and exhibit a relative velocity to the gas phase, called slip velocity. Based on the slip velocity u_s, the particle Reynolds number Re_p can be derived as:

$$\mathrm{Re}_\mathrm{p} = \frac{u_\mathrm{s} d_\mathrm{p}}{\nu} \tag{2.25}$$

The particle Reynolds number Re_p is a characteristic measure for the fluid flow around a particle and thus serving as an indicator of potential turbulence generation or dissipation due to particle presence. While for low Re_p turbulence attenuation occurs, significant turbulence augmentation is observed for $\mathrm{Re}_\mathrm{p} > 280$ due to particle-induced turbulence generation by vortex shedding [115]. Turbulence attenuation for low Re_p is also observed to increase monotonically with the particle mass fraction ϕ_m in the flow [108].

In solid fuel combustion, the description of multiphase reactive flows is even more complex. Particles exhibit diverse sizes, resulting in distinct size distributions and the assumption of spherical particles highly simplifies the real shapes of the solid fuel particles. To derive a better understanding of multiphase reactive flows, a good characterization of the used particles is inevitable.

2.2 Solid fuel combustion

2.2.1 Composition and properties of solid fuels

Solid fuels, which encompass a diverse array of materials such as coal, biomass, and waste-derived fuels, play a pivotal role in meeting global energy demands. The main focus of this thesis is on pulverized biomass combustion, while coal is also considered in the investigations.

Biomass, in general, refers to organic material derived from living or deceased organisms [116, p. 29]. Within the ecological context, biomass can be categorized into primary, secondary, and tertiary biomass. Primary biomass originates directly from the photosynthetic conversion of solar energy and encompasses organic matter derived from agricultural and forestry sources. Secondary biomass, on the other

hand, is a product of the decomposition or transformation of organic material within higher organisms, such as animals. Tertiary biomass, distinctively, emerges from one or more technical processes applied to primary and, to some extent, secondary biomass [117, p. 3]. For power and heat generation, primary biomass sources are mainly employed.

The composition and molecular structure of biomass derived from agricultural and forestry sources are constituted to 85-90% of lignin, cellulose, and hemicellulose. The rest are organic extractives and inorganic minerals [118]. This composition imparts specific properties to various types of biomass. The precise composition may vary among different biomass sources, however cellulose is the predominant organic component. Furthermore, woody biomass typically exhibits a higher lignin content compared to herbaceous biomass [119].

Biomass is considered as a renewable solid fuel, in contrast to coal, which falls under the category of fossil fuels. The formation of fossil fuels is a result of the coalification process, which involves the partial decomposition of plant matter under anaerobic conditions and elevated heat and pressure. This process evolves through stages, yielding different types of fossil fuels. Initially, peat is formed, followed by the successive development of lignite, commonly referred to as brown coal, coal (bituminous), and finally anthracite. The coalification process is characterized by a significant reduction in moisture content and volatile matter, accompanied by an increase in the fraction of solid carbon. As a result, the moisture content declines from approximately 70 wt.% in peat to roughly 15 wt.% in anthracite, the volatile matter decreases from around 75 wt.% in peat to approximately 10 wt.% in anthracite, and the carbon content increases from about 50 wt.% to more than 90 wt.% [116, p. 15].

The van Krevelen diagram, depicted in Figure 2.2 [120], classifies biomass and fossil fuels based on their elemental chemical composition. Biomass exhibits relatively high atomic ratios of hydrogen-to-carbon (H/C) and oxygen-to-carbon (O/C). As the coalification process unfolds, these atomic ratios gradually decrease. The van Krevelen diagram in Figure 2.2 marks the three solid fuels central to this study: Two biomass fuels, namely, walnut shell and beech wood, alongside one representative of lignite, specifically, Rhenish lignite.

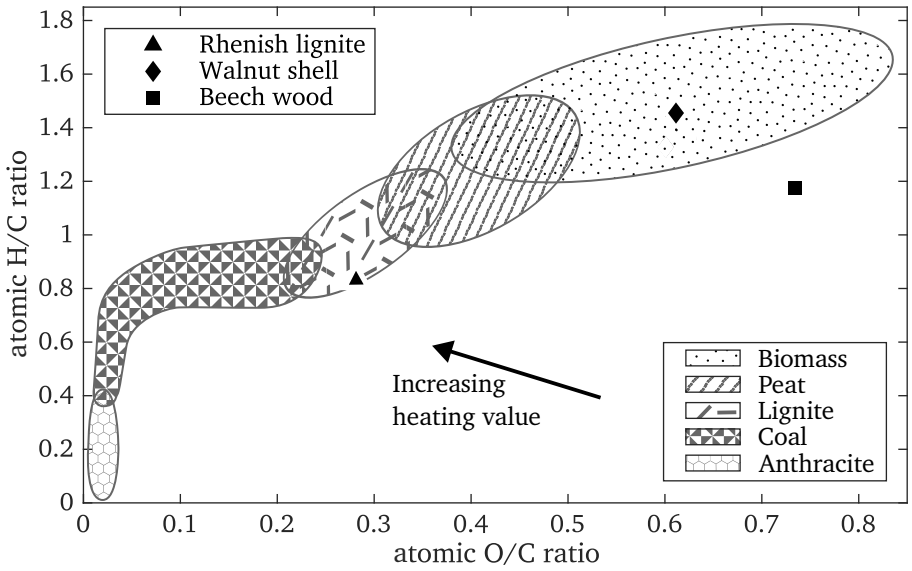

Figure 2.2: Van Krevelen diagram. Classification of biomass and coal based on its chemical composition including the solid fuels employed in this work: Rhenish lignite, walnut shell, beech wood. Illustration adapted from [120].

The heating value of a fuel represents the thermal energy released during its complete combustion process. It is typically quantified using either the higher heating value (HHV) or the lower heating value (LHV), which excludes the heat of vaporization of the water content in the fuel. In general, as

the H/C ratio increases and the O/C ratio decreases, the heating value tends to rise. For dry biomass, the LHV typically falls within the range of 15 MJ/kg to 20 MJ/kg [121], while for coal, this value varies between 16 MJ/kg and 34 MJ/kg [122].

For the characterization of solid fuels different analyses are performed. The proximate analysis quantifies essential components like moisture content, volatile matter content, fixed carbon content, and ash content. The elemental composition of the solid fuel is examined by the ultimate analysis, providing mass fractions of carbon, hydrogen, nitrogen, sulfur and oxygen with oxygen typically derived through elemental balance. Additional analyses further encompass fuel properties like heating value, density, particle size distribution, particle morphology and shapes, porosity, mineral composition of the ash, ash fusion temperature, and detailed compositional analysis of lignin, cellulose, and hemicellulose components.

2.2.2 Combustion process of pulverized solid fuels

The heterogeneous combustion of pulverized solid fuels is a multifaceted process encompassing several sub-processes. These sub-processes, which are similar for biomass and coal combustion, can be categorized as follows: drying, devolatilization, ignition, volatile combustion (homogeneous gas-phase combustion), and char combustion (heterogeneous surface combustion). These processes often overlap and are influenced by factors such as gas temperature and the composition of the surrounding gas mixture. Figure 2.3 visually illustrates the sequence of these sub-processes for a representative solid fuel particle. In the following, an overview of each sub-process is provided based on Spliethoff [116]. Additionally, a brief introduction to the formation of soot in the context of pulverized solid fuel flames is given.

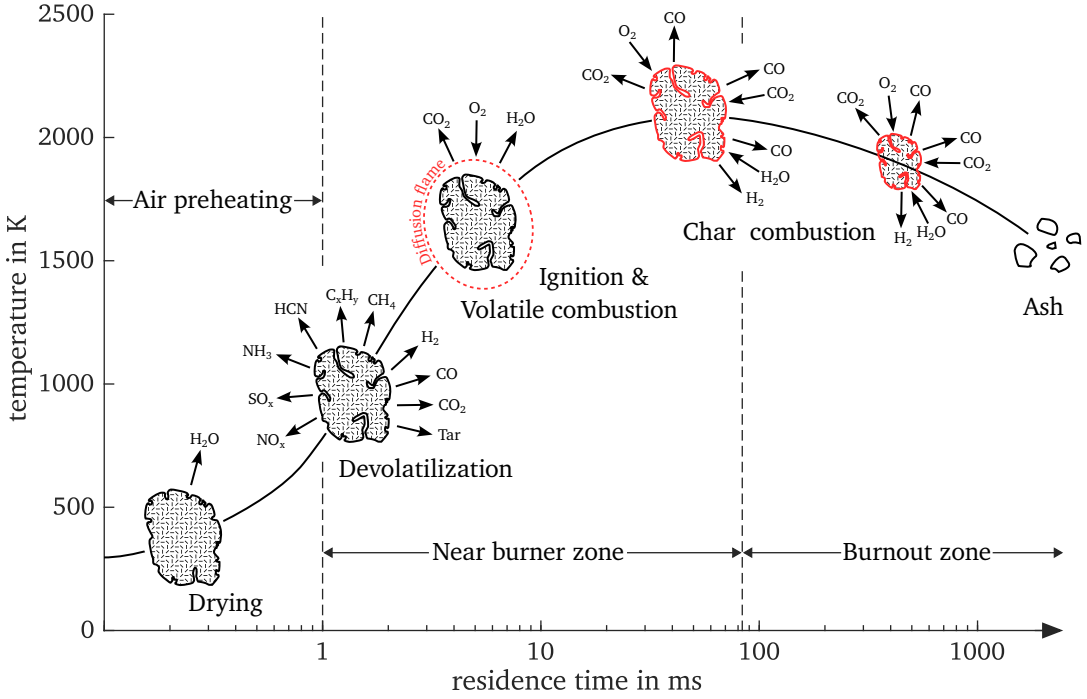

Figure 2.3: Schematic of the combustion process of pulverized solid fuel. Illustration adapted from [116, p. 224], [123].

Drying and devolatilization Upon injection into a combustion chamber, solid fuel particles undergo a rapid heating process driven by convective and radiative heating. Initially, moisture on the particle

surface and within its pores evaporates. This is followed by the devolatilization, also called pyrolysis, in which organic matter is decomposed and released as gaseous species into the surrounding atmosphere. The gaseous products depend on the heating rate and the specific composition of the solid fuel, and can be categorized into light gases and tars, based on their physical states at room temperature. Light gases that are released during devolatilization include hydrogen (H_2), carbon monoxide (CO), carbon dioxide (CO_2), methane (CH_4), small hydrocarbons (C_xH_y), nitrogen compounds such as hydrogen cyanide (HCN), ammonia (NH_3), and nitrogen oxides (NO_x), as well as sulfur compounds including sulfur oxides (SO_x). Tars consist primarily of complex hydrocarbons (C_xH_y), including polycyclic aromatic hydrocarbons (PAHs) [124]. The residual particle after devolatilization, referred to as char, is primarily composed of carbon and mineral components. Char typically exhibits a more porous structure, contributing to an increased particle surface area. The entire devolatilization process, along with the composition of its resulting products, is mainly influenced by the heating rate and the final temperature reached by the particle. Higher heating rates and elevated temperatures result in higher volatile yields.

The majority of volatile matter is released within a temperature range from 500 K and 900 K. In the devolatilization process of biomass, the release rate over temperature is significantly influenced by the composition of its primary constituents: lignin, cellulose, and hemicellulose. Hemicellulose decomposition occurs between 500 K and 600 K, followed by cellulose between 550 K and 650 K, while the complex structures of lignin are decomposed over a broad temperature range from 400 K to 900 K [125, 126].

Ignition and volatile combustion Ignition of volatiles occurs when a combustible mixture is formed and the necessary ignition temperature is reached. Hydrogen (H_2), methane (CH_4) and small hydrocarbons (C_xH_y) react with oxygen (O_2) to produce water (H_2O) and carbon dioxide (CO_2). Additionally, carbon monoxide (CO) further oxidizes into carbon dioxide (CO_2) in the gas-phase. In combustion chambers, volatile combustion is strongly influenced by turbulent mixing processes of particles, oxidizer and hot exhaust gases. As only gaseous species react, this process is based on homogeneous reactions, characterized by very high reaction rates when sufficient oxygen is present. When examining a single particle, as depicted in Figure 2.3, a diffusion flame surrounds the particle. However, in practical applications, a dense particle stream is exposed to high temperatures, resulting in a broader region where volatiles are released from the particle stream and subsequently combusted. Typically, ignition and volatile combustion occur in the near burner zone, contributing to flame stabilization through the early release of heat.

Char combustion Char combustion represents the combustion of residual char particles subsequent to devolatilization. This is a heterogeneous reaction, involving the oxidation of the fixed carbon within the particle. Initially, the carbon reacts into carbon monoxide (CO) at the particle's surface through either direct combustion with oxygen (O_2) or gasification via water vapor (H_2O) or carbon dioxide (CO_2). Following this, carbon monoxide (CO) is further oxidized within the gas phase into carbon dioxide (CO_2). In comparison to volatile combustion, char combustion proceeds at a considerably slower reaction rate, significantly impacting the overall combustion duration of solid fuel particles. Several factors, including temperature, active particle surface area, and species transport, influence the time required for complete char conversion. Char combustion is considered complete when only inert ash components remain.

Soot formation Soot formation in pulverized solid fuel combustion is assumed to be primarily driven by secondary reactions of tars at high temperatures. Within this process, PAHs contained within the tar undergo cracking and polymerization leading to the inception of particles from heavy PAH molecules. Subsequently, the particles increase in mass through the addition of gas-phase molecules and particle

agglomeration, forming nano-sized particles [124]. This mechanism differs from soot formation in single-phase combustion, where the process commences with small molecules like acetylene (C_2H_2), generated under fuel-rich conditions. These small molecules then grow into small PAHs, and subsequent reactions involve PAH-PAH radical recombinations and interactions with smaller molecules, leading to the development of larger PAHs. The subsequent steps in soot formation are analogous to those previously described [127]. PAHs released as tar from solid fuels tend to possess larger and chemically more diverse structures when compared to PAHs formed in single-phase combustion [124].

A competing process with soot formation in combustion is the oxidation of PAHs and soot structures. The dominance of either soot formation or soot oxidation depends on factors such as gas temperature and the local oxygen partial pressure. The entire process of soot formation and oxidation, particularly in the context of solid fuel combustion, remains highly intricate and not comprehensively understood at the detailed level. However, soot has a significant impact on the environment, human health, and heat transfer within a combustion chamber. Despite the relatively low soot mass fraction, soot particles collectively present a substantial surface area, which is pivotal for radiative heat transfer. A more detailed description of soot formation for solid fuel combustion is available in literature [124, 128, 129].

2.2.3 Oxy-fuel combustion

The efficient storage of CO_2 using CCS technologies necessitates a high-pressure CO_2 stream with a high degree of purity. As discussed in the introductory section 1.1, oxy-fuel combustion presents a promising approach to generate exhaust gases rich in CO_2 within the context of solid fuel combustion. In oxy-fuel combustion, solid fuel is burned in an atmosphere primarily composed of O_2, CO_2 and H_2O. This is achieved by recirculating a portion of the exhaust gases and introducing solid fuel and oxygen, which is separated from atmospheric air before. Oxy-fuel combustion has attracted significant scientific interest, with notable achievements documented in several review articles [25, 29–32]. However, the majority of research in this field has focused on applying oxy-fuel combustion to pulverized coal combustion (PCC) scenarios.

The alteration of the gas composition within a combustion chamber when operating under oxy-fuel conditions results in notable change in combustion behavior. These variations are primarily related to the substitution of N_2 with CO_2 in oxy-fuel atmospheres. Table 2.1 provides a comparison of important physical properties associated with both molecules.

Table 2.1: Important physical properties for combustion of N_2 and CO_2 at 1000 K and 1.013 bar [31].

		N_2	CO_2	CO_2/N_2
Density (ρ)	kg/m³	0.341	0.536	1.57
Specific heat capacity (c_p)	kJ/(kg K)	1.167	1.234	1.06
Volumetric heat capacity (ρc_p)	kJ/(m³ K)	0.398	0.662	1.66
Kinematic viscosity (ν)	m²/s	$1.2 \cdot 10^{-4}$	$7.7 \cdot 10^{-5}$	0.63
Mass diffusivity of O_2 in N_2 or CO_2 ($D_{O_2,X}$)	m²/s	$1.3 \cdot 10^{-4}$	$9.8 \cdot 10^{-5}$	0.78

While the specific heat capacities of N_2 and CO_2 exhibit similarities on a mass basis, there is a substantial increase in volumetric heat capacity for CO_2. Maintaining equal levels of oxygen in both air and oxy-fuel combustion scenarios leads to a significant reduction in temperature due to this difference. This becomes particularly relevant when converting conventional air-fired power plants to oxy-fuel combustion, where maintaining comparable heat transfer characteristics is crucial [31]. Achieving

comparable heat transfer characteristics involves increasing the oxygen concentration in oxy-fuel combustion to match adiabatic flame temperatures. The ensuing comparison of combustion characteristics is based on equivalent temperature conditions.

Under oxy-fuel conditions, it is observed that the yields of volatile matter are higher compared to air combustion. This increase can be primarily attributed to elevated levels of CO in the volatile composition, a consequence of the Bouduard reaction ($C + CO_2 \longleftrightarrow 2\,CO$) [32]. The mass diffusivity of O_2 in CO_2 is only approximately 78% of that in N_2. Consequently, there is reduced char reactivity under oxy-fuel conditions due to a slower rate of oxygen diffusion through the CO_2-rich boundary layer surrounding the particles. However, this reduced reactivity is compensated by an elevated char conversion rate resulting from intensified gasification reactions in oxy-fuel atmospheres [32]. In single-particle experiments, ignition is observed to occur earlier under oxy-fuel conditions at equivalent gas temperatures. This phenomenon is particularly pronounced for larger particles ($> 200\mu m$) and is attributed to the higher volumetric heat capacity in oxy-fuel atmospheres [47]. Additionally, gas radiation experiences a significant increase under oxy-fuel conditions due to the presence of the triatomic gases CO_2 and H_2O, which are not transparent to radiation, unlike N_2. However, radiation primarily originates from particles (solid fuel particles, ash, and soot) contributing between 60% and 70% of the total radiation [31]. Therefore, while gas radiation increases significantly in oxy-fuel conditions, the overall radiation experiences only a slight enhancement [32].

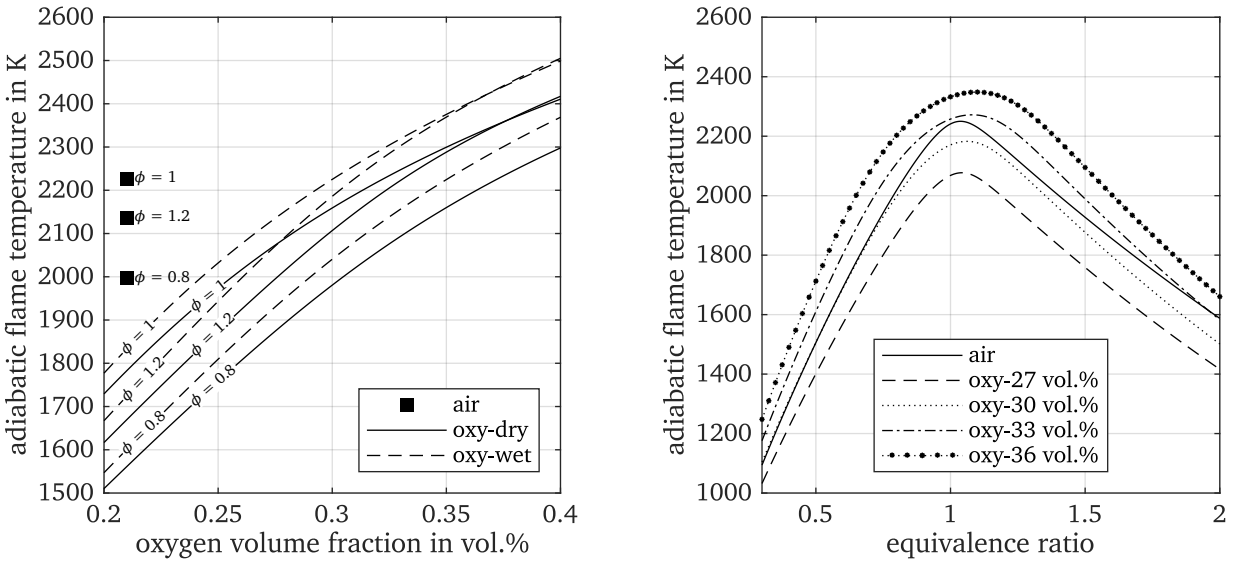

Figure 2.4: Adiabatic flame temperature (AFT) equilibrium calculations using Cantera [130] in combination with the GRI 3.0 mechanism [106] for a methane flame. Left: AFTs for oxy-dry and oxy-wet conditions for oxygen volume fractions between 20 vol.% and 40 vol.% and for equivalence ratios 0.8, 1 and 1.2. Reference AFTs for air combustion are shown. Right: AFT over equivalence ratio for air and oxy-dry conditions with 27 vol.%, 30 vol.%, 33 vol.%, and 36 vol.%.

An essential factor in determining the necessary oxygen concentration to match the adiabatic flame temperature is whether the recycled flue gas is wet or dry. In oxy-dry conditions, water is condensed and subsequently removed from the recycled flue gas, while in oxy-wet conditions, this condensation process does not occur, allowing the recycled flue gas to maintain higher temperatures. The required oxygen level to attain equal adiabatic flame temperatures varies for oxy-dry and oxy-wet conditions, caused by the higher volumetric heat capacity of CO_2 compared to H_2O [31]. On the left side of Figure 2.4, the calculated adiabatic flame temperatures are presented for varying oxygen volume fractions, ranging from 20 vol.% to 40 vol.%, and for equivalence ratios of 0.8, 1, and 1.2 in a methane flame. With increasing oxygen volume fraction, a rise in the adiabatic flame temperature is visible.

To attain adiabatic flame temperatures equivalent to those observed in air combustion, an increase to 32.2 vol.% oxygen volume fraction is needed for oxy-dry conditions, while oxy-wet conditions necessitate a rise to 30 vol.% oxygen volume fraction, considering stoichiometric combustion.

When combustion occurs under slightly lean or rich conditions, the oxygen volume fractions required to attain equal adiabatic flame temperatures as in air shift to lower values for oxy-dry and oxy-wet conditions. For a stoichiometric ratio of $\phi = 0.8$, this equilibrium is reached at 30.4 vol.% for oxy-dry conditions and 28.9 vol.% for oxy-wet conditions. Similarly, for $\phi = 1.2$, the corresponding oxygen volume fractions are 30.7 vol.% for oxy-dry and 28.9 vol.% for oxy-wet conditions. As the oxygen volume fraction increases, the adiabatic flame temperatures for $\phi = 1$ and $\phi = 1.2$ become more closely aligned, and at oxygen volume fractions exceeding 36.8 vol.% for oxy-wet conditions and 37.6 vol.% for oxy-dry conditions, the adiabatic flame temperature becomes higher for $\phi = 1.2$. This trend is evident in the right graph of Figure 2.4, illustrating the adiabatic flame temperature variation with equivalence ratio for different oxy-dry conditions and air. The position of the peak temperature shifts toward higher equivalence ratios with higher adiabatic flame temperatures, resulting from increased oxygen volume fractions. This effect is primarily attributed to enhanced dissociation of product species under higher temperatures [131]. While the adiabatic flame temperature profiles appear similar for all oxy-dry conditions, air exhibits a slightly different profile due to the distinct heat capacity of the gas mixture. This demonstrates that achieving equal adiabatic flame temperatures in both air and oxy-fuel conditions is contingent on the equivalence ratio.

Since the heat radiative transfer in oxy-fuel combustion is slightly increased, lower adiabatic flame temperatures are needed in order to attain comparable heat transfer characteristics to those observed in air combustion. The decrease in temperature due to this effect is expected to be small as the radiative heat transfer scales to the forth power of the temperature. Additionally, this effect is contingent upon the distribution of radiative heat transfer between gas and particles and exhibits variations depending on the specific configuration of the combustion chamber.

In biomass or coal combustion, the composition of volatiles mainly comprises CO and H_2 and only a minor volume fraction of CH_4 is present [32]. The different fuel composition influences the adiabatic flame temperature and is contingent upon the specific volatile matter of each solid fuel [132]. However, similar trends in adiabatic flame temperatures as those observed in methane combustion can be assumed. Furthermore, this thesis primarily focuses on the investigation of gas-assisted pulverized solid fuel combustion, employing methane combustion to achieve flame stability.

2.3 Optical laser diagnostics

2.3.1 Chemiluminescence imaging

Chemiluminescence (CL) imaging is a non-intrusive optical technique that visualizes the spatial distribution of electronically excited molecules and radicals, which are formed as intermediate species during chemical reactions. Molecules and radicals in a chemically excited state emit photons as they return to their ground state. These photons are subsequently captured with optical instruments. CL signals can provide valuable information about parameters such as volumetric heat release and equivalence ratio. In combustion research of hydrocarbon flames, chemiluminescence spectra are usually made up of contributions from hydroxyl radicals (OH*), methylidyne radicals (CH*), diatomic carbon radicals (C_2*), excited carbon dioxide molecules (CO_2*), formyl radicals (HCO*), and excited formaldehyde molecules (CH_2O*) [133]. Among these, OH*, CH*, C_2* and CO_2* are the major emitters [134].

Figure 2.5 illustrates an exemplary chemiluminescence spectrum from a $CH_4/H_2/O_2$ flame. OH* emits chemiluminescence in the ultra-violet (UV) region, specifically at approximately 280 nm, 310 nm, and

345 nm. These wavelengths correspond to the vibrational transition bands originating from the first excited state to the ground state, exhibiting variations in the vibrational levels Δv = -1,0,1. Each vibrational transition band comprises multiple rotational transition branches [133]. Following the established nomenclature of electronic states in diatomic molecules, which is introduced in detail by Herzberg [135], this transition is described as $X^2\Pi_i \leftarrow A^2\sum^+$.

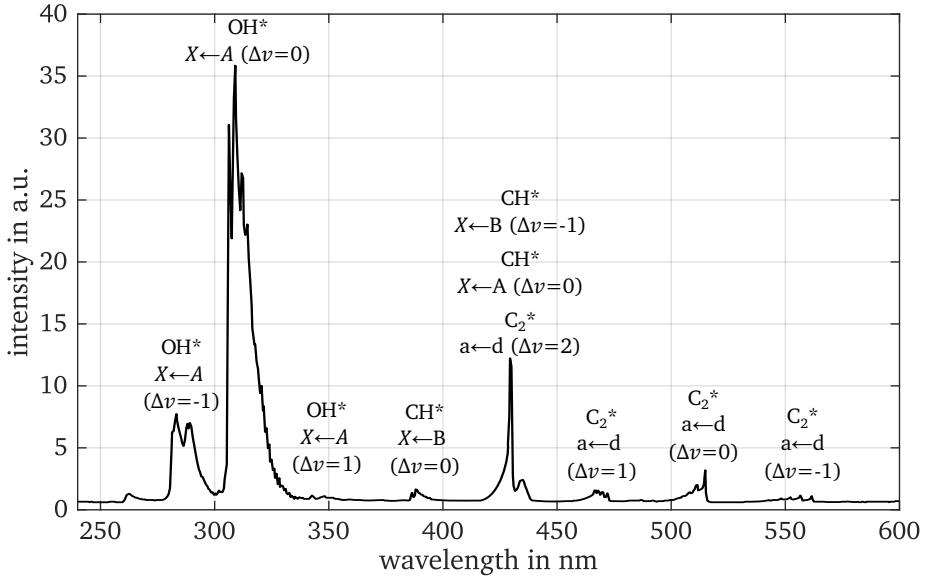

Figure 2.5: Chemiluminescence spectrum of a $CH_4/H_2/O_2$ flame. Transitions are abbreviated. Illustration adapted from [136].

In the visible range, chemiluminescence of CH*, C_2* and CO_2* occurs. CH* exhibits pronounced emissions arising from the $X^2\Pi \leftarrow B^2\sum^-(\Delta v = 0)$ transition, representing the vibrational transition band from the second excited state to the ground state without a change in the vibrational level, occurring at approximately 390 nm. Furthermore, CH* features superimposed chemiluminescence signals from $X^2\Pi \leftarrow B^2\sum^-(\Delta v = -1)$ and $X^2\Pi \leftarrow A^2\Delta(\Delta v = 0)$ transitions around 430 nm. Similarly, C_2* exhibits chemiluminescence around 430 nm, originating from the $a^3\Pi_u \leftarrow d^3\Pi_g(\Delta v = 2)$ transition. Additionally, C_2* emits chemiluminescence around 470 nm from the $a^3\Pi_u \leftarrow d^3\Pi_g(\Delta v = 1)$ transition, at about 516 nm from the $a^3\Pi_u \leftarrow d^3\Pi_g(\Delta v = 0)$ transition, and at approximately 550 nm from the $a^3\Pi_u \leftarrow d^3\Pi_g(\Delta v = -1)$ transition [133].

The triatomic radical CO_2* does not exhibit distinct emission peaks within the flame spectrum and instead features a broadband emission spectrum spanning from 250 nm to 580 nm. This phenomenon arises due to the significant increase in possible vibrational modes for triatomic molecules compared to diatomic molecules [133].

Interpreting CL signals presents several challenges and requires careful consideration of various aspects. CL imaging is a line-of-sight method, capturing all emitted chemiluminescence along the optical path. Furthermore, self-absorption of chemiluminescence by the flame can occur, although, in the case of hydrocarbon flames at atmospheric pressure, this effect is generally negligible [133]. Thermal radiation, especially from particles, soot, and nearby walls, has a temperature-dependent broadband spectrum. This radiation exhibits high intensities in the near-infrared (NIR) spectral region and substantial emissions in the visible light range. When detecting CL signals from OH* in the UV region, interference from thermal radiation is minimal. However, when detecting CL signals from CH*, C_2*, and CO_2* in the visible spectrum, substantial interferences may occur.

The chemiluminescence signal is linearly coupled to the integral heat release rate (HRR) for flames in laminar and moderately turbulent flows, assuming constant equivalence ratio, pressure, temperature,

and fuel-oxidizer composition [133]. However, in more complex flames where these assumptions are not applicable, the informative value of the CL signal is reduced. Nevertheless, CL imaging remains a valuable tool for indicating chemical reactions and can serve as a marker for identifying reaction zones within flames. While no quantitative relationship between CL intensity and HRR is possible, both OH* and CH* have proven to be good markers for the volumetric heat release in different flame configurations [137].

2.3.2 Particle image and tracking velocimetry for gas-solid multiphase flows

Particle image velocimetry (PIV) and particle tracking velocimetry (PTV) are optical measurement techniques typically employed for the determination of instantaneous planar flow fields and particle trajectories. Both methods are reliant on Mie scattering from particles suspended within the flow, which are illuminated using pulsed light. Usually a laser source is used for particle illumination. PIV and PTV are well-established techniques in the field of fluid dynamics. This section offers a detailed discussion on the tailored implementation of PIV and PTV techniques for the study of multiphase flows, preceded by an introductory overview of PIV and PTV.

Particle image velocimetry In conventional PIV measurements, the flow is seeded with tracer particles which meet the requirement of $\mathrm{St} \ll 1$ (refer to Equation (2.23)) to follow all velocity gradients of the flow instantaneously. Commonly employed tracer particles encompass oil or Di-ethyl-hexyl-sebacate (DEHS) particles for non-reactive gas flows, while in cases of reactive flows, thermally stable metal oxides such as Al_2O_3 are widely used [138]. Tracer particles are illuminated twice in rapid succession by laser pulses which are typically formed into a laser sheet. The scattered light from the particles is then captured in two sequential frames by a camera, positioned perpendicularly to the laser sheet. The particle displacement between both frames is computed by dividing the images into smaller regions known as interrogation windows, followed by employing a cross-correlation algorithm. After calculating local spatial displacements, a calibration process using imaging targets is employed to determine real-world displacement units. These local spatial displacements are then divided by the time separation Δt between both laser pulses to derive the velocity field.

Particle tracking velocimetry PTV, in contrast to PIV, focuses on tracking of individual particles rather than providing a flow field. The measurement setup closely resembles that of PIV. However, in PTV, the seeding density is reduced. To accurately compute particle displacements in PTV, prior knowledge is valuable to achieve reliable particle allocations. This prior knowledge is acquired through the assessment of an image sequence or by preprocessing the PTV data using PIV methods. Particle trajectories are then computed using information on particle displacement, time separation Δt, and spatial calibration.

PIV and PTV in gas-solid multiphase flows In gas-solid multiphase flows, the simultaneous determination of gas and particle velocities is desirable. To achieve this, phase separation is necessary. This allows for the estimation of flow fields using conventional PIV techniques and the calculation of particle trajectories through PTV processing. Methods developed for achieving simultaneous gas and particle velocity measurements can generally be classified into two categories:

1. **Individual recordings:** Separate images of tracer particles and the dispersed phase are simultaneously recorded.

2. **Simultaneous recordings with image processing:** Images of gas-phase tracers and particles are captured with the same camera, which are subsequently phase-separated using image processing algorithms.

While techniques falling into the first category necessitate additional adjustments to the measurement setup, those in the second category rely on tailored image processing algorithms customized to the specific experimental conditions.

Methods falling into the first category for non-reactive multiphase flows include the use of fluorescent tracer particles [139, 140], combinations of fluorescent tracer and fluorescent large particles at different wavelengths [141, 142], or the utilization of phosphorescent tracer and fluorescent large particles [143]. In these methods, the fluorescence or phosphorescence signal emitted by the tracer particles is captured by a camera equipped with specially designed optical filters to effectively suppress scattered light or fluorescence from the particle phase. Simultaneously, a second camera, also equipped with appropriate optical filters, records the signal originating from the particle phase. In cases where particles are detected based on Mie scattering, tracer particles are also visible and can subsequently be subtracted from the particle phase using the tracer image obtained from the first camera.

Fluorescent dyes used for particles are not combustion-resistant. To address this limitation and enable phase separation in reactive multiphase flows, Fan et al. [144, 145] introduced a novel approach that combines PIV with laser-induced incandescence (LII). In their method, black tungsten carbide particles are utilized as flow tracers. When exposed to a high-energy laser pulse, these tracer particles are rapidly heated to temperatures of several thousand degrees, emitting intense incandescence light. The phase separation is achieved through selection of appropriate optical filters. While Mie-scattered light shares the same wavelength as the laser pulse, the incandescence signal can be recorded at a distinct wavelength within the LII emission spectrum, enabling effective separation of gas and particle phases.

Two-phase methods of the second category are more widespread. These approaches typically rely on image processing algorithms that make use of the stronger and larger signals generated by larger particles to separate tracer particles from solid particles, with the average scattered intensity of particles scaling with the square of the diameter [138]. Phase separation can be accomplished by using specific thresholds for intensity and size to distinguish between small tracer particles and larger particles [75, 146–151], or by using noise filters to suppress Mie scattering signals from tracer particles and obtain images of the dispersed phase. These particle phase images are then subtracted from the original images to obtain the tracer images [152, 153]. The choice of image filters for both approaches varies depending on the specific experimental conditions and is not universally applicable.

In the context of the work presented in this thesis, Becker et al. [75] successfully conducted PIV and PTV measurements in solid fuel combustion to simultaneously determine gas and particle velocities in such a challenging environment for the first time. The phase separation technique was initially established under non-reactive conditions [150], highlighting its potential to calculate instantaneous slip, i.e., relative velocities. Determining the local slip velocity between the gas phase and solid fuel particles is a critical aspect of numerous physico-chemical processes in pulverized solid fuel combustion. This determination is pivotal for understanding and analyzing local heat transfer, gas composition, and turbulence characteristics. Therefore, experimental two-phase velocimetry is essential for investigating these phenomena.

2.3.3 Laser-induced fluorescence

Laser-induced fluorescence (LIF) is an optical laser technique used to probe and visualize molecules or atoms exhibiting a fluorescence behavior. In LIF, fluorescent species are excited to higher-energy electronic states through the absorption of laser photons. As the molecules or atoms return to their

ground states, spontaneous emission of photons occurs, denoted fluorescence, which can be detected and analyzed to visualize and quantify species distributions, investigate fluid mixing, determine velocities, or evaluate temperatures and pressures [154]. In combustion research, LIF is particularly valuable for detecting flame radicals such as OH, CH, NH, CN, or C_2 and pollutant species like NO or CO with high selectivity and sensitivity at ppm or even sub-ppm levels [155, p. 381]. This thesis employs LIF of polycyclic aromatic hydrocarbons (PAHs) to visualize the devolatilization and soot formation processes in pulverized solid fuel combustion (as discussed in Section 2.2.2). In regions with significantly high concentrations of PAHs, the application of LIF to radicals or pollutant species becomes challenging due to the strong broadband absorption characteristics of PAHs [156]. In this section, first the general physical processes underlying LIF are discussed using a diatomic molecule as an example, followed by specific fundamentals related to PAH-LIF.

LIF fundamentals Atoms and molecules possess discrete energy levels, which arise from the quantum-mechanical nature of electron motion. Figure 2.6 illustrates the discrete energy levels of the electronic ground state and the first electronically excited state for a diatomic molecule. On the left side of Figure 2.6, the vibrational energy levels and the Rydberg-Klein-Rees potential energy curves for the ground state, denoted as $V''(r_n)$, and for the excited state, denoted as $V'(r_n)$, are depicted over the internuclear distance r_n. A more detailed view on the physical processes during LIF is presented through the Jablonski diagram on the right side of Figure 2.6, showing electronic, vibrational, and rotational energy levels.

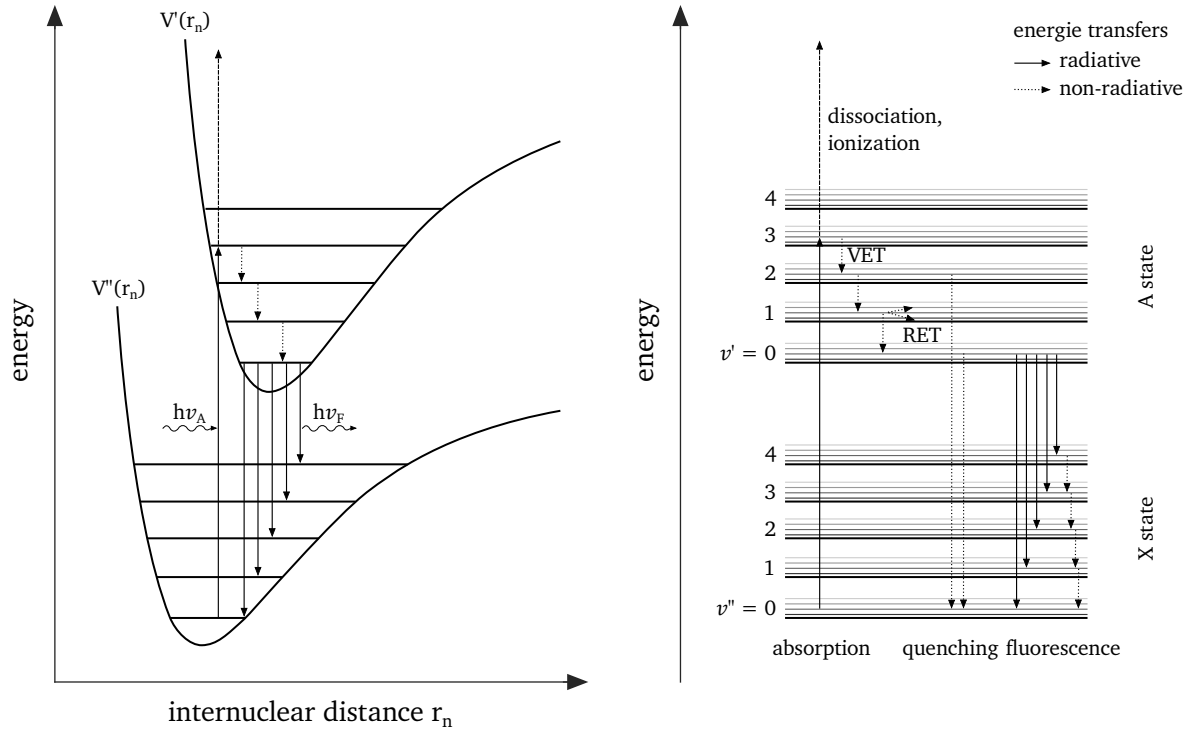

Figure 2.6: Energy level diagram and physical and chemical processes occurring during LIF. Left: Rydberg-Klein-Rees potential energy curves and vibrational levels of electronic ground and first electronically excited state. Right: Energy-level scheme (Jablonski diagram) showing vibrational and rotational levels of electronic ground state X and first electronically excited state A. VET: Vibrational energy transfer. RET: Rotational energy transfer. Illustration adapted from [154, 157].

By resonant absorption of an incident laser photon with the energy $h\nu_A$, which matches the energy gap between two distinct energy levels of the molecule, the molecule is transferred into an electronically

excited state. This transition results in a shift in the population distribution away from thermal equilibrium, described by the Boltzmann distribution. During relaxation back to the thermal equilibrium state, typically non-radiative energy transfer into the ground vibrational state $v' = 0$ of the electronically excited state by vibrational and rotational energy transfer (VET, RET) via collisions with other molecules occurs. However, for gaseous species, full relaxation to the ground vibrational state $v' = 0$ does not always happen and depends on collision rates, thus exhibiting sensitivity to pressure [156]. Subsequently, through spontaneous emission of a photon with energy $h\nu_F$, the molecule returns to a vibrational level, v'', in the electronic ground state. The energy of the emitted fluorescence photon is lower than that of the absorbed photon. This is known as the Stokes shift, a red shift in the emission spectrum compared to the absorption spectrum. Further energy transfers via VET and RET may occur if the vibrational level, v'', is higher than the original vibrational level in the electronic ground state before excitation. The relaxation to the electronic ground state by emitting fluorescence is a rapid process, typically occurring within 100 ns after excitation [156, 157].

The fluorescence intensity is affected by competing chemical and physical processes, each dependent on factors such as the excited species, temperature, pressure, and local gas composition. The fraction of excited molecules that emit fluorescence is quantified by the fluorescence quantum yield Φ_F. Competing chemical and physical processes include potential absorption of a second photon resulting in possible molecule dissociation or ionization, photo-induced reactions of the excited molecule without fluorescence emission, and non-radiative transitions from the electronically excited state to the electronic ground state due to inter-molecular collisional quenching. Collisional quenching is promoted in the presence of oxygen due to its molecular characteristics [156]. Additionally, the possibility of spin-forbidden intersystem crossing, which can result in phosphorescence, exists and is discussed in detail in Section 2.3.4.

The observed LIF signal intensity I_{LIF} is dependent upon the quantity of absorbed photons, the fluorescence quantum yield Φ_F, and characteristics of the detection system. I_{LIF} can be calculated as

$$I_{LIF} = \frac{I_L}{h\nu_L} V N_F \sigma_A \Phi_F \frac{\Omega}{4\pi} \eta. \tag{2.26}$$

Here, the absorbed photon quantity is represented by the photon flux $I_L/h\nu_L$, the measurement volume by V, the number density of the fluorescing species by N_F, and the absorption cross section by σ_A. The photon flux originates from the laser with laser intensity I_L and frequency ν_L. The observed angle $\Omega/4\pi$ and the quantum efficiency η of the detection system further influence the LIF signal intensity I_{LIF}.

PAH-LIF PAHs represent a group of organic compounds composed of multiple fused benzene rings, often referred to as aromatic rings. The broadband absorption and fluorescence spectra observed in PAHs exist due to the presence of delocalized electrons within their aromatic rings, which can be easily excited. The relaxation back to the electronic ground state tends to spontaneous emission, largely due to the structurally related inefficient vibrational relaxation processes in PAHs [158]. Consequently, PAHs exhibit notably high values for both absorption cross-section σ_A and fluorescence quantum yield Φ_F, resulting in high LIF signal intensities [159]. In combustion system, a large variety of PAHs occur in pulverized coal or biomass combustion and can be formed by incomplete combustion of organic matter. The significant diversity among PAH compounds, where naphthalene, the simplest PAH, consists of only two aromatic rings, presents challenges when investigating PAHs using LIF, primarily due to the mutual influence of their absorption and fluorescence properties.

The broadband absorption characteristics of PAHs in the UV region facilitate rather simple experimental LIF setups. Excitation using the fourth harmonic (266 nm) or third harmonic (355 nm) of a Nd:YAG

laser is feasible, and for PAHs containing more than three aromatic rings, excitation within the visible range, extending up to 680 nm, can be achieved [160].

The fluorescence spectra of PAHs is dependent on the number and position of aromatic rings. The degree of red shift in fluorescence spectra increases with the number of aromatic rings [158]. For example, when excited with 266 nm laser light at a temperature of 673 K, naphthalene (two aromatic rings) exhibits fluorescence within the range of 307 nm to 378 nm, while phenanthrene (three aromatic rings) shows fluorescence emissions spanning from 335 nm to 429 nm. The fluorescence spectra of pyrene (four aromatic rings) is red-shifted to the range between 360 nm and 451 nm, and fluoranthene (four aromatic rings) exhibits emissions spanning from 401 nm to 557 nm [159]. Fluorescence spectra of PAHs shift further towards higher wavelengths and broaden as temperatures rise, with simultaneous increases in absorption cross-sections σ_{A} and decreases in fluorescence quantum yields Φ_{F} at elevated temperatures [159].

2.3.4 Thermographic phosphor thermometry

Thermographic phosphor thermometry (TPT) is a contactless temperature measurement technique to determine temperatures of surfaces or fluids, often implemented using lasers. This method relies on thermographic phosphors, solid luminescent materials that emit fluorescence or phosphorescence upon excitation by absorbed photons. Thereby, the intensity, lifetime, or spectrum of the emitted luminescence is temperature-dependent. Typically, thermographic phosphors consist of a transparent crystalline host material doped with rare-earth elements or transition metals. Pulverized thermographic phosphors can be used as tracer particles in fluids or applied as thin coatings on surfaces using a chemical binder [161]. It is essential to ensure that the thermographic phosphors are in thermal equilibrium with the substance or material under investigation to obtain accurate temperatures. Temperature determination using TPT can be conducted through time-resolved or spectrally resolved techniques. In this section, first the general physical processes underlying phosphorescence are discussed, similar to fluorescence in Section 2.3.3, followed by an introduction of the two measurement techniques.

TPT fundamentals The physical and chemical processes central to TPT are illustrated in Figure 2.7. Similar to the fundamentals underlying LIF, the Rydberg-Klein-Rees potential energy curves are displayed as a function of internuclear distance r_n on the left side, while the right side presents the energy-level scheme in the form of a Jablonski diagram. Unlike fluorescence, which involves spin-allowed transitions within singlet states, phosphorescence relies on spin-forbidden transitions between triplet and singlet states. Most molecules in their electronic ground states have a total spin of $S = 0$, referred to as the singlet state S_0. Upon excitation, electron spins can either remain anti-parallel ($S = 0$) or align in parallel ($S = 1$), corresponding to the singlet state S_1 and the triplet state T_1, respectively [156]. The triplet state T_1 possesses lower energy than the singlet state S_1 [156, 157].

Excitation occurs through the absorption of energy, similar to the LIF process described in Section 2.3.3. Subsequently, non-radiative relaxation by energy transfer through VET and RET to lower vibrational levels v' of the electronically excited state take place. Intersystem crossing (ISC) is possible at the intersection of the potential energy curves of the singlet state S_1 and the triplet state T_1, resulting in singlet-to-triplet transitions [157]. Subsequent non-radiative relaxation to the ground vibrational level $v' = 0$ of the triplet state T_1 is probable, followed by the emission of a photon with energy $h\nu_{\mathrm{P}}$ to the singlet state S_0. This emission, termed phosphorescence, is a spin-forbidden transition according to quantum mechanical selection rules, given the necessary spin reversal [157]. Nonetheless, due to strong coupling between orbital and electronic angular momentum, especially in the presence of heavy atoms as found in thermographic phosphors, this transition becomes feasible [156]. Because of the unlikely spin-forbidden transition, phosphorescence, in contrast to fluorescence, is considerably

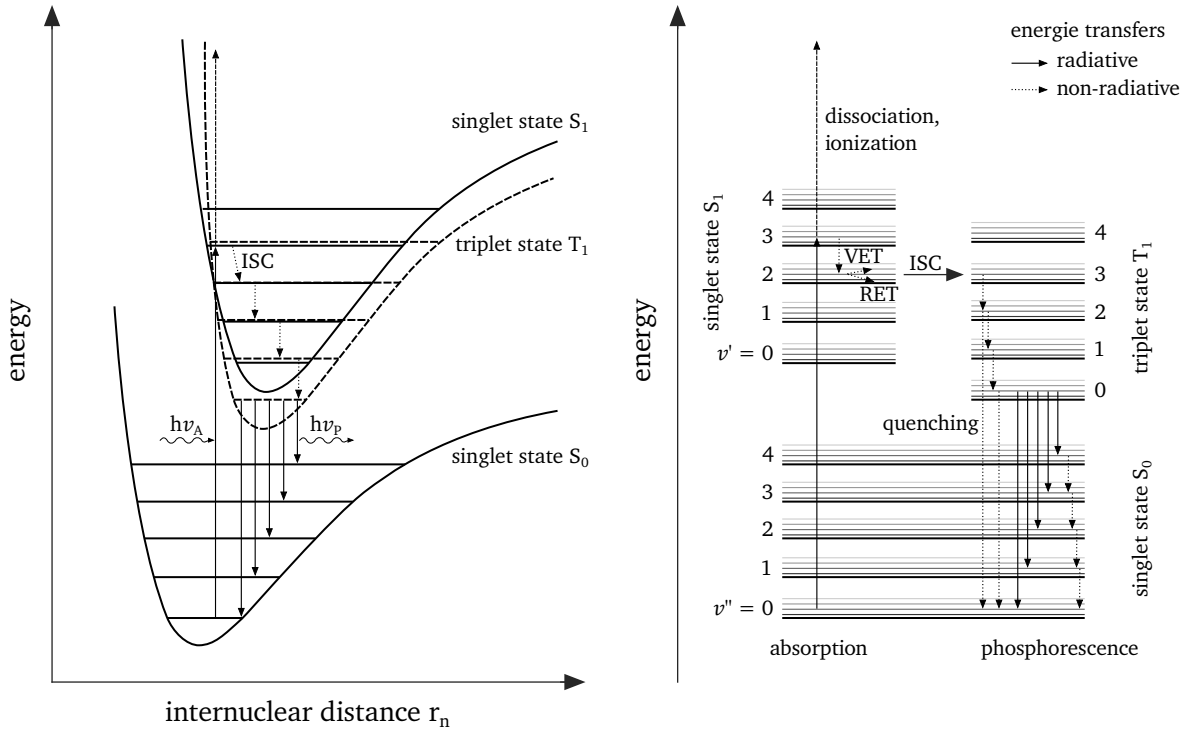

Figure 2.7: Energy level diagram and physical and chemical processes occurring during TPT. Left: Rydberg-Klein-Rees potential energy curves and vibrational levels of electronic ground state, denoted as singlet state S_0, and two potential energy curves of the first electronically excited state, denoted as singlet state S_1 and triplet state T_1. Right: Energy-level scheme (Jablonski diagram) showing vibrational and rotational levels of singlet state S_0, singlet state S_1, and triplet state T_1. VET: Vibrational energy transfer. RET: Rotational energy transfer. ISC: Intersystem crossing. Illustration adapted from [157].

slower, with phosphorescence lifetimes ranging from nanoseconds to several hours. Similar to fluorescence, the phosphorescence intensity is influenced by competing chemical and physical processes, as discussed in Section 2.3.3.

Thermographic phosphors feature a broad excitation spectrum in the near-UV range, facilitating excitation using the fourth harmonic (266 nm) or third harmonic (355 nm) of a pulsed Nd:YAG laser. The emission spectrum is further red shifted compared to fluorescence spectra due to the smaller energy difference between the triplet state T_1 and the singlet state S_0. The phosphorescence signal intensity I_{TPT} is temperature-dependent and insensitive to changes in pressure and the surrounding gas mixture [161]. However, certain thermographic phosphors exhibit sensitivity to varying oxygen partial pressures [162]. The temperature-dependent signal intensity arises due to temperature-enhanced internal energy transfer processes, commonly referred to as thermal quenching [163]. Predicting the specific characteristics of thermographic phosphors is challenging, necessitating thorough characterization. Even phosphors of the same type can exhibit different behaviors when produced under slightly altered conditions.

TPT processing methods Processing methods for TPT can be classified into two primary categories: time-resolved and spectrally resolved methods. Time-resolved methods necessitate recording the decay of the phosphorescence signal intensity at high sample rates, whereas spectrally resolved methods rely on time-integrated signals. The selection of the appropriate processing method depends on the characteristics of the specific thermographic phosphor and the intended application.

In the case of temporally sharp excitation pulses, the decay of the phosphorescence signal intensity I_{TPT} can be effectively approximated using a mono-exponential decay equation:

$$I_{\mathrm{TPT}}(t) = I_0 e^{\left(\frac{t}{\tau}\right)} \tag{2.27}$$

Here, I_0 represents the phosphorescence signal intensity immediately after the excitation at $t = 0$, and τ is the phosphorescent decay time. The decay time τ is defined by $I_{\mathrm{TPT}}(\tau) = I_0/e$ [163, 164]. By comparing the evaluated decay times to the decay times recorded during the characterization of the phosphor at well-known temperatures, it becomes possible to determine the temperature of the surface or fluid under investigation.

Spectrally resolved measurements for temperature determination typically employ an intensity ratio approach [163]. This method uses the temperature dependence of the emission spectrum by simultaneously recording signals from two distinct spectral regions. The specific spectral regions employed are unique to each thermographic phosphor, and not all thermographic phosphors exhibit spectral features that can be used with this processing method. As with time-resolved methods, temperature determination via intensity ratio analysis relies on previously established calibration data obtained at well-defined temperatures.

2.3.5 Coherent anti-Stokes Raman spectroscopy

Coherent anti-Stokes Raman spectroscopy (CARS) is a laser-based diagnostic which probes the population of rotational and vibrational modes of specific molecules. Thereby temperature and mole fractions of major species can be determined. The high signal intensity, in comparison to spontaneous Raman spectroscopy, makes CARS a valuable diagnostic for many applications in combustion. This is achieved by the high signal conversion efficiency and the coherent signal character inherent to CARS [155, p. 281]. Additionally, the generated directed coherent laser-like signal beam enables to capture the entire signal even far away from the probe volume. The following introduction into the fundamentals of CARS is given based on Eckbreth [155] and focuses on vibrational CARS only. Subsequently, high irradiance perturbation effects possibly affecting the measurement accuracy of CARS are discussed.

Within this thesis, CARS is used for N_2, O_2, and CO_2 as these are the major species occurring in solid fuel combustion with only O_2 and CO_2 being present in oxy-fuel atmospheres. Special characteristics of N_2-CARS, O_2-CARS, and CO_2-CARS are discussed subsequent to the CARS fundamentals. Additionally, dual pump CARS will be explained as this method enables measurements of different species with well separated Raman shifts simultaneously.

CARS fundamentals CARS is a four-wave mixing process with high laser energies giving rise to nonlinear phenomena in Raman spectroscopy. Three laser beams, called pump, Stokes, and probe laser, are overlapped and a coherent, laser-like signal is generated with the frequency ω_{CARS} which is determined by the energy balance $\sum \omega_i = 0$ as:

$$\omega_{\mathrm{CARS}} = \omega_1 - \omega_2 + \omega_3 \tag{2.28}$$

Here, ω_1, ω_2, and ω_3 represent the frequencies of the pump, Stokes, and probe laser, respectively.

The signal intensity of CARS can be derived using the wave equation as a simplified version of the Maxwell equation for gases and expanding the induced polarization by the electric fields as a Fourier series. For details the interested reader is referred to Eckbreth [155, p. 287 ff.]. The signal intensity of CARS I_{CARS} is given by:

$$I_{\mathrm{CARS}} = \frac{\omega_{\mathrm{CARS}}^2}{c^4 \epsilon_0^2} I_1 I_2 I_3 \, |\chi_{\mathrm{CARS}}^2| \, l^2 \left(\frac{sin\left(\frac{\Delta\vec{k}l}{2}\right)}{\frac{\Delta\vec{k}l}{2}} \right)^2 \tag{2.29}$$

Here c represents the speed of light, ϵ_0 is the permittivity of the free space, I_1, I_2, and I_3 are the laser intensities of pump, Stokes, and probe laser, respectively and l denotes the length of the probe volume where the lasers are overlapped. The signal intensity is proportional to the squared modulus of the third order susceptibility, denoted as χ_{CARS}. The CARS susceptibility χ_{CARS} can be expressed as sum of the resonant susceptibility χ_{R} and the non-resonant susceptibility χ_{NR}:

$$\chi_{\mathrm{CARS}} = \chi_{\mathrm{R}} + \chi_{\mathrm{NR}} = \sum_j \frac{K_j \Gamma_j}{2\Delta\omega_j - i\Gamma_j} + \chi_{\mathrm{NR}} \tag{2.30}$$

The resonant susceptibility χ_{R} consists of all Raman resonance transitions. Here, K_j and Γ_j represents amplitude and line width of transition j with the frequency ω_j. $\Delta\omega_j$ correspond to the detuning from the Raman resonance: $\Delta\omega_j = \omega_j - \omega_1 + \omega_2$. The transitions' amplitude K_j is given by:

$$K_j = \frac{(4\pi)^2 \epsilon_0 c^4 N \Delta_j}{\hbar \omega_2^4 \Gamma_j} \left(\frac{\partial\sigma}{\partial\Omega} \right)_j \tag{2.31}$$

From Equations (2.29), (2.30), and (2.31) the CARS signal intensity dependence on the squared number density N of the resonant species becomes obvious. Further, $\hbar$ is the reduced Planck constant, Δ_j denotes the fractional population difference between the two energy levels of transition j, and $(\partial\sigma/\partial\Omega)_j$ is the differential Raman cross section.

The non-resonant susceptibility χ_{NR} is the sum of all off-resonant contributions to the signal from other species and electronic contributions from atoms and molecules in the gas mixture [165].

For efficient signal generation, conversion of momentum $\Delta\vec{k} = 0$ in the form of the momentum balance of the wave vectors $\vec{k}_i$ with the magnitude $|\vec{k}_i| = \omega_i/c = 2\pi/\lambda_i$ has to be fulfilled. This is also referred to as phase matching and ensures that the CARS signals generated at different locations are in phase, leading to a constructive buildup of the signal [155, p. 290]. If $\Delta\vec{k} = 0$, I_{CARS} becomes maximal and the CARS wave vector $\vec{k}_{\mathrm{CARS}}$ is calculated by:

$$\vec{k}_{\mathrm{CARS}} = \vec{k}_1 - \vec{k}_2 + \vec{k}_3 \tag{2.32}$$

The energy and momentum balances are illustrated in Figure 2.8. On the left side the energy level diagram is shown implementing a broadband Stokes laser which allows for simultaneous detection of all Raman active transitions which match the energy of rotational-vibrational transitions for $\omega_{\mathrm{R}} = \omega_1 - \omega_2$. First the molecule is excited by the pump laser with frequency ω_1 to virtual states and subsequently transferred to excited rotational-vibrational states by stimulated emission through the broadband Stokes beam at frequency ω_2. The probe beam at frequency ω_3 scatters the light from the molecule again to virtual states, from where the CARS signal is generated by relaxing to the original energy states. If ω_{R} matches Raman active transitions of a species contained in the gas mixtures which is probed, then the CARS signal contains information on temperature and species concentration. For determination of temperature and species concentrations fitting algorithms are used due to the complexity of the CARS signal. In this thesis, CARS spectra are fitted with a developed code by Cutler et al. [166] to fit width-increased dual-pump enhanced CARS (WIDECARS) spectra.

Phase matching is depicted on the right side of Figure 2.8 in form of a planar BOXCARS approach where the lasers are crossed in one plane. This arrangement leads to high spatial resolutions with a

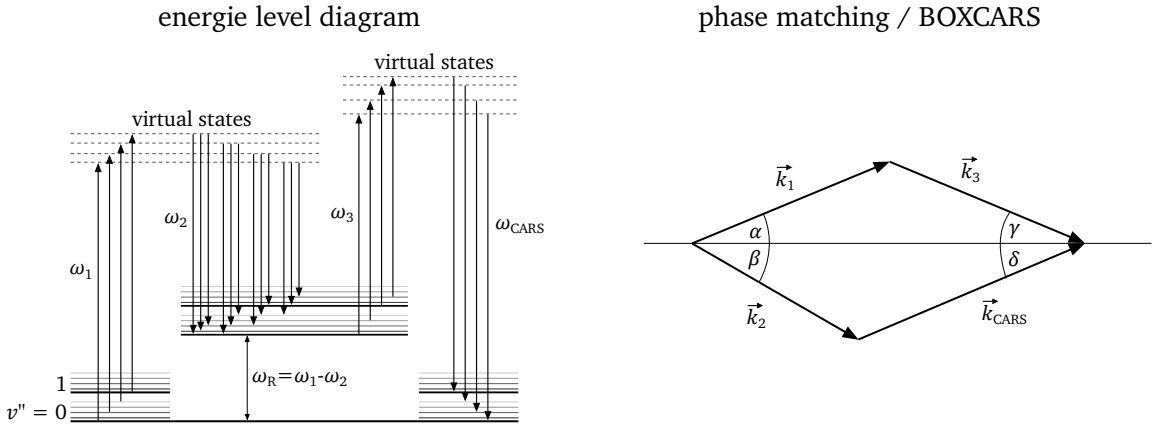

Figure 2.8: CARS energy and momentum balances. Left: Energy level diagram for broadband CARS. Right: Phase matching in the form of a planar BOXCARS approach. Illustrations adapted from [167, 168].

probe volume length in the order of 1 mm, depending on the angles α, β, and γ. Other beam arrangements, like collinear CARS (lasers are all collinear over a certain length), folded BOXCARS (lasers are crossed three dimensionally), or USED CARS (lasers are shaped in interlocking rings and are focused) are possible.

High irradiance perturbation effects in CARS In Equation (2.29) it is shown that the CARS signal intensity is proportional to the product of the laser intensities. However, signal increase by higher laser intensities is limited due high irradiance perturbation effects, namely optical breakdown, Stark broadening, and stimulated Raman pumping [169].

Optical breakdown describes a strong local ionization of the gaseous mixture due to very high amplitudes of the electric field which is generated by the focused laser pulses. Optical breakdowns also occur with less energy when a solid particle is hit. Optical breakdowns should be avoided as the strong broadband emission from the plasma may damage the sensitive senors designed to detect the CARS signal.

Unwanted alterations to the CARS spectrum are possible by the effect of Stark broadening for homonuclear molecules. At sufficiently high irradiances a dipole moment is induced, which changes the energy levels of each state and thereby causes a shift of the Raman transitions to lower frequencies and a broadening of the transition lines. The total irradiance at which Stark broadening will reduce the measurement accuracy is individual for each homonuclear molecule. For example total irradiances should be below 250 GW/cm² when performing N_2-CARS to avoid high irradiance perturbations due to Stark broadening [169].

Stimulated Raman pumping can lead to artificial changes in the population distribution of rotational and vibrational states away from thermal equilibrium towards larger populations of higher vibrational states. This effect is only dependent on the irradiances of pump and Stokes laser as stimulated Raman pumping is caused by a simultaneous two photon process to the four-wave mixing process of CARS at high irradiance products of pump and Stokes irradiances. The irradiance product of pump and Stokes at which stimulated Raman pumping becomes significant is also inherent to every species, for example the irradiance product should be below 2000 GW²/cm⁴ in O_2-CARS [169].

N_2-, O_2-, and CO_2-CARS Conventionally CARS is performed probing the N_2 molecule to determine gas temperatures. This results from the usually large N_2 concentrations in combustion atmospheres, typically in the range between 70 vol.% to 80 vol.%. However, other species with active Raman transitions like O_2 and CO_2 have also shown to be good temperature indicators for CARS [155, p. 329 ff.]. Simulated CARS spectra for N_2, O_2, and CO_2 are illustrated in Figure 2.9 for the temperatures 300 K, 1000 K, and 2000 K.

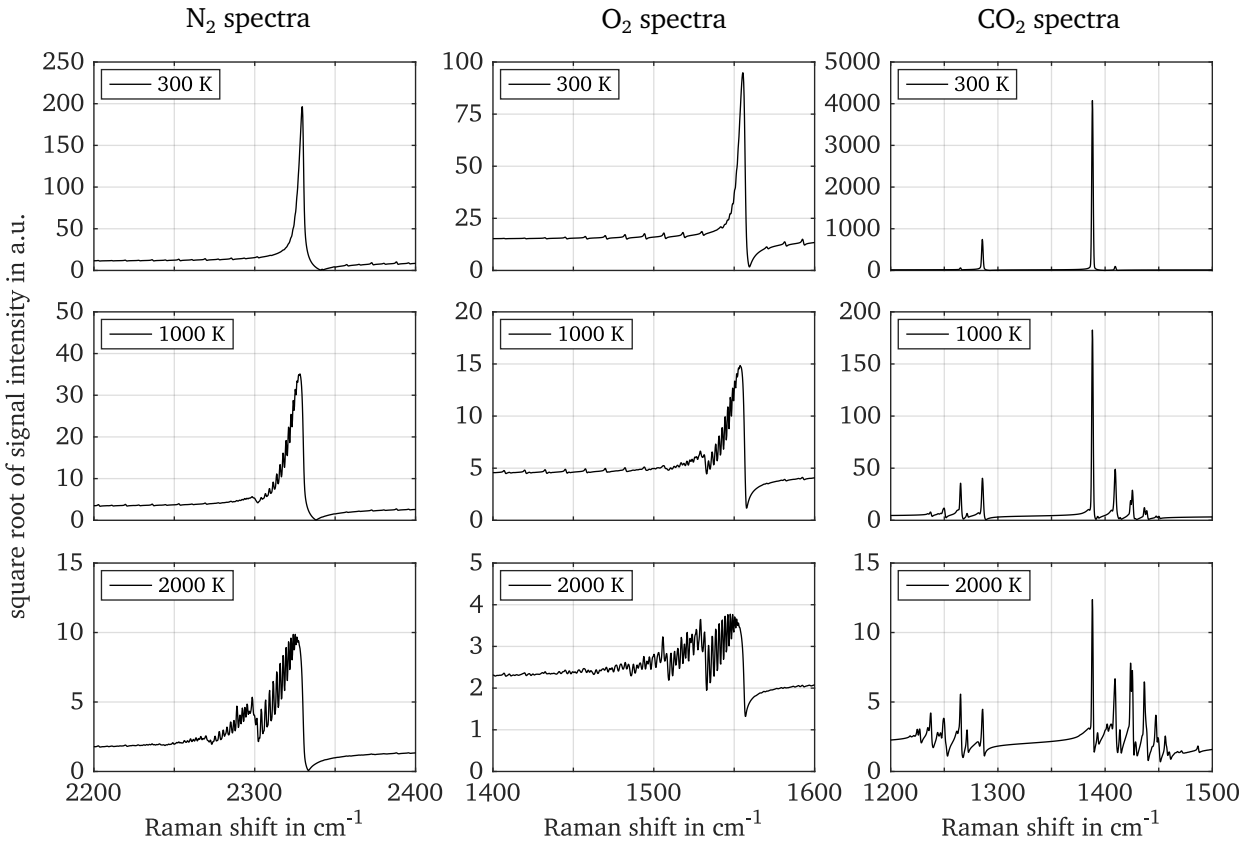

Figure 2.9: Simulated CARS spectra for N_2, O_2, and CO_2 and temperatures 300 K, 1000 K, and 2000 K. Representative volume fractions are chosen to mimic air and oxy-fuel combustion (N_2: 70 vol.%, O_2: 30 vol.%, CO_2: 70 vol.%). CARS spectra are simulated using the code developed by Cutler et al. [166] with a spectral resolution similar to experimental spectra recorded using a spectrometer with a 1 m focal length, a 2400 lines/mm grating, and a detector with a 20 µm pixel size. The signal intensity is plotted as the square root of the signal intensity and varies strongly with temperature.

For vibrational N_2-CARS typically the Q-branch transitions around a Raman shift of 2330 cm^{-1} are probed which evolve from the change of the vibrational level $\Delta v = 1$ while maintaining the rotational quantum number $\Delta J = 0$. At low temperatures only the ground vibrational state is populated and $v'' = 0 \rightarrow v'' = 1$ Q-branch transitions are observed for the N_2-spectra at 300 K. With rising temperature the first vibrational level gets populated and at about 1000 K $v'' = 1 \rightarrow v'' = 2$ Q-branch transitions appear. Additionally, single rotational lines of the ground vibrational level become visible as higher rotational states in the ground vibrational level are also more populated and the spacing between the single rotational lines increases for higher rotational quantum numbers. When the temperature is increased even further to approximate 2000 K, Q-branch transitions $v'' = 2 \rightarrow v'' = 3$ appear in the CARS signal. With increasing temperature also a strong decrease in signal intensity is observed.

The rotational-vibrational spectra of O_2 is similar to that of N_2 with O_2 Q-branch transitions around a Raman shift of 1556 cm^{-1}. With rising temperature also the first vibrational band becomes visible

around 1000 K and the second vibrational band appears at temperatures above 2000 K. The lower signal intensity of O_2 compared to N_2 in Figure 2.9 is mainly caused by the lower simulated O_2 number density.

In contrast to the diatomic molecules N_2 and O_2, CO_2 is a linear triatomic molecule whose energy levels are characterized by the vibrational quantum numbers v_1, v_2, v_3, and l_2. These are associated to symmetric stretching, bending, asymmetric stretching, and vibrational angular momentum, respectively [155, p. 334]. In the CO_2 spectra illustrated in Figure 2.9, active Raman transitions of the v_1 system around 1285 cm^{-1} and of the $2v_2$ system at 1388 cm^{-1} are shown. With rising temperature higher vibrational bands of both systems appear. While the higher vibrational bands for the v_1 system appear at lower Raman shifts than the fundamental vibrational level, higher vibrational bands for the $2v_2$ system are visible at higher Raman shifts [170], which is caused by the Fermi resonances between the two systems [201]. For CO_2 the spacing between the single rotational lines is very small and is typically not resolved. The dependence of the signal intensity on temperature is much greater than for the diatomic molecules N_2 and O_2.

Dual-pump CARS Simultaneous CARS measurements of the Q-branch of O_2 and the CO_2 $2v_2$ system are possible with broadband CARS using nanosecond lasers provided that a broadband laser with a full width at half maximum (FWHM) around 6 nm is built-up. This can be realized because the Raman shifts are close to each other. Probing of the Q-branch of N_2 simultaneous to O_2, CO_2, or both can be achieved with the dual-pump CARS (DP-CARS) approach [171]. While in single species CARS measurements the pump and probe lasers are typically obtained from the same laser source and feature the same wavelength, they have different wavelengths in DP-CARS, therefore originally called three-laser CARS. This results in the simultaneous generation of two CARS spectra at two different Raman shifts while the CARS signals frequency is similar. This can be explained by interchanging the probe and pump laser in the energy level diagram, depicted on the left side of Figure 2.8. This leads to the probed Raman shifts $\omega_{R,1} = \omega_1 - \omega_2$ and $\omega_{R,2} = \omega_3 - \omega_2$. Because Equation (2.28) for the CARS frequency is still fulfilled, the CARS signals frequencies are similar for both spectral regions. The wavenumber offset between the two probed regions is given by $\omega_{offset} = \omega_1 - \omega_3$.

2.3.6 Absorption spectroscopy

Absorption spectroscopy examines the wavelength-dependent absorption of light by matter. It provides valuable insights into the electronic structure of molecules, enabling the determination of temperature, species concentrations, and the surrounding environment of particles or molecules within a sample. When a photon's energy $h\nu$ matches the energy difference ΔE between two molecular or atomic energy levels, absorption is possible, leading to a transition to a higher energy state with a probability described by the Einstein coefficient of absorption B_{12} and the spectral energy density u_ν. First, the fundamentals of absorption spectroscopy based on Farooq and Alquaity [172] are introduced. Subsequently, the application of the tunable diode laser absorption spectroscopy (TDLAS) method is described which is applied to pulverized solid fuel combustion within this thesis.

Absorption spectroscopy fundamentals The wavelength dependent intensity attenuation $I_{AS}(\nu)$ caused by light absorption is described by the Beer-Lambert law:

$$I_{AS}(\nu) = I_0(\nu) e^{-\kappa(\nu) l} \tag{2.33}$$

Here, $I_0(\nu)$ represents the incident light intensity prior to interaction with the sample, $\kappa(\nu)$ denotes the spectral absorption coefficient, and l is the optical path length through the sample. The spectral absorption coefficient $\kappa(\nu)$ for a specific molecule with number density n is derived from the summation of all possible transitions N_S:

$$\kappa(\nu) = \sum_{i=1}^{N_S} S_i(T) n \Phi_i(\nu) \tag{2.34}$$

In this equation, S_i denotes the temperature-dependent line strength of transition i, and $\Phi_i(\nu)$ is the corresponding line-shape function. For most gaseous environments, the number density n is described using the ideal gas law as $n = xp/k_bT$, where x represents the mole fraction, and k_B denotes the Boltzmann constant. The line-shape function $\Phi(\nu)$ varies with temperature, pressure, and mole fractions and accounts for different broadening mechanisms: natural broadening, originating from energy level uncertainties (Heisenberg's uncertainty relation); Doppler broadening, due to the thermal motion of molecules; and collisional broadening, resulting from inelastic and elastic collisions of molecules. While natural broadening and collisional broadening can be described by a Lorentz function, Doppler broadening leads to a Gaussian distribution. The convolution of both profiles is called Voigt profile [172]. Databases like HITRAN [173] and HITEMP [174] provide line-shapes and line strengths for different molecules and atoms which are simulated or measured experimentally.

TDLAS The TDLAS method employs diode lasers whose wavelength is tuned through diode current modulation. Photodiodes are typically used to record the wavelength-dependent intensity attenuation $I_{AS}(\nu)$ after the sample. The tuning range of the diode lasers is in the order of a few nanometers and can be adjusted to match the absorption lines of the specific molecule under investigation, which are often found in the IR spectrum. Different types of diode lasers can be used for this purpose [175]. This approach enables the scanning of one or more absorption lines within the kilohertz frequency range.

Evaluation of TDLAS signals often involves fitting procedures using line data from databases like HITRAN or HITEMP. These data facilitate the determination of species mole fractions using one or more selected absorption lines, while temperature measurements rely on at least two absorption lines with sufficiently different temperature dependencies [176]. To overcome the limitations of line-of-sight measurements in TDLAS, various tomographic methods have been developed [175, 176].

2.3.7 Pyrometry

Pyrometry is a contactless temperature measurement technique that relies on capturing the thermal radiation emitted by surfaces. It finds widespread applications in various fields, particularly in high-temperature industrial processes and combustion. The following introduction into pyrometry is based on the review articles of Magunov [177] and Araujo [178].

The wavelength-dependent intensity of thermal radiation $I_{TR}(\lambda, T)$ emitted by a surface is described by Planck's law and the spectral emissivity $\epsilon(\lambda)$. Planck's law defines the upper limit of thermal radiation achievable by an ideal black surface, often referred to as a black body.

$$I_{TR}(\lambda, T) = \epsilon(\lambda) \frac{2hc^2}{\lambda^5} \frac{1}{e^{hc/(\lambda k_B T)} - 1} \tag{2.35}$$

The signal recorded by the pyrometer's detector is a summation of several radiation fluxes, encompassing the thermal radiation emitted by the object of interest, background radiation, radiation reflected

by the target surface, radiation stemming from the transmission path, and radiation arising from the inner surfaces of the pyrometer itself [178]. Additionally, the thermal radiation originating from the object of interest is affected by the spectral transmissivity of the transmission path between the target surface and the detector. To achieve accurate measurements of surface temperatures, it is essential to minimize these influences or take them into account when evaluating the temperature.

The value of the spectral emissivity $\epsilon(\lambda)$ ranges from 0 to 1, where $\epsilon = 1$ signifies a black body. $\epsilon(\lambda)$ is a function of the wavelength λ and can also depend on direction and temperature. While pyrometers are conventionally calibrated using a known black body radiation source, determining the spectral emissivity of the target surface becomes a critical requirement for achieving accurate temperature measurements. However, in practical applications, the spectral emissivity $\epsilon(\lambda)$ is often unknown, introducing a source of uncertainty in pyrometry [178]. To measure the temperature of surfaces with unknown spectral emissivities $\epsilon(\lambda)$, two-color and multi-color pyrometry techniques have been developed.

In two-color pyrometry systems, the object of interest is assumed to have a spectral emissivity that is independent of wavelength within the regarded spectral bands. Objects with wavelength-independent emissivity are called gray bodies, and this assumption has been demonstrated to be valid, for example, in the context of solid fuel particles [179]. By simultaneously measuring the thermal radiation at two distinct wavelengths or within two designated wavelength bands, an intensity ratio is calculated, canceling out the spectral emissivity. Subsequently, the surface temperature is determined by comparing the evaluated intensity ratio to a calibration curve, generated in advance using the same two-color pyrometry system and incorporating a calibration light source, such as a tungsten ribbon lamp or a black body [180].

Multi-color pyrometry systems are capable to measure temperatures of surfaces with wavelength-dependent spectral emissivities. However, prior knowledge of the dependence of spectral emissivity on wavelength is necessary and is integrated into the temperature assessment through the formulation of an appropriate emissivity function [178]. The emissivity function is derived by an equation system with n equations, originating from measured intensities at n distinct wavelengths or within n wavelength bands. Common mathematical functions employed to describe the wavelength-dependent spectral emissivity include polynomial functions or polynomial functions related to the natural logarithm of the spectral emissivity [178]. In combustion-related applications, multi-color pyrometry systems are used to measure soot temperatures, as soot cannot be approximated as a gray body [178].

2.3.8 Laser-induced incandescence

Laser-induced incandescence (LII) is an optical laser technique widely utilized for nanometer-sized particles to visualize spatially resolved occurrences, to determine volume fractions, or to estimate primary particle sizes. This method finds extensive application in combustion studies, particularly in the investigation of soot. The term *primary particle* refers to individual particles that are not aggregated, for instance, in the case of soot, this category encompasses mature soot particles with diameters ranging from 10 nm to 50 nm [181]. In LII, a high-energy pulsed laser is used to heat up nano-sized particles close to their sublimation temperature, leading to strong emission of thermal radiation (incandescence) in accordance with Planck's law (as defined in Equation (2.35)). The subsequent detection and analysis of the incandescence signal, including its temporal decay, provide insights into local volume fractions and primary particle sizes. In this section, the fundamentals of LII are presented based on the reviews by Michelson et al. [181] and Sipkens et al. [182].

In LII measurements, a high-energy pulsed laser, usually operating in the visible or near-infrared spectrum, is employed to heat up nanometer-sized particles. While the particle temperature is approximately proportional to the laser fluence, the LII signal increases non-linearly with particle temperature, as depicted on the left side of Figure 2.10. Soot particles, for instance, can be heated to temperatures

as high as ∼ 4000 K before sublimation occurs [181]. If the laser fluence is further increased, the peak LII signal becomes independent of the laser fluence while the time-integrated LII signal decreases due to particle sublimation.

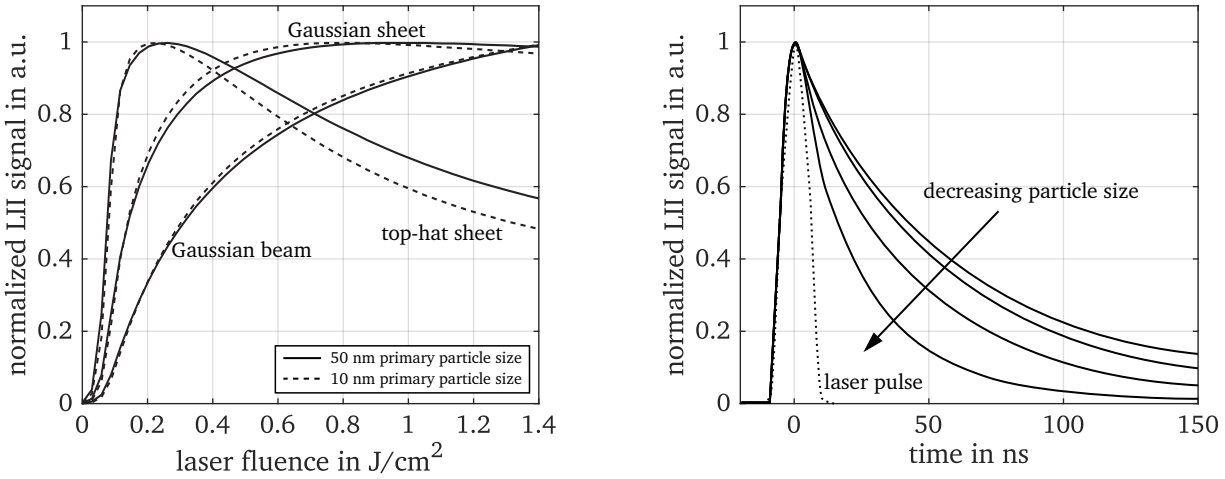

Figure 2.10: LII signal in relation to laser fluence and time. Left: Modeled laser fluence curves for soot within a 100 ns gate, starting at the laser pulse. Normalized LII signals for Gaussian sheet, top-hat sheet and Gaussian beam are shown for 10 nm and 50 nm primary particle sizes. Illustration adapted from [183]. Right: LII signal-decay rates for different particle sizes. Laser pulse is shown as dashed line. Schematic derived from measurements by Bladh et al. [184].

The spatial laser profile significantly influences the LII signal, as illustrated in the left graph of Figure 2.10. When a top-hat spatial profile is applied, all particles receive the same laser fluence, while local laser fluence variates in Gaussian sheet or Gaussian beam configurations. This results in a broader plateau region, as evident in the case of the Gaussian sheet. The plateau region is characterized by a LII signal intensity that remains independent of fluctuations in laser fluence. The Gaussian laser spatial profile is easier to shape and is most often used with high laser fluences for nano-sized particle visualization, while the top-hat profile is favorable for volume fraction measurements and particle size estimations.

The critical laser fluence $F_{\mathrm{L,sub}}$, where particle sublimation occurs and the plateau region is reached, depends on particle parameters such as particle diameter d_{p}, initial particle temperature T_0, and the particle composition.

$$F_{\mathrm{L,sub}} \approx \frac{\rho_{\mathrm{p}} c_{p,\mathrm{p}} \pi d_{\mathrm{p}}^3}{6\sigma_{\mathrm{A}}} (T_{\mathrm{sub}} - T_0) \tag{2.36}$$

In Equation (2.36), the particle composition is represented by the particle density ρ_{p}, the specific heat capacity $c_{p,\mathrm{p}}$, the wavelength-dependent absorption cross-section σ_{A}, and the sublimation temperature T_{sub} specific to the particle's composition [181]. This approximation is valid for particles in the Rayleigh regime, where the particle diameter d_{p} is much smaller than the laser wavelength λ_{L}, a condition typically met in soot LII experiments.

In LII, data acquisition can occur in two modes: time-integrated for spatially resolved visualization and volume fraction measurements, and time-resolved (TiRe-LII) for particle size estimations. In both cases, signal interferences have to be avoided. In hydrocarbon combustion systems, for example, interferences may arise from C_2 or C_3 emissions or LIF of PAHs, as described in Section 2.3.3. However, the use of the fundamental wavelength of an Nd:YAG laser at 1064 nm for LII ensures that LIF of

PAHs does not occur within the visible light range and a detection in the range between 580 nm and 820 nm excludes emissions from C_2 or C_3 [181]. When investigating non-soot nanoparticles, the radiation specific to those particles must be considered [182].

Volume fraction determinations from LII signals rely on the approximate proportionality between the maximum LII signal and the volume fraction. This proportionality is based on the Rayleigh approximation, which states that absorbed energy scales with particle volume for $d_p \ll \lambda_L$. To circumvent the influence of local laser fluence variations, volume fraction measurements are typically conducted within the plateau region of laser fluence. For estimation of absolute volume fraction values for nano-sized particles, a calibration process is necessary, often involving laser extinction measurements.

To derive information on primary particle sizes and primary particle size distribution from LII investigations, extensive modeling efforts have been made. The model is fitted to the recorded LII signal to estimate particle sizes and size distribution. These models typically consist of two coupled submodels: a spectroscopic model to describe the incandescence spectrum caused due to the particle temperature and a heat transfer model accounting for particle temperature changes [182]. Further details on LII models can be found in the literature [181, 182]. In general, LII signals exhibit higher decay rates for smaller particles compared to larger ones, primarily due to the faster cooling of smaller particles. This trend is visualized on the right side of Figure 2.10. Accurate estimation of primary particle sizes becomes particularly challenging in the presence of broader particle size distributions and is almost impossible in cases where no prior information is available.

3 Solid fuel combustor

This chapter describes the solid fuel combustor (SFC) which is used for investigations on solid fuel combustion under oxy-fuel atmospheres in this thesis. The SFC operates gas-assisted solid fuel flames in the power range up to 70 kW_{th} and aims to close the gap between unconfined laboratory systems and pilot-scale combustors. Its unique characteristic is the full optical access to the diffusor and the entire combustion chamber, while featuring well-controlled boundary conditions. The optical access allows the use of various advanced optical laser diagnostics to measure local properties of flow, particle dynamics and thermochemical state. Because of the design with short particle residence times compared to industry-scale combustors and radiative heat losses due to the large optical access, special attention is given to the near-nozzle region that is dominated by volatile combustion for analyzing flame stabilization as well as particle mixing with the surrounding gas flows, particle heat up and release of volatiles.

In this chapter, first the design of the SFC is presented in detail, including the burner, the combustion chamber, and the solid fuel feeder. Subsequently, the process operation and control is described, introducing the operation conditions and solid fuels which were used in the investigations performed in chapters 4 to 6. Well-known boundary conditions are mandatory to perform realistic numerical investigations. While the inflow conditions are defined by the operation conditions, the thermal boundary conditions were measured with thermographic phosphor thermometry (TPT) at the quartz glass walls and with thermocouples at all steel components. The results are presented in the third section of this chapter.

3.1 Design

3.1.1 Burner and combustion chamber

The test rig was first designed and constructed by Becker during his PhD studies at the Institute of Reactive Flows and Diagnostics (RSM) at the Technical University of Darmstadt [74]. The design of the SFC is based on the combustor from Heil et al. [78] which operates a self-sustained coal flame within an industry-oriented geometry.

The design of the SFC is presented in Figure 3.1, showing an overview of both the burner and the combustion chamber. For a more detailed depiction of the burner assembly, please refer to Appendix A.

The SFC is a down-fired combustor designed for the combustion of pulverized solid fuels. The combustion chamber exhibits a square cross-section measuring 420 x 420 mm^2, with chamfered corners and a height of 600 mm. It is enclosed by 3 mm thick planar quartz glass windows that allow for laser diagnostics in both the UV and near-IR spectral ranges. The burner, which includes a diffusor, commonly referred to as quarl in the context of furnaces, is located on top of the combustion chamber. The quarl has a height of 53.5 mm, an inlet diameter of 49.2 mm, and a cone angle of 21°, resulting in an outlet diameter of 90 mm towards the combustion chamber. It is made out of 5 mm thick quartz glass to provide unconstrained optical access to the near-nozzle region. The coordinate origin is located at the center of the quarl's outlet, coinciding with the top of the combustion chamber, often referred to as the dump plane. The height coordinate is oriented upwards, resulting in positive height values within the quarl and negative height values within the combustion chamber.

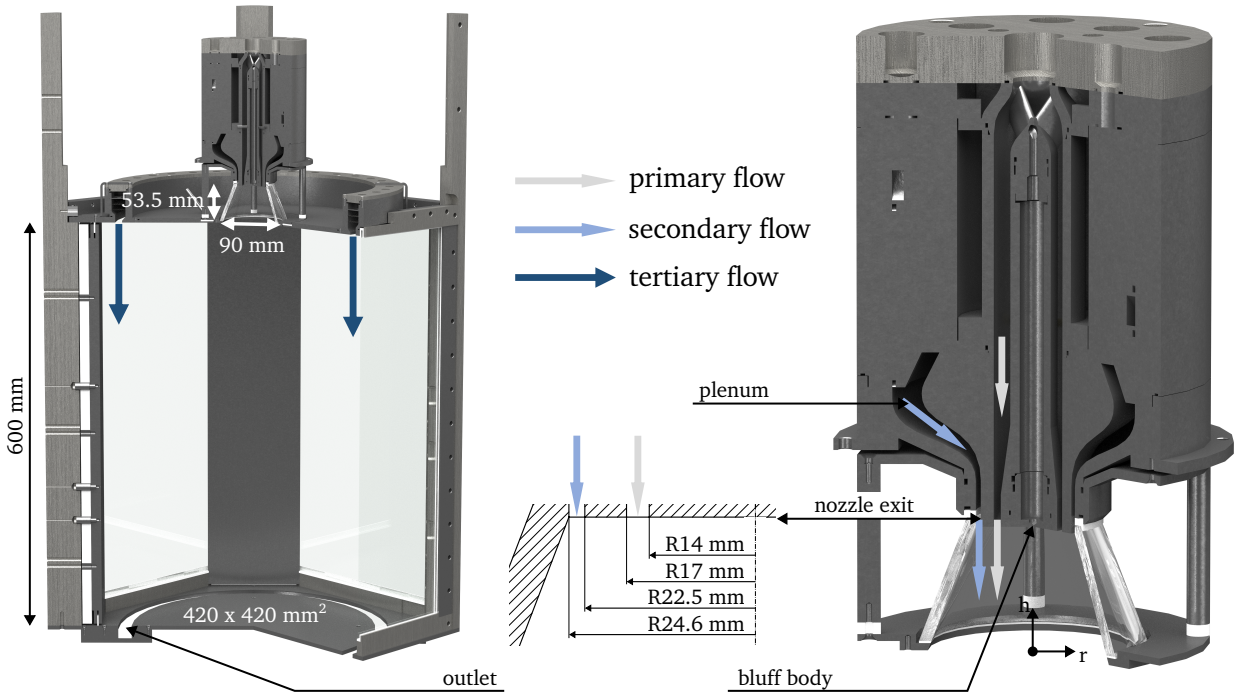

Figure 3.1: Solid fuel combustor (SFC) at the Institute of Reactive Flows and Diagnostics (RSM) at the Technical University of Darmstadt. Left: Optically accessible combustion chamber. Right: Burner with optically accessible quarl. The dimensions of the nozzle exit are highlighted in the middle. Illustration adapted from [1].

Three distinct flows are introduced into the combustion chamber. The primary (I) and secondary (II) flows enter the quarl through the burner assembly. The tertiary flow (III) is directly injected into the combustion chamber at a radius of 195 mm with a width of 10 mm. The primary flow, directed axially downwards, enters the quarl through the inner annular orifice located at radii between 14 mm and 17 mm, surrounding a central bluff body. This flow consists of partially-premixed fuel, including methane, pulverized solid fuel particles, and oxidizer. The secondary flow issues swirled oxidizer into the quarl through the outer annular orifice at radii between 22.5 mm and 24.6 mm, adjacent to the quarl wall. The swirl is generated through four axial and four inclined channels, angled at 45°, which combine into a single annular flow within a plenum upstream of the nozzle exit. This design allows for the adjustment of swirl intensity without the use of moving parts, such as vanes, leading to no necessary mesh adjustments in numerical simulations when altering swirl intensity. For this dissertation, similar swirl numbers are maintained across all operation conditions, utilizing only the inclined channels of the secondary flow. Additional oxidizer is introduced into the combustion chamber near the walls through the tertiary flow, theoretically ensuring the complete burnout of solid fuel particles given sufficient particle residence time.

The exhaust gases and predominantly partly burned solid fuel particles exit the combustion chamber through an annular orifice positioned at the chamber's bottom, at radii between 180 mm and 200 mm. This design serves to prevent any recirculation flow from the exhaust duct back into the combustion chamber, which could potentially influence the combustion process.

The central bluff body is centered by three centering pins located 83.2 mm upstream of the nozzle exit. These centering pins utilize NACA0030 profiles to prevent the influence of wakes from the centering pins on the inflow profiles at the nozzle exit, as verified through flow simulations [74]. The quarl

assembly is designed independently from the burner, enabling slight angular adjustments towards the burner during assembly to achieve a rotationally symmetric flame.

In comparison to the initial test rig designed by Becker during his PhD studies [74], several design adjustments were implemented, primarily concerning the combustion chamber configuration. The burner assembly remained unchanged to allow data comparison. The modifications were made to the chamber sealing, the tertiary flow injection, and the design of chamber corners. In particular, the former three separate windows were replaced by a single large window on each side to prevent air intrusion into the chamber. The window-to-chamber assembly was redesigned to ensure optimal sealing.

Optical access to the quarl is obstructed by the circumferential ring of the tertiary flow. While removing the tertiary flow was feasible for non-reactive conditions and single-phase combustion (methane combustion) [73, 150], it led to instabilities in gas-assisted solid fuel combustion [75]. To circumvent these issues, a rotationally symmetrical split ring design for the tertiary flow is introduced for measurements inside the quarl, with the circumferential ring of the tertiary flow used for measurements within the combustion chamber. Appendix B provides a visual representation of the two distinct tertiary flow designs along with a comparative evaluation of their impact on the flow field. The flow fields were measured by PIV and indicate no significant influence of the different tertiary flow designs on the flow field immediately downstream the dump plane. This confirms the suitability of the split ring design for measurements inside the quarl. A detailed description of the PIV setup and data processing is provided in Section 4.2.

Furthermore, the previously rounded corners of thin sheet metal were substituted with thick chamfered corners. These chamfered corners enable the installation of thermocouples, positioned 0.3 mm beneath the corner surface, without significantly impacting local temperature due to heat conduction. Three thermocouples are installed in each corner to monitor flame symmetry, with one corner equipped with an array of 17 thermocouples to determine thermal boundary conditions.

3.1.2 Solid fuel feeder

The solid fuel feeder for introducing particles into the primary flow is depicted in Figure 3.2. Originally designed by Becker during his PhD studies [74], this feeder was engineered to provide a stable and controllable feed rate for pulverized coal. Its enclosed design ensures the prevention of air intrusion, and it is assumed that particle size separation by the feeding mechanism can be neglected.

The solid fuel feeder comprises a cylindrical particle reservoir with an inner diameter of 134 mm and a height of 150 mm. At the bottom of the cylinder, a disc with multiple holes, where particles accumulate, is positioned. The disc is mounted to a drive shaft, which is driven by an electric stepper motor through a magnetic clutch. As the disc rotates, the filled holes are conveyed into the gap between the inlet and outlet pipes, allowing the particles to be injected into the oxidizer jet of the primary flow.

The feeder is positioned vertically above the burner in a straight line to avoid particle agglomeration within the piping system. It is connected to the oxidizer flow of the primary stream, and methane is introduced to the particle-laden flow downstream of the solid fuel feeder.

To determine the particle mass flow, the feeder is placed on a balance with a resolution of 1 g (Tedea-Huntleigh Inc., Model 1040), and the mass loss during operation is measured. Typically, mass flows for the SFC range between 3 kg/h and 7 kg/h. While the 1 g resolution does not enable monitoring of fast mass flow fluctuations, it effectively tracks mean mass flows. For instance, averaging over 30 s allows for the measurement of a 3 kg/h mass flow with a relative precision of 4% and a 7 kg/h mass flow with a relative precision of 2%.

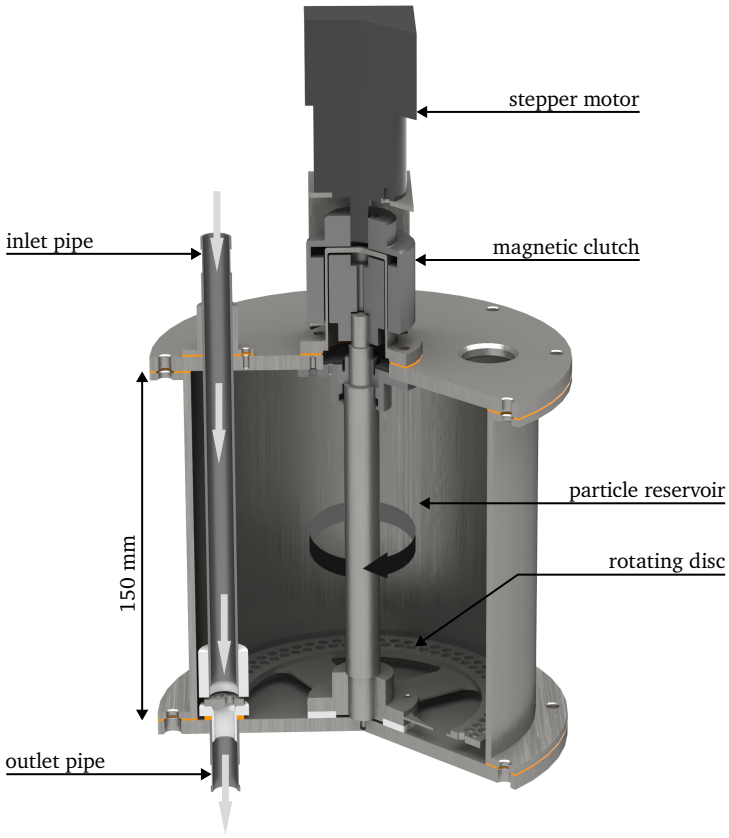

Figure 3.2: Solid fuel feeder integrated into the primary flow of the SFC.

During operation, the particle mass flow can be adjusted by controlling the rotation speed of the stepper motor. To accommodate different feeding characteristics associated with various pulverized solid fuels, which have differing particle size distributions, shapes, and densities, the following adaptations are possible: the rotating disc can be replaced with a disc featuring different hole patterns and diameters, and the gap between the inlet and outlet pipe can be adjusted, leading to an increased particle mass flow when the gap distance is enlarged.

3.2 Process operation and control

3.2.1 Operation conditions

In the SFC, exhaust gases are not recirculated, and a dry oxy-fuel atmosphere is established by mixing O_2 and CO_2 from gas tanks upstream of the burner. All volume flows are controlled using mass flow controllers (MFC) (Bronkhorst) and a detailed description of particle mass flow control can be found in Section 3.1.2. To investigate combustion characteristics under various conditions, different operation conditions are defined. The primary goal is to explore pulverized solid fuel combustion under oxy-fuel conditions, so most operation conditions feature oxy-fuel atmospheres. However, comparable conditions in air are also defined for reference.

Due to the large optical accesses in the design of the SFC, self-sustaining solid fuel flames cannot be operated. As a result, gas assistance is needed and all operation conditions feature a balanced distribution of thermal power, with both methane and solid fuel combustion contributing equally to the overall energy output. To gain a comprehensive understanding, the study covers both single-phase

and two-phase combustion. Single-phase operation pertains to the combustion of methane, whereas two-phase operation signifies the combustion of gas-assisted pulverized solid fuel.

In general, four parameters can be varied: volume flows, equivalence ratios, thermal power, and combustion atmosphere. Volume flows and equivalence ratios can be further divided into primary, secondary, and tertiary flows, each associated with specific equivalence ratios: primary stoichiometric ratio (I flow), local stoichiometric ratio (I+II flow), and global stoichiometric ratio (I+II+III flow). The combustion atmosphere can be adjusted to either air or oxy-fuel, with oxy-fuel operation allowing for control of the oxygen volume fraction.

A conventional approach to vary operation conditions is to keep the ratio of the axial momentum fluxes in all inlet flows equal [73, 77]. However, this approach led to significant deviations of the equivalence ratio from realistic conditions [73]. Constant stoichiometric ratios are chosen to approximate realistic conditions. The primary stoichiometric ratio is set to $\lambda = 0.32$, the local stoichiometric ratio, which approximates the stoichiometric ratio within the quarl, is set to $\lambda = 0.61$, and the global stoichiometric ratio is set to $\lambda = 1.25$. These values ensure slightly lean overall combustion and comparability to the oxy-fuel combustion chamber at RWTH Aachen University [80], which collaborates with TU Darmstadt within the CRC/TRR 129 Oxyflame.

With a constant equivalence ratio, three parameters remain which can be modified. However, these parameters are not independent of each other, and changing one will affect at least two of the others. Figure 3.3 illustrates possible variations, showing the influence of changing the oxygen volume fraction on total volume flow while maintaining thermal power, as well as the influence on thermal power while keeping volume flows constant.

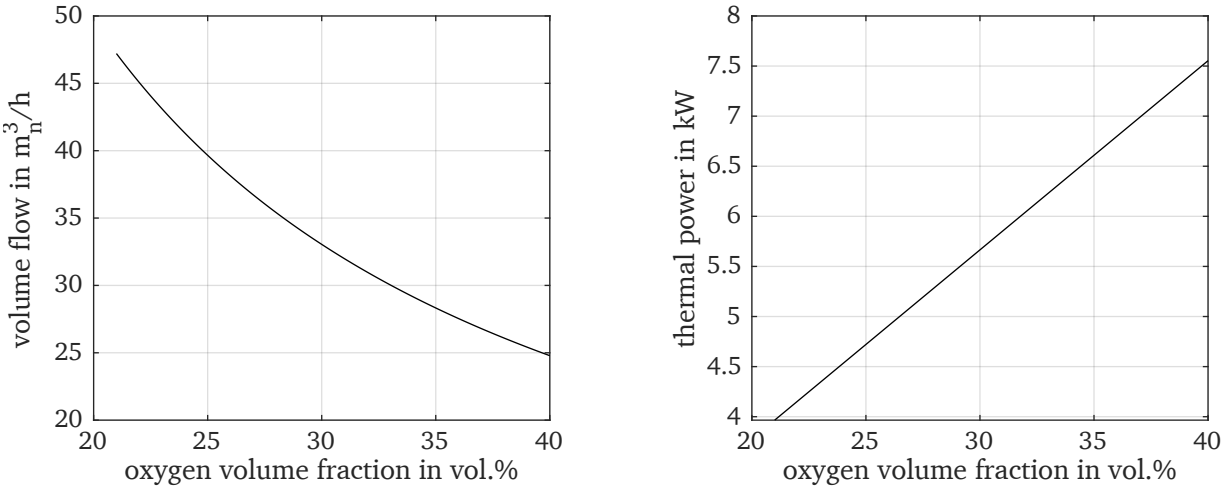

Figure 3.3: Influence of changes in the oxygen volume fraction on the parameters volume flow and thermal power. Left: Influence of changing the oxygen volume fraction on the total volume flow with constant thermal power. Right: Influence of changing the oxygen volume fraction on the thermal power with constant volume flows.

Two sets of operation conditions are used in this work. The first set focuses on a fixed oxygen volume fraction in oxy-fuel combustion and primarily uses Rhenish lignite (RL) as the solid fuel. The second set concentrates on varying the oxygen volume fraction and primarily uses walnut shells (WS) as a biomass representative. For each set, both single-phase and two-phase operation conditions are derived. Two-phase operation conditions are denoted by using the name of the corresponding single-phase condition and appending the type of solid fuel, e.g., single-phase operation condition: OXY33P, corresponding two-phase operation condition with walnut shells (WS): OXY33P-WS.

Table 3.1: First set of SFC operation conditions. Volume flows and particle load of single-phase and corresponding two-phase operation conditions OXY33, OXY33P, and AIR. The solid fuel is specified by appending "-RL" for Rhenish lignite (e.g. OXY33P-RL), or "- WS" for walnut shells. Values in brackets belong to two-phase combustion. Inflow temperatures are 20 °C. I: primary flow, II: secondary flow, III: tertiary flow. Adiabatic flame temperatures (T_{ad}) are calculated using Cantera [130] for single-phase operation conditions. Table adapted from [1].

Operation condition		OXY33	OXY33P	AIR
Oxidizer: Air/O_2/CO_2	vol.%	0/33/67	0/33/67	100/0/0
I Methane	m³/h	2.01	3.17	2.01
I Particle mass flow				
...-RL	kg/h	(3.36)	(5.29)	(3.36)
...-WS	kg/h	-	(6.02)	-
I Oxidizer	m³/h	7.68	12.10	12.10
II Oxidizer	m³/h	7.08	11.09	11.09
III Oxidizer	m³/h	15.30	24.02	24.02
Thermal power	kW_{th}	20 (40)	31.5 (63)	20 (40)
Primary stoich. ratio	-	0.63 (0.32)	0.63 (0.32)	0.63 (0.32)
Local stoich. ratio	-	1.21 (0.61)	1.21 (0.61)	1.21 (0.61)
Global stoich. ratio	-	2.46 (1.25)	2.46 (1.25)	2.46 (1.25)
Swirl number [1)]	-	0.43	0.43	0.45
Reynolds number (I)	-	2557	4028	2819
Reynolds number (II)	-	1376	2155	1475
Reynolds number (III)	-	359	564	386
T_{ad} [1)]	K	2138	2138	2053

[1)] Only primary and secondary flow are considered.

In the first set of operation conditions, two oxy-fuel conditions with an O_2 volume fraction of 33 vol.% are derived from a comparable air condition, once by maintaining the same thermal power and once by keeping the volume flows constant. This results in the three operation conditions presented in Table 3.1. Between each of these conditions, two of the four parameters have been varied while the other two remain constant. For operation condition OXY33, each volume flow was adjusted by a percentage to maintain the primary, local, and global stoichiometric ratios. The primary, local, and global stoichiometric ratios are calculated for full burnout, accounting for the solid fuel compositions presented in Section 3.2.2. With large-eddy simulations (LES) the swirl number was calculated based on Equation (2.14) for one operation condition of the SFC used by Becker during his PhD studies [73, 185]. The presented swirl numbers for the operation conditions introduced in this section are estimated from this simulation by taking the changed momentum fluxes of the primary and secondary flow into account.

The second set of operation conditions builds on the conditions AIR and OXY33P from the first set and varies the oxygen volume fraction under oxy-fuel conditions between 27 vol.% and 36 vol.%. This adjustment aims to achieve adiabatic flame temperatures similar to those observed in air combustion (see Section 2.2.3). The volume flows are maintained constant for all operation conditions, while thermal power and oxygen volume fraction are varied. Table 3.2 presents the details of the second set of operation conditions.

Photographs of both sets of SFC operation conditions are provided in Figures 3.4 and 3.5, depicting single-phase and two-phase combustion for each set. While the Rhenish lignite particles do not adhere to the quarl wall in Figure 3.4, particles that adhere to the walls largely obstruct the emission of flame

Table 3.2: Second set of SFC operation conditions. Volume flows and particle load of single-phase and corresponding two-phase operation conditions OXY27P, OXY30P, OXY33P, OXY36P, and AIR. The solid fuel is specified by appending "-WS" for walnut shells (e.g. OXY33P-WS),"- BW" for beech wood or "-RL" for Rhenish lignite. Values in brackets belong to two-phase combustion. Inflow temperatures are 20 °C. I: primary flow, II: secondary flow, III: tertiary flow. Adiabatic flame temperatures (T_{ad}) are calculated using Cantera [130] for single-phase operation conditions. Table adapted from [2].

Operation condition		OXY27P	OXY30P	OXY33P	OXY36P	AIR
Oxidizer: Air/O_2/CO_2	vol.%	0/27/73	0/30/70	0/33/67	0/36/64	100/0/0
I Methane	m³/h	2.59	2.87	3.17	3.45	2.01
I Particle mass flow						
...-WS	kg/h	(4.93)	(5.47)	(6.02)	(6.56)	(3.82)
...-BW	kg/h	-	-	(6.88)	-	-
...-RL	kg/h	-	-	(5.29)	-	-
I Oxidizer	m³/h	12.10	12.10	12.10	12.10	12.10
II Oxidizer	m³/h	11.09	11.09	11.09	11.09	11.09
III Oxidizer	m³/h	24.02	24.02	24.02	24.02	24.02
Thermal power	kW_{th}	25.8 (51.6)	28.65 (57.3)	31.5 (63)	34.35 (68.7)	20 (40)
Primary stoich. ratio	-	0.63 (0.32)	0.63 (0.32)	0.63 (0.32)	0.63 (0.32)	0.63 (0.32)
Local stoich. ratio	-	1.21 (0.61)	1.21 (0.61)	1.21 (0.61)	1.21 (0.61)	1.21 (0.61)
Global stoich. ratio	-	2.47 (1.25)	2.47 (1.25)	2.47 (1.25)	2.47 (1.25)	2.47 (1.25)
Swirl number [1)]	-	0.44	0.44	0.43	0.42	0.46
Reynolds number (I)	-	4066	4043	4028	4014	2819
Reynolds number (II)	-	2250	2201	2155	2111	1475
Reynolds number (III)	-	588	576	564	552	386
T_{ad} [1)]	K	1905	2028	2138	2228	2053

[1)] Only primary and secondary flow are considered.

radiation originating from within the quarl in Figure 3.5. Please note that the photographs in Figure 3.4 have different camera settings and white balance compared to the photographs in Figure 3.5. Nevertheless, comparability is ensured by featuring photographs of operation conditions AIR, OXY33P, and OXY33P-RL in both sets. Further discussions on the flame shapes are provided in chapters 4 to 6, accompanied by corresponding measurement data.

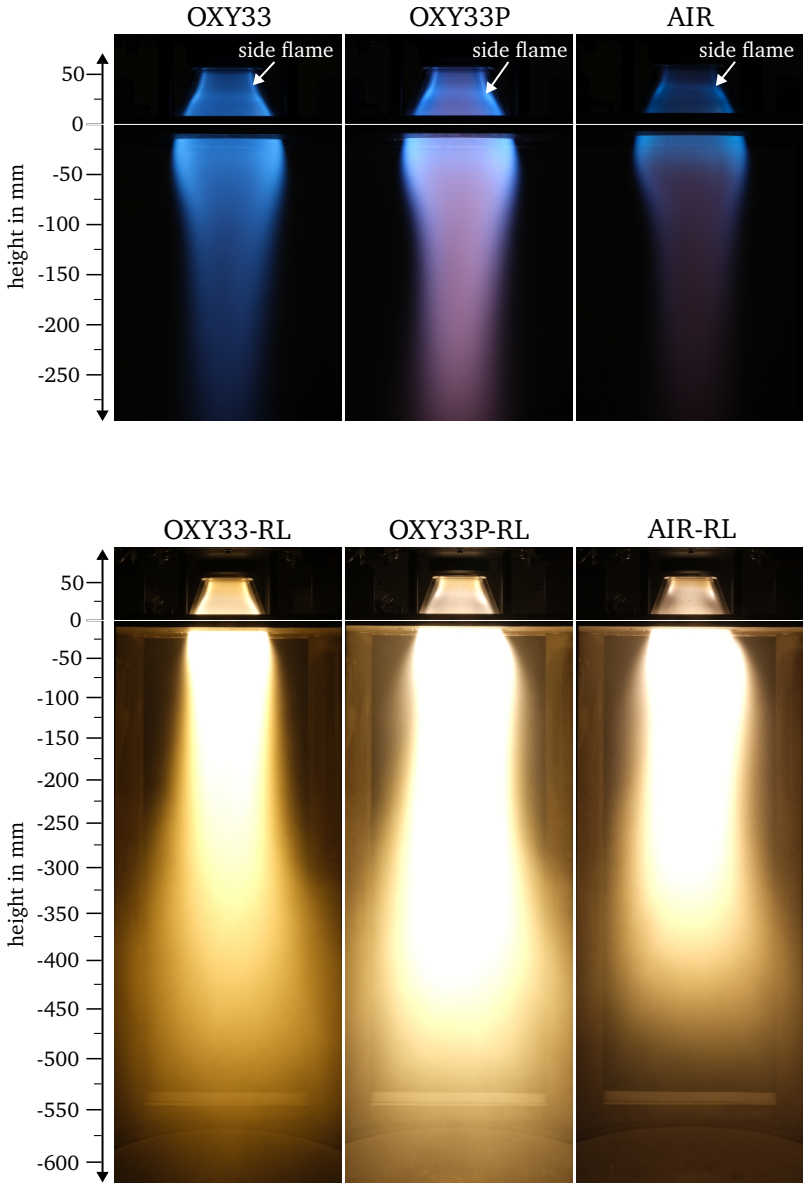

Figure 3.4: Photographs of the first set of SFC operation conditions. Top row: Single-phase operation conditions. Second row: Gas-assisted solid fuel combustion operation conditions with Rhenish lignite (RL). Camera settings are equal within the singe-phase combustion with an exposure time of 40 s and within the gas-assisted solid fuel combustion with an exposure time of 8 s. Side flames marked in the single-phase operation conditions will be discussed in Chapter 4.

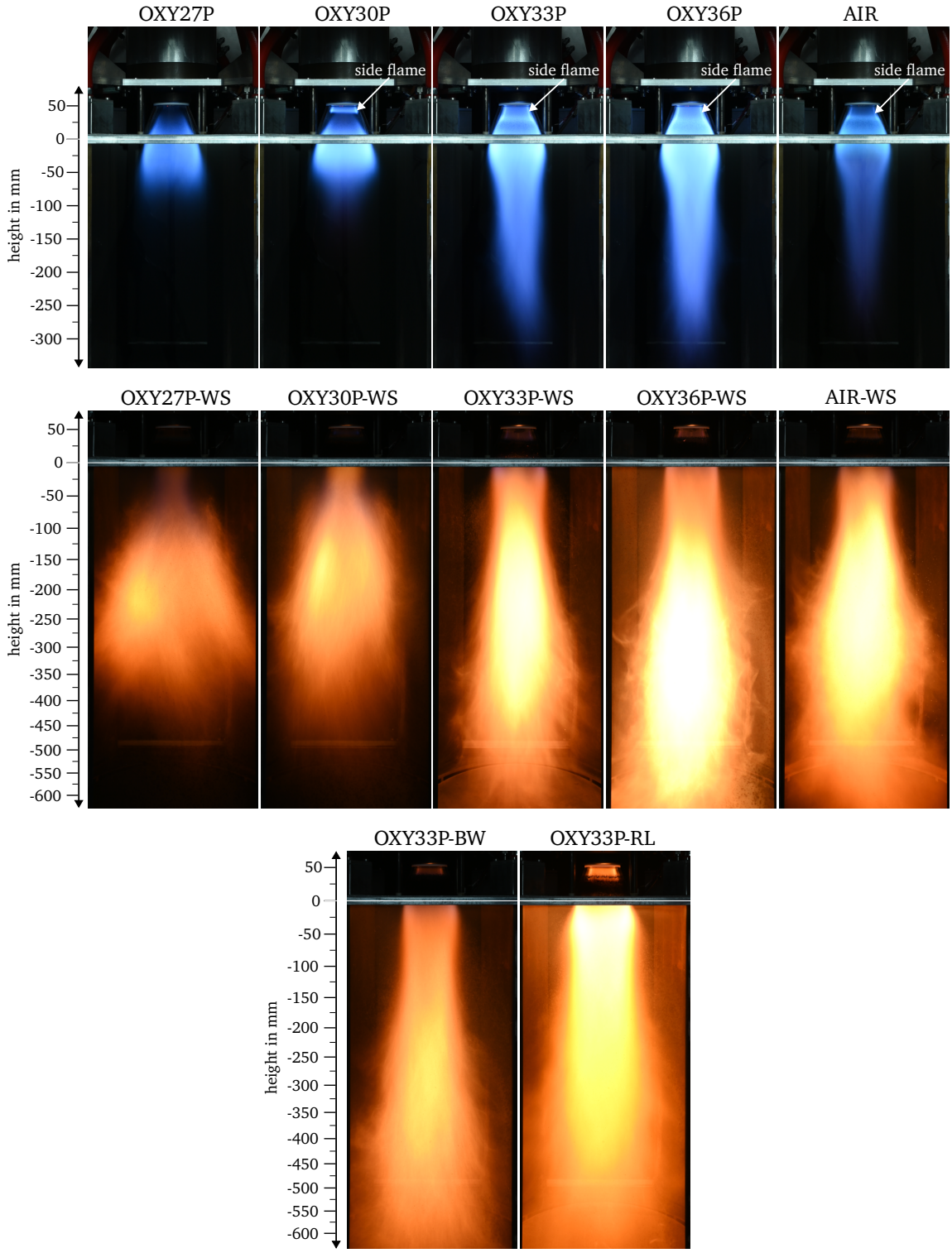

Figure 3.5: Photographs of the second set of SFC operation conditions. Top row: Single-phase operation conditions. Second row: Gas-assisted solid fuel combustion operation conditions with walnut shells (WS). Third row: Gas-assisted solid fuel combustion operation condition with 33 vol.% oxygen concentration and beech wood (BW) and Rhenish lignite (RL). The emission of flame radiation originating from within the quarl is largely obstructed by particles that adhere to the walls. Camera settings are equal within the singe-phase combustion and within the gas-assisted solid fuel combustion. All flames have an exposure time of 0.5 s. Illustration adapted from [2]. Side flames marked in the single-phase operation conditions will be discussed in Chapter 5.

3.2.2 Solid fuels

The solid fuels investigated in this thesis consist of one type of lignite: Rhenish lignite (RL), and two biomass representatives: walnut shells (WS) and beech wood (BW). Microscopic images of these fuels are shown in Figure 3.6. Proximate, ultimate, and particle size analyses are presented in Table 3.3. These fuels are positioned within the van Krevelen diagram in Figure 2.2 according to their atomic ratios of hydrogen-to-carbon (H/C) and oxygen-to-carbon (O/C).

Figure 3.6: Microscopic images of walnut shells (WS), beech wood (BW), and Rhenish lignite (RL). The scale of the images is shown in the lower right corner.

Table 3.3: Solid fuel properties of walnut shells (WS), beech wood (BW) and Rhenish lignite (RL). Proximate, ultimate, and particle size analysis. The particle size analysis of WS and BW is done by microscopy, the particle size analysis of RL by laser diffraction. LHV = Lower Heating Value, AR = Aspect ratio. Table adapted from [2].

		Walnut shells (WS)	Beech wood (BW)	Rhenish lignite (RL)
Proximate analysis (raw)				
Moisture	wt.%	9.48	5.04	9.13
Ash	wt.%	0.66	0.69	5.52
Volatile matter	wt.%	72.93	85.71	44.99
LHV	MJ/kg	18.85	16.48	21.42
Ultimate analysis (raw)				
Carbon	wt.%	46.11	45.29	58.21
Hydrogen	wt.%	5.58	4.46	4.00
Nitrogen	wt.%	0.10	0.21	0.83
Sulfur	wt.%	<0.01	<0.01	0.37
Fluorine	wt.%	0.06	-	<0.01
Chlorine	wt.%	0.05	-	0.02
Oxygen	wt.%	37.95	44.32	21.92
Particle size distribution				
D10	µm	101.5	175.8	3.1
D50	µm	140.6	318.9	23.5
D90	µm	178.8	447.4	396.2
Vol. mean dia.	µm	138.5	298.2	120.2
Vol. mean AR	-	1.49	3.14	not known

While all solid fuels share similar moisture contents, walnut shells and beech wood exhibit a significantly higher volatile matter content in contrast to Rhenish lignite. On the other hand, Rhenish lignite features a higher fixed carbon content and lower oxygen and hydrogen content than the biomass fuels.

The solid fuels are milled into different particle size distributions. Rhenish lignite is finely milled into a powder with particles ranging from as small as $d_{p,10} = 3\,\mu m$ (D10 value) to as large as $d_{p,90} = 396\,\mu m$ (D90 value). Conversely, walnut shells exhibit a relatively narrow size distribution spanning between $d_{p,10} = 102\,\mu m$ (D10 value) and $d_{p,90} = 179\,\mu m$ (D90 value). Beech wood particles are even larger, ranging from $d_{p,10} = 176\,\mu m$ (D10 value) to $d_{p,90} = 447\,\mu m$ (D90 value). Rhenish lignite and walnut shell particles exhibit a near-spherical morphology, characterized by aspect ratios (AR) close to 1. Conversely, beech wood particles display an elongated shape, resulting in a notably higher average aspect ratio of 3.14.

3.3 Temperature boundary conditions

In this section the thermal boundary conditions for the different operation conditions, introduced in Section 3.2.1 are presented. For the measurements of the inner wall temperatures of the quartz glass components, thermographic phosphor thermometry (TPT) was used. All other wall temperatures were monitored by thermocouples.

The TPT measurements have already been published in [4] for the single-phase conditions of the first set of operation conditions. Text and figures in Sections 3.3.1 and 3.3.2 are reused and partially modified to match the structure and nomenclature of this work. Accordingly, a declaration of the individual contributions of all authors is included in Appendix C. The method description in Section 3.3.1 is expanded with more details and in Section 3.3.2 the two-phase operation conditions and results from thermocouple measurements are presented and discussed in addition.

3.3.1 Methods

The method section is divided into the description of the application of thermocouples to the SFC and the utilization of phosphor thermometry. Thereby all measurement locations are outlined.

In the following, the implementation to the SFC is presented while the fundamentals of TPT are described in Section 2.3.4.

3.3.1.1 Thermocouples

Mineral insulated thermocouples of type K with a diameter of 1 mm are applied to the SFC at the bluff body and at the top cover, the chamfered corners, and the base plate of the combustion chamber. All thermocouples are positioned 0.3 mm below the surface.

Three thermocouples are placed inside the bluff body at a radius of $r = 3.5\,mm$, evenly distributed around the circumference.

At the top cover of the combustion chamber, five thermocouples are located along two radial lines. One radial line extends from the chamber center towards the chamber corner, while the other proceeds directly towards the chamber window in the most direct path. The thermocouples are positioned at the radii $r = 106\,mm$ and $r = 135.5\,mm$ in each case. Additionally, another thermocouple is placed outside the tertiary flow, along the radial line leading to the corner, at the radius $r = 219.5\,mm$.

Three thermocouples are located at the base plate of the combustion chamber. One is placed at the center and the other two thermocouples are positioned at the radii $r = 60\,\text{mm}$ and $r = 120\,\text{mm}$, respectively.

Furthermore, each corner of the combustion chamber is equipped with three thermocouples to monitor flame symmetry and one corner features an array of 17 thermocouples to determine the thermal boundary conditions. 11 of the 17 thermocouples are placed in the corner center at a distance of 50 mm in height from each other with the first one located at $h = -40\,\text{mm}$. At the heights $h = -240\,\text{mm}$, $-340\,\text{mm}$, and $-440\,\text{mm}$ one thermocouple was placed to each side of the corner center at a distance of 25 mm. All locations are shown in the results section on top of the measurement data.

3.3.1.2 Phosphor thermometry

Phosphor thermometry uses the temperature-dependent luminescence properties of rare earths or transition metal doped ceramic materials. The decay of the luminescence after a pulsed excitation is correlated with the temperature of the material and can be approximated by a mono-exponential decay of the luminescence intensity as a function of time $I_{\text{TPT}}(t)$, as described by Equation (2.27). However, in experimentally derived decay curves a time-independent offset b occurs, originating from digitization, dark current of the detector, or background signals [164]. With this, Equation (2.27) is expanded as follows:

$$I_{\text{TPT}}(t) = I_0 e^{\left(\frac{t}{\tau}\right)} + b \tag{3.1}$$

$Gd_3Ga_5O_{12}:Cr^{3+},Ce^{3+}$ (GGG:Cr,Ce) is a well-characterized thermographic phosphor [163, 186] and has shown good results in several combustion environments [187, 188]. By using the lifetime method, the temperature range between 290 K and 980 K is accessible [189] which covers the expected temperature range. To apply the phosphor on the quartz glass components, GGG:Cr,Ce was dispersed in a temperature resistant binder (ZYP Coatings, HPC Binder). Then 18 spots with a diameter of 3 mm in a grid of five by three were applied to a window and a thin line was airbrushed on the inside of the quarl.

The fourth harmonic (266 nm) of an Nd:YAG laser (Spectra-Physics, Quanta-Ray INDI) operating at 10 Hz was used as the excitation source. A photomultiplier tube (PMT, Hamamatsu, H6780-20) equipped with a camera lens (Nikkor 50 mm, f/1.2) and a bandpass filter (Thorlabs, FB730-30) was used to detect the phosphorescence signal. The analog signal was amplified by a factor of 104 V/A using a transimpedance amplifier (Femto, DHPCA-100) and recorded with an oscilloscope (Tektronix, TDS 5032B). Prior to the experiments, the phosphor was calibrated inside a temperature-controlled furnace between 323 K and 903 K. Calibration points were recorded every 20 K. At each calibration point 1000 decay curves at a sampling rate of 125 MHz were measured, leading to a discretization of each decay curve with at least 20 000 single points. Thereof 100 decay curves were averaged and the decay time τ, also to referred as lifetime, was calculated using the linear regression of the sum algorithm (LRS) suggested by Fuhrmann et al. [164].

The LRS approach uses the fact that the integral of the decay waveform can be reformulated as a linear equation, expressing the decay waveform as a function of its own integral:

$$\int_0^t I_{\text{TPT}}(t)dt = \tau(I_0 + b) - \tau I_{\text{TPT}}(t) + bt \tag{3.2}$$

$$I_{\text{TPT}}(t) = I_0 + b - \frac{1}{\tau}\int_0^t I_{\text{TPT}}(t)dt + \frac{bt}{\tau} \tag{3.3}$$

Subsequently, the method of least squares can be applied to determine the lifetime τ.

In experiments, the decay curves deviate from the mono-exponential decay approximation of the luminescence intensity, especially at the beginning and end of the curve due to multi-exponential characteristics and superimposed noise. To circumvent these effects an iteratively adapted temporal fitting window according to [190] was applied. The decay curves were fitted in the window from $t_1 = t_0 + c_1\tau$ to $t_2 = t_0 + c_2\tau$, where t_0 refers to the time of the excitation. c_1 and c_2 were determined iteratively and convergence is achieved when the value of the lifetime τ becomes constant. c_1 and c_2 are set for this application to 0.5 and 3.5, respectively.

The calibrated temperature-dependent lifetimes of GGG:Cr,Ce are depicted on the left side of Figure 3.7 and a 10th order polynomial fit of the logarithm of the lifetime τ was used for interpolation. The temporal (shot to shot) standard deviation for all calibration measurement points was below 1.4 K, as shown on the right side of Figure 3.7.

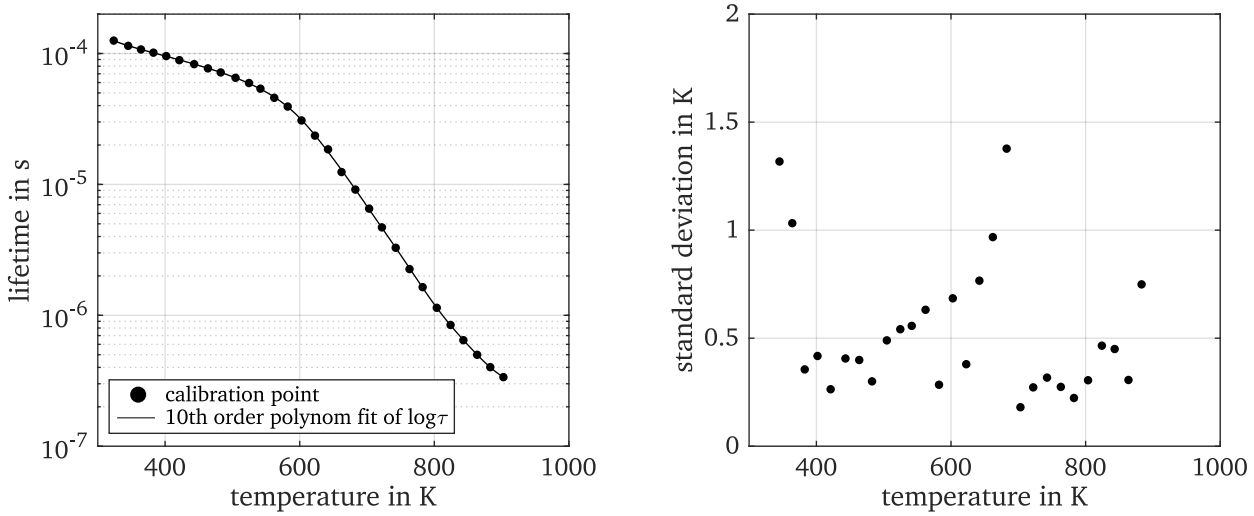

Figure 3.7: Calibration of $Gd_3Ga_5O_{12}$:Cr^{3+},Ce^{3+}. Left: Temperature-dependent lifetimes of GGG:Cr,Ce. Calibration points were recorded every 20 K in the range between 323 K and 903 K. Interpolation between the calibration points was performed using an 10th order polynomial fit of the logarithm of the lifetime τ. Right: Temporal (shot to shot) standard deviation for all calibration measurement points.

For the determination of the wall temperatures 500 decay curves were recorded for every measurement point and processed in the same way as it was done with the calibration data.

3.3.2 Results and discussion

The inner wall temperatures, which are measured by thermocouples, are depicted in Figure 3.8. Measurements at the bluff body are not available due to thermocouple damage incurred during assembly.

In the top-left section of Figure 3.8, the wall temperatures of the chamber's top cover are shown. The temperatures are inter- and extrapolated using linear fits within the component between the quarl assembly at $r = 58$ mm and the tertiary flow assembly at $r = 175$ mm. Across all operation conditions, a consistent trend of decreasing temperatures with increasing radii is observed. The temperatures in proximity to the corner, on the outside of the tertiary flow, remain comparably low. The two-phase operation conditions exhibit approximately 100 K higher wall temperatures compared to their corresponding single-phase operation condition. The operation condition OXY33-RL shows the highest wall temperatures at the top, possibly due to lower inflow velocities despite having less thermal power

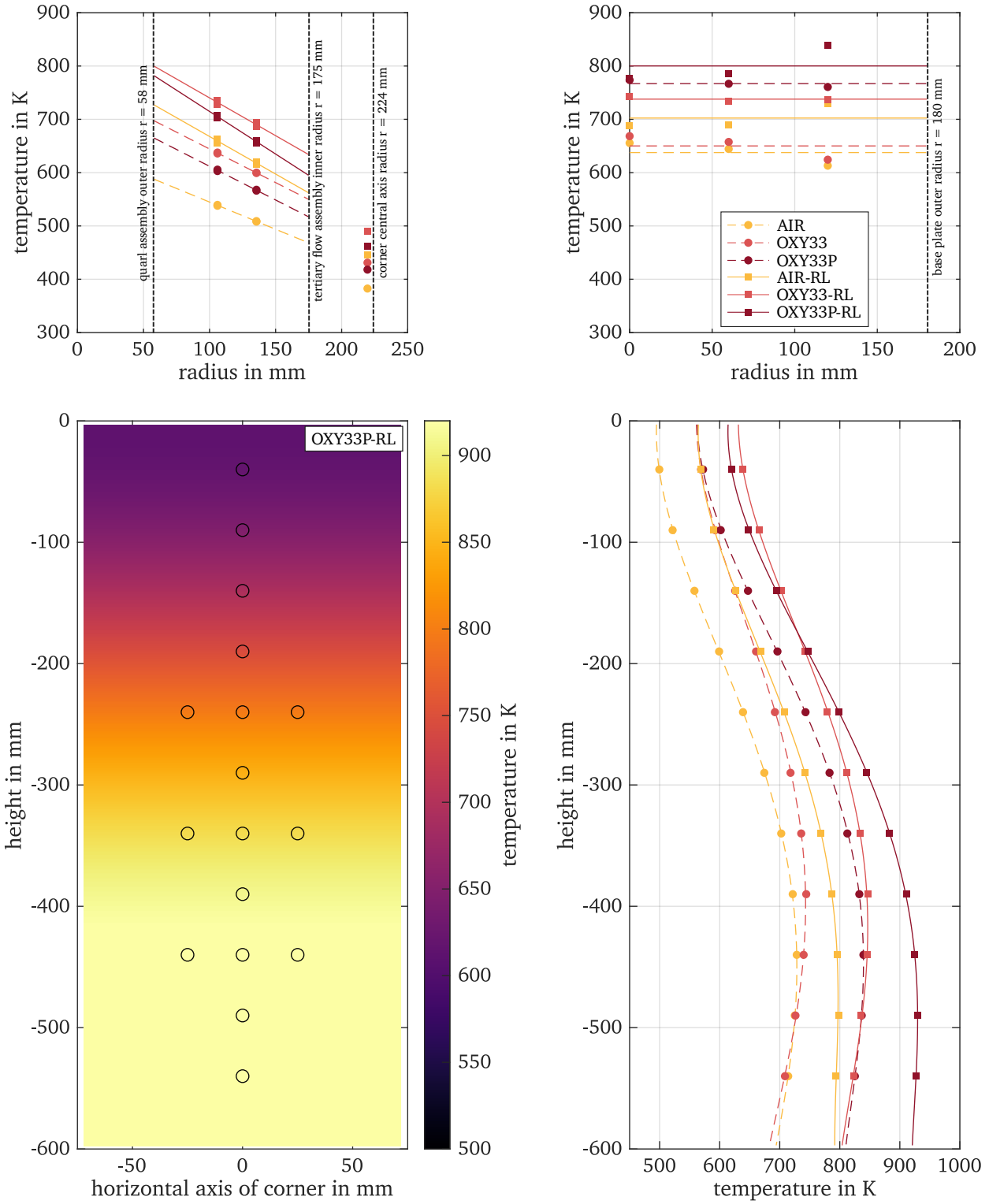

Figure 3.8: Temperature boundary conditions of the first set of operation conditions measured with thermocouples. Measurement points are marked by circles (single-phase combustion) and squares (two-phase combustion). Top left: Measured wall temperatures at the chamber top. Top right: Measured wall temperatures at the chamber bottom. Bottom left: Measured wall temperature at the chamber corner of operation point OXY33P-RL. Black circles mark the measurement points. Bottom right: Measured wall temperature profiles in the center of the chamber corner.

when compared to OXY33P-RL. Conversely, operation conditions under air atmospheres exhibit the lowest wall temperatures, primarily due to the lower heat capacity of the air atmosphere and the reduced radiation intensity compared to oxy-fuel conditions. Furthermore, the temperature difference between the two thermocouples located at the same radii but on different radial lines is less than 3 K for single-phase operation conditions and less than 8 K for two-phase operation conditions. Therefore, a Therefore, a circumferentially uniform wall temperature can be assumed.

In the top-right section of Figure 3.8, the wall temperatures of the chamber's bottom, specifically within the central base plate, are illustrated. For each operation condition, a uniform temperature is estimated for the base plate, considering significant deposits of partly burned solid fuel particles and ash that affect local temperature over time. The highest temperatures are observed for operation condition OXY33P-RL, which features a 57.5% increase in thermal power compared to AIR-RL and OXY33-RL. Operation conditions in air atmospheres exhibit the lowest temperatures for single-phase and two-phase operation conditions, respectively.

The bottom section of Figure 3.8 presents the wall temperatures of the chamber corners. The wall temperatures are inter- and extrapolated using a fourth-order polynomial along the vertical axis. A uniform horizontal temperature is assumed within each height due to the minimal variations (≤ 5 K) of temperature readings from thermocouples at a given height for each operation condition. Due to the close proximity of the tertiary stream inlets to the corners, lower temperatures are observed at the top of the corners. The maximum temperatures are reached in the lower part of the combustion chamber for AIR, AIR-RL, OXY33P, and OXY33P-RL, while the maximum wall temperatures of OXY33 and OXY33-RL are shifted upstream towards the central region. The two-phase operation conditions exhibit temperatures 50 K to 70 K higher at the top of the corner compared to their single-phase counterparts. This temperature difference increases further downstream, reaching 80 K to 120 K at the lower end of the chamber's corner. The temperature profiles of AIR and OXY33P, along with their corresponding two-phase conditions, exhibit similar trends due to comparable inflow velocities. However, these profiles differ in absolute values due to the higher thermal power of OXY33P and OXY33P-RL. Moreover, particularly in the upper part, OXY33 and OXY33-RL showcase higher wall temperatures. This phenomenon can be attributed to the lower gas velocities, subsequently resulting in reduced convectional heat transfer. This observation aligns with the wall temperatures noted at the top of the chamber.

Figure 3.9 presents the measured inner wall temperatures at the windows, which are derived using TPT. The temperatures are inter- and extrapolated using a fourth-order polynomial along the vertical axis and a second-order polynomial along the horizontal axis and the assumption of a rotationally symmetric temperature distribution. The wall temperatures at the window follow similar profiles to those at the chamber corner. However, these temperatures are approximately 100 K lower compared to the corresponding operation condition and height at the chamber corner. This difference in temperatures can be explained by the temperature insulation of the chamber corners from the chamber frame, while the 3 mm thick windows are exposed to room temperatures on the outer side.

The wall temperature profiles inside the quartz glass quarl are illustrated in Figure 3.10. The temperatures are inter- and extrapolated using a second-order polynomial and show similar characteristics for the different operation conditions when compared to the window wall temperatures. Operation conditions AIR, AIR-RL, OXY33P, and OXY33P-RL exhibit similar temperature trends, while OXY33 and OXY33-RL showcase different profiles. For each operation condition large temperature rises in the order of 200 K are measured over the quarl height.

An error analysis was performed for the TPT measurements according to [163]. The analysis revealed a systematic error below 5 K due to the calibration process and a standard deviation below 1.6 K for all temperature measurements.

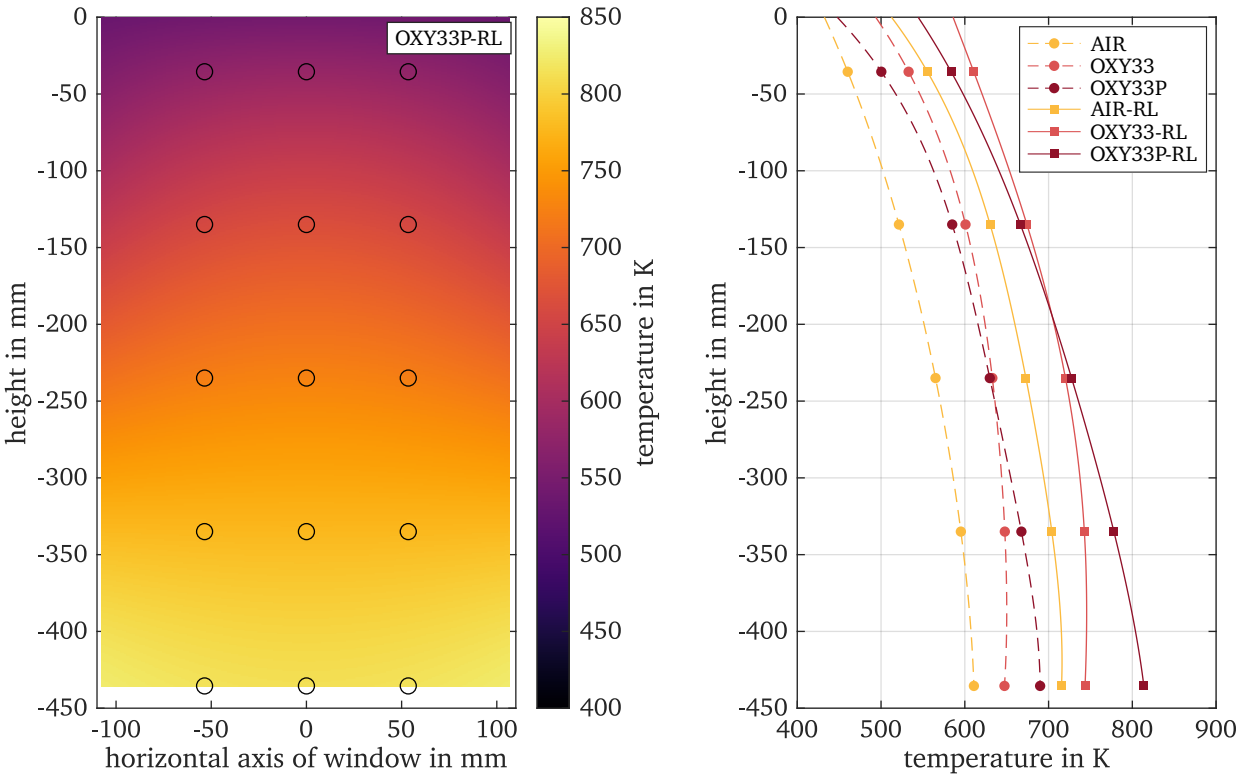

Figure 3.9: Temperature boundary conditions of the first set of operation conditions measured with TPT at the inner window wall. Left: Measured wall temperature at the window of operation point OXY33P-RL. Only data up to $h = -435$ mm are measured. Black circles mark the measurement points. Right: Measured wall temperature profiles in the center of the window. Measurement points are marked by circles (single-phase combustion) and squares (two-phase combustion). The standard deviations of the temperature are below 1.6 K and are not shown in the figure. Figure adapted from [4].

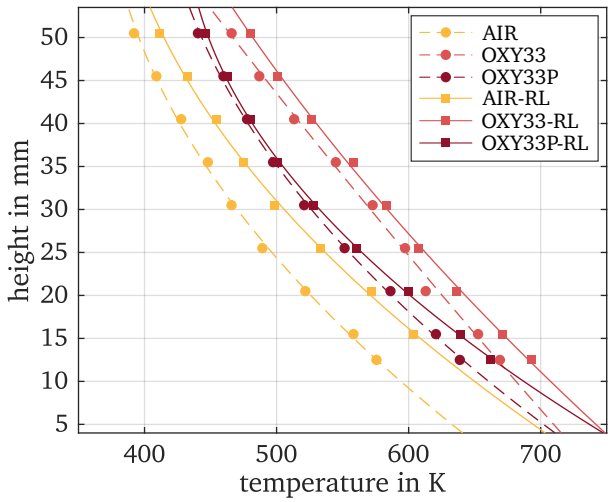

Figure 3.10: Temperature boundary conditions of the first set of operation conditions measured with TPT at the inner quarl wall. Measurement points are marked by circles (single-phase combustion) and squares (two-phase combustion). Figure adapted from [4].

3.3.3 Conclusion

Thermographic phosphor thermometry and thermocouples were used to measure the wall temperatures of a gas-assisted pulverized solid fuel combustor under air and oxy-fuel conditions. The temperature boundary conditions of all major components were determined for single-phase and two-phase conditions of the first set of operation conditions of the SFC. The analysis of the wall temperatures showed good agreement between the individual components with an overall lower wall temperature for air combustion compared to oxy-fuel operation conditions. While the lower inflow velocities and thus reduced convectional heat transfer of operation conditions OXY33 and OXY33-RL resulted in high wall temperatures at all components close to the burner, OXY33P and OXY33P-RL exhibited the highest overall temperatures due to their higher thermal power.

Knowledge about the temperature boundary conditions is crucial for numerical simulations. The wall temperatures obtained through this study serve as valuable data for implementing precise numerical simulations of the SFC.

4 Flow dynamics and particle temperatures

Within this chapter, flow dynamics and temperatures of solid fuel particles for the first set of operation conditions, introduced in Section 3.2.1, are investigated. The study focuses on gas-assisted solid fuel combustion only. The dynamics of the flow are investigated to determine gas phase velocities, particle dispersion, particle trajectories, and mean residence times of the gas and the particles phase in the near-nozzle region.

Text and figures in this chapter have already been published by Schneider et al. [1] and are reused and partially modified to match the structure and nomenclature of this work. Accordingly, a declaration of the individual contributions of all authors is included in Appendix D. Please note, that the two-color pyrometry experiments to determine particle temperatures were performed by Sarah Valentiner and Nikita Vorobiev (Institute of Energy Plant Technology, Ruhr-University, Bochum), while the interpretation of the evaluated particle temperatures in the context of the SFC was conducted in collaboration.

4.1 Aim of this investigation

In pulverized solid fuel combustion, the particle behavior throughout the entire combustion process contains fundamental information to support our understanding of flame stabilization, burnout behavior, and burnout rate. Experimental investigations on flow dynamics and temperatures of solid fuel particles provide an insight into particle conditions at different stages of the combustion. In pulverized solid fuel combustors, many phenomena affect the conversion of the fuel particles. Starting at the inflow of the particles into the combustor, particle dispersion with the surrounding gas flows, particle heat up and the release of volatiles are three major phenomena that take place close to the burner mouth.

To investigate these phenomena, experiments are carried out under well-controlled inflow and boundary conditions inside the SFC. Flow fields of small particles that represent the gas phase velocity are determined in the near-burner region by PIV using a particle separation algorithm. Trajectories of large solid fuel particles are evaluated in a two-dimensional plane using a combined high-speed PIV/PTV approach. Particle temperatures and particles sizes are measured at different levels downstream the burner exit to reveal different stages of combustion. Therefore, a two-color pyrometer that dissolves single particles is used to measure particle temperatures and particle size distributions.

4.2 Methods

The method section is divided into three subsections. Within Section 4.2.1, the experimental PIV setup including the processing approach to determine the flow field is described. Section 4.2.2 outlines the high-speed PIV/PTV experimental setup with subsequent processing to evaluate particle trajectories. The third subsection, Section 4.2.3, presents the two-color pyrometer.

In the following, the implementation to the SFC is presented while the fundamentals of PIV, PTV and pyrometry are described in Sections 2.3.2 and 2.3.7.

4.2.1 PIV using solid fuel as tracers

To determine the gas phase velocities, a conventional two-dimensional PIV-setup was used following the approach presented by Becker et al. [75, 150]. The gas phase velocity was determined from small solid fuel particles used as tracers. These tracers were separated from large particles in a post-processing procedure using the criteria of 'size' and 'intensity' to sort out large particles. Measurements were performed at two regions located inside the quarl with a field of view (FOV) of 45 x 53 mm² and directly downstream the dump plane with a FOV of 90 x 107 mm².

The beam of a double-pulsed frequency-doubled Nd:YAG laser (InnoLas SpitLight Compact 400 PIV, 532 nm) was formed into a light sheet to illuminate the particles. The sheet thickness was adjusted to 450 µm for both measurement regions. The time separation between the laser pulses (Δt) for measurements inside the quarl was set to 15 µs (AIR, OXY33P) and 20 µs (OXY33). Downstream the dump plane Δt was extended to 25 µs (AIR, OXY33P) and 35 µs (OXY33), respectively. The imaging system consisted of a sCMOS camera (LaVision, imager sCMOS, 2560 x 2160 px, 16 bit) equipped with a 105 mm Sigma macro lens and a set of three 532 nm band-pass filters to suppress flame luminosity. 3500 double images were recorded for each operation point and FOV with a repetition rate of 10 Hz. The experimental setup is illustrated in Figure 4.1.

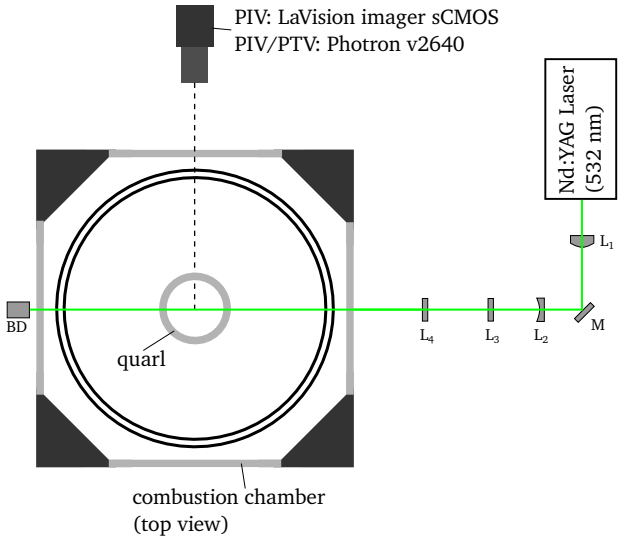

Figure 4.1: Experimental setup for PIV and PTV measurements. PIV setup: laser: InnoLas SpitLight Compact 400 PIV, camera: LaVision imager sCMOS. PTV setup: laser: Edgewave, INNOSLAB, camera: Photron v2640. BD: beam dump. L_{1-4}: sheet forming lenses, cylindrical lenses. M: mirror. Figure adapted from [1].

To determine the unbiased gas phase velocity by using small solid fuel particles as tracers, it is important to reject all particles that do not follow the gaseous flow instantaneously. To separate the tracer images, a sliding background filter with a size of 10 x 10 px was applied to the original images once inside the quarl and twice downstream the dump plane to suppress scattered light from particle clouds and remaining flame luminosity. Further, the filter function of Khalitov and Longmire [146] was used three times employing a factor of $c = 2$ from their procedure to eliminate high frequency noise. Afterwards, large particles were detected and erased using the information of connected pixels above a user-defined threshold and the mean intensity of the brightest pixels. To estimate the influence of large particles which are erroneously not classified as large particles, a sensitivity analysis was performed. Since similar particle size distributions of the solid fuel were used for all operation conditions, sensitivities are evaluated exemplarily for the operation point AIR. The parameter values

used for both FOVs are listed in Table 4.1. The main error source originates from the inhomogeneous illumination of the particles which was discussed by Becker et al. [75] in detail. Because of the low sensitivity of the user-defined separation parameters, an accurate determination of the gas velocity with this approach is confirmed.

Table 4.1: Sensitivity analysis for the parameters 'size' and 'intensity' using the operation point AIR. The absolute deviation of mean velocities (radial, axial, magnitude) with the listed separation parameters compared to the set of parameters used to determine the gas phase velocity (Quarl: 15 px, 3500 counts; Downstream dump plane: 10 px, 2000 counts) is shown. The corresponding mean axial velocity is presented in Figure 4.3.

FOV: Quarl			
	radial in m/s	axial in m/s	magnitude in m/s
10 px, 3500 counts	0.003	-0.014	0.002
15 px, 2000 counts	-0.008	-0.043	-0.012
15 px, 7000 counts	0.002	0.030	-0.044
25 px, 3500 counts	-0.000	0.021	-0.017

FOV: Downstream dump plane			
	radial in m/s	axial in m/s	magnitude in m/s
7 px, 2000 counts	0.012	-0.005	-0.008
10 px, 1500 counts	0.048	0.000	0.001
10 px, 4000 counts	-0.024	0.010	0.010
15 px, 2000 counts	-0.013	0.005	0.008

PIV processing of the tracer images was performed using the software DaVis 10.1.0 (LaVision). Tracer images inside the quarl were pre-processed by subtracting an average time filter to reduce laser reflexes originating from the quartz glass quarl. Subsequently, a sliding background with a mask of 8 x 8 px was subtracted in both FOVs to eliminate local soot luminescence. PIV vectors were calculated using multi-pass vector calculation with three initial passes (window size: 64 x 64 px, adaptive weighting, overlap: 75%) and two final passes (window size: 32 x 32 px, adaptive weighting, overlap: 50%). Vectors with a peak ratio less than 1.5 were deleted and a 7 x 7 px universal outlier detection filter was applied to detect spurious vectors. The applied PIV algorithm leads to a vector spacing of 0.66 mm inside the quarl and 1.34 mm downstream the dump plane.

4.2.2 Particle trajectories from high-speed PTV

Particle trajectories were measured in a two-dimensional plane using a high-speed PIV/PTV approach. Individual particle velocity vectors between successive images were combined to evaluate the whole trajectory within the two-dimensional plane. Measurements were performed in similar regions as done for the gas phase velocity measurements (FOV Quarl: 45 x 57 mm^2; FOV downstream dump plane: 81 x 110 mm^2). Compared to the PIV measurement setup, shown in Figure 4.1, the low-speed system was replaced by a high-speed PIV/PTV system to determine particle trajectories.

Particles were illuminated by a frequency-doubled Nd:YAG laser (Edgewave, INNOSLAB, 532 nm). The formed light sheet was aligned to 190 µm inside the quarl and to 450 µm downstream the dump plane. The Mie scattering of particles was detected by a high-speed camera (Photron v2640) equipped with a 180 mm Sigma macro lens. A set of three 532 nm band-pass filters was placed in front of the macro lens to suppress flame luminosity. Laser and camera were synchronized and images were recorded at 7.5 kHz. 20000 images were recorded and processed for each operation point and FOV.

The separation was done following the same procedure as described in Section 4.2.1. The parameters 'size' and 'intensity' were tuned to 10 connected pixels and 1300 counts for the FOV inside the quarl and to 10 connected pixels and 1200 counts for the FOV downstream the dump plane. These parameters needed to be changed due to differences in laser fluence, dynamic range of the camera and spatial resolution compared to the PIV recordings.

PIV with subsequent PTV processing was performed in DaVis 10.0.5 (LaVision). In a first step, PIV vectors were calculated using the large particle images with one initial pass (window size: 128 x 128 px, adaptive weighting, overlap: 75%) and one final pass (window size: 64 x 64 px, adaptive weighting, overlap: 50%). Vectors with a peak ratio less than 1.2 were deleted and a 7 x 7 px universal outlier detection filter was applied to detect spurious vectors. Vector post-processing was performed by using a 5 x 5 px polynomial smoothing and an interpolation to fill-up empty spaces. In the next step the PTV algorithm used the calculated PIV vectors as an estimator. A large particle shift of 80 px relative to the estimation was allowed to capture all particle movements.

Vectors were combined matching the end point of a vector with the start point of the subsequent vector allowing a difference of 0.05 mm in h and r-directions. If no vector start point is found at the estimated location, the trajectory ends. Trajectories of up to 50 combined vectors were achieved. However many trajectories are relatively short, resulting in a mean trajectory length of 3.6 vectors for the operation point OXY33-RL inside the FOV downstream the dump plane. For this FOV over 1.4 million trajectories were processed.

Velocities of the particle trajectories are estimated using a linear regression for trajectories with less than 7 combined vectors and a quadratic regression for trajectories with 7 and more combined vectors. Additionally, trajectories with a length of 3 vectors and more enable the evaluation of particle accelerations. Another useful parameter by analyzing the particle trajectories is the trajectory direction.

4.2.3 Two-color pyrometry

Ratio pyrometry, in this case two-color pyrometry, is a typical technique to determine temperatures of surfaces of unknown emissivity. Utilizing this principle, char particle temperatures were measured using the imaging pyrometer system SCOT [41] shown in Figure 4.2. The system consists of two image-intensified monochromatic cameras. The working principle of the pyrometer is as follows: Emission from the focal plane is split at 700 nm by a dichroic mirror. Each of the two spectrally separated channels is monitored by a camera. The cameras are equipped with band pass filters centered at 785 nm (FWHM = 62 nm) and 650 nm (FWHM = 100 nm), respectively, to separate two closely connected wavelength bands. The measured intensity ratio of the two wavelength bands is compared to a calibration curve to estimate the particle temperature [180]. A Questar QM 1 long range microscope is used to provide a high optical resolution. In the present setup, the resulting pixel resolution is approximately 7.4 µm/px.

As the expected particle velocities are in a range of up to 10 m/s, the exposure time of the cameras is set to t_{exp} = 5 µs to reduce particle motion during the exposure, which would have a negative influence on the size determination. The intensifiers are set to 80% amplification. Each recorded particle is evaluated for its focal position due limited focal depth of the Questar microscope. As the experimental setup did not allow to use an additional camera to record the particle position in the 3d-space simultaneously as reported previously [41], particle images are evaluated by a gradient criterion to assure a sufficient focal position, which is necessary for a precise particle size determination. The gradient in the intensity profile of each particle in each camera had to fulfill $\Delta I/\mathrm{px} = 1.15$, as focused particles will have a steep intensity rise along their outline. Furthermore, connected regions of high intensity with a size being larger than 5000 px were removed, as these regions typically represent volatile flames, and the focus was on char temperature in the given case. As second discrimination criterion, events

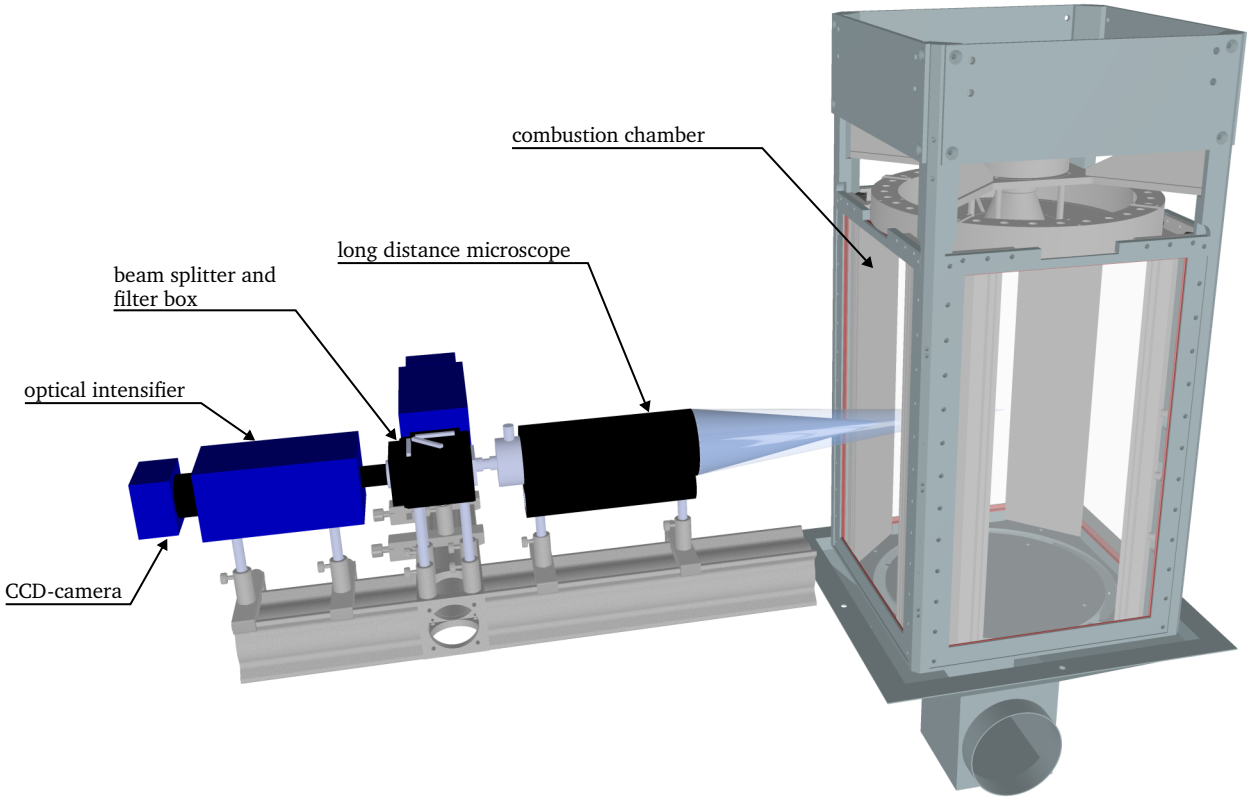

Figure 4.2: Camera system SCOT for char temperature measurements inside the combustion chamber. Figure adapted from [1].

with an intensity in the intensity center of gravity being lower than 50% of the maximum intensity of the event were removed, as these are most likely sooty volatile flames.

4.3 Results and discussion

4.3.1 Gas phase velocity

The flow field of the gas phase velocity shows the characteristics of a swirl flame in combination with a central bluff body for all investigated operation conditions. A large inner recirculation zone with low velocities is surrounded by the main stream downwards. Hot, burnt gas is transported back to the burner mouth which enhances flame stabilization. The velocity magnitude of OXY33-RL is presented on the left side of Figure 4.3.

Between the two concentric annular orifices of the primary and secondary flow, a small recirculation area is observed where the velocity profile implies that a separated side flame is stabilized. This recirculation zone is more pronounced for oxy-fuel conditions than in the reference air operation point although local stoichiometric ratios (λ_{local}) are kept equal. The reason for this is the smaller influence of flame quenching at the diffusor wall due to the higher molar heat capacity of CO_2 compared to N_2. On the left side of Figure 4.3, the smaller recirculation area of AIR-RL located between primary and secondary flow is clearly visible at the position $h = 34\,\text{mm}$. At this position the axial gas velocity of AIR-RL is negative in the region between the two main peaks and the primary flow is already pushed further towards the quarl wall compared to the oxy-fuel conditions. A larger side flame also leads to an increased axial velocity of the primary flow. While AIR-RL and OXY33P-RL have the same volume

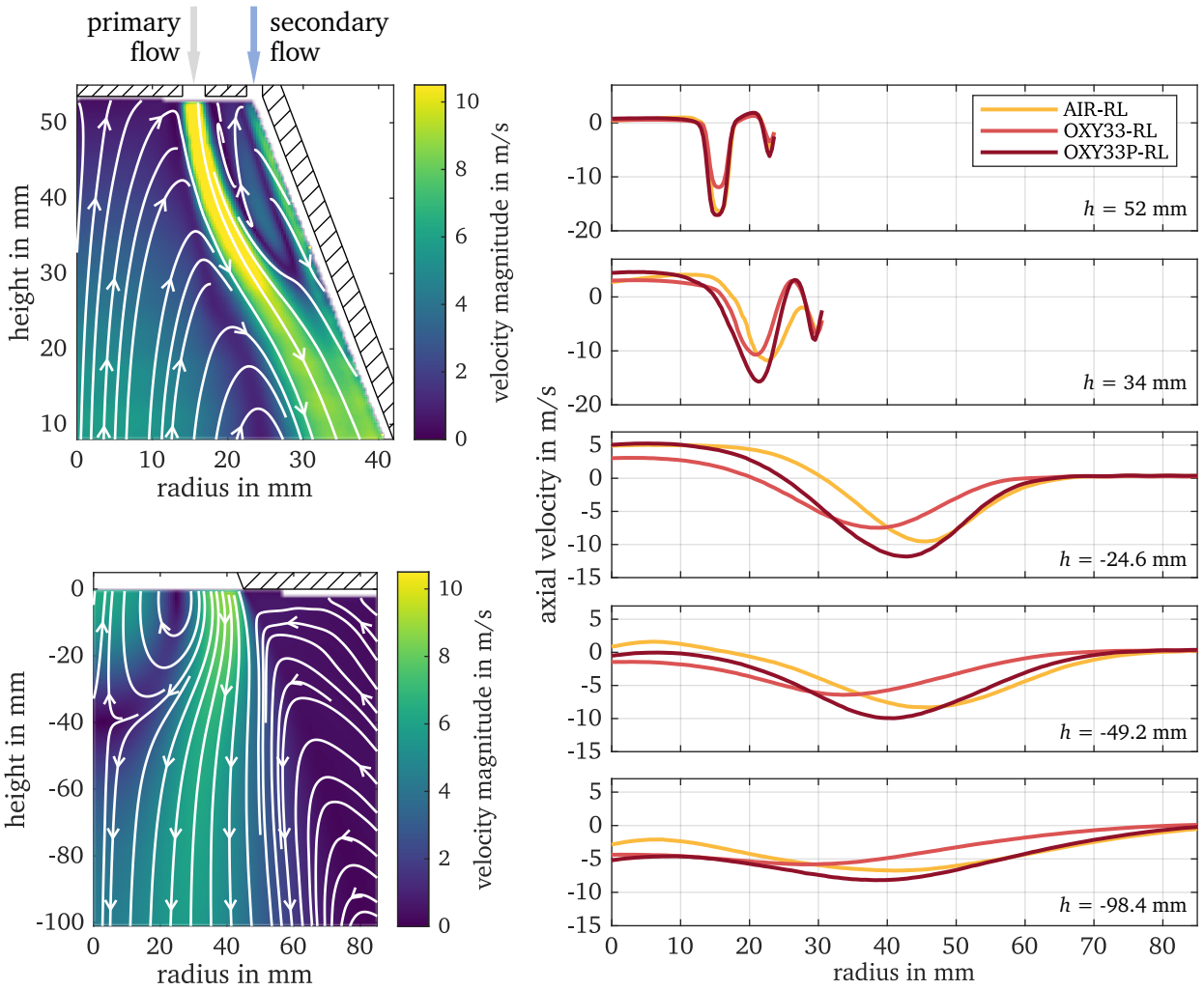

Figure 4.3: Left: Mean gas phase flow field of OXY33-RL. The velocity magnitude is shown. Right: Mean profiles of axial gas phase velocities for the investigated operation conditions at 5 different axial positions ($h = 52\,\text{mm}$, $34\,\text{mm}$, $-24.6\,\text{mm}$, $-49.2\,\text{mm}$, and $-98.4\,\text{mm}$). Figure adapted from [1].

flows by design and show the same axial velocity at $h = 52\,\text{mm}$, the axial velocity at $h = 34\,\text{mm}$ differs significantly.

Downstream the dump plane, the main axial flow expands further before a vortex breakdown is observed. The influence of the side flame is still visible in the velocity profiles. The maximum of the main flow is shifted towards the center of the burner for operation points showing a large recirculation zone between the primary and secondary flow. This is caused by the effect that the side flame prevents the primary flow to be pushed towards the quarl wall in the upper region of the diffusor. At the axial position $h = -24.6\,\text{mm}$ the different radial positions of the maximum axial velocities downwards are visible and also the resulting radial expansion of the large inner recirculation zone. This in turn leads to a larger vertical expansion of the inner recirculation zone of AIR-RL than for OXY33-RL and OXY33P-RL. The stagnation point of the gas phase velocity is located at $h = -61\,\text{mm}$ for AIR-RL and at $h = -49\,\text{mm}$ and $h = -40\,\text{mm}$ for OXY33P-RL and OXY33-RL.

Further downstream ($h = -49.2\,\text{mm}$, $-98.4\,\text{mm}$), the main axial flow broadens and the maximum axial velocity appears closer to center of the burner. At the outside of the main axial flow, an outer recirculation zone is established that transports oxidizer, issued through the inlet of the tertiary flow, to the flame.

4.3.2 Particle dispersion

Pulverized solid fuel is seeded into the primary flow and is issued through the inner annular orifice of the burner head into the combustion chamber. Inside the quarl particle-gas and particle-particle interactions take place which lead to a dispersion of the solid fuel particles. Especially the shear layers to both sides of the primary flow have a significant impact on particle dispersion. On the left side of Figure 4.4, instantaneous Mie scattering images of Rhenish lignite particles inside the diffusor and downstream the dump plane are shown. The alternating vortices to both sides of the particle stream are clearly visible. In the lower part of the diffusor the particle density inside the main particle stream is already much lower than at the entrance into the quarl.

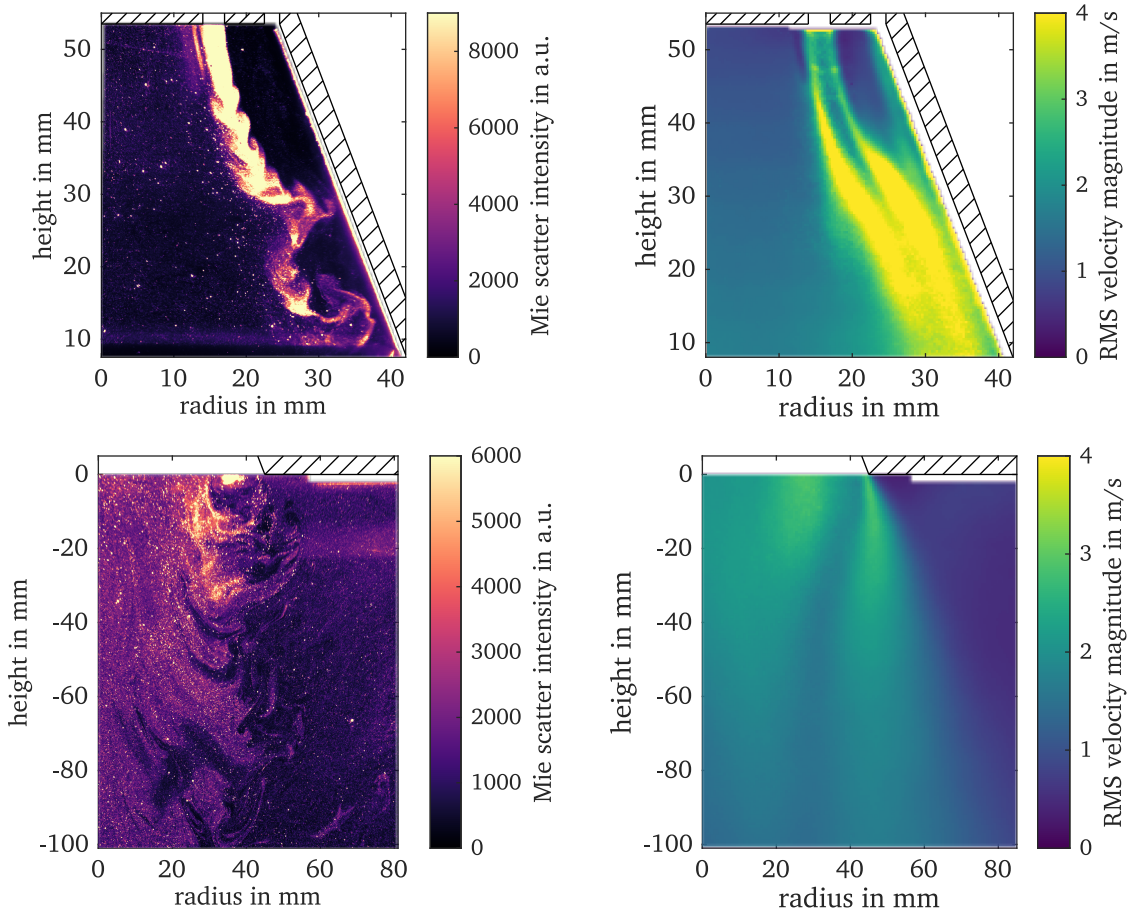

Figure 4.4: Left: Instantaneous Mie images of OXY33-RL inside the quarl and downstream the dump plane. Right: RMS of fluctuations of the gas velocity magnitude of OXY33-RL. Figure adapted from [1].

The shown RMS (Root Mean Square) values of the fluctuation of the velocity magnitude on the right side of Figure 4.4 visualize location, thickness and strength of the shear layers. While the shear layer thickness on the inside of the main particle stream starts to grow at $h = 40\,\text{mm}$, a strong shear layer at the outside of the main particle stream is formed below the recirculation zone of the side flame. Further downstream the shear layers to both sides broadens and get closer to each other. At about $h = 25\,\text{mm}$ the shear layers are almost connected and individual vortices are observed which separate particles from the main particle stream. Inside these vortices, particle clustering occurs which is also noticeable in the instantaneous Mie images downstream the dump plane. Due to laser reflections, the gas phase velocity as well as the RMS values are not accessible at the diffusor wall.

Downstream the dump plane, the main axial flow in downward direction is visible bounded by high RMS values. At the outside of the main axial flow the shear layer towards the outer recirculation zone is formed and broadens further downstream.

4.3.3 Particle trajectories

Compared to the small solid fuel particles that are used as tracers for evaluating the gas phase velocity, large solid fuel particles do not follow the gaseous flow instantaneously. To identify the influence of large particles on the combustion, particle trajectories are measured in a two-dimensional plane. Since similar findings appear for all investigated operation conditions, the operation point OXY33-RL is discussed here representatively.

Large particles are distributed non-homogeneously inside the combustion chamber. In the left column of Figure 4.5, the probability of occurrence of a large particle within an area of 466 x 466 µm² inside the quarl and 832 x 832 µm² downstream the dump plane is shown. For this evaluation the separated large particle images are binned using a grid of 16 x 16 px. High probability regions of large particles are observed on the left side of the main particle stream inside the diffusor and within the main axial flow downwards downstream the dump plane. Due to the low dynamic range of the high-speed camera, the separation of small and large particles in the enclosed main particle stream was not possible and this area will be masked out in the further analysis.

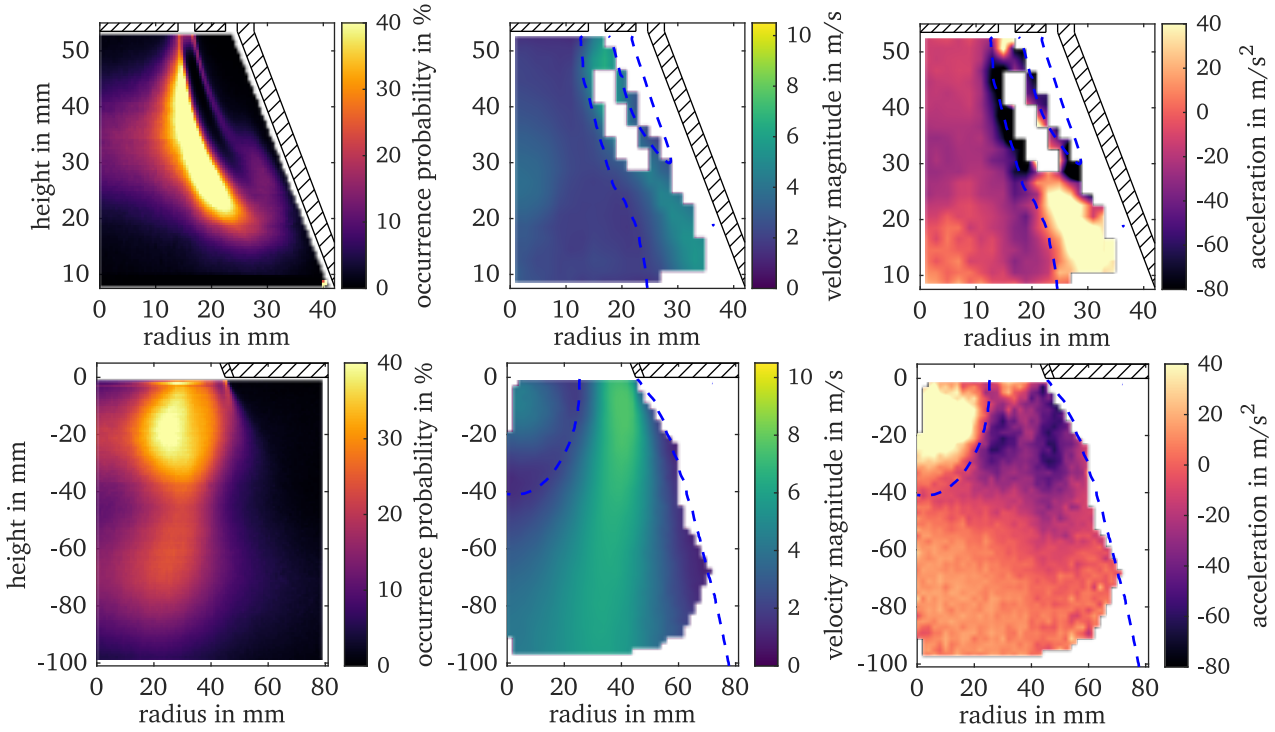

Figure 4.5: Left: Occurrence probability distribution of large particles inside the measurement volume. The probability value represents the occurrence probability of a large particle in an area of 466 x 466 µm² inside the quarl and 832 x 832 µm² downstream the dump plane. The decreasing probabilities below 18 mm are due to the edge of the laser light sheet. Center: Mean particle velocity magnitude of OXY33-RL. Right: Mean particle acceleration of OXY33-RL. Areas with less than 50 detected particle trajectories are masked out. Dashed blue lines indicate borders of gas phase recirculation zones. Figure adapted from [1].

The particle velocity magnitude and acceleration of OXY33-RL is shown in the middle and right column of Figure 4.5. Particle velocities and acceleration are evaluated in grids of 2 x 2 mm². The overall flow field features of the large particles match the flow field of the gas phase quite well. In Figure 4.6, the axial velocity of the large particles is shown on the left side together with the recirculation areas of the gas phase and the contour line where the mean axial particle velocity is equal to zero. Differences appear especially in the region where the main particle stream is pushed towards the diffusor wall. Due to their initial momentum and their inertia of mass, many large particles penetrate the central recirculation zone of the gas phase. This leads to a shift of the contour line towards the center of the burner. This is continued downstream the dump plane. It is also observed that the recirculation area of the gas phase is vertically extended further compared to the particle phase.

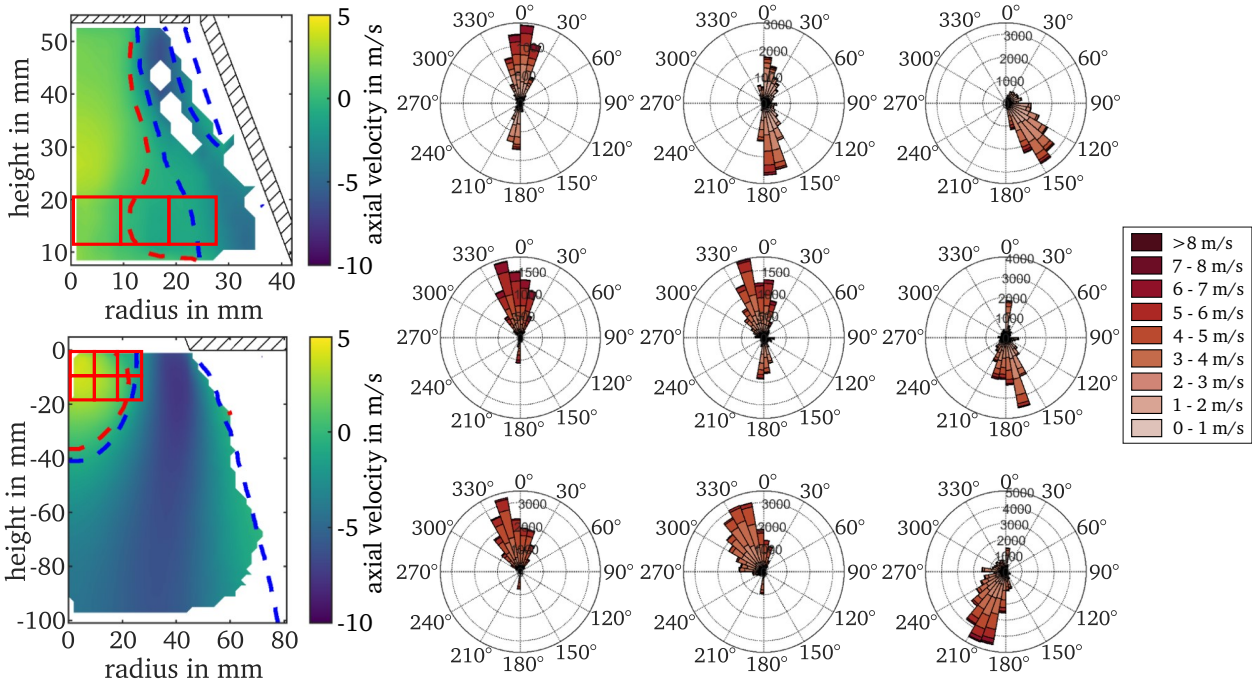

Figure 4.6: Left: Axial velocity of large particles of operating condition OXY33-RL. Dashed blue lines indicate borders of gas phase recirculation zones, dashed red lines show the contours of mean axial velocity of large particles equal to zero. Positions of polar histograms are highlighted by red squares. Right: Polar histograms of particle trajectories containing the information direction distribution, velocity distribution and amount of processed trajectories in the marked areas of the axial velocity field (red squares). Figure adapted from [1].

To visualize the transition zone between the gaseous recirculation area and the main particle flow in downwards direction, polar histograms of particle trajectories are shown on the right side of Figure 4.6. The polar histograms contain the information direction, number of trajectories and velocity. While close to the center of the combustor most particles tend to move upwards inside the recirculation zone, a small amount of large particles is observed moving in opposite direction. This particle trajectory is generated when a large particle is ejected from the main particle stream within the first millimeters after entering the quarl. At larger radial positions, an increase of particles moving downwards and a decreasing number of particles moving up can be observed. At all positions shown a wide distribution of particle velocities up to 8 m/s is monitored. Also a change of the main particle trajectory direction aligning to the gas velocity is noticeable.

The particle accelerations shown in Figure 4.5 reveal different regions of strong accelerations in downwards and upwards directions. Especially inside the recirculation area of the gas phase, large particles are accelerated positively. Either particles moving downwards are decelerated, resulting in a higher

particle residence time within an area of high gas temperatures, or particles are lifted up into the quarl and are integrated into the main particle stream again. Large particles inside the main axial flow in downwards direction are accelerated first before slowing down again when the vortex breakdown of the inner recirculation zone occurs.

4.3.4 Particle residence times

The burn out rate of pulverized solid fuel particles is an important quantity in solid fuel combustion that can be estimated from particle residence time, particle size and particle temperature history. Particle residence times of small and large particles are investigated followed by the analysis of particle sizes and particle temperatures in Section 4.3.5. As measurements were performed independently, only mean values are considered.

Mean residence times of small particles and large particles are estimated by integrating the reciprocal of the gas, respectively the particle velocity along a stream line. Various particle residence times for different particle stream lines of small and large particles are shown in Figure 4.7. Mean velocities in the gap ($h = 0$ mm to 7.5 mm, optically not accessible) are extrapolated using the velocity of the considered stream line. At an axial position of $h = -80$ mm small particles show residence times between 15 ms and 37 ms if they are not trapped inside the recirculation area. Entering the recirculation zone, small particles are transported back into the diffusor and residence times exceed 70 ms at $h = -80$ mm.

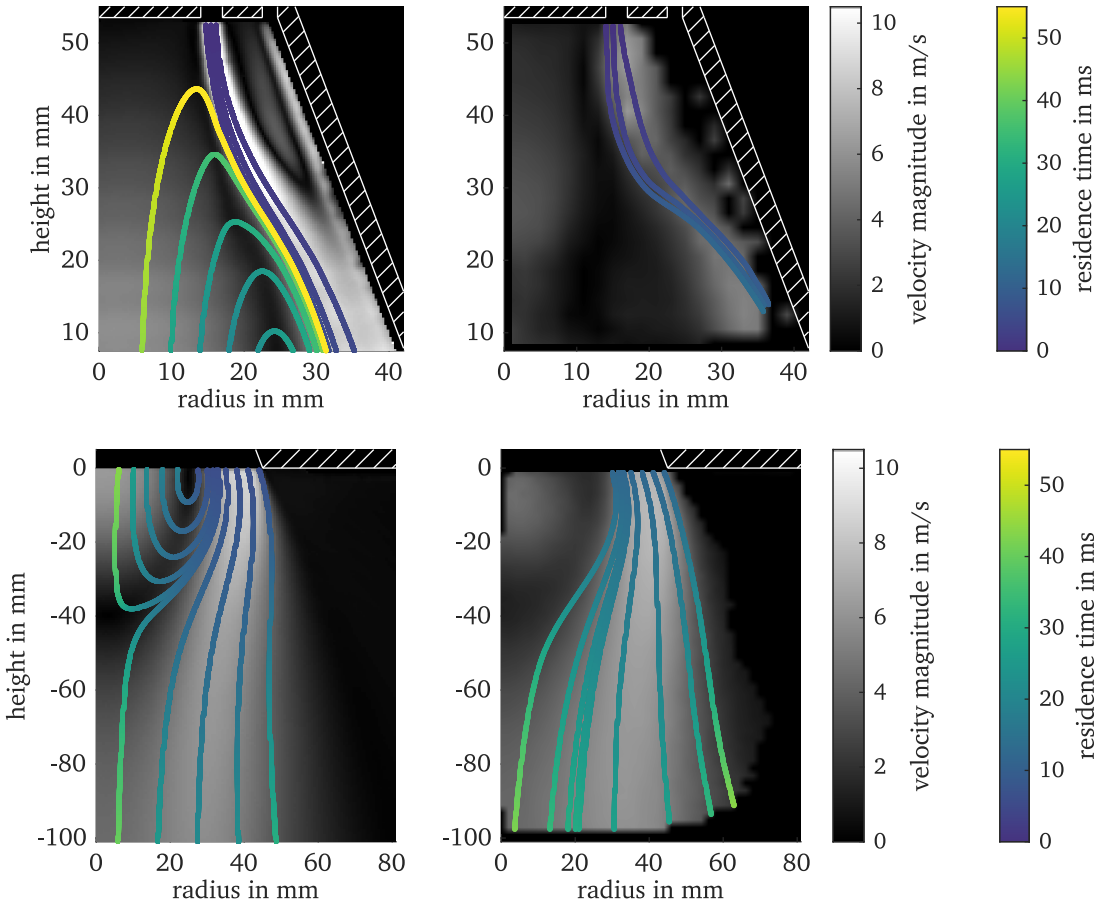

Figure 4.7: Particle residence times of OXY33-RL. Left: Residence times of small particles that follow the gas phase instantaneously. Right: Residence times of large particles derived from particle trajectories. Figure adapted from [1].

Large particles have longer residence times inside the diffusor due to their lower velocities at the inflow. This is caused by the burner design where a cross-sectional reduction is located upstream the burner mouth (see Figure 3.1). Particle velocities in regions that are marked out in Figure 4.5 due to insufficient statistics within the primary flow inside the diffusor are linearly interpolated. Residence times for large particles which do not recirculate are between 27 ms and 42 ms at an axial position of $h = -80$ mm and thus almost twice the time of the small particles. This is advantageous for the combustion of large pulverized solid fuel particles because they stay for longer times within the hot burner region. Inside the recirculation area of the gas phase, no mean residence times were estimated due to their wide distributions in direction and velocity.

The time for devolatilization and char conversion of the solid fuel particles strongly depends on the particle temperature history and particle size. In a large eddy simulation of the investigated gas-assisted combustion chamber [7] mean devolatilization times of 40 ms for small particles ($d_p \leq 25$ µm) and 120 ms for large particles ($d_p \geq 100$ µm) are reported for comparable operation conditions. While char conversion of small particles starts inside the investigated area and fully char conversion is reached for small particles which recirculate, large particles hardly reach char conversion.

4.3.5 Particle temperatures

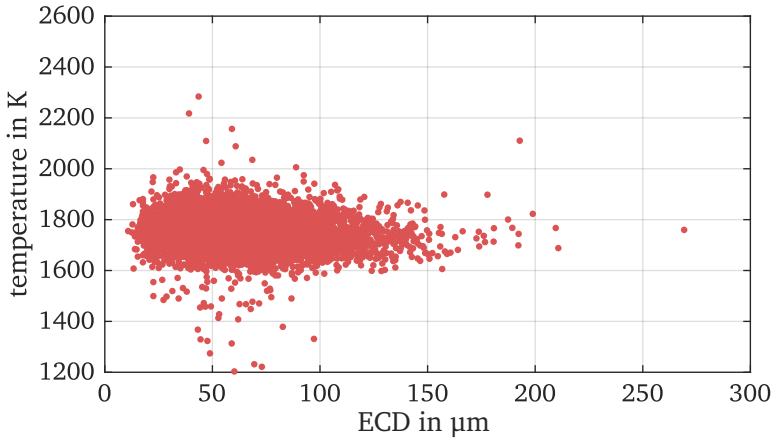

Figure 4.8: Measured particle temperatures over ECD for OXY33-RL at $h = -49.2$ mm and $r = 40$ mm. Figure adapted from [1].

The particle temperature data obtained by the pyrometer system SCOT were evaluated at different sampling levels vertically downstream of the particle inlet at $h = -24.6$ mm, -49.2 mm, and -98.4 mm to cover different mean particle residence times. At each axial position, seven radial positions were covered from the central axis ($r = 0$ mm) outwards in 20 mm steps with one intermediate measurement at 50 mm. In this way, the potentially particle rich regions of special interest were intended to be covered. At each position, several thousand image pairs were recorded with the purpose to record a statistically significant number of particles. The images were evaluated for particle size (equivalent circular diameter, ECD) and temperature, resulting in a scatter plot of d_p-T_p couples, as shown in Figure 4.8 for the operation condition OXY33-RL. These data clouds were evaluated for statistical particle temperatures in Figure 4.9, covering the whole flame zone. The boxplots show the median value for all particles, the interquartile ranges (IQR) as boxes (25% of particles being above and below the median temperature) and the whiskers represent 1.5·IQR. As only data points with more than 15 particles were included in the analysis, a few positions remain blank. This typically occurs at the symmetry axis ($r = 0$ mm) and further outwards at $r = 80$ mm and $r = 100$ mm. Particle temperatures do not show strong variations. In the zone $r = 40$ mm to 60 mm, mean particle temperatures are slightly higher, around 1800 K, compared to $\sim$ 1730 K at the reactor center. At $h = -24.6$ mm,

the trend to lower temperatures is also visible to the outer edge of the flame, while for the two other levels the decrease to the outer positions is less pronounced. The absence of detectable particles at the inner and outer limits of the flame is in agreement with the particle probability distributions shown in Figure 4.5. The temperature trends between the atmospheres show a tendency for higher particle temperatures in the OXY33P-RL case, which might be caused by higher gas temperatures. Interestingly, the OXY33P-RL particle temperatures are higher than in the AIR-RL case at most positions near the reactor wall, while this effect is slightly inverted at the reactor center. The OXY33-RL case shows the lowest particle temperatures in the majority of measurement positions. The size diagrams in Figure 4.9 reveal a trend to larger particles segregating at the outer flame, while smaller particles are favorably recorded closer to the symmetry axis.

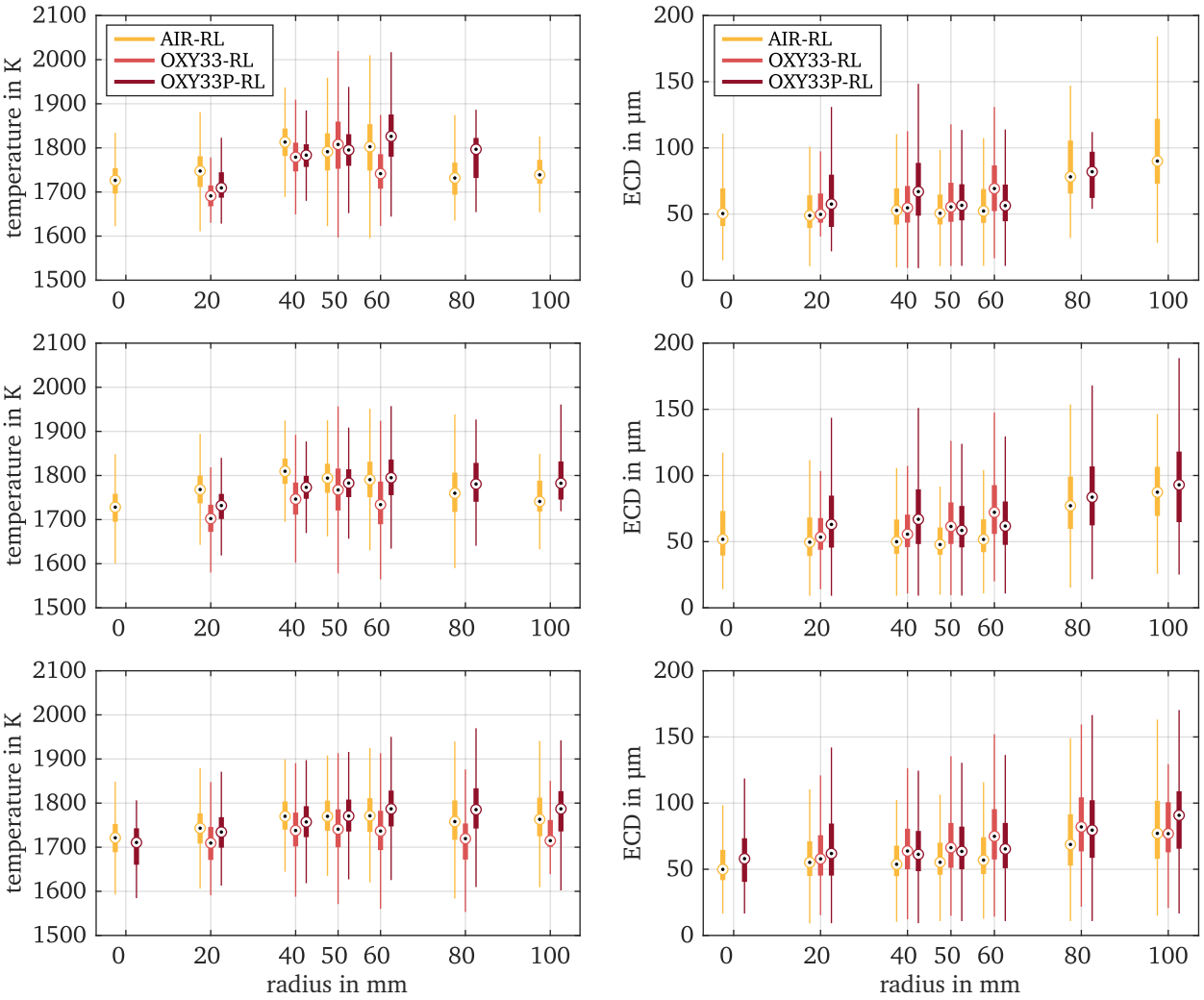

Figure 4.9: Particle temperatures and ECD over radial position for AIR-RL, OXY33-RL, and OXY33P-RL. Three different axial positions ($h = -24.6\,\text{mm}$, $-49.2\,\text{mm}$, and $-98.4\,\text{mm}$), each with 7 radial positions ($r = 0\,\text{mm}$, $20\,\text{mm}$, $40\,\text{mm}$, $50\,\text{mm}$, $60\,\text{mm}$, $80\,\text{mm}$, and $100\,\text{mm}$), are shown. Boxplots of different operation conditions are pulled apart for better visibility. Only measurement positions containing more than 15 samples are shown. Outliers are not considered for better visibility, but are shown in Figure 4.8. Figure adapted from [1].

The particle temperatures observed in the gas-assisted combustion chamber lie between particle temperature data measured in single particle combustion and self-sustaining coal flames for comparable operation conditions and solid fuels [33, 82]. In [33] particle temperatures are measured in a drop-

tube furnace for different oxygen contents in oxy-fuel flames, showing particle temperatures around 2200 K for an oxygen content of 33 vol.% for a lignite coal. In a self-sustaining combustor of similar burner design and flow field [82], particle temperatures of up to 1600 K are measured for Rhenish lignite in air atmosphere. A similar trend as for the combustion chamber used in this study was observed in the radial particle temperature profile.

In summary, the observed trends in particle temperature give some novel insight into the effect of oxy-fuel atmospheres on the thermal profile of oxy-fuel flames compared to their conventional counterparts. Although the gas flow conditions were adjusted to meet the adiabatic flame temperature of the air-based reference case, local differences in average (median) particle temperatures up to 80 K occur between the AIR-RL and the OXY33-RL case, which will change the radiative fluxes significantly. Increasing the mass flow (OXY33P-RL), this effect inverts and particle temperatures are higher than in the AIR-RL case by tendency. In combination with the flow data, which add further information on the impact of diluent substitution, this provides deeper insight and adds an opportunity to use flow and particle temperature data as reference for numerical simulations.

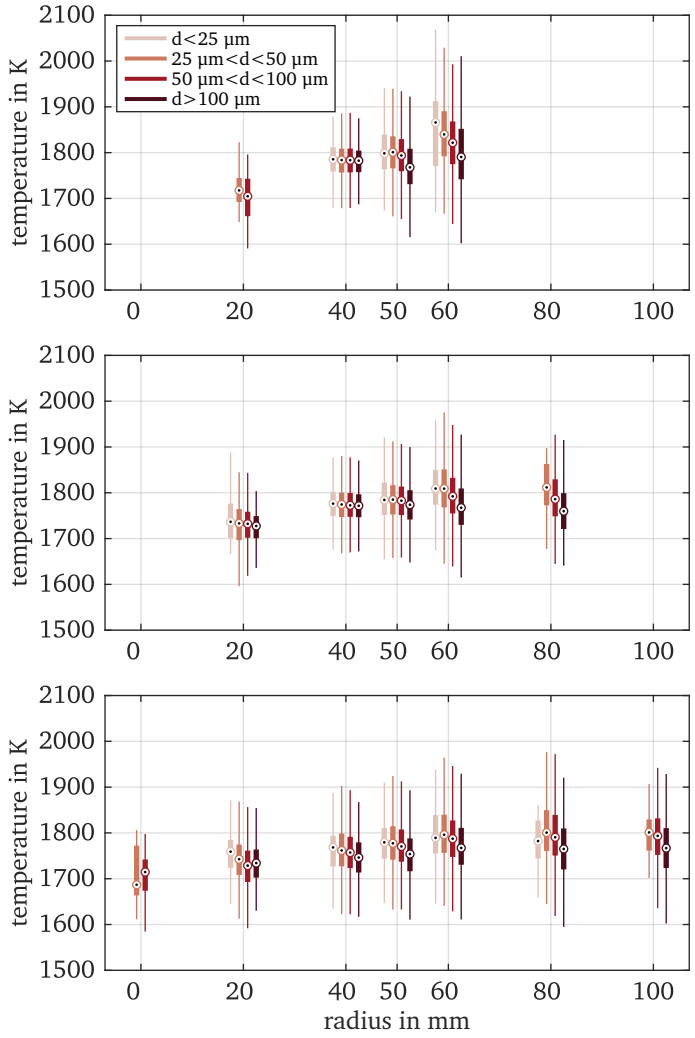

Figure 4.10: Particle temperatures over radial position for different particle size classes of operation point OXY33P-RL. Three different axial positions ($h = -24.6$ mm, -49.2 mm, and -98.4 mm), each with 7 radial positions ($r = 0$ mm, 20 mm, 40 mm, 50 mm, 60 mm, 80 mm, and 100 mm), are shown. Boxplots of different operation conditions are pulled apart for better visibility. Only measurement positions containing more than 15 samples are shown. Figure adapted from [1].

In Figure 4.10, the particle population is divided into four size classes for the OXY33P atmosphere. With only a few exceptions, where the mean temperature and the scatter are equal for all particle size classes, a decreasing trend with increasing particle size is visible, which meets the expectations as transport processes (boundary diffusion) are more dominant for larger particles.

4.4 Conclusion

PIV, PTV and two-color pyrometry are used to investigate the flow dynamics and particle temperatures of pulverized coal inside a turbulent swirl flame. While this study is focused on pulverized solid fuel combustion in an oxy-fuel atmosphere, a reference air case was also examined. Flow fields of the gas phase and trajectories of large particles are evaluated in the near-burner region where the flame is stabilized. The dispersion of the particles inside the quarl and downstream the dump plane is investigated additionally. The mean particle residence times as well as temperature and size measurements of single particles at different locations within the hot region of the flame are analyzed.

The main findings are summarized as follows:

- The spatial expansion of the side flame inside the recirculation area between primary and secondary flow has a substantial impact on the overall flow field. For oxy-fuel operation conditions the side flames are more pronounced. This leads to a decreased vertical expansion of the inner recirculation zone by 11% for OXY33P-RL and by 18% for OXY33-RL compared to the reference air case.
- Particle dispersion with the surrounding gas phase primarily occurs inside the quarl. Shear layers at both sides of the main particle stream enhance particle dispersion. In the lower part of the diffusor single vortices are released from the primary particle jet leading to particle clustering downstream the dump plane.
- The velocity of large particles, determined from particle trajectories, show differences especially inside the diffusor where the downwards oriented main axial flow is pushed towards the quarl wall. Large particles penetrate the recirculation zone of the gas phase due to their initial momentum and inertia.
- Particle trajectories are analyzed within the transition zone between the inner recirculation area and the main axial flow showing wide distributions in trajectory directions and particle velocities up to 8 m/s.
- Significant particle accelerations are observed within the inner recirculation area of the gas phase and inside the downwards oriented main axial flow at the transition from the diffusor to the combustion chamber. In these regions, large particle slip velocities and a high heat release occur.
- Estimated particle residence times of large particles (27 ms to 42 ms) show almost double the time compared to small particles (15 ms to 37 ms) inside the investigated area. Consequently, large particles are residing for longer times within the hot burner region leading to higher burnout rates in the near-burner region.
- Particle temperature and size measurements reveal similar particle temperatures for all investigated oxy-fuel and air operation conditions. Particles within the main flow show slightly higher temperatures, around 1800 K, compared to particles closer to the center of the burner or at larger radial positions. Separate statistical analysis of different particle size fractions in all three atmospheres demonstrates the complexity of coupling between particle and gas phase, as particle size and temperature dispersion are of different character under air and oxy-fuel conditions, although inflow parameters were chosen to keep the adiabatic flame temperature equal.

- Decreasing particle temperatures are observed with increasing particle sizes which is expected due to the more dominate role of transport processes for larger particles. Differences in mean particle temperatures of up to 70 K occur between particles smaller than 25 µm and particles larger than 100 µm.

5 Combined chemiluminescence, flow, temperature and soot investigations

In this chapter, a comprehensive analysis of single-phase and two-phase combustion is conducted using information on CH* chemiluminescence, gas, particle, and slip velocities, gas temperatures, and PAH and soot occurrences. The analysis focuses on oxy-fuel biomass combustion with different oxygen concentrations in the oxidizer by employing the second set of operation conditions, which is described in Section 3.2.1.

Text and figures in this chapter have already been published by Schneider et al. [2] and are reused and partially modified to match the structure and nomenclature of this work. Accordingly, a declaration of the individual contributions of all authors is included in Appendix E. Please note, that the tomographic absorption spectroscopy experiments to determine gas temperatures were performed by Matthias Bonarens and Hardy Hamel (Institute of Reactive Flows and Diagnostics (RSM), TU Darmstadt), while the interpretation of the evaluated gas temperatures in the context of the SFC was conducted in collaboration. The method descriptions in Section 5.2.1 and Section 5.2.3 are expanded with more details and the figures added as supplementary material to [2] are placed within the text of the related section.

5.1 Aim of this investigation

In pulverized oxy-fuel biomass combustion, intricate interaction of complex fluid-mechanical, particle-dynamical, and chemical processes already manifest at intermediate scales. Understanding these complex processes and their interaction has become crucial to unlock the full potential of oxy-fuel biomass combustion and to address the challenges associated with its widespread implementation. Consequently, there arises a compelling necessity for multiple experimental datasets dedicated to investigate the intricate interaction of these processes. Analyzing multiple major quantities at once can provide valuable insights into burnout efficiency, pollutant formation and operational stability in oxy-fuel biomass combustion.

In this study, a comprehensive analysis of the influence of oxygen concentration on oxy-fuel combustion in the near-nozzle region is presented. Effects on flame stabilization, pollutant formation and the combustion process of biomass particles are investigated. For this purpose different operation conditions inside the SFC are studied applying oxygen concentration in oxy-fuel between 27 vol.% and 36 vol.% as well as a comparable operation condition in air. To gain a deeper understanding of the underlying physical and chemical processes in pulverized solid fuel combustion, a large dataset is generated using imaging and laser-optical diagnostics. The dataset includes chemiluminescence imaging of CH*, flow velocities of the gas and solid phase, gas temperatures and qualitative soot measurements including visualization of PAH occurrences as soot precursors.

The study follows a step wise approach starting with a comprehensive analysis of the single-phase combustion (methane combustion). Subsequently, biomass particles are added to the single-phase operation conditions and their influence is evaluated. Flame stabilization is investigated using information on CH* chemiluminescence, gas flow velocities, particle velocities, and gas temperatures. The combustion process of biomass particles and the formation of pollutants is analyzed using qualitative

soot and PAH measurement data in combination with information on the flow field and the gas temperature distribution. Additionally, the solid fuel type is varied for one operation condition to study its influence on the combustion process.

5.2 Methods

In the pursuit of a thorough investigation of the combustion processes and the resulting pollutant generation, various laser-optical diagnostics are applied to the solid fuel combustor. This study employs chemiluminescence imaging of the CH* radical to visualize heat release regions near the nozzle. Signal acquisition entails the use of an sCMOS camera (LaVision, imager sCMOS, 2560 x 2160 px, 16 bit) paired with a 180 mm Sigma macro lens for the field of view (FOV) inside the quarl and a 105 mm Sigma macro lens for the FOV inside the chamber, alongside a 434 nm band-pass filter (Semrock, 434/17 nm BrightLine). Each operation condition and FOV yields 600 images, captured at a repetition rate of 10 Hz. All images have the same exposure time of 80 ms, with a depth of field of ∼0.5 mm (FOV: Quarl, f/3.5) and ∼1.5 mm (FOV: Chamber, f/2.8), respectively.

In order to quantitatively assess gas flow velocities, particle trajectories, and slip velocities, a comprehensive two-phase particle image velocimetry/particle tracking velocimetry (PIV/PTV) methodology is employed. Concurrently, gas temperatures are derived utilizing a tomographic absorption spectroscopy (TAS) arrangement within the solid fuel combustor. For qualitative analysis of polycyclic aromatic hydrocarbon (PAH) occurrences and soot structures, a quasi-simultaneous laser-induced fluorescence/laser-induced incandescence (LIF/LII) configuration is deployed. The implementation of these advanced laser-based diagnostic techniques, along with their corresponding data processing methodologies, is elaborated in subsequent sections.

5.2.1 Two-phase particle image velocimetry/particle tracking velocimetry

Simultaneous quantification of gas flow velocities and particle trajectories is achieved through the utilization of a two-phase PIV/PTV methodology, as initially introduced by Becker et al. [150]. This approach allows the determination of instantaneous slip velocities. For single-phase operation, the conventional PIV technique is exclusively employed to measure gas flow velocities. Gas flows are seeded with Al_2O_3 particles (MARTOXID MR-70, d_{50} = 0.5-0.8 µm).

The implementation of the two-phase PIV/PTV technique necessitates the acquisition of double-frame images of Mie scattering, like in conventional PIV or PTV setups. These images encompass both small particles, serving as gas tracers, and larger particles. A separation algorithm is employed to differentiate the small gas tracer particles from their larger counterparts. This algorithm separates the particles depending on 'size' and 'intensity'. Subsequently, gas flow velocities are acquired through the application of a conventional PIV algorithm to the double-frame images, wherein solely small gas tracer particles are present. Concurrently, the trajectories of particles are computed with a PTV algorithm utilizing double-frame images featuring large particles.

The experimental setup is similar to the PIV setup which is illustrated in Figure 4.1. Particle illumination is achieved using a double-pulsed, frequency-doubled Nd:YAG laser (Innolas SpitLight 600 PIV, 532 nm), shaped into a thin light sheet. The light sheet's thickness is adjusted to 750 µm (FWHM) within the quarl's FOV and 500 µm (FWHM) within the chamber's FOV, ensuring that individual particles do not obstruct the laser. The laser pulses are temporally separated by a Δt of 25 µs (FOV: Quarl) and 35 µs (FOV: Chamber). Mie scattering images are captured with a high-resolution sCMOS camera (LaVision, imager sCMOS, 2560 x 2160 px, 16 bit), coupled with a 180 mm Sigma macro lens (FOV: Quarl) and a 105 mm Sigma macro lens (FOV: Chamber). To mitigate the impact of flame luminosity, a filter set comprising three 532 nm bandpass filters (1x Edmund Optics 68-907 with 3 nm FWHM,

2x Edmund Optics 65-216 with 10 nm FWHM) is employed. At a 10 Hz repetition rate, 3500 image pairs were captured for each operation condition and FOV. The substantial adhesion of particles to the quartz glass wall necessitated the exclusive measurement of OXY33P-WS within the quarl's FOV for two-phase operation conditions. For this FOV and operation condition a reduced dataset, consisting of 288 image pairs, was recorded.

Prior to segregation, the images underwent preprocessing involving a sliding background filter with dimensions of 60 x 60 px (FOV: Quarl) and 27 x 27 px (FOV: Chamber). This preprocessing step effectively minimized the influence of scattered light from fixed geometries, such as the glass diffusor, and residual flame luminosity. Furthermore, a threefold application of the Khalitov and Longmire filter [146] ensued, utilizing a Gaussian filter that applies a five-point blur, with the central point being weighted by a factor of two. This iterative process progressively attenuated high-frequency noise. Subsequent to these preprocessing operations, the identification and segregation of large particles is executed through the application of a connected pixel threshold in conjunction with an intensity threshold.

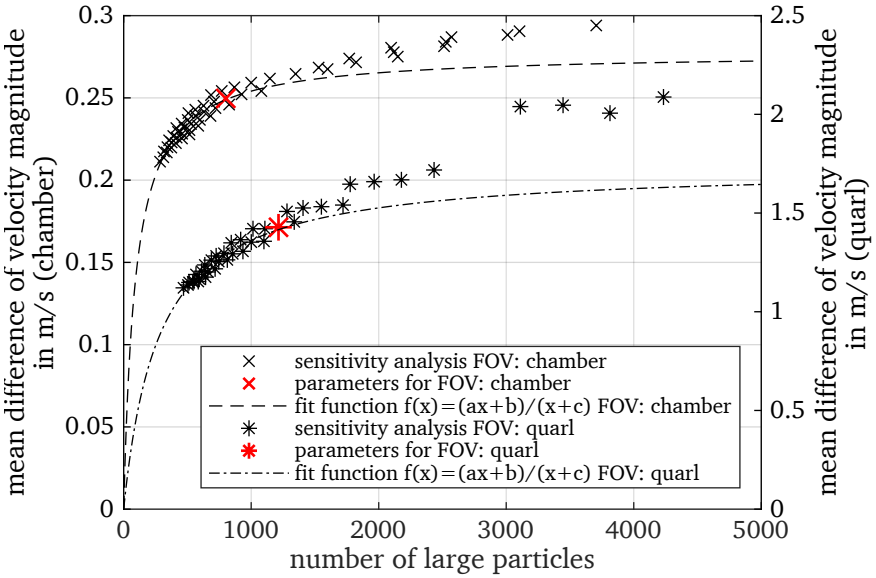

Figure 5.1: Sensitivity analysis for FOV quarl (right y axis) and FOV chamber (left y axis). The mean difference of the velocity magnitude represents the difference between the separated image pair and the raw image pair. Red marks represent the chosen parameters for processing. The fit function $f(x) = (ax + b)/(x + c)$ is chosen to feature the expected asymptotic behavior. Figure adapted from [2].

The determination of optimal thresholds for 'size' and 'intensity' was guided by a sensitivity analysis, which examined the impact of misclassified large particles, focusing on one operation condition. The sensitivity analysis uses 54 image pairs for the FOV inside the quarl and 1000 image pairs for the FOV inside the chamber. A broad spectrum of 'size' and 'intensity' thresholds is assessed, followed by PIV computation and averaging of gas flow velocities in tracer images. The analysis focuses on quantifying mean velocity magnitude differences between separated and raw image pairs. The hypothesis is that after removing all large particles, additional particle detection won't significantly alter mean velocity magnitude differences. Figure 5.1 displays the result of the sensitivity analysis for both FOVs. Red markers indicate the selected thresholds. For the FOV inside the quarl the thresholds are set to size: 6 px and intensity: 200 counts and for the FOV inside the chamber thresholds are size: 10 px and intensity: 700 counts. Increased velocity differences and deviations from the fit with more detected large particles occur due to dense tracer regions being fully masked. The primary source of error arises from the non-uniform illumination of particles, a phenomenon explored in the study by Becker et al.

[74]. The low sensitivity of the user-defined separation parameters around and above the selected thresholds underscores the capability of this approach to reliably determine gas velocity.

The resulting separated images along the original image are illustrated in Figure 5.2. The removal of large particles in the image of the small tracer particles is clearly visible and the area where large particles were detected is masked out in the further processing steps.

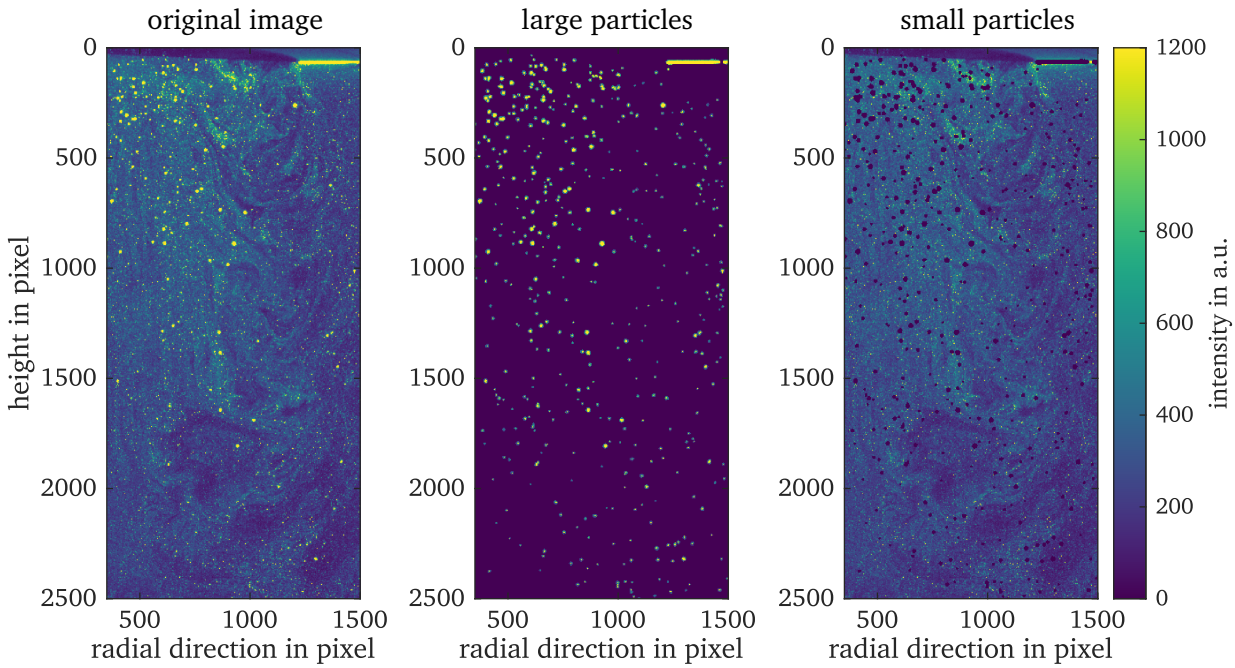

Figure 5.2: Result of particle separation algorithm. Left: Original image. Middle: Image with large particles. Right: Image with small tracer particles. A zoomed view of the images is presented, the raw image contains 2560 x 2160 px.

PIV and PTV processing utilized DaVis 10.2.1 software (LaVision). Preprocessing for tracer images involved a 3 x 3 px smoothing filter and a sliding background filter with a filter length of 27 px. Multi-pass vector calculation is used: two initial passes (window: 128 x 128 px, overlap: 50%) and three final passes (window: 32 x 32 px, overlap: 75%) with an adaptive weighting to account for the complex flow field. Vectors with peak ratios smaller than 1.3 are eliminated. A 9 x 9 px outlier detection filter removed spurious vectors. PIV evaluation resulted in 0.18 mm vector spacing within the quarl, and 0.36 mm downstream of the dump plane. PTV processing utilizes PIV correlations, employing the previously described parameters for the PIV algorithm on the large particle images. Following this, particles are correlated and matched with an 8 x 8 px window, allowing a large vector shift of 20 px relative to the reference. Subsequently, particle tracks are organized onto a structured grid measuring 0.73 x 0.73 mm^2 within the quarl and 0.72 x 0.72 mm^2 within the chamber.

Gas flow velocities and particle trajectories of the operation condition OXY33P-RL have been extracted from a prior investigation [1].

5.2.2 Tomographic absorption spectroscopy

The temperature field in the combustion chamber is measured by tomographic absorption spectroscopy (TAS). The measurement system is based on that previously employed in two studies by Emmert et al. [5, 176], where it is described in more detail. By means of tunable diode laser absorption spectroscopy (TDLAS), absorption spectra are acquired in the wavenumber ranges of 7178.0 cm^{-1} to 7183.4 cm^{-1}

and 4997.7 cm^{-1} to 5001.8 cm^{-1}. These spectral domains were selected as they contain temperature-sensitive absorption features of both water and carbon dioxide, and thus provide sufficient information for temperature reconstruction in both H_2O-rich and CO_2-rich regions over the entire expected temperature interval. As light sources two diode lasers are used, which are successively modulated in ramp shapes at a repetition rate of 1039.8 Hz. The current modulation scheme includes a short laser-off interval which is used to compensate for thermal background radiation. Through glass fibers, the laser light is guided to the measurement system. It consists of eight scanning probes, a schematic of which is provided on the left side in Figure 5.3. In these, the laser light is collimated through a fiber lens and directed onto a rotating mirror, which deflects them onto water-cooled retroreflectors on the opposite side of the combustor. An off-axis parabolic mirror focuses the reflected light onto a photo diode. The analogue signals from the eight probes are amplified and digitalized with 4 MS/s. Each probe acquires intensity spectra at 35 different angles, generating the horizontal beam pattern depicted on the right side in Figure 5.3 inside the combustion chamber. Due to spatial constraints, it is not possible to position the retroreflectors at exactly the same height as the optical access to the scanning probes. Thus, the beams are slightly inclined with respect to the horizontal plane and only intersect in the center (refer to Figure 5.3, side view). Thus, the vertical spatial resolution decreases with distance from the center up to a maximum of 10 mm. Height indications always refer to the intersection point of all beams in the center. The TAS system can only measure one vertical plane at a time. To allow measurements at different heights, the combustion chamber is moved vertically in increments of 5 mm ranging from 15 mm to 100 mm below the dump plane. The typical measurement duration per height is 30 s.

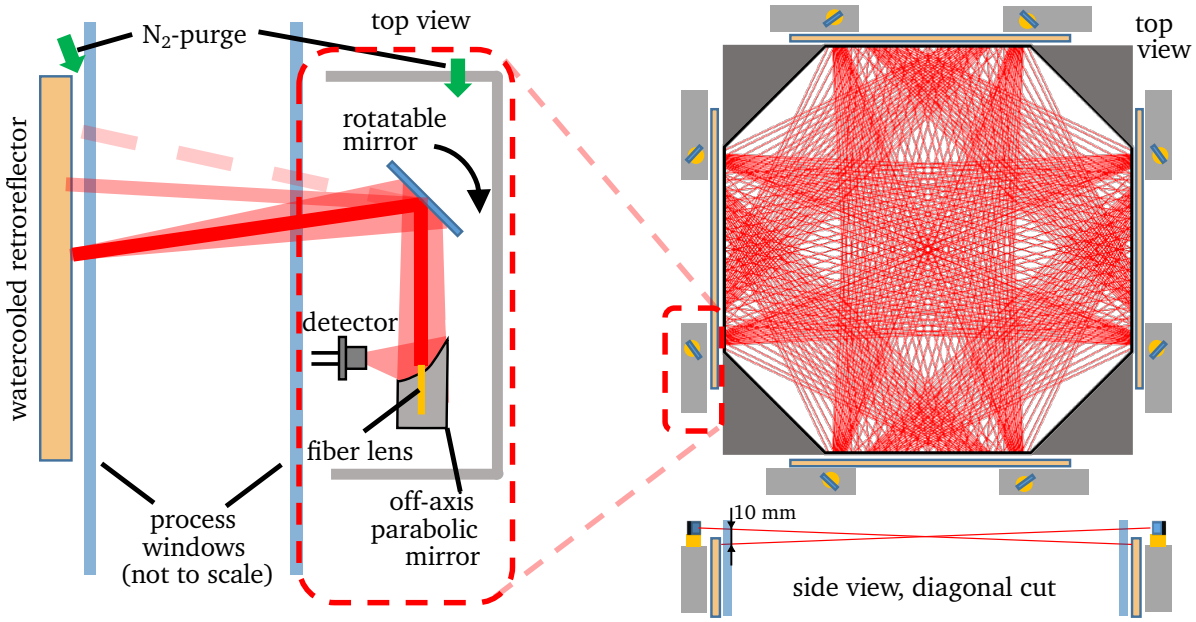

Figure 5.3: Schematic of the tomographic measurement system. Left: Structure of the scanning heads. Right: Beam arrangement in the combustor in top and side view. Figure adapted from [5].

After the recorded intensity traces for each mirror position are averaged, absorbance spectra are inferred using Bayesian absorbance estimation [191]. Example spectra are provided in Figure 5.4, left. While in the domain around 7181 cm^{-1} only water transitions are relevant, both water and CO_2 absorption features need to be considered in the domain around 5000 cm^{-1}. HITRAN [173] line data are used for both molecules. For the tomographic reconstruction, linear hyperspectral absorption tomography (LHAT) is employed [192]. The evaluation is based on the Beer-Lambert law, which states that the absorbances derived from the TDLAS measurements equal the integral of the local absorption coefficients along the path. As the absorption properties of the probed species depend on their

thermochemical state, the local absorption coefficient spectra contain the desired information on temperature, which can be deduced by fitting reference spectra from HITRAN. To reconstruct the local absorption coefficients, the measuring plane is discretized, and the wavenumber-specific absorbance of the i-th of the $8 \times 35 = 280$ beams, $(\alpha_\nu)_i$, is approximated as the sum of the absorption coefficients at each node, $(\kappa_\nu)_j$, weighted by the distance traveled in the vicinity of the respective node estimated through piece-wise linear interpolation, $s_{i,j}$:

$$(\alpha_\nu)_i \approx \sum_{j=1}^{N} s_{i,j} \cdot (\kappa_\nu)_j \tag{5.1}$$

This employed grid is depicted in Figure 5.4, right. It has been shown to be suitable for tomographic temperature measurements in a previous study on the same combustor [5]. It takes advantage of the symmetry of the flow in the central region. Up to radii of 190 mm, i.e., within the tertiary flow, the plane is discretized using 380 concentric rings of 0.5 mm radial extension, while the outer region is triangulated. Since the number of nodes clearly exceeds the number of beams, the equation system given by Equation (5.1) is underdetermined. To solve it, additional information is provided in the form of a first-order Tikhonov regularization prior, reflecting the expected smoothness of the temperature field due to turbulent diffusion [5]. To guarantee comparability between measurements at different operating conditions, the same regularization parameter is used for the analysis of all measurements. To prevent over-regularization, the regularization parameter must be selected such that the steepest temperature gradients in the combustion chamber are resolved. For the operating conditions discussed here, the steepest temperature gradient is expected to occur in the OXY36P case directly below the quarl ($h = -15$ mm, radii between $r = 35$ mm and 65 mm). In analogy to the procedure developed by Emmert et al. [5], the regularization parameter is determined heuristically by minimizing the residuum of the spectroscopic fit in this region. Based on the result of this procedure, the regularization parameter is set to $\gamma = 0.0367$.

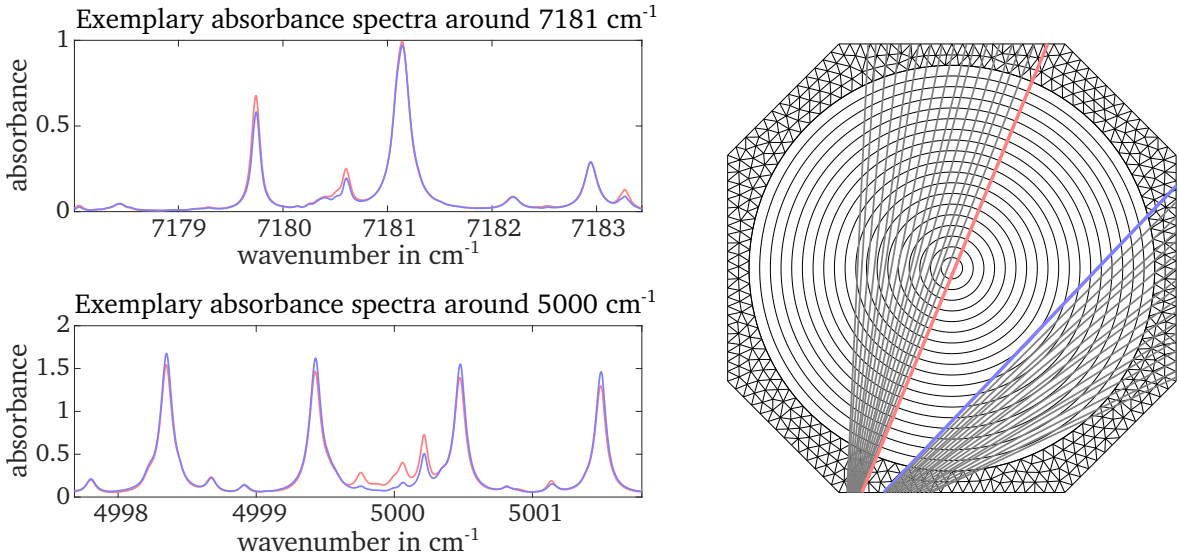

Figure 5.4: Exemplary absorbance spectra inferred from the measured intensity traces corresponding to the red and blue line of sights indicated on the grid used for the tomographic reconstruction. For better visibility, only a reduced number of rings is depicted. Figure adapted from [2].

In the spectroscopic fit, model uncertainties in the line data are assumed to dominate compared to uncertainties due to noise. As these are relative errors that scale with the absolute value of the absorbance, the absorbance spectra of both spectral ranges are normalized to the same area before the fit is performed. This heuristic approach ensures that both have a comparable influence on residuum

and consequently the fit result. In consequence, providing uncertainties based on the Jacobian of the fit result is not reasonable.

5.2.3 Laser-induced incandescence and laser-induced fluorescence

In this study volatile release and soot formation is examined through the simultaneous application of LII and LIF of intermediate hydrocarbons for two-phase operation conditions. For LIF examination, excitation at 266 nm is selected, as it is anticipated to yield a predominantly fluorescence signal attributable to PAHs, including smaller PAHs containing only two aromatic rings [160, 193]. Recording of the fluorescence signal is executed employing a CMOS camera (LaVision, Imager M-lite 2M) in tandem with an image intensifier (LaVision, Low-Speed IRO) and a 100 mm UV lens (Cerco). The image intensifier is temporally gated for a duration of 50 ns, synchronized to initiate concurrently with the laser pulse. Spectral data acquisition is confined within the range of 275 nm to 325 nm, facilitated by a filter configuration encompassing two longpass filters (Asahi, ZUL0275, cutoff wavelength: 275 nm) to mitigate laser reflections, one short pass filter (Asahi, ZUV0325, cutoff wavelength: 325 nm), and an additional bandpass filter (Thorlabs, FGUV11S, transmission: 275 nm to 375 nm) for suppression of near-infrared emissions. The spectral range chosen for this study enhances the sensitivity towards smaller PAHs, owing to the characteristic red-shift observed in the fluorescence signal of larger PAHs [159, 160]. This selection, however, is driven by the primary objective of effectively attenuating thermal radiation originating from solid fuel particles.

An excitation wavelength of 1064 nm is chosen for LII to circumvent potential interferences with the fluorescence emissions of PAHs [181]. The LII signal acquisition setup comprises an sCMOS camera (LaVision, imager sCMOS) in conjunction with an image intensifier (LaVision, Low-Speed IRO X), concomitantly integrated with a 180 mm Sigma macro lens for the FOV inside the quarl and a 105 mm Sigma macro lens for the FOV inside the chamber. The image intensifier is temporally gated for a duration of 50 ns, starting with the laser pulse. A bandpass filter with a center wavelength of 600 nm (Edmund Optics, 86-668 with 25 nm FWHM) is employed. This filter serves to effectively eliminate potential interferences stemming from C_2 Swan-band or C_3 Swing-band emission [181]. Furthermore, an infrared cut-off filter (Edmund Optics, 54-516) is positioned in front of the lens to mitigate any potential risks of damage to the experimental setup.

The experimental setup is depicted in Figure 5.5. For excitation, a double-pulsed Nd:YAG laser (Innolas SpitLight 600 PIV) is employed. The initial frequency-quadrupled pulse at 266 nm is utilized for LIF, while the subsequent pulse at the fundamental wavelength 1064 nm of the Nd:YAG laser is dedicated to LII. Both laser beams are s-polarized to minimize energy losses upon entry into the quarl and are shaped into light sheets. The light sheets are overlapped before entering the solid fuel combustor and are temporally separated by 1 µs to ensure signal separation. LIF employs a laser fluence of $\sim$35 mJ/cm², while LII utilizes $\sim$0.2 J/cm² to enhance LII signal strength while mitigating substantial particle sublimation [181].

The spatial resolution of the LIF and LII setups is evaluated through the measurement of the contrast transfer function (CTF), utilizing a Siemens star target with 36 bars/360° and a maximal resolution of 57.5 lp/mm. The CTFs of both systems and FOVs is presented in Figure 5.6. Adhering to the Rayleigh criterion, which mandates a minimum contrast of $8/\pi^2$, the spatial resolution of the LIF system is determined to be 320 µm (FOV: Quarl) and 300 µm (FOV: Chamber), while that of the LII system is derived as 200 µm (FOV: Quarl) and 285 µm (FOV: Chamber), respectively.

The LIF and LII images have been dewarped, and a frequency-domain lowpass filter with a cutoff frequency of 100 Hz is employed to smoothen the LIF images, compensating for the increased noise introduced by the image intensifier.

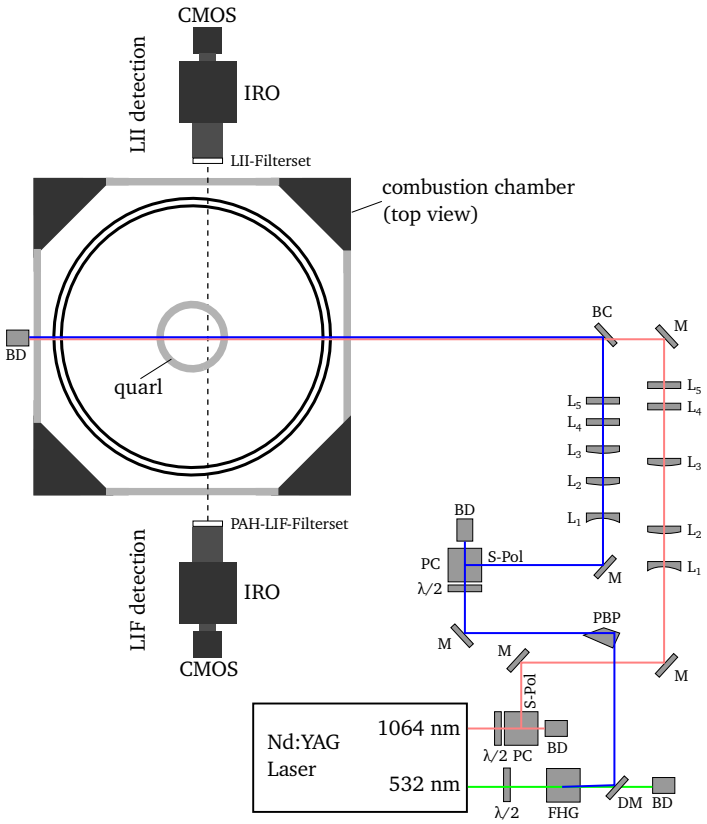

Figure 5.5: Experimental LII/LIF setup. BC: beam combiner. BD: beam dump. DM: dichroic mirror. FHG: fourth harmonic generation unit. IRO: intensified gated relay optics. L_{1-2}: Galilean telescope, spherical lenses. L_{3-5}: sheet forming lenses, cylindrical lenses. M: mirror. PBP: Pellin–Broca prism. PC: polarizing beamsplitter cube. S-Pol: vertical polarized. $\lambda/2$: zero-order half-wave plate.

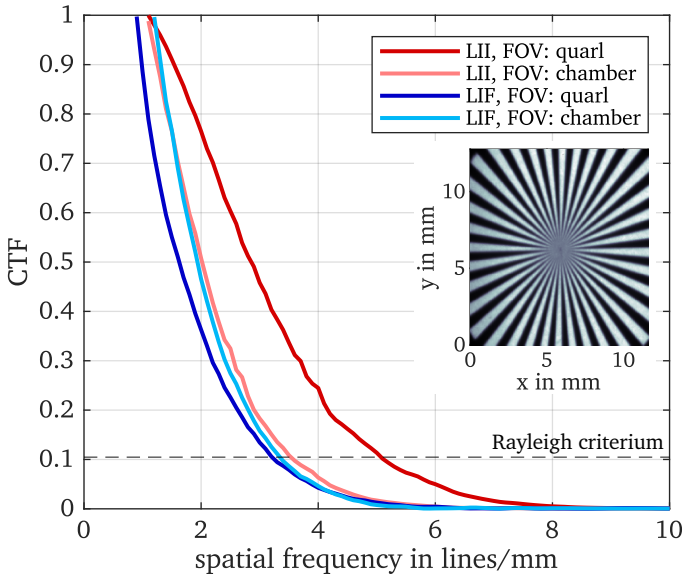

Figure 5.6: Contrast transfer function (CTF) of the LII and LIF imaging systems for the FOVs inside the quarl and inside the chamber. Siemens star target captured by the LII system inside the quarl is shown as an example.

5.3 Results and discussion

5.3.1 Flow and temperature structures in single phase combustion

In this section, the single-phase operation conditions are systematically investigated first to understand the combustion characteristics in different flame environments. Four different flames in an oxy-fuel atmosphere are studied, alongside a comparable flame in air. Photographs of the single-phase combustion are shown in Figure 5.7, where mean flame images are obtained using an exposure time of 0.5 s and same camera settings for all operation conditions.

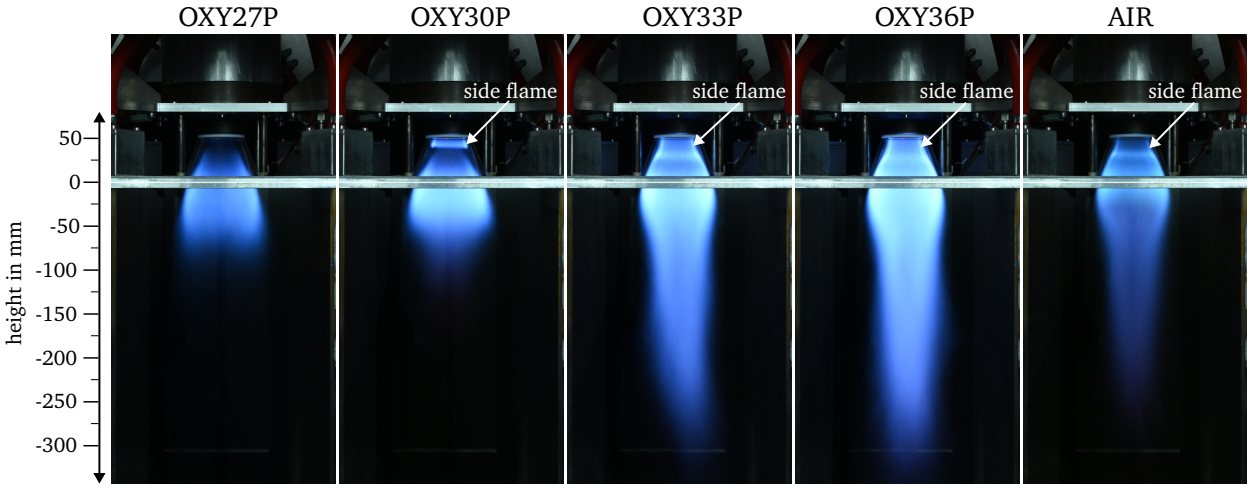

Figure 5.7: Photographs of the single-phase operation conditions (methane combustion). Oxygen concentration is increased from left to right. Last photography on the right represents the comparable air operation condition. Camera setting are equal for all flames. The location of the side flames is marked. Figure adapted from [2].

A consistent observation is the stabilization of a side flame located within the quarl, between the primary and secondary flows, across all operation conditions except for OXY27P. The length of these side flames correlates positively with increasing oxygen content in oxy-fuel conditions. This relationship becomes more evident in the CH* chemiluminescence images depicted in Figure 5.10. Notably, for OXY27P and OXY30P, the flame length remains relatively modest, extending to approximately $h = -80\,\text{mm}$ downstream the dump plane. In contrast, the other operation conditions exhibit notably longer flames, extending as far as $h = -250\,\text{mm}$ downstream the dump plane. This variation in flame length could potentially be attributed to the side flames, leading to early heat release near the nozzle and thus to increased flow acceleration. The considerable influence of the side flame on the overall flame structure has been previously shown in a prior study [1].

5.3.1.1 Combined flow and temperature analysis of operation condition OXY33P

In the following, operation condition OXY33P is analyzed in more detail to show the interplay between flow and temperature characteristics within the single-phase combustion process. Figure 5.8 shows on the left side the mean flow field of the gas phase velocity magnitude and the corresponding root mean square (RMS) velocities. The characteristic flow field inherent to a swirl flame becomes evident, featuring a substantial inner recirculation zone (IRZ) that extends up to approximately $h = -47\,\text{mm}$ downstream the dump plane, encompassed by the main flow downwards. Inside the quarl, the primary flow is pushed towards the quarl wall, where it converges with the secondary flow, resulting in the main flow downwards. The strong IRZ transports hot exhaust gases back to the nozzle, which is the

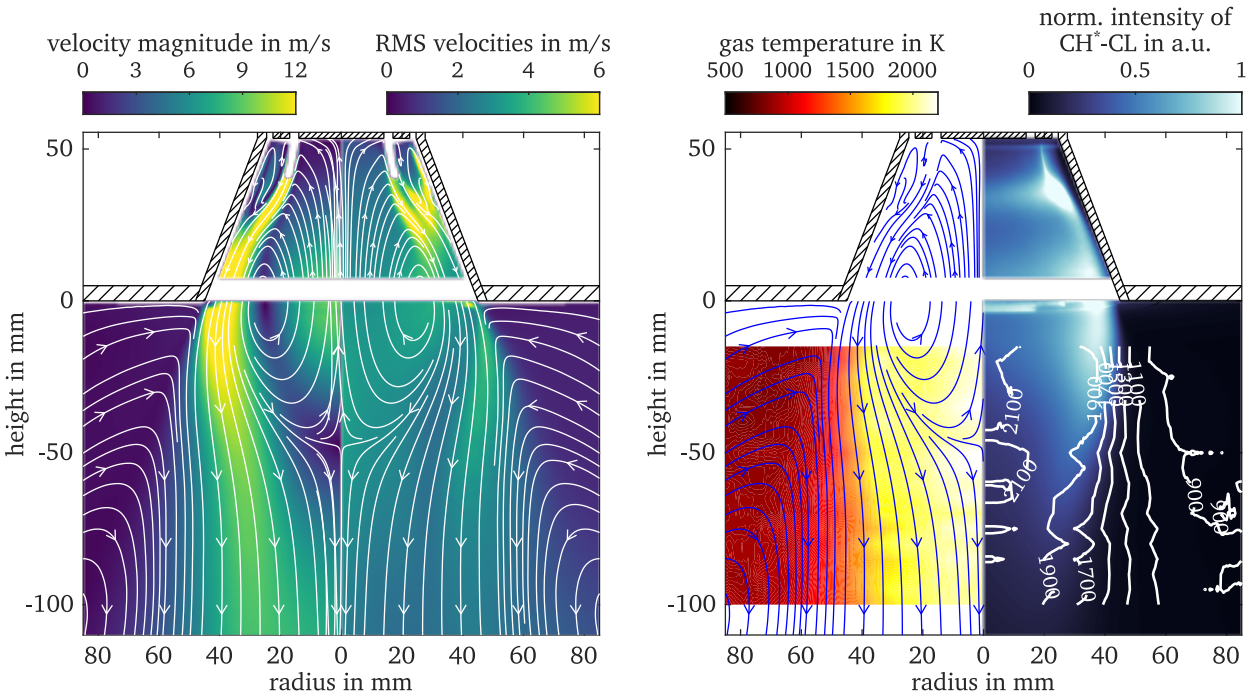

Figure 5.8: Operation condition OXY33P. Left: Mean flow field of the gas phase velocity magnitude with streamlines and RMS velocities with streamlines. Right: Mean gas temperature with streamlines and mean CH* chemiluminescence images with gas temperature isolines. Regions that remained unrecorded due to limitations in the measurement setup or exhibited saturation are excluded and marked white.

key feature of the stabilization mechanism of a swirl flame. At lager radii the outer recirculation zone (ORZ) is present, responsible for the transport of fresh oxidizer from the tertiary flow towards the combustion zone. The side flame zone is situated between the primary and secondary flows within the interstitial recirculation zone, extending to nearly half of the quarl's length.

The RMS velocities, shown on the left side of Figure 5.8, provide a visual depiction of shear layer locations, thickness, and intensity. Notably, strong RMS velocities are exhibited by the shear layers on either side of the primary flow, their intensity escalating towards the mid-quarl region, where the primary flow is pushed towards the diffusor wall. Downstream the dump plane, the main flow downwards is visibly bounded by pronounced RMS velocities. At the outer side of the main flow, a shear layer towards the ORZ forms and broadens as it progresses downstream. The inner shear layer towards the IRZ coupled with high RMS velocities relative to the mean velocity magnitude inside the IRZ highlights dynamic fluctuations in both the dimensions and magnitude of the IRZ.

Figure 5.8 exhibits on the right side the mean gas temperature in conjunction with streamlines and chemiluminescence of CH*, featuring superimposed temperature isolines. Temperature measurements are confined to measurements from $h = -15\,\text{mm}$ to $h = -100\,\text{mm}$, governed by experimental constraints. Notably, temperatures exceeding 2000 K are recorded within the IRZ. A steep temperature gradient is observed within the shear layer between the main flow downwards and the ORZ. This gradient diminishes progressively in the downstream direction, consistent with the concurrent broadening of the shear layer observed in the RMS velocities. This is confirmed in Figure 5.9, showcasing mean axial gas velocity and mean gas temperature profiles for specific heights ($h = -100\,\text{mm}$, $-60\,\text{mm}$, $-20\,\text{mm}$, and $20\,\text{mm}$). Flatter gradients are evident as the flow progresses downstream. Within the IRZ, the gas temperature maintains a plateau slightly above 2000 K, while within the ORZ, fresh oxidizer attains a preheated gas temperature of approximately 900 K.

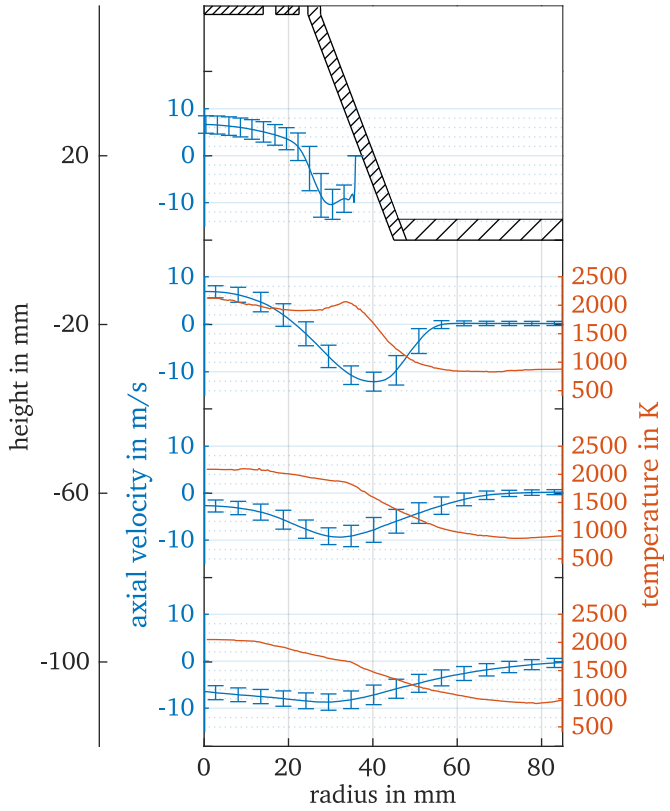

Figure 5.9: Operation condition OXY33P. Profiles of the mean axial gas velocity and the mean gas temperature at the heights $h = -100\,\text{mm}$, $-60\,\text{mm}$, $-20\,\text{mm}$, and $20\,\text{mm}$. RMS velocities are only shown for every 15^{th} point for better visibility. The baseline of the gas velocity corresponds to the measured height of each profile. Figure adapted from [2].

The chemiluminescence of CH* in Figure 5.8 reveals a strong signal inside the quarl, particularly at the lower end of the recirculation zone situated between the primary and secondary flows. This indicates a high heat release within the side flames, which subsequently leads to a gas velocity acceleration and exerts a considerable influence on the overall flame shape. Downstream the dump plane the highest CH* chemiluminescence signal is observed within the main flow downwards, coinciding with the zone characterized by a steep temperature gradient.

5.3.1.2 Influence of oxygen concentration on flow and temperature structures

In order to assess the impact of varying oxygen concentrations on single-phase oxy-fuel combustion, an analysis of CH* chemiluminescence, flow fields, and gas temperature distributions is conducted. The comparative evaluation of all operation conditions is depicted in Figure 5.10. Additionally, mean axial gas velocity and mean gas temperature profiles at specific heights ($h = -100\,\text{mm}$, $-60\,\text{mm}$, $-20\,\text{mm}$, and $20\,\text{mm}$) are provided in Figure 5.11.

Notably, the signal intensity of CH* chemiluminescence exhibits a progressive rise alongside increasing oxygen concentrations indicating an enhanced heat release. The higher CH* chemiluminescence intensities are also attributed to the increased thermal power observed at conditions featuring higher oxygen levels, a necessary adjustment to maintain the equivalence ratio. Specifically, the thermal power increases by 33% for OXY36P compared to OXY27P, and by 72% when compared with the comparable operation condition in air. While OXY27P displays no side flame, OXY30P shows a discrete, well-separated side flame from the main combustion zone further downstream. In contrast,

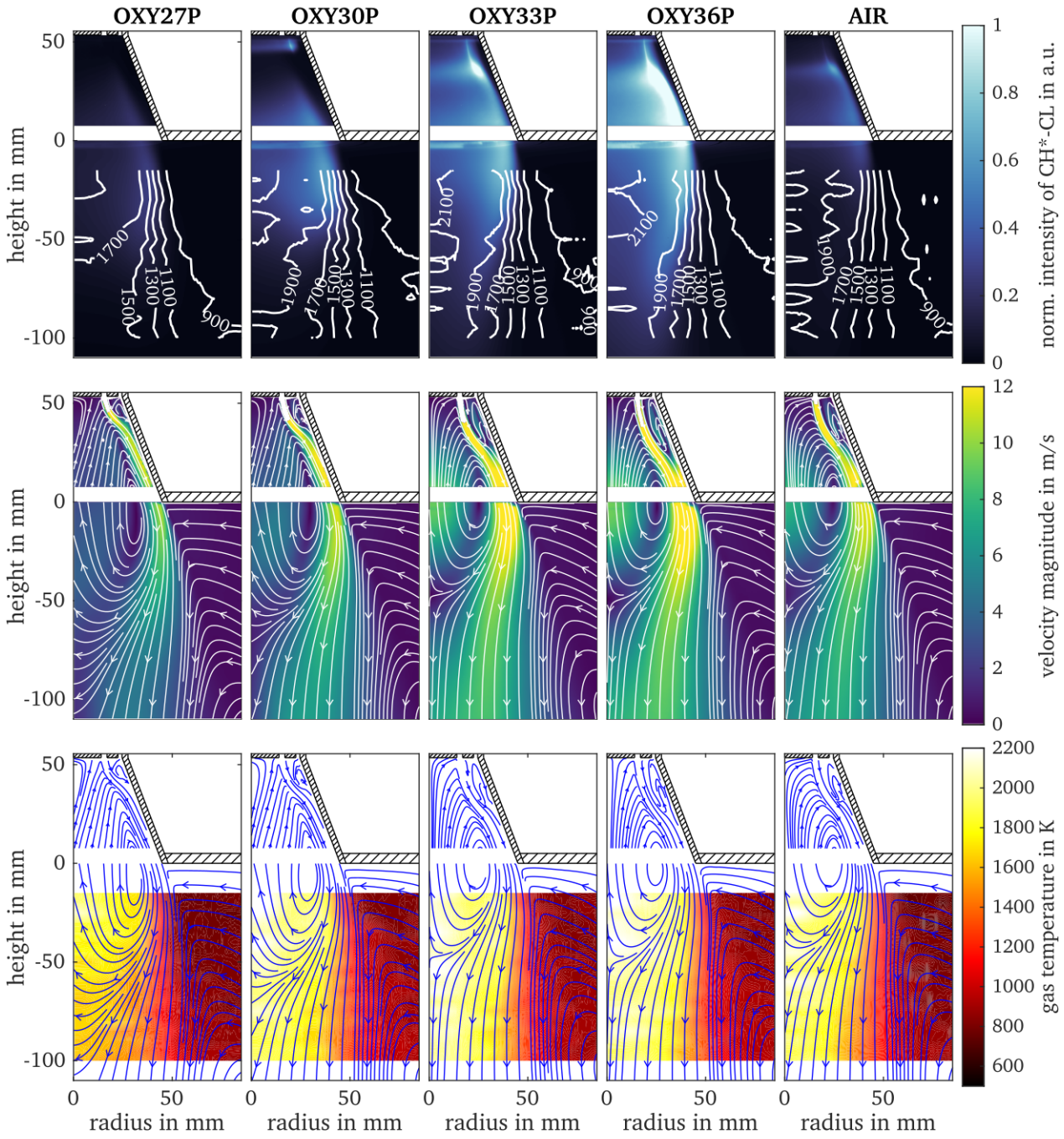

Figure 5.10: Comparison of operation conditions for single-phase operation. Top row: CH* chemiluminescence images with gas temperature isolines. All images are normalized to the same value. Middle row: Mean velocity magnitude with streamlines. Bottom row: Mean gas temperature with streamlines. Figure adapted from [2].

operation conditions OXY33P, OXY36P, and AIR manifest seamlessly integrated side flames in the main combustion zone.

The examination of flow fields unveils a trend where the IRZ becomes more compact with rising oxygen concentrations, coinciding with a rise in velocity magnitudes within the IRZ. Furthermore, the velocity magnitude within the main flow downwards experiences an acceleration due to intensified heat release in proximity to the nozzle which is affirmed by CH* chemiluminescence observations,

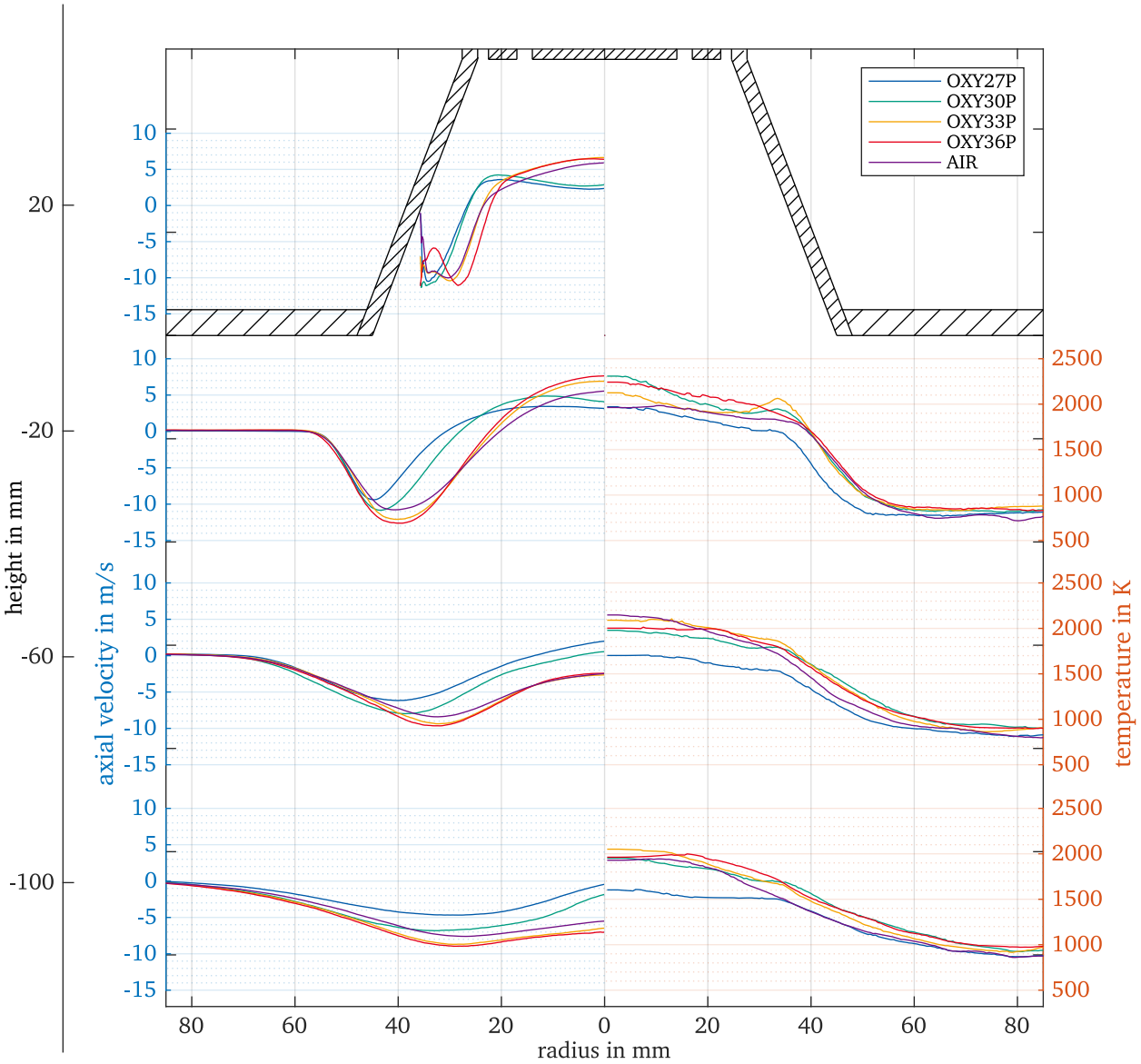

Figure 5.11: Mean axial gas velocity and mean gas temperature profiles of single-phase operation conditions at the heights $h = -100\,\text{mm}$, $-60\,\text{mm}$, $-20\,\text{mm}$, and $20\,\text{mm}$. Left: Mean axial gas velocity profiles. Right: Mean gas temperature profiles. Gas temperatures were not measured within the quarl. Figure adapted from [2].

and increased velocities within the IRZ. Concurrently, gas temperatures exhibit a rise with elevated oxygen concentrations. Remarkably, the maximum of temperatures across all operation conditions resides within the IRZ.

Comparatively, combustion in air mirrors the flow field characteristics of OXY33P, although exhibiting marginally reduced velocity magnitudes within the main flow downwards and slightly lower temperatures. Conclusively, for single-phase operations within the solid fuel combustor, oxy-fuel combustion with an oxygen concentration ranging between 30 vol.% and 33 vol.% — potentially leaning towards 33 vol.% — displays analogous behavior to combustion in air. This observation highlights the importance of achieving similar adiabatic flame temperatures in both air and oxy-fuel combustion (as indicated in Table 3.1) to achieve similar combustion behaviors, although the adiabatic flame temperature of AIR is closer to that of OXY30P than OXY33P.

5.3.2 Interaction of flow, temperature and soot in gas-assisted solid fuel combustion

In the context of the investigation presented in the previous section into single-phase combustion, biomass in the form of walnut shell particles are added to the single-phase operation conditions for the following study. Figure 5.12 visually illustrates the resultant two-phase combustion, with each image captured using an exposure time of 0.5 s.

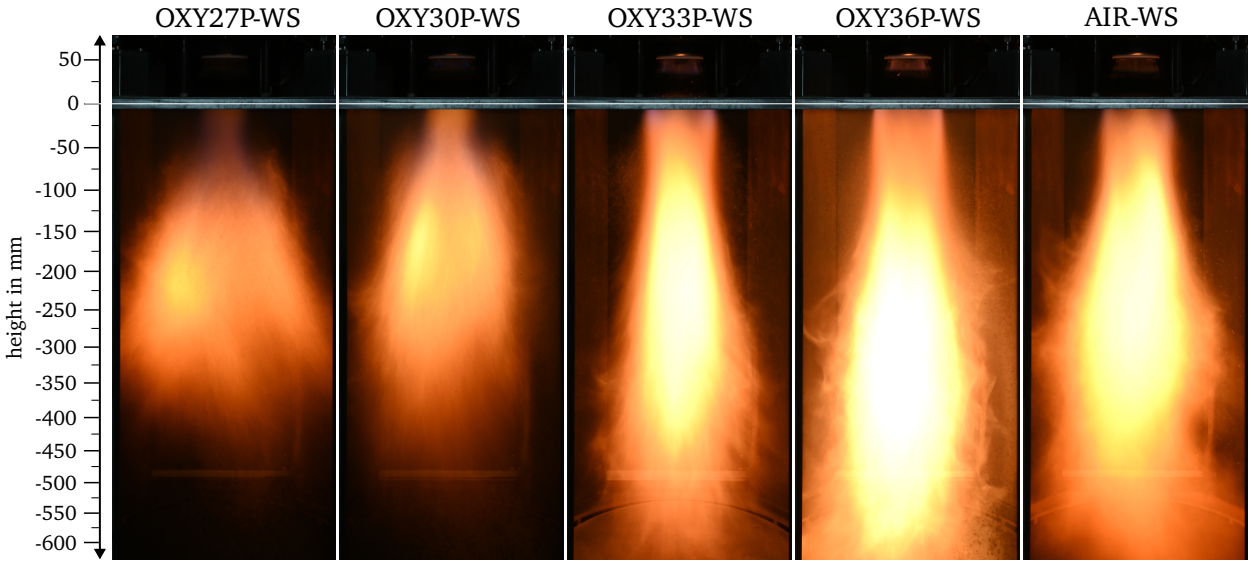

Figure 5.12: Photographs of the gas-assisted solid fuel combustion operation conditions with walnut shells (WS). Oxygen concentration is increased from left to right. Last photography on the right represents the comparable air operation condition. The emission of flame radiation originating from within the quarl is largely obstructed by particles that adhere to the walls. Camera settings are equal for all flames. Figure adapted from [2].

Upon examination, it becomes evident that the presence of particles exerts a discernible influence on the combustion dynamics. Specifically, in cases such as OXY27P-WS and OXY30P-WS, the flames experience a downstream displacement, leading to their detachment from the quarl wall. This behavior is likely attributed to the potential heat loss close to the nozzle resulting from heat up of the particles. Despite these alterations, a persistent flame radiation signature remains within the central region at the upper end of the combustion chamber, an area presumably located within the IRZ. The flame of OXY27P-WS showcases an expansion and proximity to the combustor walls, while flames tied to the quarl exhibit more concentrated behavior at the center of the combustion chamber. Notably, the flame length exhibits a positive correlation with oxygen concentration, a result arising from the interplay of flow characteristics and increased particle loading, essential for maintaining equivalence ratios. The comparison of OXY36P-WS in relation to OXY33P-WS and AIR-WS reveals a downstream shift in the distribution of flame radiation.

5.3.2.1 Analysis of particle influence on flow and gas temperature

In order to assess the influence of particles on oxy-fuel combustion, an analysis encompassing gas and particle flow and gas temperature distributions is undertaken, employing operation condition OXY33P-WS as a representative case study. Figure 5.13 compares CH* chemiluminescence images obtained from the single-phase operation condition OXY33P with those from the two-phase operation condition OXY33P-WS. Notably, the addition of WS particles yields an overall enhancement in the CH*

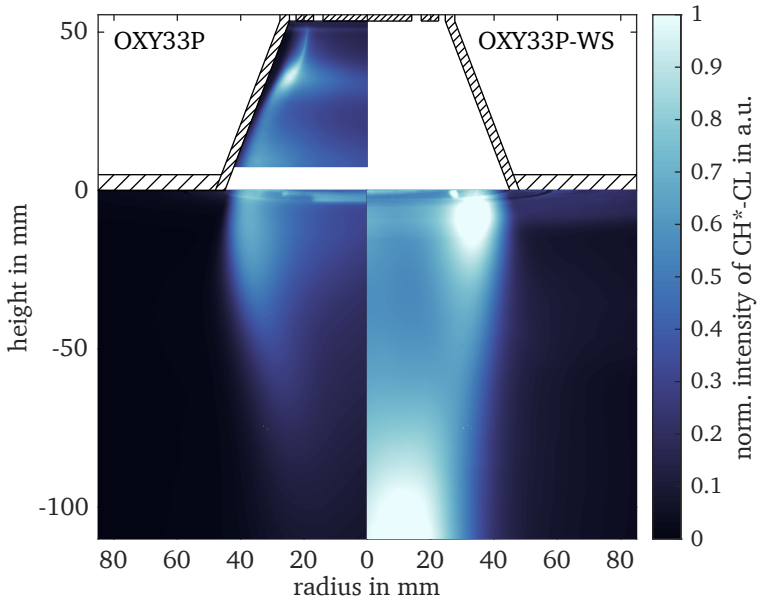

Figure 5.13: Comparison of CH* chemiluminescence between single-phase and two-phase combustion. Images are taken with the same camera settings and are normalized to the same value. Left: OXY33P. Right: OXY33P-WS. Data are only shown below the dump plane due to particle adhesion to the quartz glass walls of the quarl. Figure adapted from [2].

chemiluminescence signal. Just below the dump plane, a distinct zone with increased heat release is observable within the main flow. Furthermore, downstream of the IRZ, specifically below $h = -80\,\text{mm}$, the CH* chemiluminescence signal experiences an increase in the two-phase operation. This elevation likely indicates the initiation of char combustion. This interpretation is corroborated by the presence of increased flame radiation in that area captured in the photography of Figure 5.12, which interferes with the CH* signal.

Alterations in the mean gas velocity and the mean gas temperature in the two-phase combustion case are presented through height-specific profiles depicted in Figure 5.14. Noticeable differences are evident in both mean velocity and mean temperature profiles. The magnitude of the axial velocity as well as the gas temperature within the IRZ are notably decreased in the two-phase combustion case. Furthermore, the introduction of particles yields a reduced peak velocity within the main flow downwards, particularly within the quarl and directly downstream of the dump plane. Concurrently, the gas temperature of the main flow downwards at $h = -20\,\text{mm}$ experiences a decrease, while the temperature gradient in the outer shear layer, directed toward the ORZ, exhibits a comparatively flatter trend in the two-phase case, in contrast to the single-phase combustion. These observation serve as a clear indicator of delayed combustion, attributed to particle heat up.

Moving downstream, the presence of particles slightly shifts the velocity maximum of the main flow outward, while the axial velocity magnitudes of OXY33P-WS approach those of the single-phase operation condition. Within the main flow downwards, the gas temperature of OXY33P-WS rises, even exceeding that of OXY33P, although lower gas temperatures prevail at the chamber's center. Notably, the temperature maximum in the two-phase combustion case resides slightly at a larger radial position compared to the maximum downward velocity. The peak temperature is situated beyond the prominent signal illustrated in the CH* chemiluminescence image below $h = -80\,\text{mm}$, presented in Figure 5.13. Furthermore, within the ORZ of OXY33P-WS, the temperature level markedly surpasses that of OXY33P, exceeding 1000 K.

Further exploration into the flow characteristics of the gas and particle phases within OXY33P-WS reveals large differences in gas streamlines and mean particle trajectories, particularly within the IRZ.

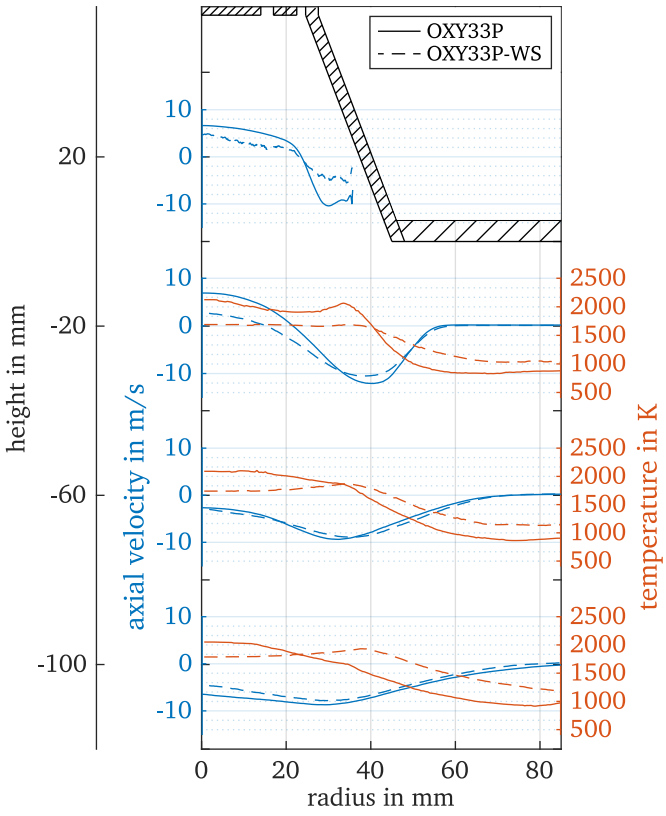

Figure 5.14: Comparison of operation conditions OXY33P and OXY33P-WS. Profiles of the mean axial gas velocity and the mean gas temperature at the heights $h = -100\,\text{mm}$, $-60\,\text{mm}$, $-20\,\text{mm}$, and $20\,\text{mm}$. The baseline of the gas velocity corresponds to the measured height of each profile. Figure adapted from [2].

The corresponding mean flow field of the gas velocity magnitude and the mean particle trajectories are visualized in Figure 5.15. Notably, the mean particle trajectories do not exhibit a transport of the particles back toward the nozzle. A majority of particles traverse directly through the IRZ in a relatively straight trajectory. The velocity magnitude of both gas and particle phases within the main flow downwards is comparable.

The simultaneous measurement of gas and particle velocities allows the instantaneous slip velocity to be estimated. The derived mean slip velocity is illustrated on the right in Figure 5.15. High slip velocities are observed within the IRZ, especially within two specific regions. The first region is situated on the inner side of the main flow downwards within the quarl. Here, the main flow downwards is coerced towards the quarl wall, while particles penetrate with elevated axial velocities into the IRZ due to their inertia. Inside the IRZ, particles undergo deceleration but are not transported upwards. The second region characterized by high slip velocity is centered within the IRZ, where gas phase velocity magnitude is substantial, yet particles continue their downward trajectory. Increased slip velocities are also evident within the shear layers of the main flow downwards.

To gain a deeper insight into the movement of individual particles, histograms in polar coordinates detailing particle direction, velocity, and frequency of occurrence are shown at the bottom of Figure 5.15 for heights ranging from $h = -10\,\text{mm}$ to $-20\,\text{mm}$, and various radial positions within both the IRZ and the main flow downwards. In the combustor's center, positioned between radial coordinates $r = 0\,\text{mm}$ and $10\,\text{mm}$, the predominant particle motion is downward, with a slight inclination towards the centerline. Furthermore, a minority of particles exhibit an upward trajectory toward the nozzle. As radial positions increase, particle trajectories exhibit a distinct preferred direction, with limited instances of upward particle movement. Particle velocities exhibit a wide-ranging distribution, with the highest

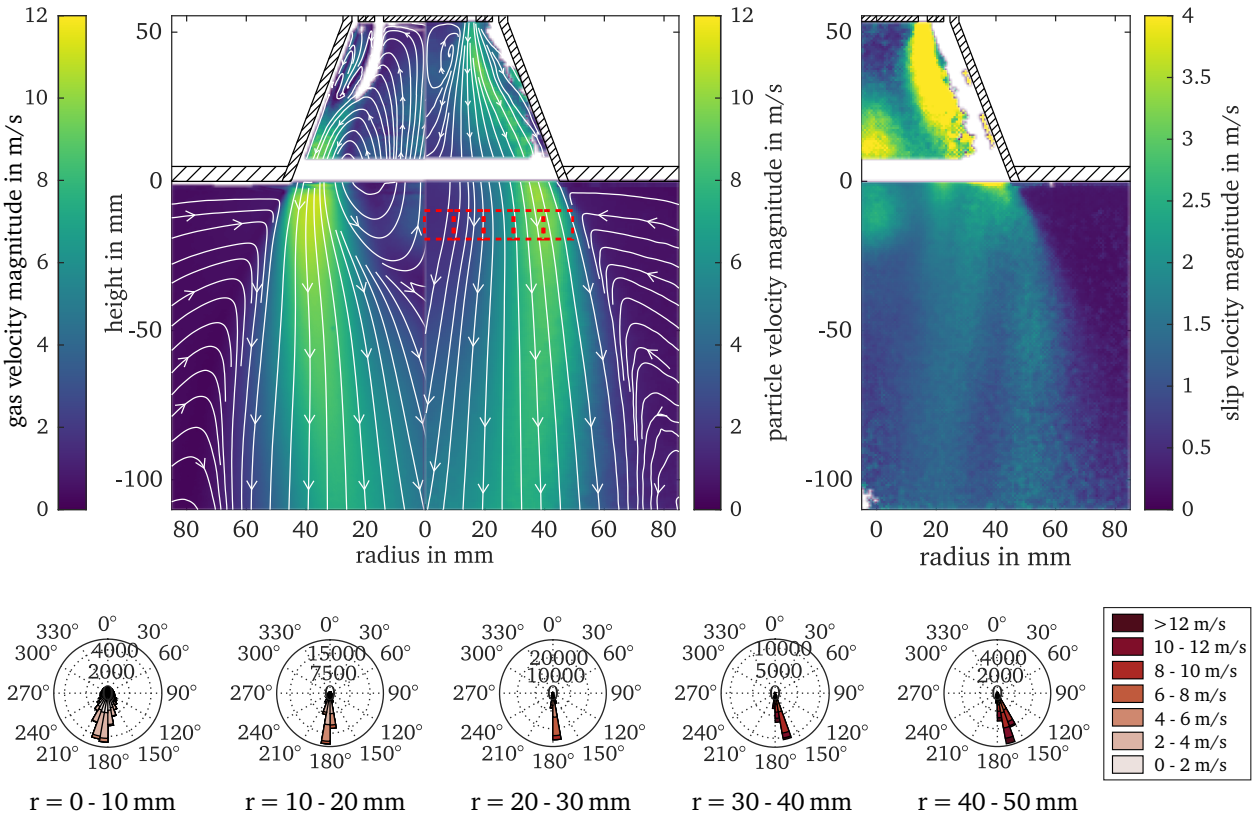

Figure 5.15: Mean gas, particle and slip velocity magnitudes of operation condition OXY33P-WS. Only areas with more than 30 vectors are shown. Left: Mean gas velocity magnitude and mean particle velocity magnitude. Right: Mean slip velocity magnitude. Bottom: Polar histograms of particle velocities at different radial positions accumulated at a height between $h = -10\,\text{mm}$ and $h = -20\,\text{mm}$. Areas of the histograms are marked as red dashed squares in the particle velocity field. Figure adapted from [2].

velocities found within the main flow downwards. The peak particle counts are observed within the radial range of $r = 10\,\text{mm}$ to $30\,\text{mm}$.

The particle Reynolds number Re_p characterizes the fluid flow around a particle, thus serving as an indicator of potential turbulence generation or dissipation due to particle presence. The comprehensive measurements allow for the determination of particle Reynolds numbers downstream of the dump plane, considering the average values for slip velocity and gas temperature. Highest Re_p within the high-slip-velocity region of the IRZ are estimated to $\text{Re}_\text{p} = 3$, considering a particle diameter of $d_{\text{p},90} = 178.8\,\mu\text{m}$ (D90 value), maximum slip velocity of $u_{\text{s,max}} = 4.5\,\text{m/s}$ (calculated as the sum of the maximum mean slip velocity of $u_{\text{s,mean}} = 2.5\,\text{m/s}$ and the maximum standard deviation of slip velocity of $u_{\text{std}} = 2\,\text{m/s}$), mean gas temperature within the IRZ of $T_{\text{mean}} = 1700\,\text{K}$, and an exhaust gas composition (71 vol.% CO_2, 24 vol.% H_2O, 5 vol.% O_2). This estimated Re_p is significantly below 280, a threshold indicating particle-induced turbulence generation by vortex shedding [194]. Although individual particle Re_p values may span a wide range, the collective analysis suggests that turbulence within the studied solid fuel combustor is more likely to be dampened by the presence of particles rather than intensified.

Understanding the spatial distribution of fuel particles within a combustor is of significant interest due to its direct influence on combustion efficiency, emissions, and overall performance. The location and behavior of fuel particles affect various combustion regimes, such as volatile release, heat release, and pollutant formation. However, assessing particle concentration based on Mie images is challenging, as

large errors can easily arise by calculating the particle concentration based on the lasersheet thickness [195]. The measurement depth is influenced by multiple variables such as the lasersheet's intensity profile, multiple scattering, potential laser reflections, and separation algorithm parameters. Consequently, the spatial distribution of fuel particles is illustrated as a particle occurrence probability map on the right in Figure 5.16. This map offers a qualitative depiction of particle density and distribution within the solid fuel combustor. The particle occurrence probability is determined by calculating the likelihood of detecting a large particle using the separation algorithm within a camera pixel across all captured images.

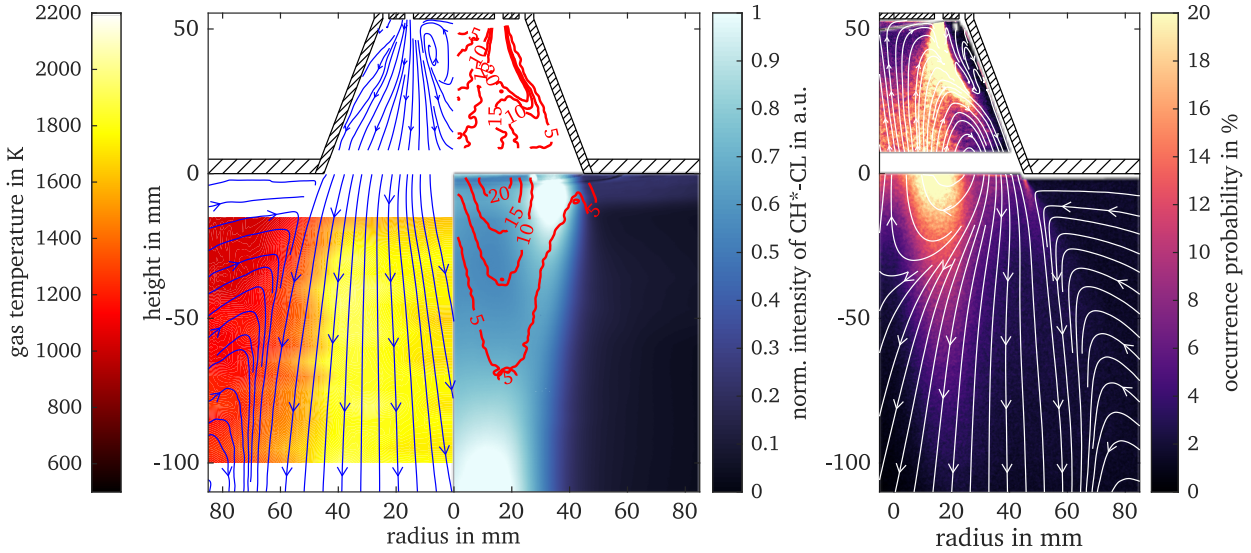

Figure 5.16: Gas temperature and particle occurrence probability distribution of operation condition OXY33P-WS. Left: Gas temperature with mean particle trajectories and CH* chemiluminescence image with particle occurrence probability isolines. Right: Occurrence probability distribution of large particles. The probability value represents the likelihood of detecting a large particle using the separation algorithm within a camera pixel across all captured images. The occurrence probability inside the quarl is corrected for the different laser sheet width. Figure adapted from [2].

On the left in Figure 5.16, the analysis combines mean gas temperature with mean particle trajectories and the CH* chemiluminescence signal, superposed with the spatial distribution of fuel particles indicated by isolines. Figure 5.16 shows at the right the particle occurrence probability in relation to the flow field. The particle density is highest downstream the primary inlet where the particle jet disintegrates inside the IRZ at the radial range of $r = 5\,\text{mm}$ to $25\,\text{mm}$ due to slow particle velocities. As particles accelerate downstream the IRZ, particle density decreases. Given that most particles traverse through the IRZ, rapid particle heating and volatile release in proximity to the nozzle can be assumed. Notably, the strong CH* chemiluminescence signal observed in the chamber's center downstream of the IRZ, previously associated with the onset of char combustion, is crossed by the majority of particles, thereby confirming the hypothesis.

5.3.2.2 Devolatilization and soot formation

The devolatilization of particles and subsequent soot formation is strongly linked for pulverized solid fuel combustion. The formation of polycyclic aromatic hydrocarbons (PAHs) during secondary pyrolysis of tar species, released from primary pyrolysis, can lead to the formation of soot nanoparticles through collisions and clustering [124, 196]. Despite PAHs emerging from pyrolysis (petrogenic PAHs), PAHs can also be formed during the combustion process (pyrogenic PAHs) [193], potentially

enhancing soot formation and growth. The process of soot formation is notably sensitive to the local atmosphere, as the pathways for PAH and soot particle reactions strongly rely on oxygen concentration. In the presence of sufficient oxygen levels, PAH and soot particles are oxidized to CO_2 and H_2O. To investigate this process, a quasi-simultaneous experimental setup is designed, capturing the LIF signal arising from PAHs and the incandescence from soot nanoparticles with a separation of 1 µs to prevent signal interference.

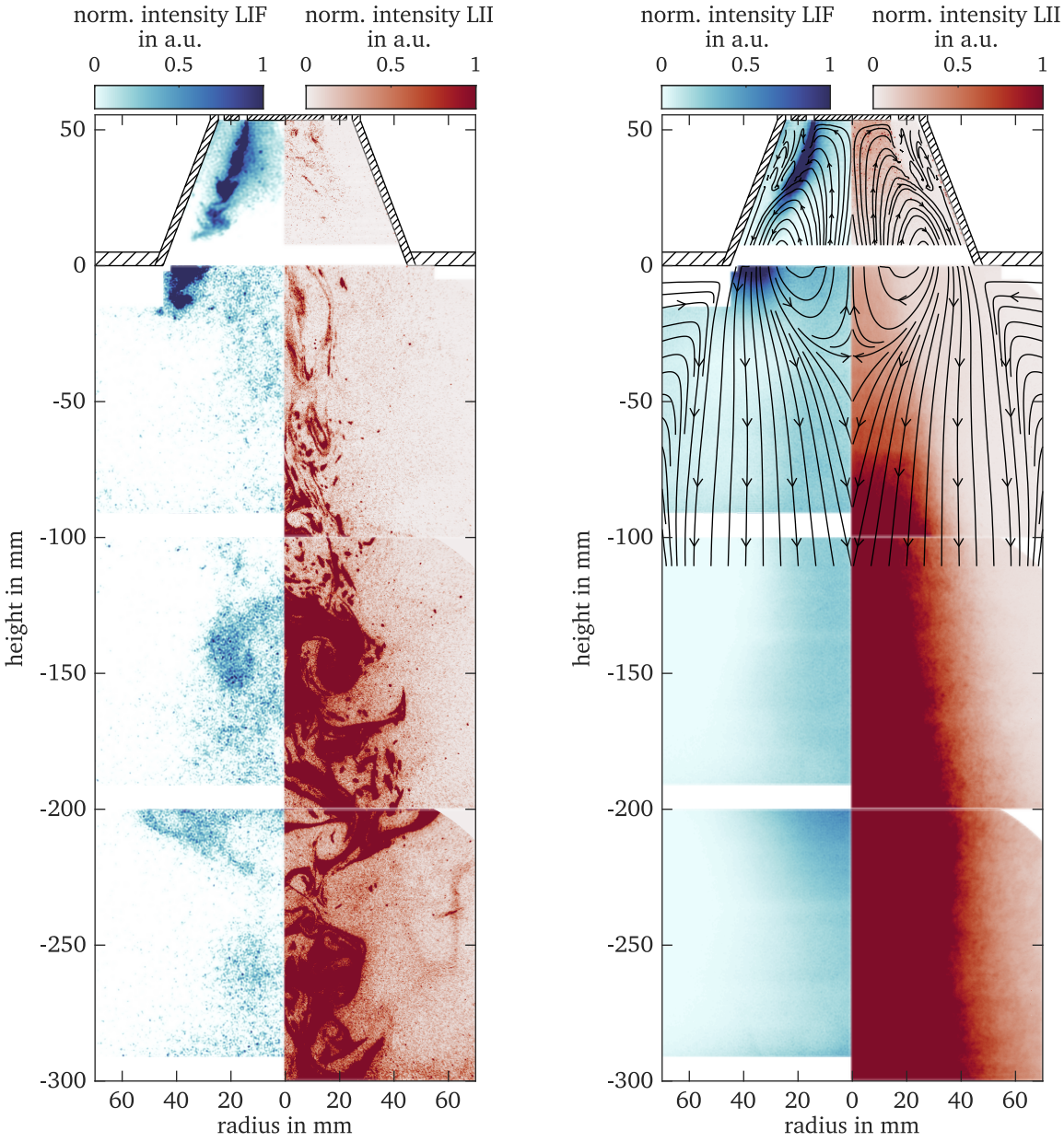

Figure 5.17: LIF signal from PAH and LII signal from soot particles of operation condition OXY33P-WS. Left: Instantaneous image. 4 different FOVs are sequentially recorded. LIF and LII signals are acquired quasi-simultaneously. Right: Averaged images of LIF and LII signals with gas velocity streamlines. Regions that remained unrecorded due to limitations in the optical setup or show intense reflections are excluded and marked white. Figure adapted from [2].

Figure 5.17 illustrates the signals obtained from LIF and LII measurements. On the left of Figure 5.17 instantaneous snapshots of PAH and soot occurrences are presented. To analyze the range up to $h = -300\,\text{mm}$, four FOVs are sequentially recorded. For each FOV, LIF and LII signals are acquired

quasi-simultaneously. Note that the measurement region has been extended downstream compared to previous data to encompass the soot formation process.

The instantaneous LIF signal reveals substantial PAH occurrences within the quarl, particularly in close proximity to the particle-laden jet of the primary stream. The mixing of the different flows is visible in the LIF signal. It should be noted that particle adhesion to the quarl's lower end may influence the LIF signal, which could not be corrected for. Downstream of the dump plane, PAH occurrences are observed within the main flow downwards close to the dump plane. The PAH-LIF signal commences on the inner side of the primary inlet, indicating rapid volatile release from particles directly after injection into the quarl.

Soot incandescence signals increase with longer residence times downstream of the dump plane and are visible near the centerline of the chamber. Only minor soot presence is detected within the IRZ, with small soot structures beginning to form below the IRZ and expanding downstream. The pattern of these soot structures likely relates to the vortexes present in the turbulent flow.

A comparison of PAH and soot occurrences reveals that locations identified as volatile release by the PAH-LIF signal do not display any soot. Further downstream, a weak PAH-LIF signal coincides with regions of soot occurrence. The cause for this overlap remains uncertain, but it may arise from either the formation of pyrogenic PAHs that coexist with soot in soot-rich areas, or from an incandescence signal generated by the LIF setup, despite the laser excitation employs much less energy.

In the averaged PAH-LIF and LII images in Figure 5.17, the LIF signal inside the quarl is located between the primary flow and the IRZ. In this region the majority of the biomass particles penetrate the IRZ, as previously indicated by the analysis of the flow, rapidly heating up and releasing their volatiles. Immediately below the dump plane, the high LIF signal intensity within the main flow downwards likely results from the devolatilization of particles that follow the main flow downwards, or PAHs transported to this region before oxidation. These findings closely align with the observations made by Becker et al. [75], who simultaneously captured Mie and PAH-LIF images of coal particles in the same test rig as in this study. Inside the quarl, a clear distinction of the averaged LII signal is evident between the primary flow and the IRZ. Minor soot structures, transported upwards and back into the primary flow by the IRZ are presumably oxidized upon entering the oxygen-enriched flow. The pronounced soot occurrences downstream of the IRZ intensify with prolonged residence times and exhibit a broader distribution further downstream. These soot particles are positioned within a region of likely reduced oxygen content, situated away from the shear layer toward the ORZ where fresh oxidizer is mixed into the main flow downwards.

This investigation showcases a clear separation between PAH occurrences and soot formation. This finding contrasts with the outcomes of a prior investigation by Hayashi et al. [66], where they observed PAH and soot occurrences close to each other in a gas-assisted coal jet flame. However, direct comparison between both experimental setups is challenging due to different flow configurations. Notably, while Hayashi et al. observed particle devolatilization and soot formation in a region characterized by relatively low oxygen content, the flow dynamics within the solid fuel combustor in our study are much more complex. Consequently, it can be concluded that the process of soot formation in the context of pulverized solid fuel combustion is significantly influenced by the local gas composition. Additionally, PAHs that occur in the near-nozzle region do not necessarily transform immediately into soot nanoparticles.

5.3.3 Influence of oxygen concentration on solid fuel combustion

Analogous to the analysis conducted in Section 5.3.1.2 concerning the influence of oxygen concentration on single-phase operation conditions, a corresponding investigation is carried out to explore the effects of varying oxygen concentration on gas-assisted biomass flames in this section. This analysis

encompasses CH* chemiluminescence, gas flow fields, mean particle trajectories, particle occurrence probabilities, gas temperature distributions, PAH occurrences, and soot occurrences. The outcomes of this investigation are visualized in Figure 5.18. Furthermore, mean axial gas velocity and mean gas temperature profiles for specific heights ($h = -100\,\text{mm}$, $-60\,\text{mm}$, $-20\,\text{mm}$, and $20\,\text{mm}$) are provided in Figure 5.19. Please note that not all data could be captured within the quarl due to particle adhesion to the quarl wall.

The CH* chemiluminescence signals confirm the observations made in the photographs presented in Figure 5.12 regarding the downstream displacement of OXY27P-WS and OXY30P-WS flames, leading to their detachment from the quarl wall. This observation is further supported by the gas temperature distribution, which indicates relatively lower temperatures within the main flow downwards, even dropping below 1000 K for OXY27P-WS. However, the gas temperature within the IRZ is substantially higher, important for rapid heat-up of the flow and particles near the nozzle, essential for flame stabilization. While the CH* chemiluminescence signal for OXY27P-WS is distributed rather broadly with low intensity up to $h = -100\,\text{mm}$, OXY30P-WS displays a compact region of strong heat release, likely attributed to methane combustion, located below $h = -40\,\text{mm}$ at the center of the combustion chamber. This assumption is substantiated by the temperature isolines, indicating temperatures exceeding 1900 K for this specific area, although corresponding photographs in Figure 5.12 do not show a pronounced radiation signal from particles. In contrast, the flames OXY33P-WS, OXY36P-WS, and AIR-WS remain attached to the quarl walls and exhibit an elevated CH* chemiluminescence signal within the main flow downwards immediately below the dump plane. A plausible explanation for this phenomenon could be intense volatile combustion in this region, supported by the presence of PAHs. Toward the lower end of the FOV, the onset of char combustion becomes visible for OXY33P-WS below $h = -80\,\text{mm}$ and for AIR-WS below $h = -60\,\text{mm}$. In the case of OXY36P-WS, the onset of char combustion occurs further downstream.

The trend of the IRZ becoming more compact with increasing oxygen concentration, observed during single-phase combustion, is similarly apparent in two-phase combustion. In comparison to the single-phase operation conditions, the size of the IRZ becomes notably reduced, accompanied by lower velocity magnitudes. OXY27P-WS and OXY30P-WS display noticeably lower velocity magnitudes in the main flow downwards due to the downstream displacement of the combustion zone. In the flow field of OXY36P-WS, an expansion of the main flow downwards toward the ORZ at $h = -50\,\text{mm}$ is observed before subsequently constricting further downstream. This behavior, distinct to OXY36P-WS, can likely be attributed to the high particle load.

The occurrence probability of large particles reveals substantial discrepancies across various operation conditions. While a noticeable number of particles at the operation conditions OXY27P-WS and OXY30P-WS are observed within the main flow downwards, only a few particles are evident in that region for the other operation conditions. Although flow fields within the quarl for OXY27P-WS and OXY30P-WS are not measured, this effect might be linked to the smaller recirculation zone between primary and secondary inflow, the area containing the side flames, as previously revealed in the analyses of single-phase combustion. High particle densities are observed within the IRZ, and mean particle trajectories indicate that most particles traverse the IRZ without being transported back towards the nozzle across all operation conditions. Although peak particle densities predominantly fall within the radial range of $r = 5\,\text{mm}$ to $25\,\text{mm}$ for most operation conditions, OXY36P-WS exhibits a substantial quantity of particles in the center of the chamber as well. Reduced signals at the air operation case can be attributed to the lower particle load.

The gas temperatures of the two-phase operation conditions are lower within the IRZ and the main flow downwards compared to single-phase combustion, with temperatures not exceeding 2000 K. In contrast, the ORZ exhibits significantly higher temperatures, a consequence of the overall augmented thermal power. Gas temperature distributions for OXY33P-WS, OXY36P-WS, and AIR-WS share a sim-

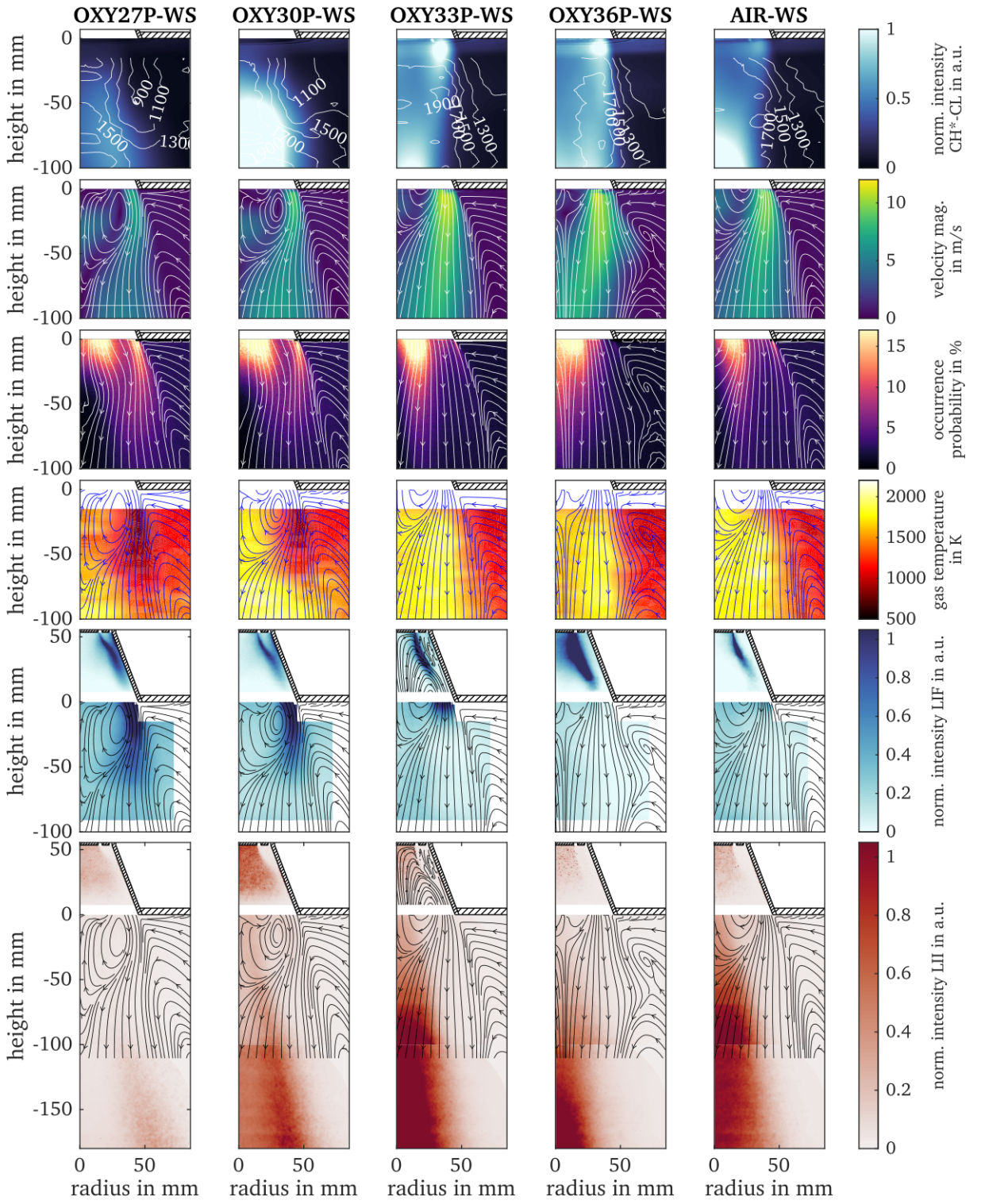

Figure 5.18: Comparison of operation conditions for two phase operation with walnut shells. Top row: CH* chemiluminescence images with gas temperature isolines. Second row: Mean gas-phase velocity magnitude with gas streamlines. Third row: Occurrence probability distribution of large particles with mean particle trajectories. Fourth row: Mean gas-phase temperature with gas streamlines. Fifth row: Mean LIF signal from PAH with gas streamlines. Sixth row: Mean LII signal from soot particles with gas streamlines. Figure adapted from [2].

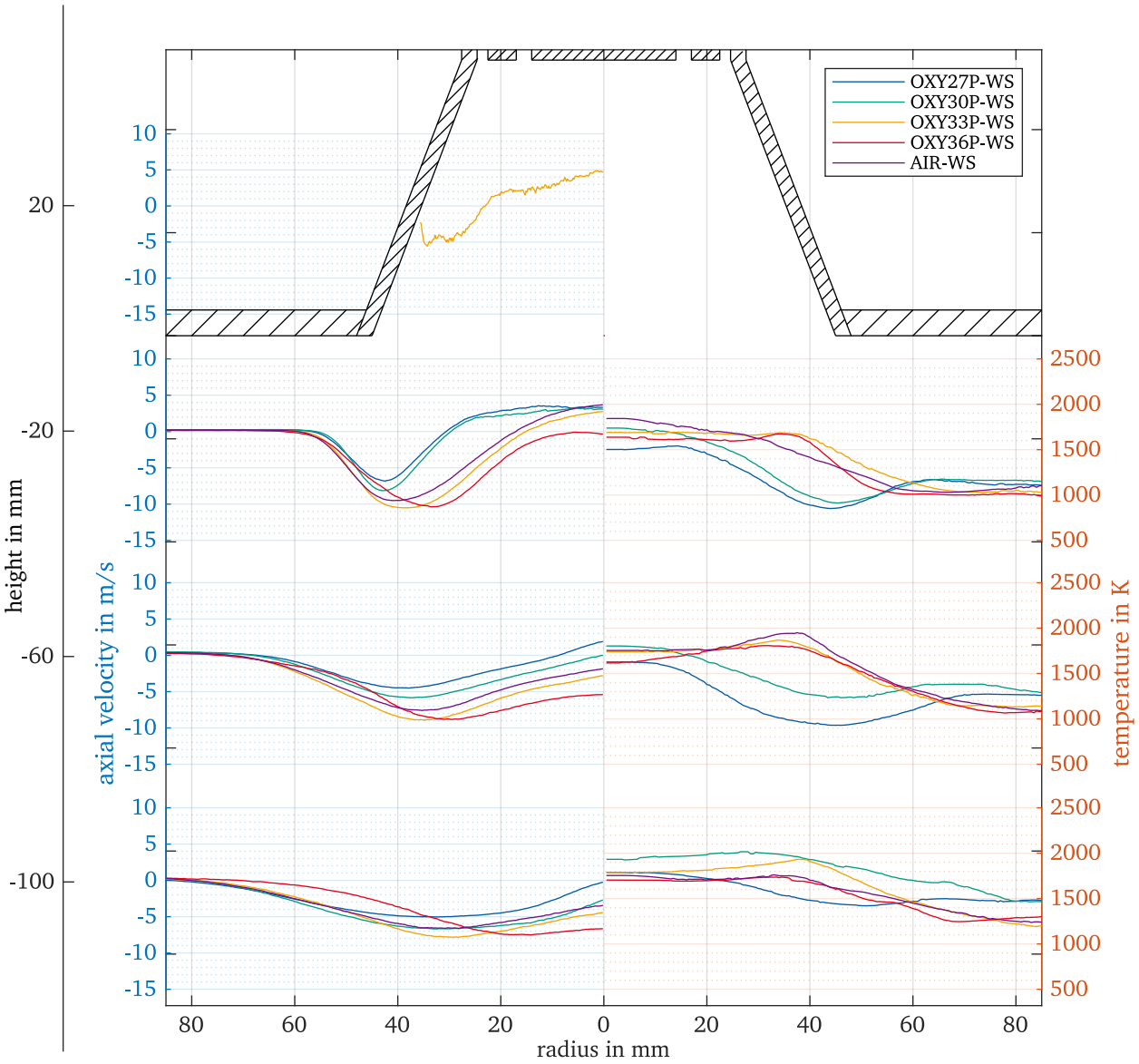

Figure 5.19: Mean axial gas velocity and mean gas temperature profiles of two-phase operation conditions at the heights $h = -100\,\text{mm}$, $-60\,\text{mm}$, $-20\,\text{mm}$, and $20\,\text{mm}$. Left: Mean axial gas velocity profiles. Only operation condition OXY33P-WS was measured within the quarl. Right: Mean gas temperature profiles. Gas temperatures were not measured within the quarl. Figure adapted from [2].

ilar pattern, whereas those of OXY27P-WS and OXY30P-WS mirror the delayed combustion behavior as previously outlined.

The relatively lower gas temperatures in proximity to the nozzle for OXY27P-WS and OXY30P-WS contribute to slower particle heating, evident in the delayed volatile release depicted within the PAH LIF images. However, fluorescence signals are also visible directly downstream from the primary inlet, indicating high temperature levels within the IRZ. Regions with elevated PAH occurrences downstream the dump plane correspond with areas in the main flow downwards featuring comparable low temperatures. As the oxygen concentration increases in the oxy-fuel atmosphere, devolatilization takes place earlier and closer to the nozzle. For OXY36P-WS and AIR-WS, devolatilization is almost complete within the quarl.

Soot formation is enhanced with higher oxygen concentration up to OXY33P-WS, while diminished soot is observed in the upper region of the combustion chamber for OXY36P-WS. Although these measurements visualize areas of soot formation, it is important to note that no definitive statement regarding overall soot mass production can be made. The observed soot occurrences closely correlate with flow fields and temperature distributions, thus explaining the downstream-shifted soot formation for OXY27P-WS and OXY30P-WS. While high soot occurrences are distributed around the chamber's center for OXY33P-WS, OXY36P-WS, and AIR-WS, the peak soot occurrences for the operation condition with reduced oxygen content shift radially outward as the flow progresses downstream. This behavior of flame expansion is also discernible in the photographs of Figure 5.12 and is likely a result of the small recirculation zones between primary and secondary flow within the quarl, influencing the overall shape of the flame. The delayed soot formation in OXY36P-WS compared to OXY33P-WS is in accordance with the subsequently delayed onset of char combustion. This phenomenon is likely linked to the increased particle load in OXY36P-WS relative to OXY33P-WS, which in turn leads to a delay in combustion resulting from particle heat-up. This observation is substantiated by the lower temperature level observed in OXY36P-WS, as depicted in Figure 5.19.

From the observations of oxygen variation in single-phase combustion, it can be concluded that the air operation condition mirrors the flame characteristics of an oxy-fuel condition with an oxygen concentration slightly below 33 vol.%. This conclusion extends to two-phase combustion operation conditions with walnut shells as a biomass representative. Minor deviations, such as the slightly premature onset of char combustion, marginally lower particle density, and reduced volatile release, can be attributed to the different particle load required for maintaining equivalence ratios.

5.3.4 Influence of different solid fuels on flame structure

To study the impact of different solid fuels on combustion characteristics, beech wood and Rhenish lignite are introduced as additional solid fuels to the oxy-fuel operation condition OXY33P. Photographs depicting the gas-assisted solid fuel combustion of the various solid fuels under investigation are presented in Figure 5.20.

The visual analysis of the photographs reveals comparable flame shapes among the diverse solid fuel flames, while their respective flame radiation exhibits significant disparities. Notably, the highest flame radiation is observed when Rhenish lignite is introduced to the oxy-fuel flame, manifesting immediately downstream of the dump plane and likely extending into the quarl. In contrast, the radiation is diminished when beech wood serves as the solid fuel. These observations are likely attributed to the distinct particle size distributions inherent to each fuel type. Rhenish lignite is finely milled into a powder, encompassing particles ranging from as small as $d_{p,10} = 3\,\mu m$ (D10 value) to as large as $d_{p,90} = 396\,\mu m$ (D90 value). On the other hand, walnut shells exhibit a relatively narrow size distribution spanning between $d_{p,10} = 102\,\mu m$ (D10 value) and $d_{p,90} = 179\,\mu m$ (D90 value), while beech wood particles are even larger, ranging from $d_{p,10} = 176\,\mu m$ (D10 value) to $d_{p,90} = 447\,\mu m$ (D90 value) (refer to Table 3.3). As smaller particles tend to heat up more rapidly, the start of char combustion initiates earlier and closer to the nozzle, consequently leading to increased flame radiation in the upstream areas.

Similar to the preceding analysis on the influence of oxygen concentration, this investigation encompasses CH* chemiluminescence, gas flow fields, mean particle trajectories, particle occurrence probabilities, gas temperature distributions, PAH occurrences, and soot occurrences. The outcomes of this study are illustrated in Figure 5.21 and Figure 5.22. LII measurements for OXY33P-RL were infeasible due to the presence of small particles in the fuel, which generated an incandescence signal resembling that of soot particles.

Upon comparing the combustion characteristics of walnut shells and beech wood, notable consistencies are evident within the flow field, mean particle trajectories, and gas temperature distribution.

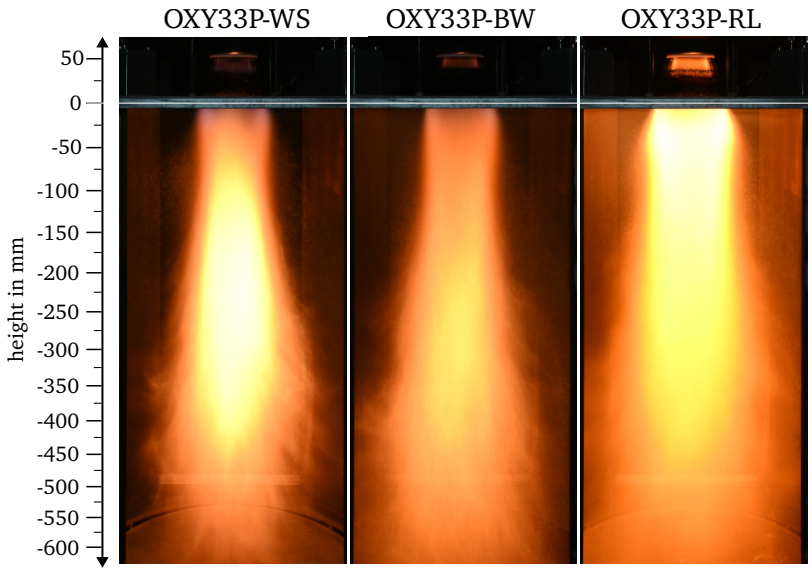

Figure 5.20: Photographs of the gas-assisted solid fuel combustion in an oxy-fuel atmosphere with 33 vol.% oxygen concentration. Type of solid fuel is varied. Left: Walnut shells (WS). Middle: Beech wood (BW). Right: Rhenish lignite (RL). The emission of flame radiation originating from within the quarl is largely obstructed by particles that adhere to the walls. Camera setting are equal for all flames using an exposure time of 0.5 s. Figure adapted from [2].

The occurrence probability of larger beech wood particles is generally lower compared to walnut shell particles, owing to the reduced number of particles arising from their larger sizes. While CH* chemiluminescence images exhibit similarities, the signal intensity immediately below the dump plane within the main flow downwards is more pronounced for the walnut shell flame. This observation aligns with the slightly earlier and more prominent PAH occurrences detected in the LIF images. Furthermore, the prominent signal downstream of $h = -80\,\mathrm{mm}$ in the chemiluminescence image of the walnut shell flame, presumably indicative of the onset of char combustion, is absent in the corresponding region of the beech wood flame. A substantial disparity in soot formation between walnut shells and beech wood is evident. Although soot is observed in similar regions, the signal intensity is notably higher for the walnut shell flame.

The addition of Rhenish lignite to the operation conditions OXY33P resulted in a strong increase of the chemiluminescence signal, a phenomenon likely attributed to the potential interference of particle radiation. Moreover, the gas temperature level experienced an increase of approximately 200 K within the investigated area, surpassing those observed during walnut shell and beech wood combustion. The flow field analysis unveils substantially increased velocity magnitudes within the main flow downwards, accompanied by the expansion of the IRZ, where the stagnation point is shifted downward by 17 mm. This phenomenon was also observed by Li et al. [72], who illustrated an enlargement of the IRZ with decreasing particle size in a dual swirl pulverized coal combustion burner. The occurrence probability analysis of larger Rhenish lignite particles depicts a substantial concentration within the main flow downwards, while mean particle trajectories closely mirror the gas streamlines, signifying a transport of particles back toward the nozzle. This phenomenon leads to prolonged residence times of fuel particles within the near-nozzle region. In regard to PAH occurrences during Rhenish lignite combustion, noticeable resemblances with walnut shell combustion are observed. Particularly, strong occurrences are concentrated immediately downstream of the dump plane within the main flow downwards.

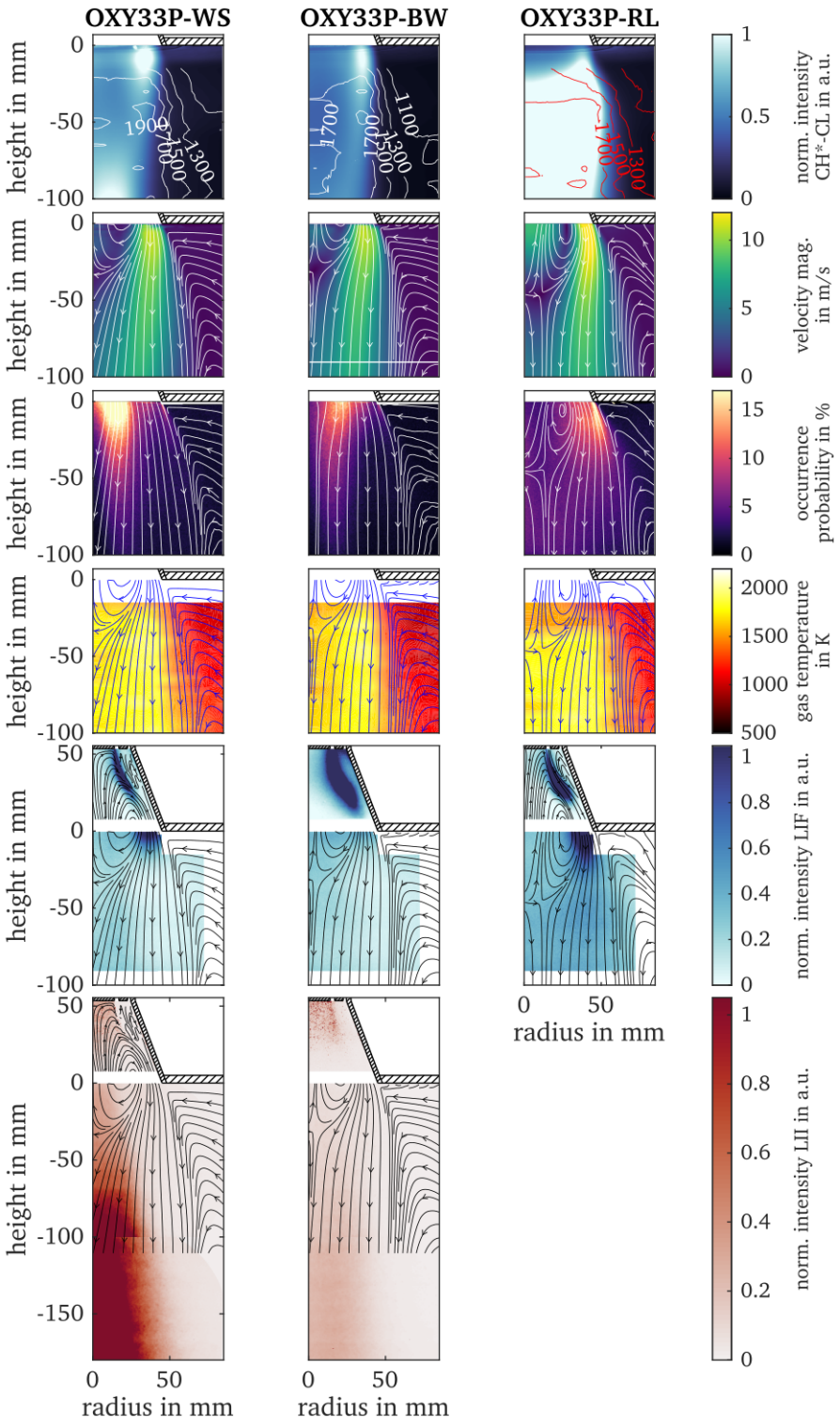

Figure 5.21: Comparison of different solid fuels (WS, BW, RL) used for operation condition OXY33P. Top row: CH* chemiluminescence images with gas temperature isolines. Second row: Mean gas-phase velocity magnitude with gas streamlines. Third row: Occurrence probability distribution of large particles with mean particle trajectories. Fourth row: Mean gas-phase temperature with gas streamlines. Fifth row: Mean LIF signal from PAH with gas streamlines. Sixth row: Mean LII signal from soot particles with gas streamlines. LII measurements for OXY33P-RL were infeasible. Figure adapted from [2].

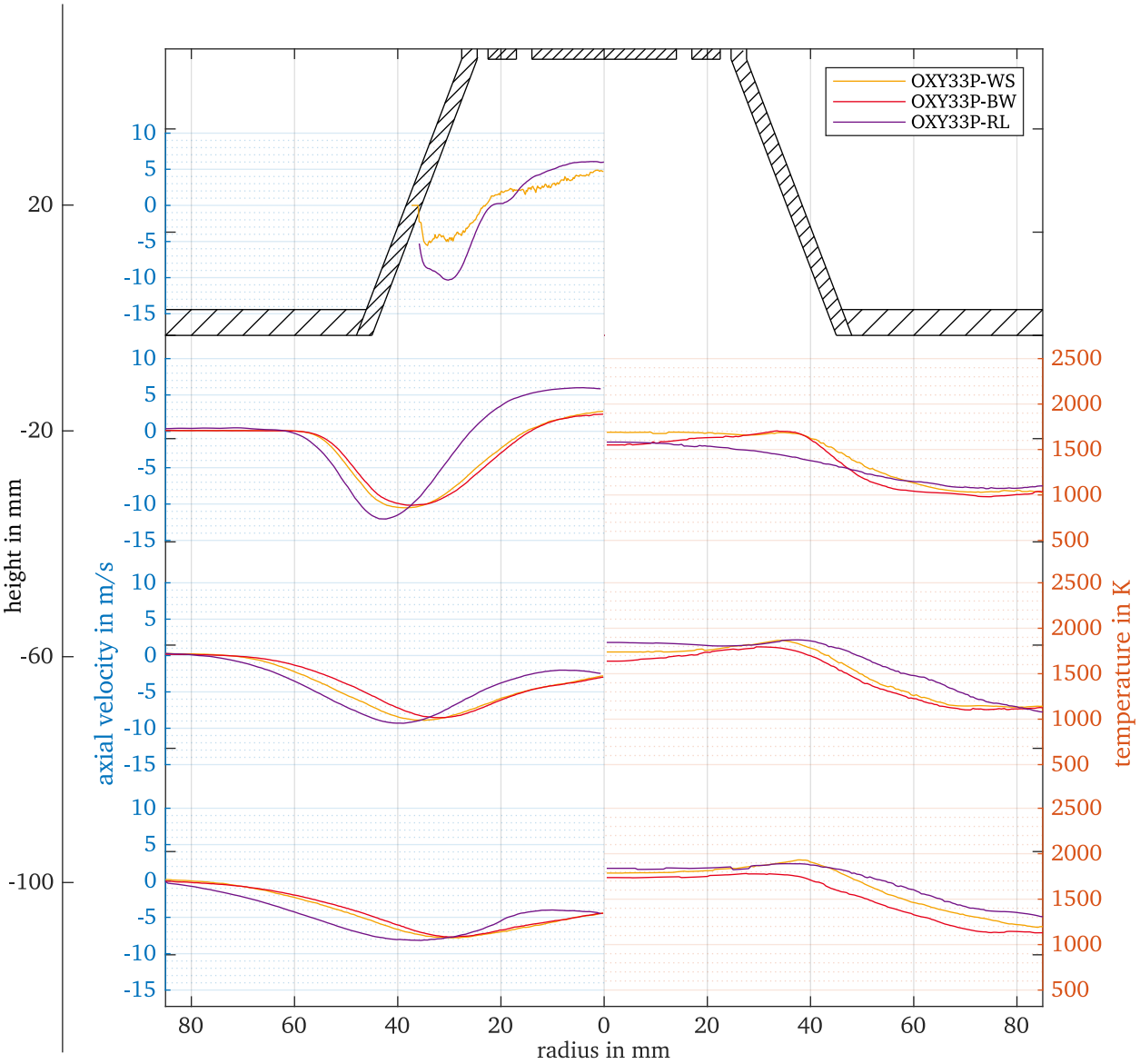

Figure 5.22: Mean axial gas velocity and mean gas temperature profiles of different solid fuels (WS, BW, RL) used for operation condition OXY33P at the heights $h = -100\,\text{mm}$, $-60\,\text{mm}$, $-20\,\text{mm}$, and $20\,\text{mm}$. Left: Mean axial gas velocity profiles. Operation condition OXY33P-BW was not measured within the quarl. Right: Mean gas temperature profiles. Gas temperatures were not measured within the quarl. Figure adapted from [2].

In conclusion, the investigation reveals discernible alterations in flame characteristics when shifting between different types of solid fuels. Given the distinct particle size distributions associated with each fuel, these changes cannot be attributed solely to shifts in particle size or fuel type. The substantial disparities identified in the case of OXY33P-RL, in comparison to OXY33P-WS and OXY33P-BW, suggests that the particle size distribution likely exerts a more pronounced influence on these changes than the specific choice of solid fuel.

5.4 Conclusion

A comprehensive analysis of the influence of oxygen concentration on oxy-fuel combustion within the near-nozzle region of a gas-assisted solid fuel combustor is presented for single-phase and two-phase combustion. By systematically altering the oxygen concentration across different operation conditions, ranging from 27 vol.% to 36 vol.%, a thorough understanding of the ensuing effects on flame stabilization, pollutant formation, and the combustion behavior of biomass particles has been attained. The uniqueness of this research lies in the utilization of an extensive and distinct dataset, which includes chemiluminescence imaging of CH*, gas and solid phase flow velocities, gas temperatures, and qualitative soot measurements, including the visualization of PAH occurrences as soot precursors. To record this comprehensive dataset, a range of advanced laser-optical diagnostics has been employed within the solid fuel combustor. These techniques encompass the utilization of two-phase particle image velocimetry/particle tracking velocimetry for simultaneous measurements of flow and particle velocities, the application of tomographic absorption spectroscopy to elucidate three-dimensional gas temperature distributions, and the establishment of a quasi-simultaneous laser-induced incandescence and laser-induced fluorescence experimental setup to capture both PAH and soot occurrences.

The present analysis provides valuable insights into the intricate interplay between complex fluid-mechanical, particle-dynamical, and chemical processes in oxy-fuel biomass combustion. The main findings of the analysis are summarized as follows:

- The single-phase operation conditions show a considerable influence of the side flames, established between primary and secondary flow within the quarl, on the overall flame structure. Longer side flames lead to a more compact flame shape with an extended flame length. The length of these side flames correlates positively with increasing oxygen content in oxy-fuel conditions.

- The IRZ becomes more tightly compacted with rising oxygen concentrations, coinciding with a rise in velocity magnitudes within the IRZ. Furthermore, the velocity magnitude within the main flow downwards experiences an acceleration due to intensified heat release in proximity to the nozzle with increasing oxygen content. This trend is observed for single-phase and two-phase combustion while the size of the IRZ becomes notably reduced, accompanied by lower velocity magnitudes for two-phase combustion with walnut shells.

- In the context of two-phase operation conditions, a discernible delay in combustion was evident when compared to the single-phase combustion. This effect is caused by the particle heat up and devolatilization and even leads to the downstream displacement of the oxy-fuel flames featuring 27 vol.% and 30 vol.% oxygen content. Notably, the gas temperature within the IRZ remained at a relatively high level, significant for the process of flame stabilization.

- The quasi-simultaneous laser-induced incandescence and laser-induced fluorescence measurements revealed a clear separation between the locations of PAH occurrences and soot formation. It is concluded that the process of soot formation in the context of pulverized solid fuel combustion is significantly influenced by the local gas composition and PAHs that occur in the near-nozzle region do not necessarily transform immediately into soot nanoparticles.

- The combustion behavior observed in an air atmosphere mirrors the flame characteristics of an oxy-fuel condition with an oxygen concentration slightly below 33 vol.% for the studied solid fuel combustor. This observation remains consistent for both single-phase and two-phase combustion utilizing walnut shells as the solid fuel. This highlights the importance of achieving similar adiabatic flame temperatures in both air and oxy-fuel combustion to achieve similar combustion behaviors.

- It is observed that alterations of particle size distribution likely exert a more pronounced influence on the combustion behavior than changes arising from altering the type of the solid fuel.
- The comprehensive analysis carried out in this study underscores the necessity of a substantial dataset to understand the intricate interplay between complex fluid-mechanical, particle-dynamical, and chemical processes in oxy-fuel biomass combustion.

6 Thermochemical state

This chapter presents a coupled investigation of gas temperature and major educt and product species in single-phase combustion and gas-assisted pulverized biomass combustion under oxy-fuel and air atmospheres. Mole fraction measurements of major educt and product species include O_2 and CO_2. The second set of operation conditions, described in Section 3.2.1, of the SFC are used.

Text and figures in this chapter have already been published by Schneider et al. [3] and are reused and partially modified to match the structure and nomenclature of this work. Accordingly, a declaration of the individual contributions of all authors is included in Appendix F. The method descriptions in Section 6.2 are expanded with more details, and Section 6.2.1.2 is added describing N_2-CO_2-DP-CARS measurements. In addition to the work published by Schneider et al. [3], measurements of the entire second set of operation conditions are presented and discussed (Sections 6.3.2.2 and 6.3.3.2). A comparison with tomographic absorption spectroscopy (TAS) is added in Section 6.3.4.

6.1 Aim of this investigation

Thermochemical states provide insight into the reaction transport manifolds of combustion processes. This information goes far beyond what has been measured in pulverized biomass combustion. Analyzing thermochemical states requires the simultaneous measurement of at least two scalars. In harsh environments such as biomass combustion, this is a challenging task.

Coherent anti-Stokes Raman spectroscopy (CARS) allow the simultaneous measurement of gas temperature and mole fractions of major educt or product species. However, most conventional setups use the probe molecule N_2, which is not present under oxy-fuel conditions. In a first step, CARS measurements using O_2 as probe molecule were conducted in collaboration with the Institute of Engineering Thermodynamics (TTS) of the University of Siegen [4]. This investigation reveals good results in regions where local O_2 concentrations are sufficiently high, leading to appropriate signal-to-noise ratios. However, in regions with a lack of O_2, no measurements were possible. Inside the SFC, this particularly affects the inner recirculation zone (IRZ), partly the main flow downwards, and the central region of the burner downstream the IRZ.

The aim of this investigation is to extend the O_2-CARS measurements to simultaneous O_2 and CO_2 measurements. This enables the determination of the thermochemical state under oxy-fuel conditions even in regions with low O_2 concentrations. To assess the thermochemical state for air operation conditions, a dual-pump CARS (DP-CARS) approach is used to probe N_2 and CO_2 simultaneously. The novel O_2-CO_2-CARS approach is thoroughly quantified in terms of accuracy and precision with measurements over a flat flame operated under oxy-fuel conditions by comparison with equilibrium calculations.

Thermochemical states, reaction progress, and local oxidizer concentrations are analyzed for single-phase and two-phase operation conditions in dependence of oxygen concentration in the oxy-fuel atmospheres, type of atmosphere (air/oxy-fuel), and type of biomass (WS/BW). Additionally, a comparison of the measurement techniques used within this thesis to estimate gas phase temperatures, tomographic absorption spectroscopy (TAS), and CARS is presented.

6.2 Methods

The method section is divided into the description of the experimental CARS setup applied to the SFC in Section 6.2.1 and the explanation of the processing of the CARS spectra in Section 6.2.2. While a combined O_2-CO_2-CARS approach is used for the determination of the thermochemical state under oxy-fuel conditions, DP-CARS on N_2 and CO_2 is applied for air operation conditions. Recorded spectra are first pre-processed to account for effects related to the experimental setup and the combustion process and subsequently fitted with the "carsfwsc" algorithm, which was developed and provided by Cutler et al. [166].

In the following, the implementation to the SFC is presented while the CARS fundamentals are described in Section 2.3.5.

6.2.1 Coherent anti-Stokes Raman spectroscopy

6.2.1.1 O_2-CO_2-CARS

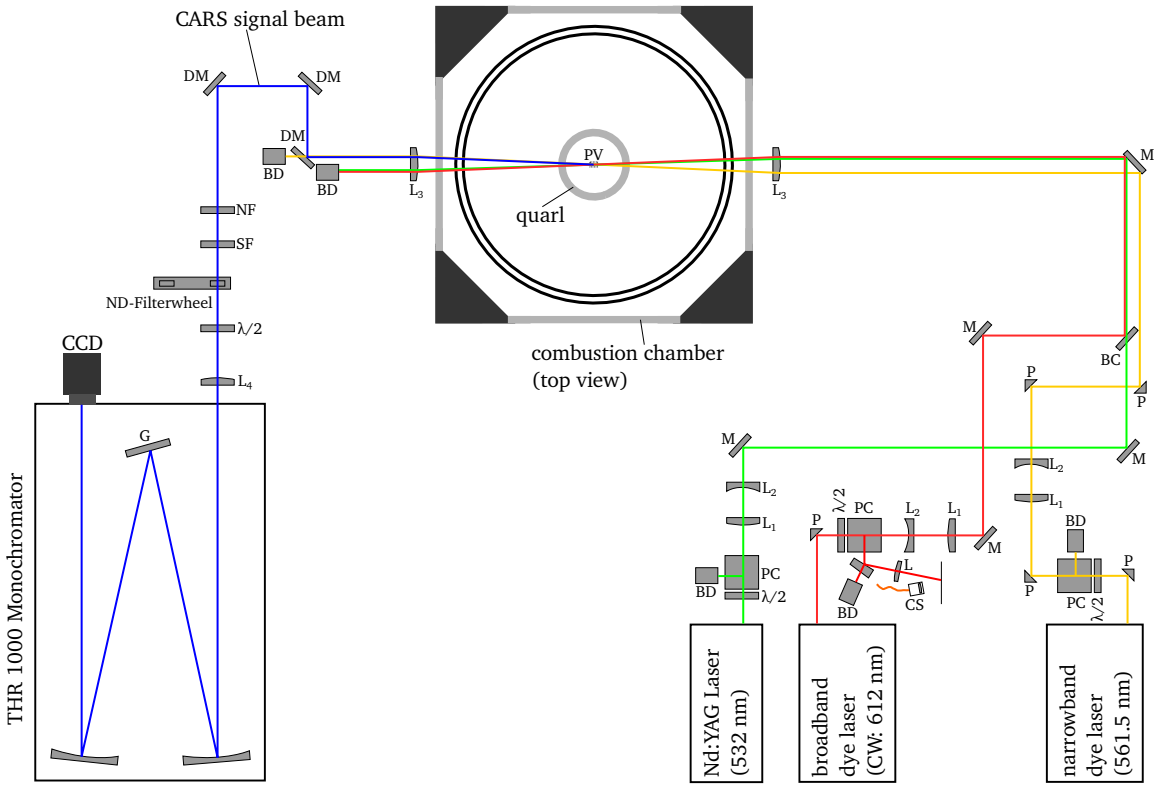

Figure 6.1: Experimental O_2-CO_2-CARS setup in BOXCARS arrangement. Additional mirrors used for directing the laser beams towards the SFC are not shown to improve clarity. BC: beam combiner. BD: beam dump. CS: compact spectrometer (Thorlabs Inc., CCS200/M). CW: central wavelength. DM: dichroic mirror (Thorlabs Inc., DMLP550L). G: grating with 2400 lines/mm. L_{1-2}: Galilean telescope for divergence adjustment. L_3: focusing lens f=300 mm. L_4: focusing lens f=100 mm. M: mirror. ND: neutral density. NF: notch filter. P: prism. PC: polarizing beamsplitter cube. PV: probe volume. SF: short pass filter (Thorlabs Inc., FESH0550). $\lambda/2$: zero-order half-wave plate.

The experimental O_2-CO_2-CARS setup is based on the DP-CARS setup designed by Zentgraf during his PhD studies at the Institute of Reactive Flows and Diagnostics (RSM) at the Technical University of Darmstadt [168]. While Zentgraf performed N_2-CO_2-DP-CARS measurements on a side-wall quenching burner, the setup had to be adapted to perform simultaneous CARS measurements of O_2 and CO_2 at the SFC.

The adapted experimental CARS setup to the SFC is illustrated in Figure 6.1. The laser wavelengths were chosen to 561.5 nm, 612.3 nm, and 532 nm for pump, Stokes, and probe laser, respectively. Since the Stokes laser was spectrally broadband, this results in the detection of all Raman active transitions around $\omega_R = 1478\,\mathrm{cm^{-1}}$, which included the Q-branch transitions of O_2 around a Raman shift of $1556\,\mathrm{cm^{-1}}$ and the $2\nu_2$ system of CO_2 around $1388\,\mathrm{cm^{-1}}$.

A Q-switched, frequency-doubled Nd:YAG laser with two Nd:YAG cavities (Spectra-Physics PIV 400, 10 Hz, 5 −8 ns pulse width) was modified for individual operation of both cavities [168]. One cavity was used to optically pump a narrowband dye laser (Radiant Dyes Laser & Accessories GmbH, NarrowScan) to generate the pump laser beam at 561.5 nm. Rhodamine 590 dye dissolved in ethanol was used as the lasing medium. The laser from the other cavity was split into two paths, one serving as the probe beam at 532 nm and one to optically pump a custom-built broadband dye laser (BBDL) to produce the Stokes laser beam around 612 nm (not shown in Figure 6.1).

The custom-built BBDL was constructed by Kissel during his PhD studies [197] based on the design by Ewart [198]. The modeless broadband dye laser consisted of a transversally pumped oscillator followed by two longitudinally pumped amplifier stages. The dye Rhodamine 640 dissolved in ethanol was used as the lasing medium to produce spectrally broadband laser radiation with a center wavelength of 612.3 nm and a full width at half maximum (FWHM) of approx. 5 nm. The mean spectral profile recorded with a compact spectrometer (Thorlabs Inc., CCS200/M) is shown in Figure 6.2.

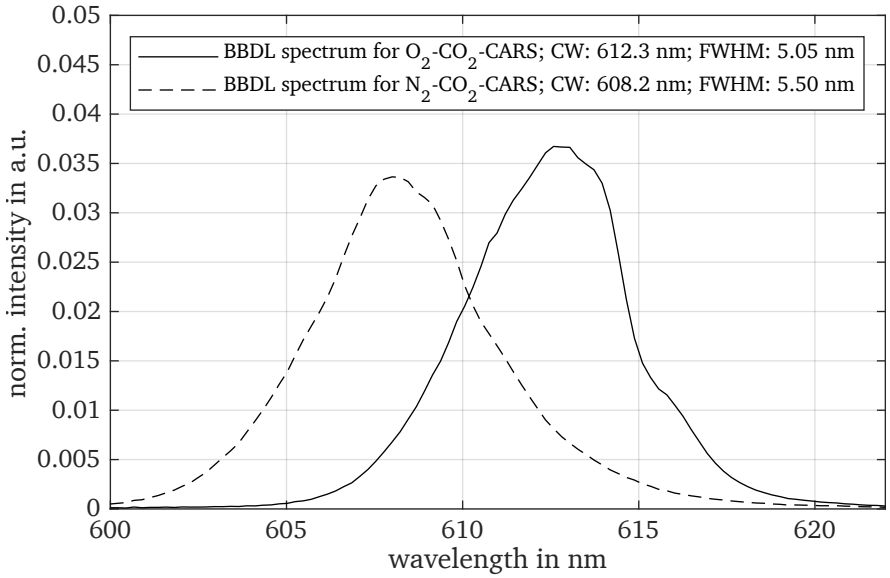

Figure 6.2: Laser spectrum of the broadband dye laser (BBDL) for O_2-CO_2-CARS and N_2-CO_2-CARS. CW: central wavelength. FWHM: full width at half maximum.

All lasers were energy controlled by a combination of a zero-order half-wave plate and a polarizing beamsplitter cube. Beam divergences were adjusted by two lenses arranged as a Galilean telescope in each beam path. To synchronize the temporal overlay of Stokes and probe beams, a delay line was constructed within the beam path of the probe laser. The timing of the pump beam with respect to the probe and Stokes lasers was adjusted by the Q-switch delay. The lasers were overlapped and directed toward the SFC with anti-reflective coated mirrors. To determine the temporal resolution, individual

temporal intensity profiles of pump, Stokes, and probe laser were recorded by a high-speed photo detector (Thorlabs Inc., DET210/M) in combination with an oscilloscope (Tektronix Inc., TDS5032B). The temporal resolution was calculated as the $1/e^2$-value of the convolved intensity of the normalized individual temporal intensity profiles to 8.1 ns with a standard deviation of 0.45 ns.

The laser beams were focused to the probe volume by a spherical lens with a focal length of $f = 300$ mm. Phase matching was achieved by a planar BOXCARS arrangement to allow measurements close to the combustor dump plane. The angles were set to $\alpha \approx -2°$, $\beta \approx 2.2°$, and $\gamma \approx 1.9°$ with respect to the optical axis for pump, Stokes, and probe beams, respectively. The size of the probe volume was determined by traversing a beam monitor (DataRay Inc., WinCam D) in increments of 0.5 mm along the optical axis in the vicinity of the probe volume. The size of the CARS probe was derived as the $1/e^2$-value of the normalized convolved intensity to an elliptical area at the center with a minor axis of $a \approx 40$ µm and a major axis of $b \approx 50$ µm. The length of the probe volume was calculated by interpolating the normalized convolved intensity to $l \approx 0.7$ mm.

The CARS signal was collimated with a spherical lens of the same focal length as the focusing lens ($f = 300$ mm). Due to the applied phase matching scheme, the CARS signal was spatially close to the pump beam. Separation of the pump and CARS beams was performed by three short pass dichroic mirrors (Thorlabs Inc., DMLP550L) and a short pass filter (Thorlabs Inc., FESH0550). Additionally, a notch filter removed scattered radiation at 532 nm. A motorized filter wheel with different neutral density (ND) filters, ranging from ND0 (no filter) to ND2.9, was positioned in the beam path to account for local variations in signal strength due to changes in temperature and mole fraction. To optimize the polarization of the CARS signal with respect to the spectrometer, an achromatic half-wave plate (Thorlabs Inc., AHWP10M-600) was placed in the beam path. Subsequently, the CARS signal was focused into the entrance slit of a spectrometer (Jobin Yvon S.A.S., THR 1000 Monochromator, focal length 1 m, 2400 lines/mm grating) by a spherical lens with a focal length of $f = 100$ mm. The chip of a back-illuminated CCD camera (Princeton Instruments, Pixis 400B, 1340x 400 px, 16 bit) was placed at the position of the exit slit to record the CARS spectra. The chip was fully hardware binned in the vertical direction and the camera frame rate was set to 20 Hz, twice the laser repetition rate to record background spectra between the CARS spectra.

In order to normalize the CARS spectra to the spectral profile of the broadband Stokes laser, non-resonant spectra were recorded several times during the measurements in pure argon.

The pulse energies of the pump, Stokes, and probe lasers within the probe volume were set to 25 mJ, 23.5 mJ, and 30 mJ. To check for high irradiance perturbation effects, the laser energies were varied and CARS spectra above a flat flame, operated under oxy-fuel conditions with 20 vol.% O_2 excess in the flue gas, were recorded. The total irradiance I_{total} was varied to check for possible Stark broadening effects, evident as a shift of the Raman transitions to lower frequencies and broadening of the transition lines, and the irradiance product of pump and Stokes laser $I_1 I_2$ was varied to prove the absence of stimulated Raman effects, evident as artificial changes in the population distribution of rotational and vibrational states towards larger populations of higher vibrational states. Further details on high irradiance perturbation effects are described in Section 2.3.5. The result of the laser energy variation, illustrated in Figure 6.3, showed no significant changes to the spectra, proving that the selected laser energies did not lead to high irradiance perturbation effects [169].

6.2.1.2 N_2-CO_2-DP-CARS

Simultaneous measurements of N_2 and CO_2 were achieved by a dual-pump CARS (DP-CARS) approach, which is explained in more detail in Section 2.3.5. The experimental setup was similar to the setup described for O_2-CO_2-CARS in Section 6.2.1.1 and only modifications to the setup are discussed in the following.

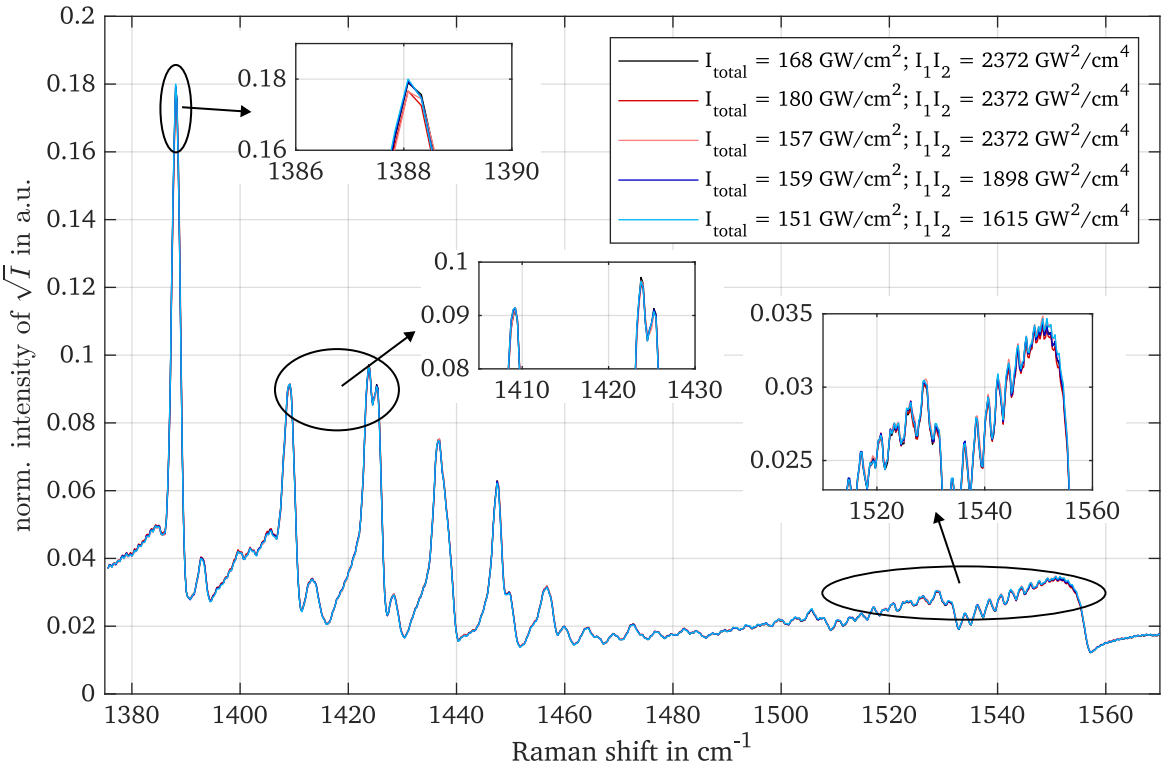

Figure 6.3: Variation of pulse energies to check for high irradiance perturbation effects. Mean CARS spectra are shown. Variation of the total irradiance I_{total} to check for possible Stark broadening effects. Variation of the irradiance product of pump and Stokes laser $I_1 I_2$ to check for stimulated Raman effects. Spectra are normalized by non-resonant spectra and area. Figure adapted from [3].

The central wavelength of the broadband Stokes laser was tuned to 608.2 nm, which was achieved by using a mixture of Rhodamine 640 and Rhodamine 610 solved in ethanol. The resulting broadband spectrum is presented in Figure 6.2. By interchanging the pump and probe laser, all Raman active transitions around $\omega_{\text{R,1}} = 1367\,\text{cm}^{-1}$ and $\omega_{\text{R,2}} = 2355\,\text{cm}^{-1}$ were probed. This included the $2\nu_2$ system of CO_2 around 1388 cm^{-1} and the Q-branch transitions of N_2 around a Raman shift of 2330 cm^{-1}. In the resulting CARS signal, the Raman transitions were close to each other and the wavenumber offset was $\omega_{\text{offset}} = 988\,\text{cm}^{-1}$. The wavelength selection ensured good signal quality of the probed Raman transitions of both molecules because the transitions did not interfere with each other strongly.

6.2.2 Data Processing

6.2.2.1 Pre-processing of CARS spectra

The pre-processing of the CARS spectra involved preparing the spectra to be processed using the "carsfwsc" algorithm of Cutler et al. [166]. Special algorithms were required to remove spectra suffering from saturation, low signal-to-noise ratios, or laser-induced breakdowns. Optical breakdowns occurred when particles were inside the probe volume and were hit by the lasers, which is inevitable in pulverized fuel combustion.

Saturation of the spectra was detected at a threshold of 65 000 counts and occurred most frequently at positions where cold oxidizer and hot exhaust gases mix. At all other positions, saturation was successfully prevented by a suitable choice of ND filter in front of the spectrometer. To avoid a bias at

positions with saturated spectra, the same position was measured again with a higher ND filter. In post-processing, the two datasets were merged by appending the n spectra with the highest intensity counts from the dataset recorded with the higher ND filter to the first dataset where n spectra experienced saturation.

Spectra with low signal-to-noise ratios were removed when the intensity of the peak signal was less than six times the standard deviation of the spectra. This criterion was chosen to avoid dependence of the signal-to-noise ratio on the measurement results. For the single-phase operation conditions 1 % of all recorded spectra and for pulverized fuel combustion 3.9 % of all recorded spectra were removed due to too low signal-to-noise ratios.

Laser-induced breakdowns led to a deformation of the recorded spectra. Examples of spectra with optical breakdowns are illustrated in Figure 6.4. Most spectra affected by optical breakdown showed a strong overall increase in intensity. These spectra could be easily removed by applying a threshold to the sum of the intensities in a spectral region where no transitions were expected. However, there were also smaller, spectrally confined distortions that were removed by detecting artificially high intensity values in regions where no Raman active transitions exist.

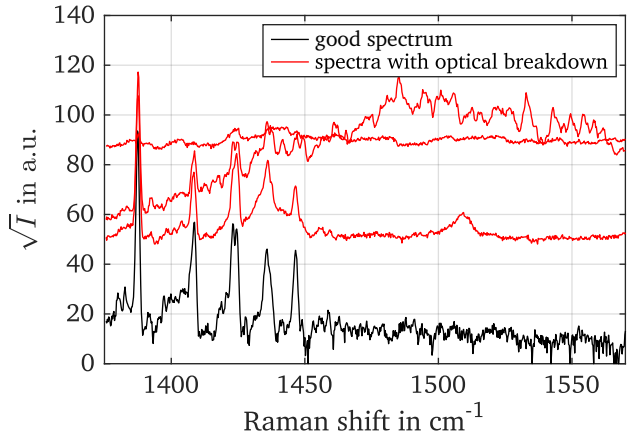

Figure 6.4: Recorded raw CARS spectra. Different characteristics of spectra with optical breakdowns are depicted.

For single-phase operation conditions almost no laser induced breakdowns were detected, whereas for pulverized solid fuel combustion the number of optical breakdowns was highly dependent on the measurement position. Analyses are given in the results section.

All good spectra underwent further pre-processing. First, the background intensity was subtracted from the recorded CARS spectra. In the case of single-phase operation conditions, an average background signal was calculated and then subtracted from each CARS spectrum. However, this approach was not feasible for the two-phase operation conditions due to the high intensity fluctuations of the background signal. Therefore, the mean background signal was weighted by the mean intensity value of a spectral band where no Raman transitions were expected.

The recorded CARS spectra were normalized to the non-resonant spectrum measured in pure argon. The non-resonant spectrum was interpolated in time using non-resonant spectra recorded before and after the measurement.

Finally, the square root of the intensity was extracted and the pixel to wavenumber conversion was performed. The wavenumber axis related to the dispersion of the spectrometer was calibrated using a measured spectrum over a flat flame operated under oxy-fuel conditions for the O_2-CO_2-CARS setup and under air conditions for the N_2-CO_2-DP-CARS setup, and a simulated spectrum of the same conditions. The spectrum was simulated using the “carsfwsc” algorithm. A second order polynomial fit of all

transition peaks was performed to convert pixels to wavenumbers using a least square method. While linear fits were successfully applied for small spectral fit windows [168, 199], non-linear behavior is evident for large spectral fit windows [169].

6.2.2.2 CARS spectra fitting

CARS spectra were fitted using the "carsfwsc" algorithm of Cutler et al. [166]. Different parameter sets were used for processing O_2-CO_2-CARS spectra above a flat flame, O_2-CO_2-CARS spectra of the SFC, and N_2-CO_2-DP-CARS spectra of the SFC. The parameter sets are summarized in Table 6.1.

Table 6.1: Parameter sets for evaluation of CARS spectra with the "carsfwsc" algorithm [166]. FFB: flat flame burner.

Parameter			O_2-CO_2-CARS (FFB)	O_2-CO_2-CARS (SFC)	N_2-CO_2-DP-CARS (SFC)
Fit variables		-	T, x_{O_2}, x_{CO_2}, ω_{shift}	T, x_{O_2}, x_{CO_2}, ω_{shift}	T, x_{N_2}, x_{CO_2}, ω_{shift}
Bounds: T	T_{min}	K	500	500	500
	T_{max}	K	2800	2800	2800
Bounds: x_{O_2}	$x_{O_2,min}$	-	0	0	-
	$x_{O_2,max}$	-	1	1	-
Bounds: x_{CO_2}	$x_{CO_2,min}$	-	0	0.3	0
	$x_{CO_2,max}$	-	1	1	0.3
Bounds: x_{N_2}	$x_{N_2,min}$	-	-	-	0
	$x_{N_2,max}$	-	-	-	1
Bounds: ω_{shift}	$\omega_{shift,min}$	cm^{-1}	-5	-5	-5
	$\omega_{shift,max}$	cm^{-1}	5	5	5
Fitting range		cm^{-1}	2360 to 2560	2370 to 2560	2275 to 2425
Blocked from fitting		cm^{-1}	2432 to 2438	2432 to 2438	-
ω_{offset}		cm^{-1}	987.55	987.55	984.2
χ_{NR}		[1]	$19.74 \cdot 10^{-18}$	$19.74 \cdot 10^{-18}$	$19.74 \cdot 10^{-18}$
Probe line width		cm^{-1}	0.95	0.95	0.75
Pump line width		cm^{-1}	0.05	0.05	0.05
2nd-pump line width		cm^{-1}	1	1	0.5

[1] cm^3/(erg amagat)

The bounds for the fit variables were set wide to avoid any influence of the bounds on the precision of the measurement. The "carsfwsc" algorithm was written for DP-CARS processing which results in the adapted fitting range for O_2-CO_2-CARS and the usage of a value for ω_{offset}. The range 2432 cm^{-1} to 2438 cm^{-1} had to be blocked from fitting, since the Raman active rotational line S(5) of H_2 at 1447.28 cm^{-1} [200] affected the measured spectra. The third-order non-resonant susceptibility χ_{NR} was set to $19.74 \cdot 10^{-18}$ cm^3/(erg amagat) [169] as it was assumed that H_2O makes up the majority of the buffer gas. The parameters for the line widths were adjusted to minimize the residuum.

Examples of measured and fitted spectra are shown in Figure 6.5. Both mean and instantaneous spectra were well fitted with the described parameters, resulting in a low residuum. Arising measurement accuracy and precision are analyzed in Section 6.3.1.

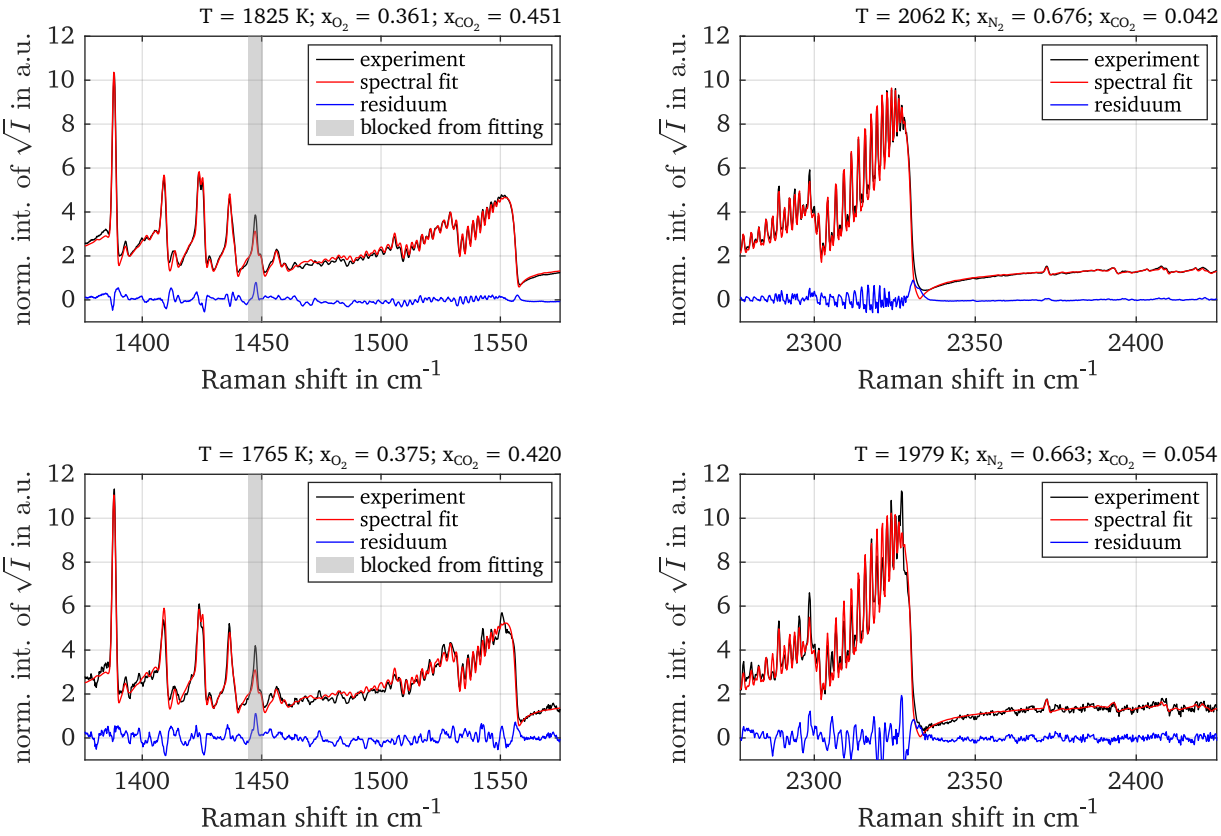

Figure 6.5: Experimental and fitted CARS spectra. Top left: Mean O_2-CO_2-CARS spectra. Top right: Mean N_2-CO_2-DP-CARS spectra. Bottom left: Instantaneous O_2-CO_2-CARS spectra. Bottom right: Instantaneous N_2-CO_2-DP-CARS spectra. Figure adapted from [3].

6.3 Results and discussion

6.3.1 Experimental validation

The experimental validation of O_2-CO_2-CARS was performed to determine the accuracy and precision of the experimental setup in combination with the "carsfwsc" algorithm of Cutler et al. [166]. To the author's knowledge, only in the study by Mazza et al. [201] CARS experiments were performed solely on O_2 and CO_2. However, they used an ultra-broadband two-beam femtosecond/picosecond CARS approach and a self-developed fitting code for processing, which does not allow a comparison with the setup used in this study.

The accuracy and precision of the N_2-CO_2-DP-CARS experimental setup was investigated in the work of Zentgraf et al. [202]. They reported a relative accuracy of 3% and a relative precision of 4% for the gas phase temperature. The derived CO_2 mole fractions showed a relative accuracy between 5% and 20% and an average relative precision of approximately 16% [202].

Measurements were conducted in the exhaust of a premixed flat flame and compared with reference values calculated with Cantera [130] in combination with the GRI 3.0 mechanism [106] to derive a statement about the accuracy and precision of the O_2-CO_2-CARS setup. The flat flame was stabilized over a ceramic honeycomb structure with a square cross-section of 76.2x 76.2 mm² and a cross-section of each channel of 1.07x 1.07 mm² with a length of 50 mm. Various gas mixtures of $CH_4/O_2/CO_2$ were premixed and issued from the ceramic honeycomb structure. For more details, see [203].

O_2-CO_2-CARS spectra were recorded approximately 10 mm above the flat flame for flames with different equivalence ratios and processed as described in Section 6.2.2. For each operation condition, 500 individual O_2-CO_2-CARS spectra were evaluated. For the thermal equilibrium calculations, a preheated gas temperature of 70 °C was used, approximated from thermocouple measurements inside one selected channel of the ceramic honeycomb structure close to its exit. The results of the measurements together with the calculated values are presented in Figure 6.6. In addition, the relative accuracies and relative precisions for the gas temperature and the mole fractions of O_2 and CO_2 are depicted.

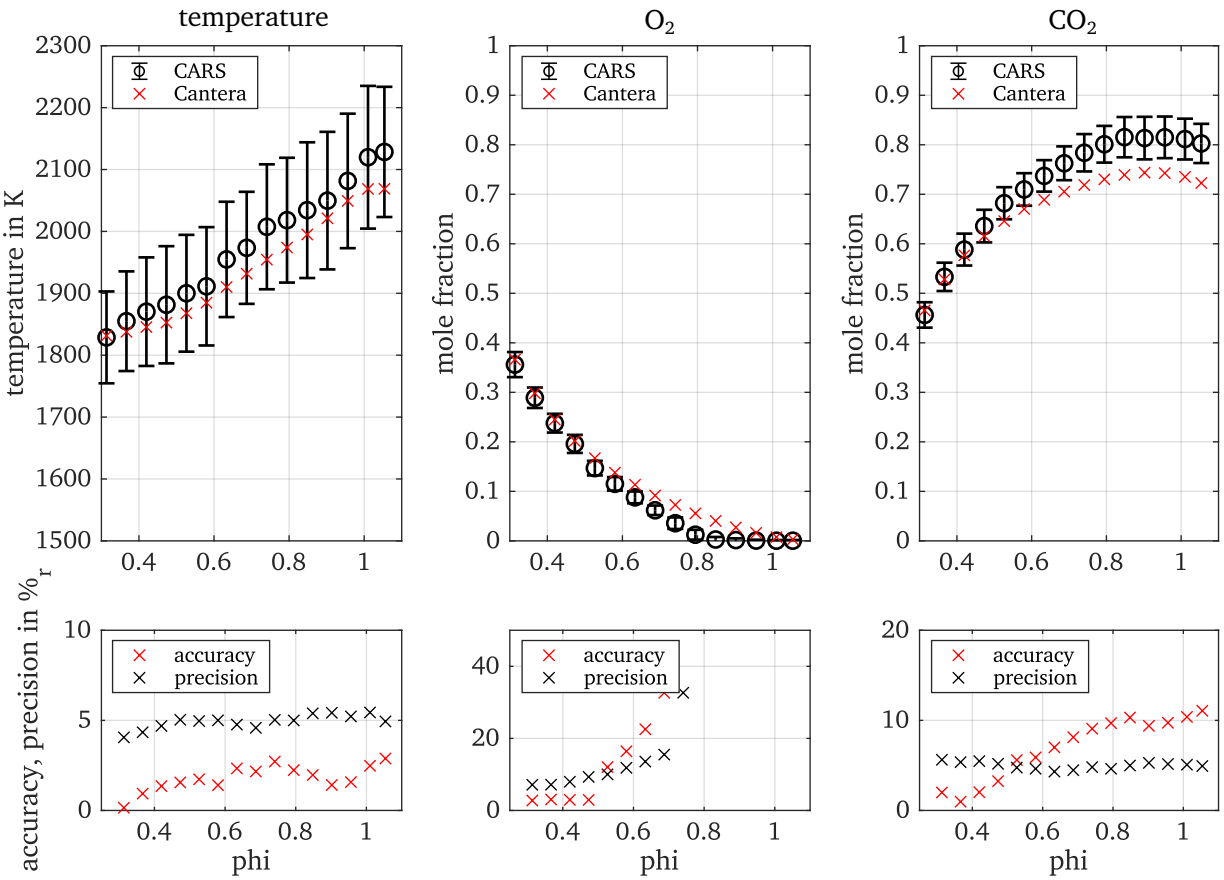

Figure 6.6: Relative accuracies and precisions of the O_2-CO_2-CARS setup for different equivalence ratios. Experiments were conducted over a flat flame under oxy-fuel conditions. Reference values were calculated with Cantera [130] in combination with the GRI 3.0 mechanism [106] and a preheated gas temperature of 70 °C. Figure adapted from [3].

The experimental validation shows that the relative accuracy for the gas phase temperature is below 3% and the relative precision is around 5%. While the relative precision is almost constant over the temperature range considered, the relative accuracy decreases slightly with increasing temperature. This is probable due to the decreasing mole fraction of O_2 at equivalence ratios closer to 1. Similar accuracies and precisions have been reported from an N_2-CO_2 dual-pump CARS setup [168] and from the study by Mazza et al. [201] using an ultra-broadband two-beam femtosecond/picosecond O_2-CO_2-CARS approach.

O_2 and CO_2 mole fractions show relative accuracies below 6% when both species are present in the gas mixture with mole fractions greater than 0.2. For operation conditions with low O_2 concentrations in the flue gas of the flat flame, the relative accuracies decrease significantly for O_2 mole fractions and the absolute accuracy is also worse. The reason for this is the poor signal to noise ratio in the O_2-CO_2-CARS spectra in the spectral region of the Q-branch transitions of O_2. The relative accuracy

of the CO_2 mole fractions for spectra containing primary spectral features of CO_2 is about 10% while the relative precision of the CO_2 mole fractions for all operation conditions is approximately 5%.

While the determination of accuracy and precision over an oxy-fuel flat flame only covered the expected conditions in the hot regions of the SFC, an additional evaluation of accuracy and precision at low temperatures was conducted. To evaluate the performance of the experimental setup in combination with the “carsfwsc” algorithm, CARS spectra were recorded in gas mixtures of O_2 and CO_2 diluted in Ar. To account for the changed buffer gas, the third-order non-resonant susceptibility χ_{NR} was adjusted to $9.46 \cdot 10^{-18}\,cm^3/(erg\ amagat)$ [165] in the processing.

Figure 6.7 presents the results obtained from 5 different gas mixtures. The first two gas mixtures have different concentrations of O_2 diluted in Ar. Gas mixtures 3 and 4 feature different concentrations of CO_2 diluted in Ar and gas mixture 5 contains O_2, CO_2, and Ar. Relative accuracies and precisions are evaluated using thermocouple measurements as a reference for the gas temperature and the set points of the MFCs used.

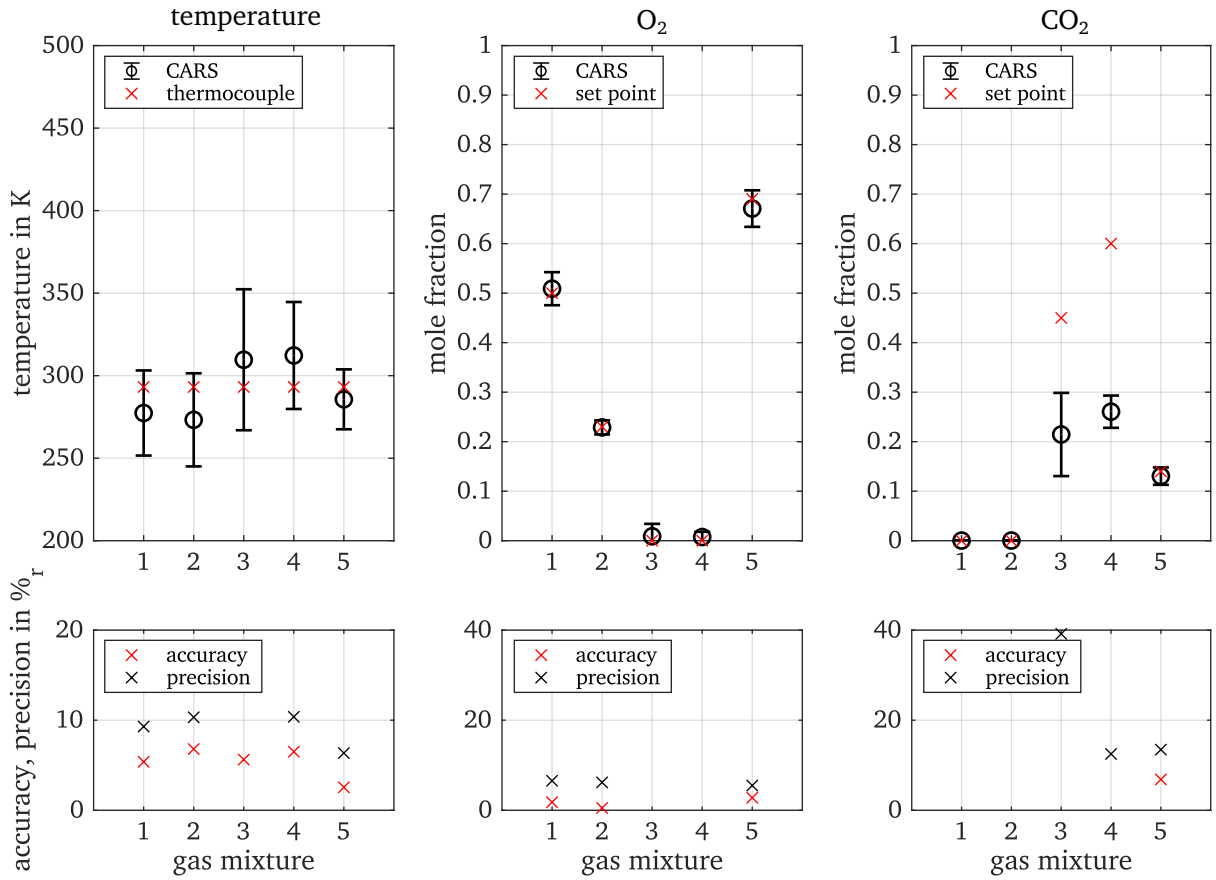

Figure 6.7: Relative accuracies and precisions of the O_2-CO_2-CARS setup for different O_2/CO_2/Ar gas mixtures at 20 °C and atmospheric conditions. Gas mixtures 1 and 2 present different O_2 mole fractions in Ar. Gas mixtures 3 and 4 present different CO_2 mole fractions in Ar. Gas mixture 5 consists of O_2, CO_2, and Ar.

For all cases where only one species is diluted in Ar the relative accuracy of the gas temperature is around 6% and the relative precision is about 10%. For the gas mixture containing O_2 and CO_2, the relative accuracy of the gas temperature is improved to 2.5% and the relative precision to 6.4%. The evaluation of the O_2 mole fractions shows a relative accuracy below 3% and a relative precision below 7% for gas mixtures containing O_2. The CO_2 mole fraction cannot be predicted satisfactorily at low temperatures when no O_2 is present in the gas mixture. This is due to the limited information available

to the fitting algorithm, as only the ground vibrational band of the $2\nu_2$ system is visible in the spectra (refer to Figure 2.9). With O_2 present in the gas mixture, the relative accuracy of the CO_2 mole fraction is 6.8% and the relative precision is 13.5%.

6.3.2 Single-phase combustion

In this section, the thermochemical states of the single-phase operation conditions are analyzed. First, the operation condition OXY33P is evaluated in detail. Subsequently, a comparison of the gas temperatures and O_2 and CO_2 mole fractions of all single-phase operation conditions is conducted.

For all single-phase operation conditions, CARS measurements were performed at the heights $h = -24.6\,\text{mm}$, $-49.2\,\text{mm}$, and $-98.4\,\text{mm}$. At each height the SFC was traversed to record radial CARS spectra in steps of 3 mm in the range between $r = -15\,\text{mm}$ and 60 mm and in steps of 5 mm between $r = 60\,\text{mm}$ and 90 mm. The outer radial limit at $r = 90\,\text{mm}$ results from the design of the chamber corners. For each position, 500 CARS spectra were recorded and processed as discussed in Section 6.2.2.

6.3.2.1 Thermochemical state of operation condition OXY33P

Radial mean gas temperature profiles of operation condition OXY33P at the heights $h = -24.6\,\text{mm}$, $-49.2\,\text{mm}$, and $-98.4\,\text{mm}$ are presented in Figure 6.8.

The radial mean gas temperature profiles of operation condition OXY33P are presented in Figure 6.8. A high temperature plateau region above 2100 K in the center of the SFC with a steep temperature gradient towards an outer region of temperatures around 750 K is observed. According to the axial velocity, the high temperature plateau region at height $h = -24.6\,\text{mm}$ is within the IRZ of the swirl flame. The steep temperature gradient is formed in the shear layer towards the ORZ, indicated by high RMS values of the axial velocity. Height $h = -49.2\,\text{mm}$ is approximately at the height of the stagnation point of the flow field and height $h = -98.4\,\text{mm}$ is downstream of the IRZ.

The highest mean gas temperature of 2310 K is measured at $h = -49.2\,\text{mm}$ and $r = 27\,\text{mm}$ which is about 150 K higher than the gas temperature in the center. In comparison with equilibrium calculations carried out with Cantera [130] (refer to Figure 2.4) and given the determined accuracy in Section 6.3.1, this temperature is close to the maximum adiabatic flame temperature under slightly fuel-rich conditions.

The probability density functions (PDFs) of the measurement points reveal rather narrow distributions within the IRZ, within the ORZ, and near the center downstream of the IRZ. Here, the relative standard deviations of the gas temperature are close to the relative precision of the O_2-CO_2-CARS setup, indicating locally homogeneous temperature conditions. At locations where mixing of different flows occurs, the PDFs become broad. The peaks of the PDFs show a shift towards higher temperatures than the mean temperatures on the inner side of the region characterized by the steep temperature gradient. This contrasts with a shift towards lower temperatures than the mean temperatures of the PDF peaks at the lower end of the steep temperature gradient. These observations are typical of fluid mixing in a shear layer [97].

The steep temperature gradient decreases progressively in the downstream direction due to the broader shear layer. This is indicated by the radial profiles of the relative temperature standard deviation and the RMS values of the axial velocity. This is consistent with the findings from the flow field investigations in Section 5.3.1.1.

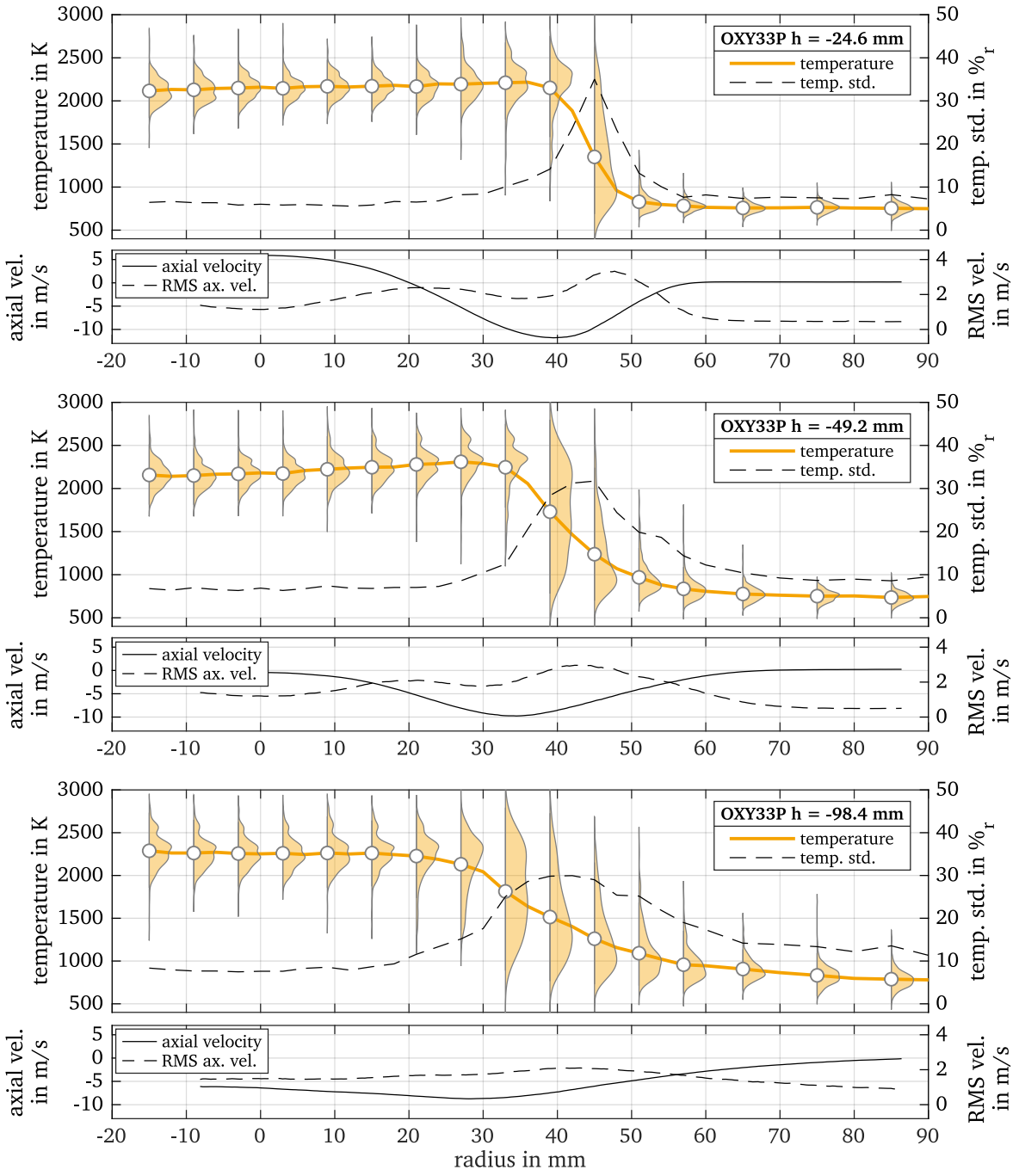

Figure 6.8: Gas temperature profiles of single-phase operation condition OXY33P at the heights $h = -24.6\,\text{mm}$, $-49.2\,\text{mm}$, and $-98.4\,\text{mm}$. The mean temperature is shown as solid line and the probability density function (PDF) of every second measurement point is illustrated. PDFs are multiplied by 10 for good visibility. The relative standard deviation of the gas temperature is plotted as dashed line. Axial velocity profiles and the respective RMS values are provided for comparison and are taken from Section 5. Figure adapted from [3].

The thermochemical state is examined for the location at the center of the IRZ ($h = -24.6\,\text{mm}$, $r = 0\,\text{mm}$) and for a location within the mixing zone ($h = -49.2\,\text{mm}$, $r = 39\,\text{mm}$). The results are illustrated in Figure 6.9.

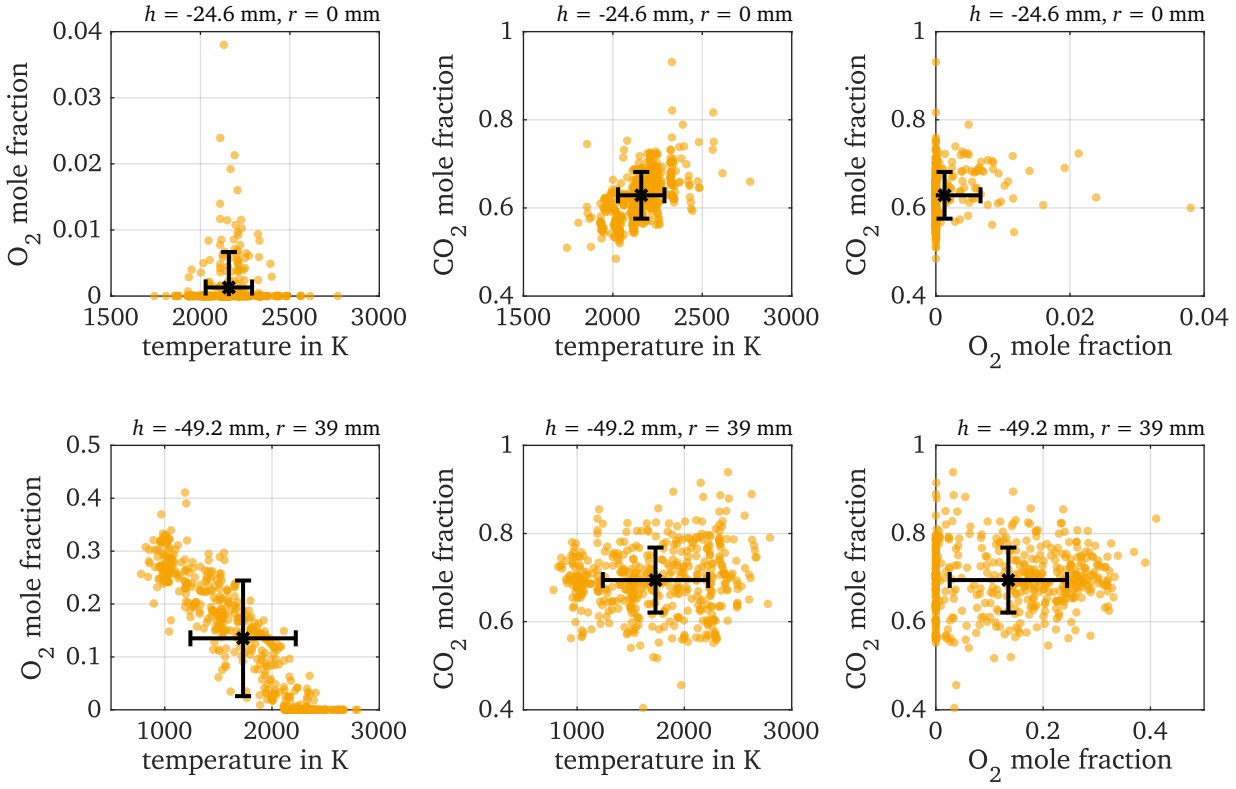

Figure 6.9: Thermochemical state for two locations of single-phase operation condition OXY33P. Each yellow point represents a single measurement. Mean values are shown as black squares and standard deviations are shown as error bars. Upper row: Location: $h = -24.6\,\mathrm{mm}$, $r = 0\,\mathrm{mm}$. Bottom row: Location: $h = -49.2\,\mathrm{mm}$, $r = 39\,\mathrm{mm}$. Please note the different scales of the top and bottom row.

The thermochemical state of the location within the IRZ yields a mean O_2 mole fraction of nearly 0 and a mean CO_2 mole fraction of 0.63. The evaluated O_2 and CO_2 mole fractions are spread over a rather narrow mole fraction range, and the relative standard deviation of the CO_2 mole fraction of 9% is only slightly above the determined measurement precision of approximately 5%. The distribution of the individual measurements within the O_2-T, CO_2-T, and O_2-CO_2 state spaces is uniform. It is concluded that the thermochemical state in the center of the IRZ is almost constant with time.

The location within the mixing zone at $h = -49.2\,\mathrm{mm}$ and $r = 39\,\mathrm{mm}$ exhibits a mean O_2 mole fraction of 0.14 and a mean CO_2 mole fraction of 0.69. Examination of the O_2-T state space reveals a linear relationship between gas temperature and O_2 mole fraction, with decreasing O_2 mole fractions with increasing temperature. The individual measurements are evenly distributed over the entire temperature range, indicating the presence of all thermochemical statesbetween the high temperature plateau region of the IRZ and the thermochemical state of the ORZ. The CO_2-T and O_2-CO_2 state spaces exhibit no clear correlations, while the distribution of individual measurements is broad.

6.3.2.2 Influence of oxygen concentration on the thermochemical state

Oxy-fuel operation conditions with four different O_2 concentrations (27 vol.%, 30 vol.%, 33 vol.%, and 36 vol.%) and a comparable air operation condition were investigated. The evaluated radial mean gas temperature profiles are illustrated in Figure 6.10.

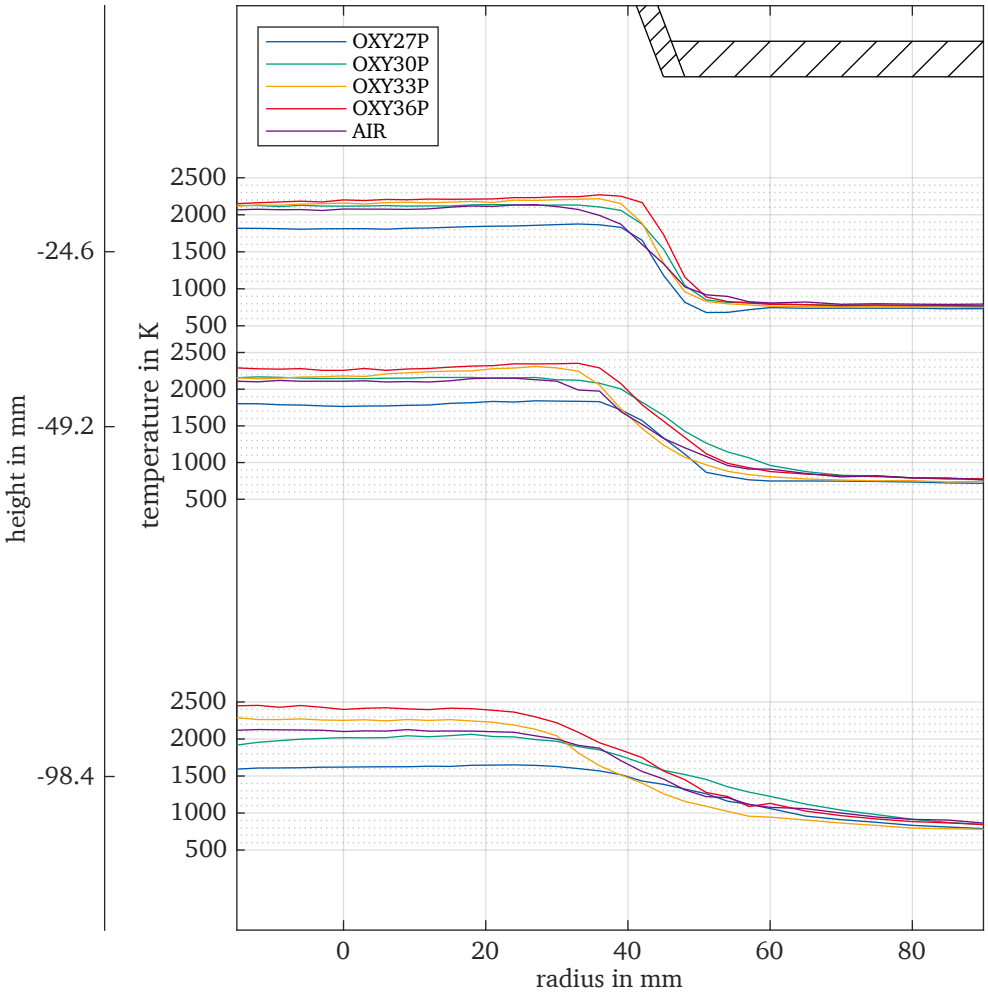

Figure 6.10: Mean gas temperature profiles of all single-phase operation conditions at the heights $h = -24.6\,\text{mm}$, $-49.2\,\text{mm}$, and $-98.4\,\text{mm}$. The SFC geometry is partially shown (quarl end and dump plane).

All operation conditions show similar radial gas temperature profiles, while operation condition OXY27P exhibits a significantly lower temperature around 1800 K within the IRZ and about 1600 K in the center downstream the IRZ compared to the other conditions. Within the IRZ the gas temperatures of operation conditions with O_2 concentrations between 30 vol.% and 36 vol.% are very similar and increase only slightly with increasing O_2 concentration in the oxy-fuel atmosphere, from approximately 2050 K for OXY30P to about 2200 K for OXY36P. Downstream the IRZ, the gas temperature difference enlarges, probably due to the increased thermal power of operation conditions with higher O_2 concentrations.

The temperature gradient towards the ORZ is steeper for OXY33P and OXY36P compared to OXY27P and OXY30P. This effect is mainly attributed to the altered flow fields due to the effect of the side flame in the intermediate zone between the primary and secondary inlet, as discussed in detail in Section 5.3.1.2.

The comparable air operation condition exhibits slightly lower temperatures within the IRZ than OXY30P, OXY33P, and OXY36P. In the center downstream the IRZ, the gas temperature of operation condition AIR is between OXY30P and OXY33P, while the thermal power of operation condition AIR is 30% lower compared to OXY30P and 37% lower compared to OXY33P.

The radial profiles of the mean O_2 and CO_2 mole fractions are presented in Figure 6.11. Measurements at high radial positions required the use of high ND filters to prevent saturation caused by the strong CO_2 signals at low temperatures. This resulted in low signal-to-noise ratios in the spectral region of the Q-branch transitions of O_2. As discussed in Section 6.3.1, this results in significantly lower accuracies in the determination of O_2 and CO_2 mole fractions, while the gas temperature evaluation is satisfactory. The erroneous O_2 and CO_2 mole fractions were removed during post-processing based on signal-to-noise ratios within the spectral range of the Q-branch transitions of O_2.

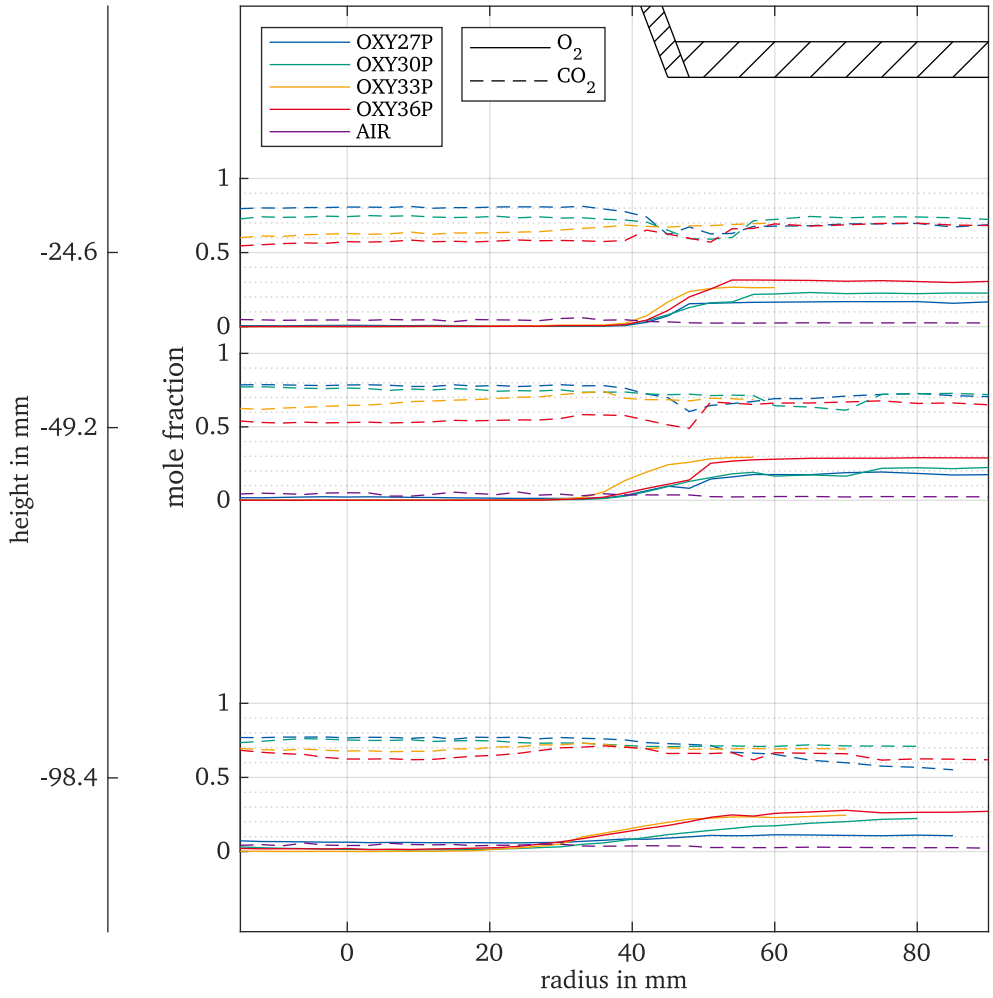

Figure 6.11: Profiles of mean mole fractions of O_2 and CO_2 for all single-phase operation conditions at the heights $h = -24.6$ mm, -49.2 mm, and -98.4 mm. Only mean mole fractions of CO_2 are shown for operation condition AIR. O_2 and CO_2 mole fraction values at high radial positions are partly erroneous due to the choice of ND filter and the low gas temperatures and are removed. The SFC geometry is partially shown (quarl end and dump plane).

As expected, the IRZ is dominated by hot exhaust gases and the O_2 mole fractions are close to 0. The gas mixture within the IRZ shows a strong dependence on the O_2 concentration within the oxy-fuel atmosphere with significantly increased CO_2 mole fractions for operation conditions with lower O_2 concentrations. The level of the O_2 mole fraction rises in the region of the steep temperature gradient toward the ORZ to values close to the set O_2 mole fraction within the respective oxidizer for each operation condition. Downstream the IRZ at the height $h = -98.4$ mm, the CO_2 mole fractions of the oxy-fuel operation conditions converge, while the O_2 mole fractions are still close to 0, despite for OXY27P.

The CO_2 mole fraction under air combustion is between 0.02 and 0.06, with higher CO_2 mole fractions observed close to the center of the SFC. This agrees well with equilibrium calculations which estimate a global CO_2 mole fraction of 0.04, while the CO_2 mole fraction is 0.08 considering only primary and secondary flows.

The distribution of individual measurements and the thermochemical states of all oxy-fuel single phase operation conditions are similar to those of OXY33P discussed in Section 6.3.2.1. A small difference exists in the scatter of the individual measurements within the mixing region for OXY27P and OXY30P. The radial temperature profile of operation condition OXY27P at the height $h = -49.2\,\text{mm}$ along with the O_2-T, CO_2-T, and O_2-CO_2 state spaces for a location within the mixing region ($h = -49.2\,\text{mm}$, $r = 45\,\text{mm}$) is depicted in Figure 6.12.

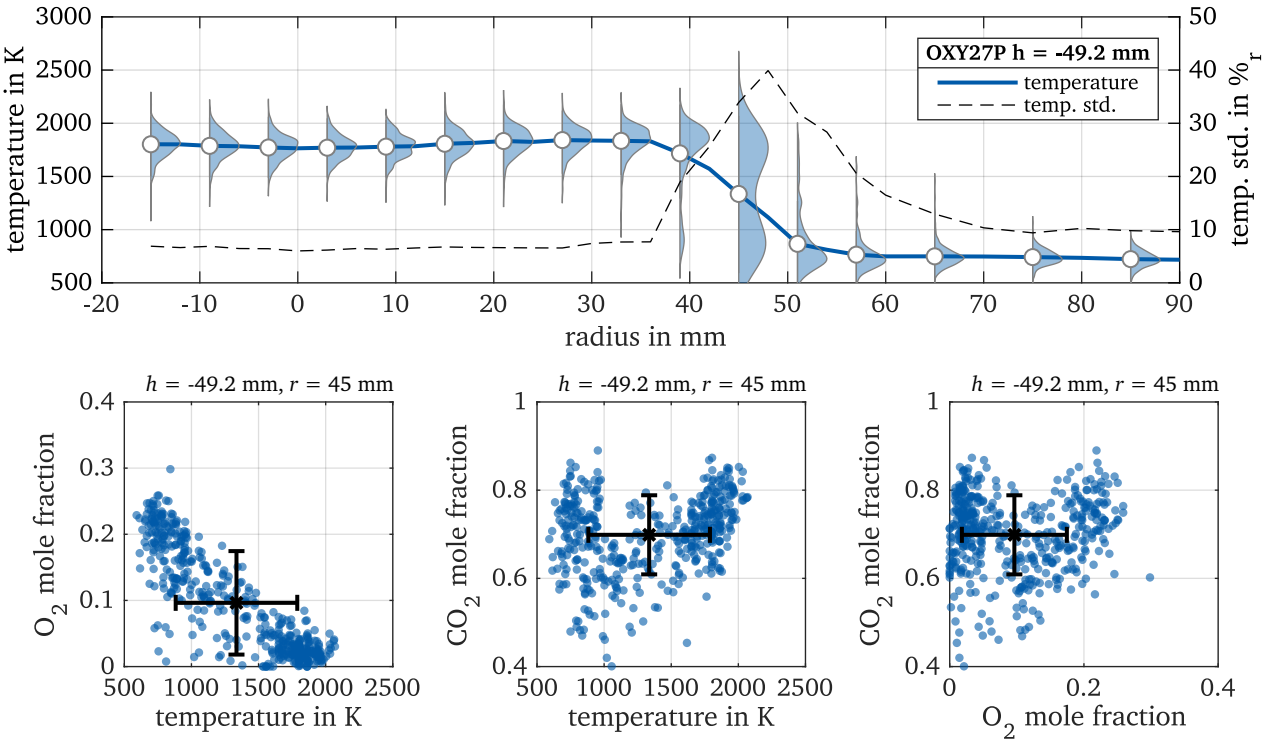

Figure 6.12: Gas temperature profile and thermochemical state of operation condition OXY27P. Top: Gas temperature profile at the height $h = -49.2\,\text{mm}$. The mean temperature is shown as solid line, while the probability density function (PDF) of every second measurement point is presented as a violin plot. PDFs are normalized for good visibility. The relative standard deviation of the gas temperature is plotted as dashed line. Bottom: Thermochemical state for the location: $h = -49.2\,\text{mm}$, $r = 45\,\text{mm}$. Each blue point represents a single measurement. Mean values are shown as black squares and standard deviations are shown as error bars.

In the center of the mixing zone of operation condition OXY27P, a bimodal distribution of thermochemical states is obtained. Most of the recorded spectra can be attributed either to the hot flue gas region in the center or to the ORZ region with low temperatures and high O_2 mole fractions. The CO_2 mole fractions are equal in both states, while lower CO_2 mole fractions are evaluated in intermediate states between the two peaks of the temperature PDF. The observed bimodal distribution can be attributed to the altered flow field between the operation conditions OXY27P and OXY30P and the operation conditions OXY33P and OXY36P. This change is caused by the side flames within the quarl and reduced velocities in the main flow downwards, possibly leading to less optimal mixing between the ORZ and the main flow downwards.

6.3.3 Gas-assisted solid fuel combustion

Similar to Section 6.3.2, the central two-phase operation condition with walnut shells (WS), OXY33P-WS, is analyzed first. Subsequently, the influence of the oxygen concentration in the oxy-fuel atmospheres, the type of atmosphere (air/oxy-fuel), and the type of biomass (WS/BW) are examined.

For all gas-assisted solid fuel combustion cases, CARS measurements were performed at the heights $h = -24.6\,\text{mm}$, $-49.2\,\text{mm}$, and $-98.4\,\text{mm}$. At each height the SFC was traversed to record radial CARS spectra in steps of 6 mm in the range between $r = -15\,\text{mm}$ and 60 mm and in steps of 10 mm between $r = 60\,\text{mm}$ and 90 mm. For each position, 600 to 1000 CARS spectra were recorded to account for spectra containing laser-induced breakdowns. This ensured that at least 300 spectra were processed for each position, while most positions had 500 to 600 spectra that could be evaluated.

6.3.3.1 Thermochemical state of operation condition OXY33P-WS

Radial mean gas temperature profiles are shown in Figure 6.13 for the heights $h = -24.6\,\text{mm}$, $-49.2\,\text{mm}$, and $-98.4\,\text{mm}$ along with the respective fraction of good spectra at each measurement position. Spectra removed during processing and classified as 'not good' suffered mainly from laser-induced breakdowns, while saturation or low signal-to-noise ratios played a minor role as discussed in Section 6.2.2.1. However, the harsh experimental conditions of gas-assisted solid fuel combustion and the high thermal radiation of the test rig resulted in slightly unstable temperature conditions of the laser setup, leading to lower pulse energies over time. This in turn reduced the signal-to-noise ratio of the recorded spectra. To avoid a bias of the evaluated temperatures and mole fractions, data from measurement positions where more than 10% of all spectra have signal-to-noise ratios too low to be processed were removed.

The radial mean gas temperature profile at $h = -24.6\,\text{mm}$ exhibits a temperature drop to about 1700 K within the IRZ. Within the zone of the main flow downwards, surrounding the IRZ, the gas temperature rises and is at the same level as the gas temperature of the single-phase operation condition OXY33P. The fraction of good spectra is reduced by laser-induced breakdown due to particles within the probe volume, mostly within a radius of 20 mm around the center. In this region, 20% to 35% of all recorded spectra suffered from breakdown. These observations suggest that the IRZ is predominantly influenced by the solid fuel particles, which heat up and release volatiles into an environment with a low O_2 concentration. In contrast, the main flow downwards is dominated by methane and volatile combustion. The analysis of particle occurrences in Section 5.3.2.1 support this statement.

The temperature gradient towards the ORZ is flattened for gas-assisted solid fuel combustion compared to single-phase combustion, and the temperature level within the ORZ is about 250 K higher, caused by the increase in total thermal power.

Further downstream, at heights $h = -49.2\,\text{mm}$ and $h = -98.4\,\text{mm}$, the gas temperature of the central zone is between 1500 K and 2000 K. The highest radial gas temperatures are obtained at the radial position of about $r = 40\,\text{mm}$. In contrast to OXY33P, the steep temperature gradient towards the ORZ is expanded radially outward, flattened, and obtains a reduced absolute temperature difference between the temperature level in the center and in the ORZ.

The gas temperature distribution of the individual measurements is similar to that of the single-phase operation condition OXY33P and is further examined in the O_2-T, CO_2-T, and O_2-CO_2 state spaces, which are presented in Figure 6.14.

The state spaces are analyzed for a position within the IRZ ($h = -24.6\,\text{mm}$, $r = 3\,\text{mm}$) and a position within the mixing zone ($h = -49.2\,\text{mm}$, $r = 45\,\text{mm}$).

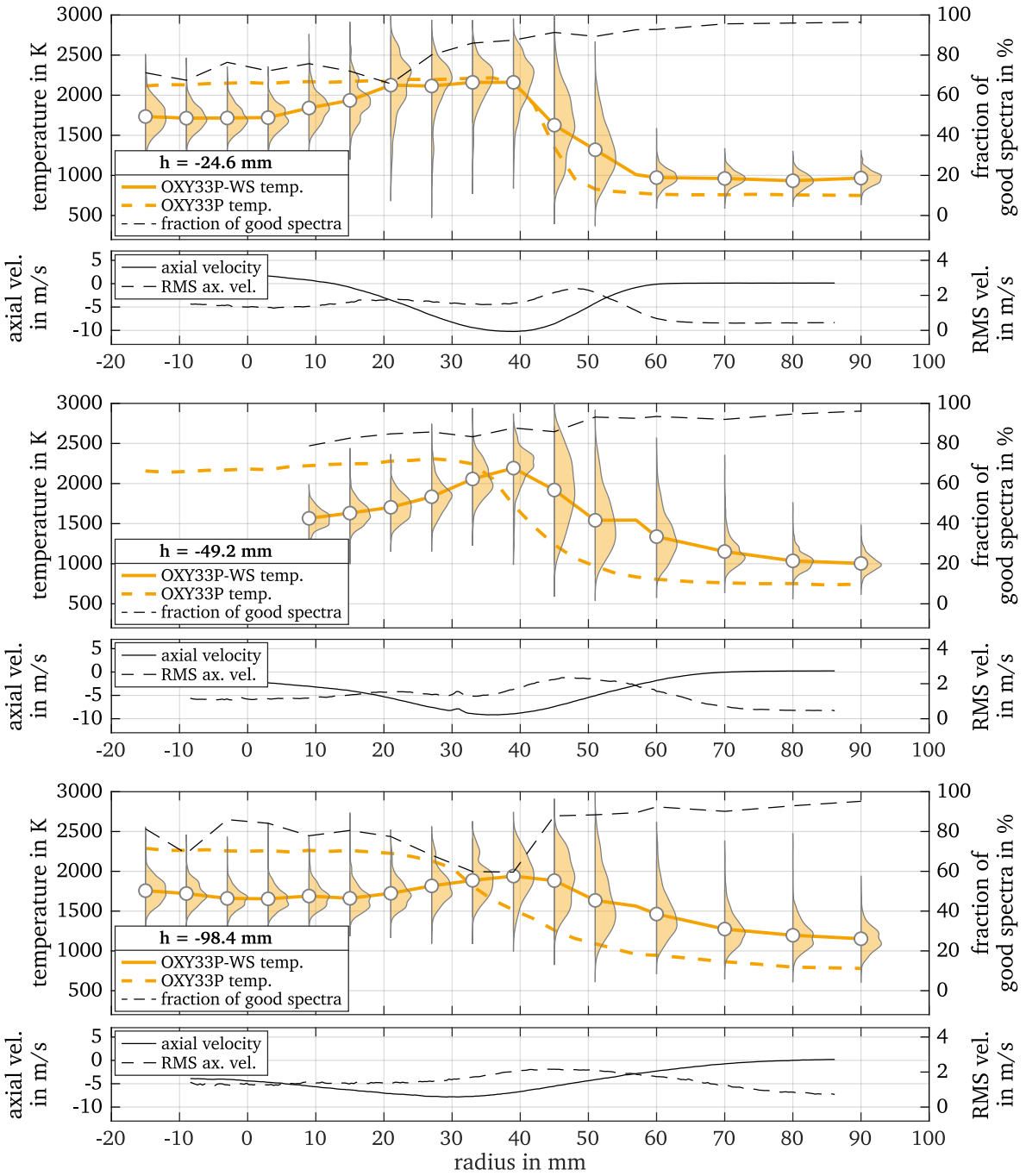

Figure 6.13: Gas temperature profiles of the two-phase operation condition OXY33P-WS at heights $h = -24.6\,\text{mm}$, $-49.2\,\text{mm}$, and $-98.4\,\text{mm}$. The mean temperature is shown as a solid line and the PDF is presented. PDFs are multiplied by 10 for good visibility. The mean gas temperature of OXY33P is depicted for comparison. The fraction of evaluated good spectra is shown as a black dashed line. Measurements in the center at $h = -49.2\,\text{mm}$ have been removed due to low signal-to-noise ratios. Axial velocity profiles and the respective RMS values are provided for comparison and are taken from Section 5. Figure adapted from [3].

The location within the IRZ exhibits a narrow distribution of individual measurements with a mean gas temperature of 1720 K (relative standard deviation: 8%), an O_2 mole fraction close to 0, and a mean CO_2 mole fraction of 0.45 (relative standard deviation: 12%). Compared to the measurement preci-

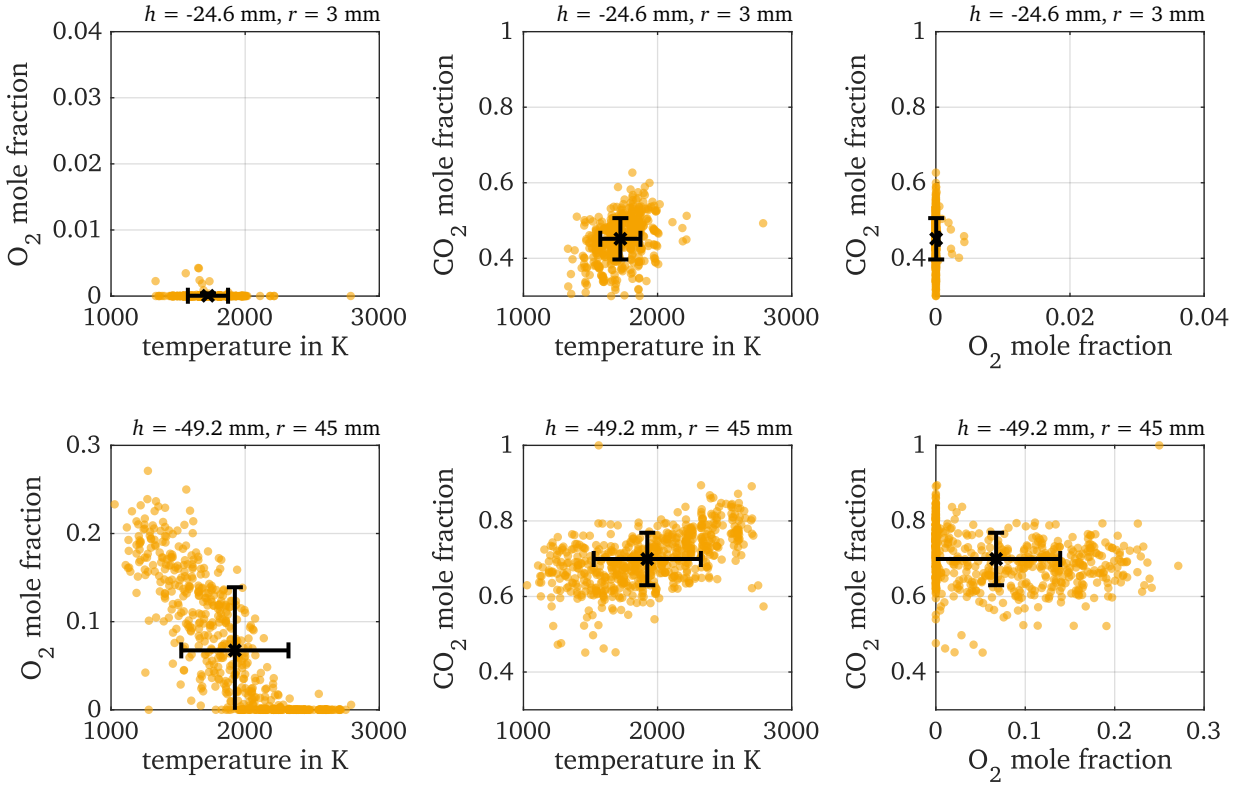

Figure 6.14: Thermochemical state for two locations of two-phase operation condition OXY33P-WS. Each yellow point represents a single measurement. Mean values are shown as black squares and standard deviations are shown as error bars. Upper row: Location: $h = -24.6\,\mathrm{mm}$, $r = 3\,\mathrm{mm}$. Bottom row: Location: $h = -49.2\,\mathrm{mm}$, $r = 45\,\mathrm{mm}$. Please note the different O_2 mole fraction scale of the top and bottom row. Figure adapted from [3].

sion, the relative standard deviations are only slightly larger, indicating almost spatially homogeneous thermochemical states in the center of the IRZ.

The O_2-T, CO_2-T, and O_2-CO_2 state spaces in the mixing zone of OXY33P-WS reveal similar phenomena as the investigated location within the mixing zone of OXY33P. The O_2-T state space reveals also a linear relationship between gas temperature and O_2 mole fraction, while the absolute O_2 mole fraction is decreased from approximately 0.3 in the ORZ of OXY33P to around 0.2 in the ORZ of OXY33P-WS. The CO_2-T and O_2-CO_2 state spaces exhibit no clear correlations, while the distribution of individual measurements is broad.

6.3.3.2 Influence of oxygen concentration and biomass type on gas-assisted solid fuel combustion

Walnut shell (WS) particles were added to all single-phase operation conditions, including four different oxy-fuel conditions with O_2 concentrations of 27 vol.%, 30 vol.%, 33 vol.%, and 36 vol.% and one comparable operation condition in air. Additionally, beech wood (BW) particles were added to the operation condition with 33 vol.% O_2. The radial mean gas temperature profiles of all gas-assisted solid fuel combustion cases are shown in Figure 6.15.

A significant effect of particles on the gas temperature within the IRZ is observed not only for operation condition OXY33P-WS, but also for OXY36P-WS, AIR-WS, and OXY33P-BW. In contrast, the operation conditions OXY27P-WS and OXY30P-WS obtain higher gas temperatures within the IRZ,

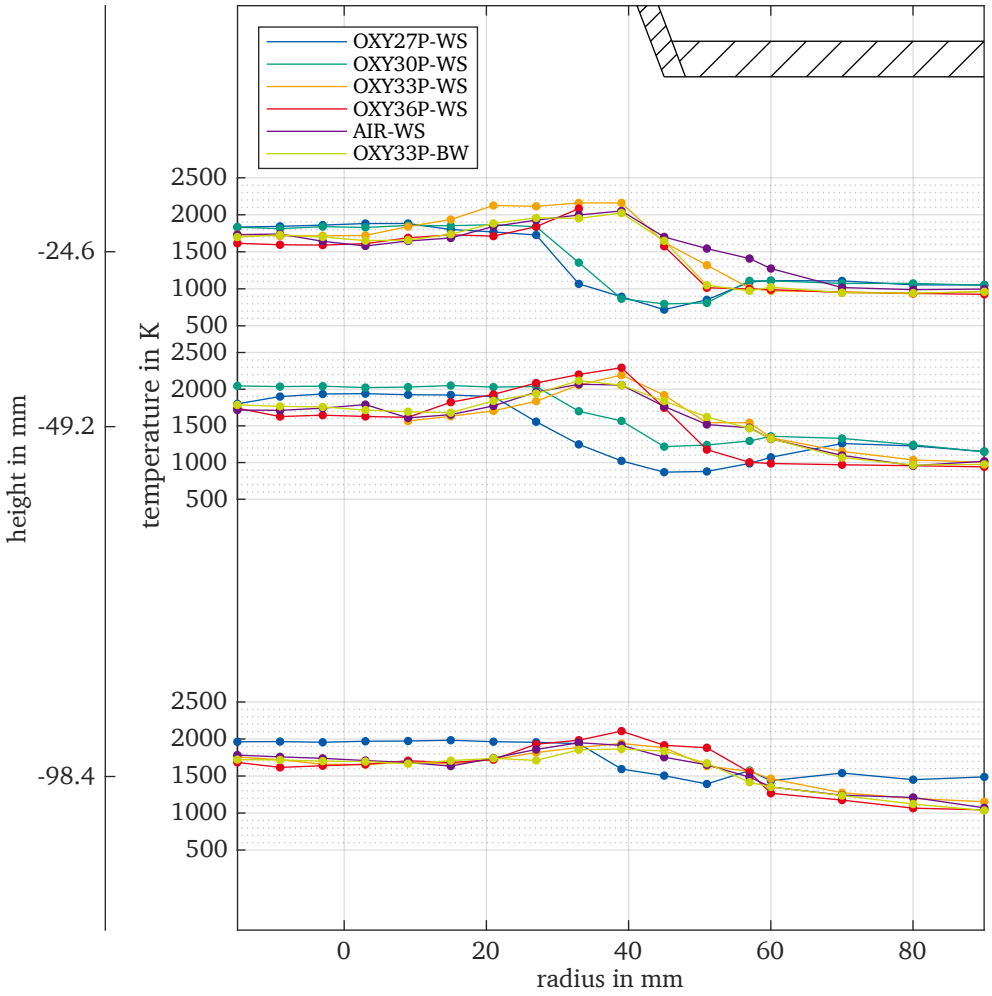

Figure 6.15: Mean gas temperature profiles of all two-phase operation conditions with walnut shells (WS) and OXY33P with beech wood (BW) at the heights $h = -24.6\,\text{mm}$, $-49.2\,\text{mm}$, and $-98.4\,\text{mm}$. The SFC geometry is partially shown (quarl end and dump plane). Missing data points have been removed due to low signal-to-noise ratios.

which is probably due to the significantly enlarged areas of the respective IRZ (refer to Figure 5.18). While the operation conditions OXY33P-WS, OXY36P-WS, AIR-WS, and OXY33P-BW exhibit a temperature maximum within the main flow downwards at $h = -24.6\,\text{mm}$, OXY27P-WS and OXY30P-WS show a temperature minimum below 1000 K. The combustion zone of OXY27P-WS and OXY30P-WS is displaced downstream due to particle heating and volatile release, as already discussed in Section 5.3.3.

Contrary to expectations, the gas temperatures inside the ORZ are highest for the operation conditions OXY27P-WS and OXY30P-WS. This phenomenon can be attributed to the different structure of the flow fields of these cases, leading to a flame expansion towards the combustor walls below $h = -100\,\text{mm}$ (refer to Figure 5.12).

The evaluation of the O_2 and CO_2 mole fractions from gas-assisted solid fuel combustion is shown in Figure 6.16.

The adjusted background subtraction for CARS spectra recorded in solid fuel combustion is expected to be less accurate than the accuracy determined in Section 6.3.1 due to the strong and fluctuating background signals and the strong relationship between the intensity level of the CARS spectra and

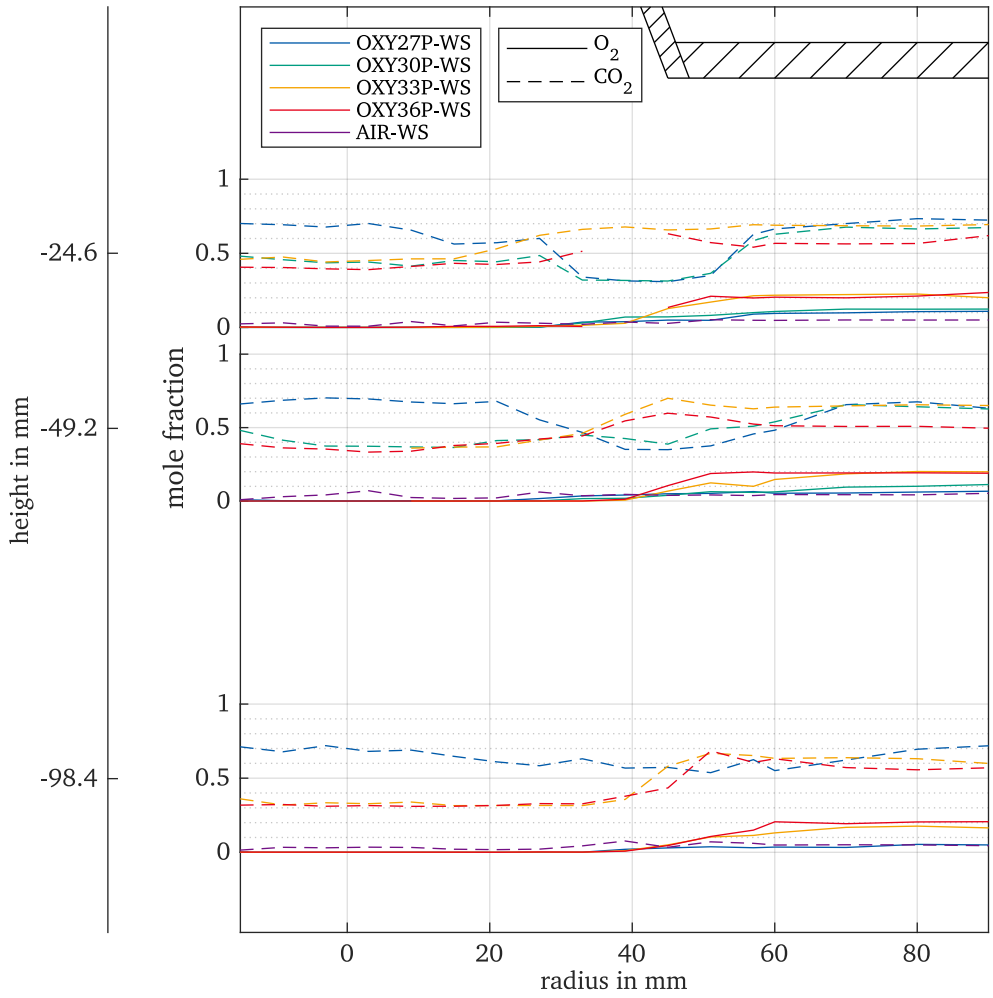

Figure 6.16: Profiles of mean mole fractions of O_2 and CO_2 for all two-phase operation conditions with walnut shells (WS) at the heights $h = -24.6$ mm, -49.2 mm, and -98.4 mm. Only mean mole fractions of CO_2 is shown for operation condition AIR-WS. The SFC geometry is partially shown (quarl end and dump plane). Missing data points have been removed due to low signal-to-noise ratios.

the evaluated mole fractions. However, the accuracy of the mole fractions obtained by CARS in solid fuel combustion could not be quantified in this investigation.

The O_2 and CO_2 mole fractions determined are consistent with the results discussed from the mean gas temperature profiles. The O_2 mole fractions within the ORZ are lower than those obtained for single-phase combustion, indicating an interaction between the tertiary inflow and the solid fuel particles prior to recirculation. The O_2 mole fractions are particularly low for the operation conditions OXY27P-WS and OXY30P-WS due to the altered flow fields (refer to Section 5.3.3).

A further discussion of the O_2 and CO_2 mole fractions, especially in the main flow downwards and in the IRZ where strong and fluctuating background signals occurred, is not made due to the unknown accuracies. The O_2 and CO_2 mole fractions in the center of the combustor, shown in Figure 6.16, are presented for completeness.

6.3.4 Comparison of gas temperature measurement techniques: CARS and TAS

In this thesis, two different laser-based measurement techniques were used to estimate gas phase temperatures during combustion: Tomographic absorption spectroscopy (TAS) and coherent anti-Stokes Raman spectroscopy (CARS). Both techniques require considerable experimental effort. In this section, a comparison is made regarding the experimental setups and the respective evaluated gas temperatures for the operation conditions OXY33P and OXY33P-WS.

TAS is based on the line-of-sight measurement technique of tunable diode laser absorption spectroscopy (TDLAS) and implements a multiple beam arrangement to allow tomographic reconstruction of two-dimensional mean temperature fields. On the other hand, CARS is a point measurement technique and probes the population of rotational and vibrational states of specific molecules. Both techniques evaluate temperatures and mole fractions based on spectral fitting algorithms. While the applied TAS setup is based on the absorption of H_2O and CO_2, CARS probes O_2, CO_2, and N_2.

The spatial and temporal resolution of the two techniques differ strongly. While CARS records spectra within a probe volume of 40 x 50 x 700 µm³ and a temporal resolution of 8.1 ns, TAS evaluates the gas temperatures within a plane with a vertical spatial resolution decreasing with distance from the center up to 10 mm. The plane is discretized into concentric rings of 0.5 mm within the tertiary flow and with triangles in the outer region. The resulting underdetermined equation system is solved in combination with a first-order Tikhonov regularization prior that reflects the smoothness of the temperature field. Due to spectra averaging within the processing of TAS, the temporal resolution of the setup used is 30 s. In comparison, to record a radial gas temperature profile with CARS, several recorded spectra at different radial positions are required. Given the selected procedure described in this chapter, a radial gas temperature profile was recorded within 40 min to 120 min depending on the operation condition.

A comparison of the gas temperatures evaluated by TAS and CARS for the single-phase operation condition OXY33P and the two-phase operation condition OXY33P-WS is shown in Figure 6.17. Due to the different measurement grids, similar heights are compared as indicated.

Differences in the gas temperature profiles of the two measurement techniques are particularly evident in the region of the steep temperature gradient. Here, the first-order Tikhonov regularization prior leads to a smearing effect on the temperature gradient. Also local temperature increases, for example within the radius of $r = 20$ mm to 40 mm at the height $h = -24.6$ mm/-25 mm, cannot be properly covered by the tomographic reconstruction. In cases where the temperature gradients are rather small ($h = -98.4$ mm/-100 mm), the gas temperature profiles determined by TAS and CARS are similar. The evaluated gas temperatures in the center of the combustor and in the ORZ are also similar.

In summary, both measurement techniques have their advantages and disadvantages. With CARS, instantaneous gas temperatures can be measured within a small probe volume. A statistical distribution can be derived from multiple measurements at the same location. By traversing, radial gas temperature profiles can be determined with an individual step size and steep temperature gradients can be resolved if the step size is small enough. TAS offers the possibility of the evaluation of two-dimensional gas temperature fields in a short period of time. The entire plane within the SFC is accessible. By traversing in the third direction, measurements of the entire space are possible. The spatial resolution of TAS dependents on the beam arrangement and the number of beams. It turned out that for the resolution of steep temperature gradients more than the 280 beams used are necessary (refer to Section 5.2.2).

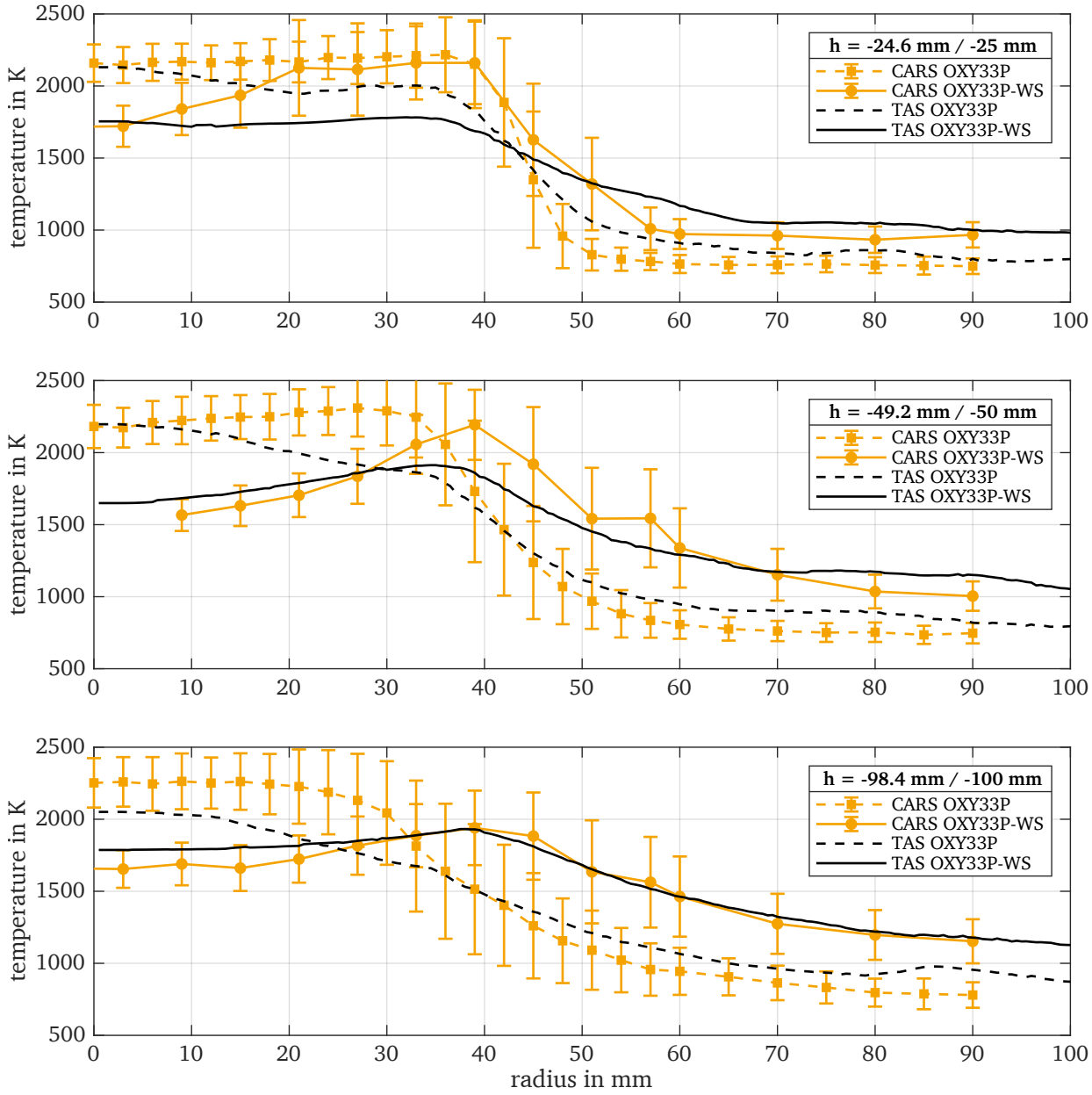

Figure 6.17: Comparison of evaluated gas temperatures with TAS and CARS for the operation conditions OXY33P and OXY33P-WS. The CARS measurement heights $h = -24.6\,\text{mm}$, $-49.2\,\text{mm}$, and $-98.4\,\text{mm}$ are compared against the heights $h = -25\,\text{mm}$, $-50\,\text{mm}$, and $-100\,\text{mm}$ determined with TAS. TAS only evaluates mean gas temperatures, while for CARS measurements mean gas temperatures and standard deviations of the temperature are depicted.

6.4 Conclusion

This study presents a comprehensive analysis of the thermochemical states of oxy-fuel combustion in the near-nozzle region of a gas-assisted solid fuel combustor for single-phase and two-phase reactive flows. To achieve this, a novel O_2-CO_2-CARS approach was successfully implemented and experimentally validated using a flat flame and equilibrium calculations performed with Cantera [130] for high temperatures and gas mixtures of $O_2/CO_2/Ar$ to estimate relative accuracies and precisions at low temperatures. The results show high relative accuracies (below 3%) and high relative precisions (∼5%) for hot gas temperature evaluations. Mole fractions of O_2 and CO_2 are well estimated (rel. accuracy

below 6%) when both species are present in the gas mixture with mole fractions greater than 0.2. CO_2 mole fractions for smaller amounts of O_2 exhibit relative accuracies about 10%. The relative precision of CO_2 mole fractions is approx. 5% for the oxy-fuel atmospheres studied. Investigations under cold conditions showed good estimates of gas temperatures (rel. accuracy below 6%), while CO_2 mole fractions are only well determined (rel. accuracy below 7%) in the presence of significant amounts of O_2.

To compare combustion under oxy-fuel and air atmospheres, an N_2-CO_2-DP-CARS setup was implemented to derive gas temperatures and CO_2 mole fractions of a comparable air operation condition.

To process CARS spectra recorded during pulverized fuel combustion, a special algorithm was developed to remove spectra suffering from laser-induced breakdowns caused by particles within the probe volume. At positions with high particle densities, 20% to 35% of the recorded spectra were affected by optical breakdowns and were removed.

The main findings of the analysis of the thermochemical states of single-phase and two-phase combustion are summarized as follows:

- For both single-phase and two-phase operation conditions, the thermochemical states within the IRZ are almost spatially homogeneous.
- The single-phase operation conditions show gas temperatures close to the respective maximum adiabatic flame temperatures within the main flow downwards, which surrounds the IRZ.
- In gas-assisted solid fuel combustion, the IRZ is predominantly influenced by the solid fuel particles which experience heat up and release volatiles, while the main flow downwards is dominated by the combustion of methane and volatiles.
- A linear relationship between O_2 mole fractions and gas temperature is observed within the mixing zone of the main flow downwards and the ORZ. For oxy-fuel operation conditions with O_2 concentrations of 33 vol.% and 36 vol.%, the individual measurements are uniformly distributed between the states observed in the main flow downwards and within the ORZ. In contrast, a bimodal distribution is obtained for operation conditions with O_2 concentrations of 27 vol.% and 30 vol.%. The bimodal distribution is likely due to the altered flow field, possibly leading to less optimal mixing between the ORZ and the main flow downwards.
- The operation conditions with 27 vol.% and 30 vol.% O_2 concentrations exhibit different radial gas temperature profiles due to the altered flow fields. The two-phase operation conditions OXY27P-WS and OXY30P-WS also show a downstream displacement of the combustion zone.

In addition, a comparison of the laser-based measurement techniques tomographic absorption spectroscopy (TAS) and coherent anti-Stokes Raman spectroscopy (CARS) is performed, revealing the respective advantages and disadvantages of each method.

7 Summary and outlook

7.1 Summary

In this thesis, various advanced optical laser diagnostics were applied to pulverized solid fuel combustion under oxy-fuel conditions to improve our understanding of the complex fluid-mechanical, particle-dynamical, and chemical processes and their interactions. The research object was a solid fuel combustor (SFC), which operates gas-assisted solid fuel flames in the power range up to 70 kW_{th}. The SFC exhibits important characteristics of state-of-the-art combustors and stabilizes a swirl flame. The major challenge was to successfully adapt the various optical laser diagnostics, highly developed for small generic experiments, to the harsh environment of biomass and coal combustion. In particular, the novel O_2-CO_2-CARS approach, its experimental validation, and implementation in pulverized oxy-fuel biomass combustion showed the first CARS measurements in particle-laden reactive flows that go beyond demonstration.

The applied optical laser diagnostics are grouped into three investigations, each analyzing a comprehensive data set in combination with parametric variations. All investigations focused on the near-burner region where the flame is stabilized and several important combustion processes such as particle heating, volatile release, volatile combustion, onset of char combustion, and particle-fluid mixing take place. In addition, the boundary conditions of the studied solid fuel combustor were precisely defined to allow the validation of numerical simulations and to improve models for solid fuel combustion.

The first investigation focused on the analysis of flow dynamics and particle temperatures in the near-burner region under oxy-fuel and air conditions. The applied optical laser diagnostics included PIV, high-speed PTV, and two-color pyrometry to determine the flow field, particle trajectories, gas and particle residence times, particle temperatures, and particle sizes. In the PIV and PTV processing, small gas phase tracers and large particles were separated. The establishment of a side flame and its spatial expansion between the orifices where primary and secondary flows enter the quarl showed a significant influence on the overall flow field and the spatial expansion of the inner recirculation zone (IRZ) of the swirl flame. Observations of particle mixing within the shear layers revealed the formation of particle clusters. Large particles were found to penetrate the IRZ, resulting in a faster heating and earlier volatile release. Additionally, large particles remain in the hot burner region longer than the gas flow, which is beneficial for high burnout rates. Particle temperatures in an oxy-fuel atmosphere with 33 vol.% O_2 showed similar temperatures compared to combustion in air.

In the second investigation, a comprehensive analysis of the influence of oxygen concentration on oxy-fuel combustion in the near-burner region was conducted. Effects on flame stabilization, pollutant formation and the combustion process of biomass particles were investigated. The applied optical laser diagnostics included CH* chemiluminescence imaging, a two-phase PIV/PTV approach, tomographic absorption spectroscopy (TAS), and a quasi-simultaneous laser-induced fluorescence/laser-induced incandescence (LIF/LII) configuration. Measurements of local CH* chemiluminescence intensity, gas and solid phase flow velocities, gas temperatures, and qualitative soot measurements including visualization of polycyclic aromatic hydrocarbon (PAH) occurrence as soot precursors were obtained. As in the first investigation, a strong influence of the side flames on the overall flame structure was

observed. The length of the side flame was found to correlate positively with increasing oxygen concentration in oxy-fuel combustion, leading to a more tightly compacted IRZ at high O_2 concentrations. Accelerated flow velocities in the main flow downwards were observed under oxy-fuel conditions with increasing O_2 concentrations, indicating intensified heat release near the nozzle. Comparing single-phase (methane combustion) to two-phase (gas-assisted solid fuel combustion) operation conditions, a smaller IRZ with lower velocity magnitudes was present in two-phase combustion. For oxy-fuel conditions with O_2 concentrations at 30 vol.% or below, a significant delay in combustion was evident when particles were added, resulting in a downstream displacement of the flame. Analysis of the LII and PAH-LIF signals showed a clear separation between initial PAH occurrences and soot formation, probably due to the significant influence of the local gas composition. It could be concluded that PAHs released from biomass particles during devolatilization do not necessarily transform immediately into soot nanoparticles. Comparison of combustion behavior under oxy-fuel and air conditions showed that solid fuel combustion in an air atmosphere mirrors the flame characteristics of an oxy-fuel condition with an oxygen concentration slightly below 33 vol.% for the solid fuel combustor studied. This highlights the importance of achieving similar adiabatic flame temperatures in both air and oxy-fuel combustion to achieve similar combustion behavior.

The third investigation examined the thermochemical state at different locations in single-phase and two-phase combustion in air and for different O_2 concentrations under oxy-fuel conditions. A novel O_2-CO_2-CARS approach was developed and experimentally validated using a flat flame burner. For the relevant thermochemical states, high relative accuracies and relative precisions of temperature (below 3% / ∼5%) and O_2 and CO_2 mole fractions (below 10% / ∼5%) were determined. In gas-assisted solid fuel flames, spectra with optical breakdowns due to particles within the probe volume were successfully removed. At least 65% of all spectra recorded at a location could be evaluated, even for positions within high particle densities. Thermochemical states within the IRZ were observed to be almost spatially homogeneous for both single-phase and two-phase operation conditions. Gas temperatures close to the respective maximum adiabatic flame temperatures were measured for methane combustion in the main flow downwards. The analysis of gas-assisted biomass combustion showed a predominant particle influence on the IRZ, and a linear relationship between O_2 mole fractions and gas temperature within the mixing zone of the main flow downwards and the outer recirculation zone (ORZ) was observed.

7.2 Outlook

The solid fuel combustor investigated in this thesis has been studied in great detail and results in a unique comprehensive data set for solid fuel combustion under oxy-fuel atmospheres. Its use for validation of numerical studies and model development offers the opportunity to further improve existing numerical approaches.

Despite the large parameter variations performed in this thesis, variations in the type of biomass could provide further insight into the different combustion behaviors, since the composition of biomass can differ greatly. In this thesis (see Chapter 5.3.4) it has been shown that similar particle sizes are essential for such studies in order to explicitly relate the observations to the different fuel compositions. However, providing large amounts of different biomasses with similar particle distributions is challenging.

The advanced optical laser diagnostics developed and adapted in this thesis can be used in the future for measurements on combustors of different scales to determine scale dependent combustion behavior. It is also important to provide similar comprehensive data sets within different combustion chambers to identify effects related to the combustor design.

References

List of own publications

[1] **Schneider, H.**, Valentiner, S., Vorobiev, N., Böhm, B., Schiemann, M., Scherer, V., Kneer, R. and Dreizler, A.: "Investigation on flow dynamics and temperatures of solid fuel particles in a gas-assisted oxy-fuel combustion chamber." In: *Fuel* 286 (2021), p. 119424. DOI: 10.1016/j.fuel.2020.119424 (cit. on pp. 42, 46, 59, 60, 63–71, 78, 83).

[2] **Schneider, H.**, Bonarens, M., Hebel, J., Hardy, H., Emmert, J., Böhm, B., Wagner, S., Kneer, R. and Dreizler, A.: "Combined flow, temperature and soot investigation in oxy-fuel biomass combustion under varying oxygen concentrations using laser-optical diagnostics." In: *Fuel* 362 (2024), p. 130771. DOI: 10.1016/j.fuel.2023.130771 (cit. on pp. 47, 49, 50, 75, 77, 80, 83, 85–93, 96, 97, 99–101).

[3] **Schneider, H.**, Hebel, J., Böhm, B., Kneer, R. and Dreizler, A.: "Rotational-vibrational O2–CO2 coherent anti-Stokes Raman spectroscopy for determination of thermochemical states in oxy-fuel biomass combustion." In: *Proceedings of the Combustion Institute* 40 (2024), p. 105457. DOI: 10.1016/j.proci.2024.105457 (cit. on pp. 105, 109, 112, 113, 116, 122, 123).

[4] Meißner, C., **Schneider, H.**, Sidiropoulos, E., Hölzer, J. I., Heckmann, T., Böhm, B., Dreizler, A. and Seeger, T.: "Investigation on wall and gas temperatures inside a swirled oxy-fuel combustion chamber using thermographic phosphors, O2 rotational and vibrational CARS." In: *Fuel* 289 (2021), p. 119787. DOI: 10.1016/j.fuel.2020.119787 (cit. on pp. 51, 56, 105).

[5] Emmert, J., **Schneider, H.**, Meißner, C., Sidiropoulos, E., Hölzer, J. I., Seeger, T., Böhm, B., Dreizler, A. and Wagner, S.: "Characterization of temperature distributions in a swirled oxy-fuel coal combustor using tomographic absorption spectroscopy with fluctuation modelling." In: *Applications in Energy and Combustion Science* 6 (2021), p. 100025. DOI: 10.1016/j.jaecs.2021.100025 (cit. on pp. 78–80).

[6] Emmert, J., **Schneider, H.**, Böhm, B., Dreizler, A. and Wagner, S.: "Phase-locked absorption tomography for retrieving 5 kHz time-resolved tracer profiles in solid fuel combustion." In: *Applications in Energy and Combustion Science* 12 (2022), p. 100093. DOI: 10.1016/j.jaecs.2022.100093.

[7] Nicolai, H., Kuenne, G., Knappstein, R., **Schneider, H.**, Becker, L. G., Hasse, C., Di Mare, F., Dreizler, A. and Janicka, J.: "Large Eddy Simulation of a laboratory-scale gas-assisted pulverized coal combustion chamber under oxy-fuel atmospheres using tabulated chemistry." In: *Fuel* 272 (2020), p. 117683. DOI: 10.1016/j.fuel.2020.117683 (cit. on p. 69).

[8] Wen, X., Nicolai, H., **Schneider, H.**, Cai, L., Janicka, J., Pitsch, H. and Hasse, C.: "Flamelet LES of a swirl-stabilized multi-stream pulverized coal burner in air and oxy-fuel atmospheres with pollutant formation." In: *Proceedings of the Combustion Institute* 38.3 (2021), pp. 4141–4149. DOI: 10.1016/j.proci.2020.05.061.

[9] Luu, T. D., Shamooni, A., Stein, O. T., Kronenburg, A., Popp, S., Nicolai, H., **Schneider, H.**, Wen, X. and Hasse, C.: "Flame characterisation of gas-assisted pulverised coal combustion using FPV-LES." In: *Proceedings of the Combustion Institute* 39.3 (2023), pp. 3249–3258. DOI: 10.1016/j.proci.2022.07.080.

[10] **Schneider, H.**, Becker, L. G., Kneer, R. and Dreizler, A.: "Visualisierung und Analyse von Gasphasengeschwindigkeit und Partikeltrajektorien in einem gasassistierten Oxyfuel-Staubbrenner." In: *29. Deutscher Flammentag, Bochum, Germany* (2019).

[11] **Schneider, H.**, Becker, L. G., Pielsticker, S., Böhm, B., Kneer, R. and Dreizler, A.: "Experimental investigation and comparison of particle-laden flows in a gas-assisted oxy-coal combustion chamber for reacting and non-reacting conditions." In: *Proceedings of the European Combustion Meeting 2019, Lisbon, Portugal* (2019).

[12] Luu, T. D., Shamooni, A., Stein, O. T., Kronenburg, A., Popp, S., Nicolai, H., **Schneider, H.**, Wen, X. and Hasse, C.: "Analysis of heat transfer effects in flamelet/progress variable LES of gas-assisted pulverised coal flames." In: *30. Deutscher Flammentag, Hannover-Garbsen, Germany* (2021).

[13] Hebel, J., **Schneider, H.**, Böhm, B. and Dreizler, A.: "Particle velocity measurements of gas-assisted iron dust flames in a swirl stabilized combustion chamber." In: *Proceedings of the European Combustion Meeting 2023, Rouen, France* (2023).

[14] Sidiropoulos, E., Meißner, C., Hölzer, J. I., **Schneider, H.**, Dreizler, A. and Seeger, T.: "Determination of temperature profiles on turbulent pulverized solid fuel flames." In: *Proceedings of the European Combustion Meeting 2023, Rouen, France* (2023).

[15] Sidiropoulos, E., Meißner, C., Hölzer, J. I., **Schneider, H.**, Dreizler, A. and Seeger, T.: "Vibrations-CARS Thermometrie an einer optisch zugänglichen Drallbrennkammer für die Oxyfuel-Verbrennung." In: *31. Deutscher Flammentag, Berlin, Germany* (2023).

[16] Richter, M., **Schneider, H.**, Özer, B., Massmeyer, A., Ströhle, J. and Epple, B.: "Untersuchung der Flammenstabilität und thermischen Strahlung in einer 1-MWth-Brennkammer unter Oxyfuel-Bedingungen." In: *31. Deutscher Flammentag, Berlin, Germany* (2023) (cit. on p. 6).

Other references

[17] IEA: *World Energy Outlook 2023*. Ed. by IEA. Paris, France, 2023. URL: https://www.iea.org/reports/world-energy-outlook-2023 (cit. on pp. 1, 2).

[18] IPCC: *Climate Change 2021 – The Physical Science Basis: Contribution to the Sixth Assessment Report of the Intergovernmental Panel on Climate Change*. Ed. by Cambridge University Press, Cambridge, United Kingdom and New York, NY, USA. 2023. DOI: 10.1017/9781009157896. URL: https://www.ipcc.ch/report/ar6/wg1/ (cit. on p. 1).

[19] United Nations: *The Paris Agreement*. Ed. by United Nations Framework Convention on Climate Change. 2016. URL: https://unfccc.int/sites/default/files/resource/parisagreement_publication.pdf (cit. on p. 1).

[20] IEA: *CO2 Emissions in 2022*. Ed. by IEA. Paris, France, 2023. URL: https://www.iea.org/reports/co2-emissions-in-2022 (cit. on pp. 1, 2).

[21] Kemper, J.: "Biomass and carbon dioxide capture and storage: A review." In: *International Journal of Greenhouse Gas Control* 40 (2015), pp. 401–430. DOI: 10.1016/j.ijggc.2015.06.012 (cit. on p. 1).

[22] Shahbaz, M., AlNouss, A., Ghiat, I., Mckay, G., Mackey, H., Elkhalifa, S. and Al-Ansari, T.: "A comprehensive review of biomass based thermochemical conversion technologies integrated with CO2 capture and utilisation within BECCS networks." In: *Resources, Conservation and Recycling* 173 (2021), p. 105734. DOI: 10.1016/j.resconrec.2021.105734 (cit. on p. 1).

[23] Gough, C., Thornley, P., Mander, S., Vaughan, N. and Lea-Langton, A. R.: *Biomass energy with carbon capture and storage (BECCS): Unlocking negative emissions*. Hoboken, NJ: John Wiley & Sons Ltd, 2018 (cit. on p. 1).

[24] Global CCS Institute: *Global Status of CCS 2023: Scaling up through 2030*. Ed. by Global CCS Institute. Melbourne , Australia, 2023 (cit. on p. 2).

[25] Wall, T., Liu, Y., Spero, C., Elliott, L., Khare, S., Rathnam, R., Zeenathal, F., Moghtaderi, B., Buhre, B., Sheng, C., Gupta, R., Yamada, T., Makino, K. and Yu, J.: "An overview on oxyfuel coal combustion—State of the art research and technology development." In: *Chemical Engineering Research and Design* 87.8 (2009), pp. 1003–1016. DOI: 10.1016/j.cherd.2009.02.005 (cit. on pp. 2, 3, 21).

[26] Kanniche, M., Gros-Bonnivard, R., Jaud, P., Valle-Marcos, J., Amann, J.-M. and Bouallou, C.: "Pre-combustion, post-combustion and oxy-combustion in thermal power plant for CO2 capture." In: *Applied Thermal Engineering* 30.1 (2010), pp. 53–62. DOI: 10.1016/j.applthermaleng.2009.05.005 (cit. on p. 2).

[27] Adams, D. M. B. and Davison, J.: *Capturing CO_2*. [Cheltenham, Eng.?]: IEA Greenhouse Gas R & D Programme, 2007 (cit. on p. 2).

[28] Abraham, B. M., Asbury, J. G., Lynch, E. P. and Teotia, A. P.: “Coal-oxygen process provides CO2 for enhanced recovery.” In: *Oil Gas J.; (United States)* Volume: 80:11 (1982) (cit. on p. 2).

[29] Toftegaard, M. B., Brix, J., Jensen, P. A., Glarborg, P. and Jensen, A. D.: “Oxy-fuel combustion of solid fuels.” In: *Progress in Energy and Combustion Science* 36.5 (2010), pp. 581–625. DOI: 10.1016/j.pecs.2010.02.001 (cit. on pp. 3, 21).

[30] Scheffknecht, G., Al-Makhadmeh, L., Schnell, U. and Maier, J.: “Oxy-fuel coal combustion—A review of the current state-of-the-art.” In: *International Journal of Greenhouse Gas Control* 5 (2011), S16–S35. DOI: 10.1016/j.ijggc.2011.05.020 (cit. on pp. 3, 21).

[31] Chen, L., Yong, S. Z. and Ghoniem, A. F.: “Oxy-fuel combustion of pulverized coal: Characterization, fundamentals, stabilization and CFD modeling.” In: *Progress in Energy and Combustion Science* 38.2 (2012), pp. 156–214. DOI: 10.1016/j.pecs.2011.09.003 (cit. on pp. 3, 21, 22).

[32] Stanger, R., Wall, T., Spörl, R., Paneru, M., Grathwohl, S., Weidmann, M., Scheffknecht, G., McDonald, D., Myöhänen, K., Ritvanen, J., Rahiala, S., Hyppänen, T., Mletzko, J., Kather, A. and Santos, S.: “Oxy-fuel combustion for CO2 capture in power plants.” In: *International Journal of Greenhouse Gas Control* 40 (2015), pp. 55–125. DOI: 10.1016/j.ijggc.2015.06.010 (cit. on pp. 3, 21–23).

[33] Bejarano, P. A. and Levendis, Y. A.: “Single-coal-particle combustion in O2/N2 and O2/CO2 environments.” In: *Combustion and Flame* 153.1-2 (2008), pp. 270–287. DOI: 10.1016/j.combustflame.2007.10.022 (cit. on pp. 3, 4, 70).

[34] Khatami, R., Stivers, C., Joshi, K., Levendis, Y. A. and Sarofim, A. F.: “Combustion behavior of single particles from three different coal ranks and from sugar cane bagasse in O2/N2 and O2/CO2 atmospheres.” In: *Combustion and Flame* 159.3 (2012), pp. 1253–1271. DOI: 10.1016/j.combustflame.2011.09.009 (cit. on pp. 3, 4).

[35] Khatami, R., Stivers, C. and Levendis, Y. A.: “Ignition characteristics of single coal particles from three different ranks in O2/N2 and O2/CO2 atmospheres.” In: *Combustion and Flame* 159.12 (2012), pp. 3554–3568. DOI: 10.1016/j.combustflame.2012.06.019 (cit. on pp. 3, 4).

[36] Maffei, T., Khatami, R., Pierucci, S., Faravelli, T., Ranzi, E. and Levendis, Y. A.: “Experimental and modeling study of single coal particle combustion in O2/N2 and Oxy-fuel (O2/CO2) atmospheres.” In: *Combustion and Flame* 160.11 (2013), pp. 2559–2572. DOI: 10.1016/j.combustflame.2013.06.002 (cit. on pp. 3, 4).

[37] Riaza, J., Khatami, R., Levendis, Y. A., Álvarez, L., Gil, M. V., Pevida, C., Rubiera, F. and Pis, J. J.: “Combustion of single biomass particles in air and in oxy-fuel conditions.” In: *Biomass and Bioenergy* 64 (2014), pp. 162–174. DOI: 10.1016/j.biombioe.2014.03.018 (cit. on pp. 3, 4).

[38] Riaza, J., Khatami, R., Levendis, Y. A., Álvarez, L., Gil, M. V., Pevida, C., Rubiera, F. and Pis, J. J.: “Single particle ignition and combustion of anthracite, semi-anthracite and bituminous coals in air and simulated oxy-fuel conditions.” In: *Combustion and Flame* 161.4 (2014), pp. 1096–1108. DOI: 10.1016/j.combustflame.2013.10.004 (cit. on pp. 3, 4).

[39] Khatami, R., Levendis, Y. A. and Delichatsios, M. A.: “Soot loading, temperature and size of single coal particle envelope flames in conventional- and oxy-combustion conditions (O2/N2 and O2/CO2).” In: *Combustion and Flame* 162.6 (2015), pp. 2508–2517. DOI: 10.1016/j.combustflame.2015.02.020 (cit. on pp. 3, 4).

[40] Schiemann, M., Scherer, V. and Wirtz, S.: “Optical Coal Particle Temperature Measurement under Oxy–Fuel Conditions: Measurement Methodology and Initial Results.” In: *Chemical Engineering & Technology* 32.12 (2009), pp. 2000–2004. DOI: 10.1002/ceat.200900354 (cit. on pp. 3, 4).

[41] Vorobiev, N., Valentiner, S., Schiemann, M. and Scherer, V.: “Comprehensive Data Set of Single Particle Combustion under Oxy-fuel Conditions, Part I: Measurement Technique.” In: *Combustion Science and Technology* 193.14 (2021), pp. 2423–2444. DOI: 10.1080/00102202.2020.1743696 (cit. on pp. 3, 4, 62).

[42] Vorobiev, N., Valentiner, S., Schiemann, M. and Scherer, V.: “Comprehensive Data Set of Single Particle Combustion under Oxy-fuel Conditions, Part II: Data Set.” In: *Combustion Science and Technology* 193.15 (2021), pp. 2643–2658. DOI: 10.1080/00102202.2020.1754207 (cit. on pp. 3, 4).

[43] Tarlinski, D., Geschwindner, C., Li, T., Böhm, B. and Schiemann, M.: “Particle temperature and composition measurements in the ignition phase of single coal particles and particle groups under conventional and oxy-fuel atmospheres.” In: *Fuel* 332 (2023), p. 125894. DOI: 10.1016/j.fuel.2022.125894 (cit. on pp. 3, 4).

[44] Molina, A. and Shaddix, C. R.: “Ignition and devolatilization of pulverized bituminous coal particles during oxygen/carbon dioxide coal combustion.” In: *Proceedings of the Combustion Institute* 31.2 (2007), pp. 1905–1912. DOI: 10.1016/j.proci.2006.08.102 (cit. on pp. 3, 4).

[45] Shaddix, C. R. and Molina, A.: “Particle imaging of ignition and devolatilization of pulverized coal during oxy-fuel combustion.” In: *Proceedings of the Combustion Institute* 32.2 (2009), pp. 2091–2098. DOI: 10.1016/j.proci.2008.06.157 (cit. on pp. 3, 4).

[46] Liu, Y., Geier, M., Molina, A. and Shaddix, C. R.: “Pulverized coal stream ignition delay under conventional and oxy-fuel combustion conditions.” In: *International Journal of Greenhouse Gas Control* 5 (2011), S36–S46. DOI: 10.1016/j.ijggc.2011.05.028 (cit. on pp. 3, 4).

[47] Li, T., Farmand, P., Geschwindner, C., Greifenstein, M., Köser, J., Schumann, C., Attili, A., Pitsch, H., Dreizler, A. and Böhm, B.: “Homogeneous ignition and volatile combustion of single solid fuel particles in air and oxy-fuel conditions.” In: *Fuel* 291 (2021), p. 120101. DOI: 10.1016/j.fuel.2020.120101 (cit. on pp. 3, 4, 22).

[48] Li, T., Geschwindner, C., Dreizler, A. and Böhm, B.: “Particle-resolved optical diagnostics of solid fuel combustion for clean power generation: a review.” In: *Measurement Science and Technology* 34.12 (2023), p. 122001. DOI: 10.1088/1361-6501/acef49 (cit. on pp. 3, 4).

[49] Moroń, W. and Rybak, W.: “Ignition behaviour and flame stability of different ranks coals in oxy fuel atmosphere.” In: *Fuel* 161 (2015), pp. 174–181. DOI: 10.1016/j.fuel.2015.08.065 (cit. on pp. 3, 4).

[50] Lei, K., Ye, B., Cao, J., Zhang, R. and Liu, D.: “Combustion Characteristics of Single Particles from Bituminous Coal and Pine Sawdust in O2/N2, O2/CO2, and O2/H2O Atmospheres.” In: *Energies* 10.11 (2017), p. 1695. DOI: 10.3390/en10111695 (cit. on pp. 3, 4).

[51] Zhang, L., Binner, E., Qiao, Y. and Li, C.-Z.: “In situ diagnostics of Victorian brown coal combustion in O2/N2 and O2/CO2 mixtures in drop-tube furnace.” In: *Fuel* 89.10 (2010), pp. 2703–2712. DOI: 10.1016/j.fuel.2010.04.020 (cit. on pp. 3, 4).

[52] Kim, Y.-G., Kim, J.-D., Lee, B.-H., Song, J.-H., Chang, Y.-J. and Jeon, C.-H.: “Experimental Investigation into Combustion Characteristics of Two Sub-bituminous Coals in O 2 /N 2 and O 2 /CO 2 Environments.” In: *Energy & Fuels* 24.11 (2010), pp. 6034–6040. DOI: 10.1021/ef100978n (cit. on pp. 3, 4).

[53] Yuan, Y., Li, S., Xu, Y. and Yao, Q.: “Experimental and theoretical analyses on ignition and surface temperature of dispersed coal particles in O 2 /N 2 and O 2 /CO 2 ambients.” In: *Fuel* 201 (2017), pp. 93–98. DOI: 10.1016/j.fuel.2016.09.079 (cit. on pp. 3, 4).

[54] Xu, Y., Li, S., Yao, Q. and Yuan, Y.: “Investigation of steam effect on ignition of dispersed coal particles in O2/N2 and O2/CO2 ambiences.” In: *Fuel* 233 (2018), pp. 388–395. DOI: 10.1016/j.fuel.2018.06.047 (cit. on pp. 3, 4).

[55] Prationo, W. and Zhang, L.: “Influence of steam on ignition of Victorian brown coal particle stream in oxy-fuel combustion: In-situ diagnosis and transient ignition modelling.” In: *Fuel* 181 (2016), pp. 1203–1213. DOI: 10.1016/j.fuel.2016.03.003 (cit. on pp. 3, 4).

[56] Prationo, W., Zhang, J., Cui, J., Wang, Y. and Zhang, L.: “Influence of inherent moisture on the ignition and combustion of wet Victorian brown coal in air-firing and oxy-fuel modes: Part 1: The volatile ignition and flame propagation.” In: *Fuel Processing Technology* 138 (2015), pp. 670–679. DOI: 10.1016/j.fuproc.2015.07.008 (cit. on pp. 3, 4).

[57] Farazi, S., Attili, A., Kang, S. and Pitsch, H.: “Numerical study of coal particle ignition in air and oxy-atmosphere.” In: *Proceedings of the Combustion Institute* 37 (2019), pp. 2867–2874. DOI: 10.1016/j.proci.2018.07.002 (cit. on p. 4).

[58] Li, T., Geschwindner, C., Dreizler, A. and Böhm, B.: “An experimental study of coal particle group combustion in conventional and oxy-fuel atmospheres using multi-parameter optical diagnostics.” In: *Proceedings of the Combustion Institute* 39.3 (2023), pp. 3259–3269. DOI: 10.1016/j.proci.2022.07.081 (cit. on p. 4).

[59] Balusamy, S., Schmidt, A. and Hochgreb, S.: “Flow field measurements of pulverized coal combustion using optical diagnostic techniques.” In: *Experiments in Fluids* 54.5 (2013). DOI: 10.1007/s00348-013-1534-2 (cit. on pp. 4, 5).

[60] Balusamy, S., Kamal, M. M., Lowe, S. M., Tian, B., Gao, Y. and Hochgreb, S.: "Laser diagnostics of pulverized coal combustion in O2/N2 and O2/CO2 conditions: velocity and scalar field measurements." In: *Experiments in Fluids* 56.5 (2015). DOI: 10.1007/s00348-015-1965-z (cit. on pp. 4, 5).

[61] Hwang, S. m., Kurose, R., Akamatsu, F., Tsuji, H., Makino, H. and Katsuki, M.: "Application of Optical Diagnostics Techniques to a Laboratory-Scale Turbulent Pulverized Coal Flame." In: *Energy & Fuels* 19.2 (2005), pp. 382–392. DOI: 10.1021/ef049867z (cit. on pp. 4, 5).

[62] Hwang, S. m., Kurose, R., Akamatsu, F., Tsuji, H., Makino, H. and Katsuki, M.: "Observation of Detailed Structure of Turbulent Pulverized-Coal Flame by Optical Measurement (Part 2, Instantaneous Two-Dimensional Measurement of Combustion Reaction Zone and Pulverized-Coal Particles)." In: *JSME International Journal Series B* 49.4 (2006), pp. 1328–1335. DOI: 10.1299/jsmeb.49.1328 (cit. on pp. 4, 5).

[63] Hwang, S. m., Kurose, R., Akamatsu, F., Tsuji, H., Makino, H. and Katsuki, M.: "Observation of Detailed Structure of Turbulent Pulverized-Coal Flame by Optical Measurement (Part 1, Time-Averaged Measurement of Behavior of Pulverized-Coal Particles and Flame Structure)." In: *JSME International Journal Series B* 49.4 (2006), pp. 1316–1327. DOI: 10.1299/jsmeb.49.1316 (cit. on pp. 4, 5).

[64] Hayashi, J., Hashimoto, N., Nakatsuka, N., Tsuji, H., Watanabe, H., Makino, H. and Akamatsu, F.: "Soot formation characteristics in a lab-scale turbulent pulverized coal flame with simultaneous planar measurements of laser induced incandescence of soot and Mie scattering of pulverized coal." In: *Proceedings of the Combustion Institute* 34.2 (2013), pp. 2435–2443. DOI: 10.1016/j.proci.2012.10.002 (cit. on pp. 4, 5).

[65] Hashimoto, N., Hayashi, J., Nakatsuka, N., Tainaka, K., UMEMOTO, S., Tsuji, H., Akamatsu, F., Watanabe, H. and Makino, H.: "Primary soot particle distributions in a combustion field of 4 kW pulverized coal jet burner measured by time resolved laser induced incandescence (TiRe-LII)." In: *Journal of Thermal Science and Technology* 11.3 (2016), JTST0049–JTST0049. DOI: 10.1299/jtst.2016jtst0049 (cit. on pp. 4, 5).

[66] Hayashi, J., Hashimoto, N., Nakatsuka, N., Tainaka, K., Tsuji, H., Tanno, K., Watanabe, H., Makino, H. and Akamatsu, F.: "Simultaneous imaging of Mie scattering, PAHs laser induced fluorescence and soot laser induced incandescence to a lab-scale turbulent jet pulverized coal flame." In: *Proceedings of the Combustion Institute* 37.3 (2019), pp. 3045–3052. DOI: 10.1016/j.proci.2018.09.028 (cit. on pp. 4, 5, 94).

[67] Sung, Y. m., Moon, C. e., Kim, J. r., Kim, S. c., Kim, T. h., Seo, S. i., Choi, G. m. and Kim, D. j.: "Influence of pulverized coal properties on heat release region in turbulent jet pulverized coal flames." In: *Experimental Thermal and Fluid Science* 35.4 (2011), pp. 694–699. DOI: 10.1016/j.expthermflusci.2011.01.003 (cit. on pp. 4, 5).

[68] Moon, C., Sung, Y., Ahn, S., Kim, T., Choi, G. and Kim, D.: "Effect of blending ratio on combustion performance in blends of biomass and coals of different ranks." In: *Experimental Thermal and Fluid Science* 47 (2013), pp. 232–240. DOI: 10.1016/j.expthermflusci.2013.01.019 (cit. on pp. 4, 5).

[69] Moon, C., Sung, Y., Ahn, S., Kim, T., Choi, G. and Kim, D.: "Thermochemical and combustion behaviors of coals of different ranks and their blends for pulverized-coal combustion." In: *Applied Thermal Engineering* 54.1 (2013), pp. 111–119. DOI: 10.1016/j.applthermaleng.2013.01.009 (cit. on pp. 4, 5).

[70] Sung, Y. and Choi, G.: "Non-intrusive optical diagnostics of co- and counter-swirling flames in a dual swirl pulverized coal combustion burner." In: *Fuel* 174 (2016), pp. 76–88. DOI: 10.1016/j.fuel.2016.01.011 (cit. on pp. 4, 5).

[71] Sung, Y., Choi, M., Lee, S., Lee, G., Shin, M., Choi, G. and Kim, D.: "Generation mechanisms of tube vortex in methane-assisted pulverized coal swirling flames." In: *Fuel Processing Technology* 156 (2017), pp. 228–234. DOI: 10.1016/j.fuproc.2016.08.034 (cit. on pp. 4, 5).

[72] Li, X., Choi, M., Kim, K., Park, Y., Sung, Y., Muramatsu, M. and Choi, G.: "Effects of pulverized coal particle size on flame structure in a methane-assisted swirl burner." In: *Fuel* 242 (2019), pp. 68–76. DOI: 10.1016/j.fuel.2019.01.009 (cit. on pp. 4, 5, 99).

[73] Becker, L. G., Kosaka, H., Böhm, B., Doost, S., Knappstein, R., Habermehl, M., Kneer, R., Janicka, J. and Dreizler, A.: "Experimental investigation of flame stabilization inside the quarl of an oxyfuel swirl burner." In: *Fuel* 201 (2017), pp. 124–135. DOI: 10.1016/j.fuel.2016.09.002 (cit. on pp. 4, 5, 7, 43, 45, 46).

[74] Becker, L. G., Langenthal, T. von, Pielsticker, S., Böhm, B., Kneer, R. and Dreizler, A.: "Experimental investigation of particle-laden flows in an oxy-coal combustion chamber for non-reacting conditions." In: *Fuel* 235 (2019), pp. 753–762. DOI: 10.1016/j.fuel.2018.08.076 (cit. on pp. 4, 5, 41–43, 78).

[75] Becker, L. G., Pielsticker, S., Böhm, B., Kneer, R. and Dreizler, A.: "Particle dynamics in a gas assisted coal combustion chamber using advanced laser diagnostics." In: *Fuel* 269 (2020), p. 117188. DOI: 10.1016/j.fuel.2020.117188 (cit. on pp. 4, 5, 26, 43, 60, 61, 94).

[76] Strömberg, L., Lindgren, G., Jacoby, J., Giering, R., Anheden, M., Burchhardt, U., Altmann, H., Kluger, F. and Stamatelopoulos, G.-N.: "Update on Vattenfall's 30 MWth oxyfuel pilot plant in Schwarze Pumpe." In: *Energy Procedia* 1.1 (2009), pp. 581–589. DOI: 10.1016/j.egypro.2009.01.077 (cit. on p. 6).

[77] Toporov, D., Bocian, P., Heil, P., Kellermann, A., Stadler, H., Tschunko, S., Förster, M. and Kneer, R.: "Detailed investigation of a pulverized fuel swirl flame in CO2/O2 atmosphere." In: *Combustion and Flame* 155.4 (2008), pp. 605–618. DOI: 10.1016/j.combustflame.2008.05.008 (cit. on pp. 6, 45).

[78] Heil, P., Toporov, D., Stadler, H., Tschunko, S., Förster, M. and Kneer, R.: "Development of an oxycoal swirl burner operating at low O2 concentrations." In: *Fuel* 88.7 (2009), pp. 1269–1274. DOI: 10.1016/j.fuel.2008.12.025 (cit. on pp. 6, 41).

[79] Habermehl, M., Hees, J., Maßmeyer, A., Zabrodiec, D., Hatzfeld, O. and Kneer, R.: "Comparison of Flame Stability Under Air and Oxy-Fuel Conditions for an Aerodynamically Stabilized Pulverized Coal Swirl Flame." In: *Journal of Energy Resources Technology* 138.4 (2016). DOI: 10.1115/1.4032940 (cit. on p. 6).

[80] Hees, J., Zabrodiec, D., Massmeyer, A., Habermehl, M. and Kneer, R.: "Experimental Investigation and Comparison of Pulverized Coal Combustion in CO2/O2− and N2/O2−Atmospheres." In: *Applied Scientific Research* 96.2 (2016), pp. 417–431. DOI: 10.1007/s10494-015-9662-9 (cit. on pp. 6, 45).

[81] Hees, J., Zabrodiec, D., Massmeyer, A., Pielsticker, S., Gövert, B., Habermehl, M., Hatzfeld, O. and Kneer, R.: "Detailed analyzes of pulverized coal swirl flames in oxy-fuel atmospheres." In: *Combustion and Flame* 172 (2016), pp. 289–301. DOI: 10.1016/j.combustflame.2016.07.028 (cit. on p. 6).

[82] Zabrodiec, D., Becker, L., Hees, J., Maßmeyer, A., Habermehl, M., Hatzfeld, O., Dreizler, A. and Kneer, R.: "Detailed Analysis of the Velocity Fields from 60 kW Swirl-Stabilized Coal Flames in CO 2 /O 2 - and N 2 /O 2 -Atmospheres by Means of Laser Doppler Velocimetry and Particle Image Velocimetry." In: *Combustion Science and Technology* 189.10 (2017), pp. 1751–1775. DOI: 10.1080/00102202.2017.1332598 (cit. on pp. 6, 70, 71).

[83] Zabrodiec, D., Hees, J., Massmeyer, A., vom Lehn, F., Habermehl, M., Hatzfeld, O. and Kneer, R.: "Experimental investigation of pulverized coal flames in CO2/O2- and N2/O2-atmospheres: Comparison of solid particle radiative characteristics." In: *Fuel* 201 (2017), pp. 136–147. DOI: 10.1016/j.fuel.2016.11.097 (cit. on p. 6).

[84] Zabrodiec, D., Hees, J., Möller, G., Hatzfeld, O. and Kneer, R.: "Pulverized coal swirl flames in oxy-fuel conditions: Effects of oxidizer O2 concentration on flow field and local gas composition." In: *Proceedings of the Combustion Institute* 37.4 (2019), pp. 4471–4478. DOI: 10.1016/j.proci.2018.06.163 (cit. on p. 6).

[85] Hees, J., Zabrodiec, D., Massmeyer, A., Hatzfeld, O. and Kneer, R.: "Experimental investigation into the influence of the oxygen concentration on a pulverized coal swirl flame in oxy-fuel atmosphere." In: *Fuel* 240 (2019), pp. 64–74. DOI: 10.1016/j.fuel.2018.11.111 (cit. on p. 6).

[86] Maßmeyer, A., Zabrodiec, D., Hees, J., Kreitzberg, T., Hatzfeld, O. and Kneer, R.: "Flame pattern analysis for 60kWth flames under conventional air-fired and oxy-fuel conditions for two different types of coal." In: *Fuel* 271 (2020), p. 117457. DOI: 10.1016/j.fuel.2020.117457 (cit. on p. 6).

[87] Zabrodiec, D., Massmeyer, A., Hees, J., Hatzfeld, O. and Kneer, R.: "Flow pattern and behavior of 40 kWth pulverized torrefied biomass flames under atmospheric and oxy-fuel conditions." In: *Renewable and Sustainable Energy Reviews* 138 (2021), p. 110493. DOI: 10.1016/j.rser.2020.110493 (cit. on p. 6).

[88] Özer, B., Zabrodiec, D., Kneer, R. and Maßmeyer, A.: "Experimental investigation of 40 kW th methane-assisted and self-sustained pulverized biomass flames." In: *Proceedings of the Combustion Institute* 39.3 (2023), pp. 3343–3351. DOI: 10.1016/j.proci.2022.07.112 (cit. on p. 6).

[89] Pyper, D. K.: "The study of flame stability near lean blow out in non-premixed non-swirl and swirl burners and the design of a research combustor facility." PhD thesis. Brigham Young University, 1994 (cit. on pp. 6, 7).

[90] Tree, D. R., Black, D. L., Rigby, J. R., McQuay, M. Q. and Webb, B. W.: “Experimental measurements in the BYU controlled profile reactor.” In: *Progress in Energy and Combustion Science* 24.5 (1998), pp. 355–383. DOI: 10.1016/S0360-1285(97)00017-8 (cit. on p. 6).

[91] Nazeer, W. A., Pickett, L. M. and Tree, D. R.: “In-Situ Species, Temperature and Velocity Measurements in a Pulverized Coal Flame.” In: *Combustion Science and Technology* 143.1-6 (1999), pp. 63–77. DOI: 10.1080/00102209908924193 (cit. on pp. 6, 7).

[92] Pickett, L. M., Jackson, R. E. and Tree, D. R.: “LDA Measurements in a Pulverized Coal Flame at Three Swirl Ratios.” In: *Combustion Science and Technology* 143.1-6 (1999), pp. 79–107. DOI: 10.1080/00102209908924194 (cit. on pp. 6, 7).

[93] Eckbreth, A.: “CARS thermometry in practical combustors.” In: *Combustion and Flame* 39.2 (1980), pp. 133–147. DOI: 10.1016/0010-2180(80)90013-9 (cit. on p. 6).

[94] Aldén, M. and Wallin, S.: “CARS experiments in a full-scale (10 x 10 m) industrial coal furnace.” In: *Applied optics* 24.21 (1985), pp. 3434–3437. DOI: 10.1364/AO.24.003434 (cit. on p. 6).

[95] Beiting, E. J.: “Multiplex CARS temperature measurements in a coal-fired MHD environment.” In: *Applied optics* 25.10 (1986), p. 1684. DOI: 10.1364/AO.25.001684 (cit. on p. 6).

[96] Hughes, P. M. J., Lacelle, R. J. and Parameswaran, T.: “A Comparison of Suction Pyrometer and CARS Derived Temperatures in an Industrial Scale Flame.” In: *Combustion Science and Technology* 105.1-3 (1995), pp. 131–145. DOI: 10.1080/00102209508907743 (cit. on p. 6).

[97] Pope, S. B.: *Turbulent flows*. First published 2000, 5th printing 2019. Cambridge: Cambridge University Press, 2019 (cit. on pp. 9, 115).

[98] Beér, J. M. and Chigier, N. A.: *Combustion aerodynamics*. Repr. of 1972 ed. Fuel and energy science series. Malabar, Fla.: Krieger, 1983, 1972 (cit. on pp. 11–13).

[99] Sheen, H. J., Chen, W. J., Jeng, S. Y. and Huang, T. L.: “Correlation of swirl number for a radial-type swirl generator.” In: *Experimental Thermal and Fluid Science* 12.4 (1996), pp. 444–451. DOI: 10.1016/0894-1777(95)00135-2 (cit. on p. 12).

[100] Leuckel, W.: *Swirl Intensities, Swirl Types and Energy Losses of Different Swirl Generating Devices*. 1973. URL: https://books.google.de/books?id=AfzrPgAACAAJ (cit. on p. 12).

[101] Greitzer, E. M., Tan, C. S. and Graf, M. B.: *Internal Flow*. Cambridge University Press, 2010. DOI: 10.1017/CBO9780511616709 (cit. on p. 13).

[102] Boushaki, T.: *Swirling Flows and Flames*. [Erscheinungsort nicht ermittelbar]: IntechOpen, 2019. DOI: 10.5772/intechopen.86495 (cit. on p. 13).

[103] Glassman, I., Glumac, N. G. and Yetter, R. A.: *Combustion*. 5. ed. Amsterdam u.a.: Elsevier, 2015 (cit. on p. 13).

[104] Warnatz, J., Maas, U. and Dibble, R. W.: *Combustion: Physical and chemical fundamentals, modelling and simulation, experiments, pollutant formation*. 4th ed. Berlin: Springer, 2006 (cit. on pp. 13, 15).

[105] Cant, R. S. and Mastorakos, E.: *An introduction to turbulent reacting flows*. London: Imperial College Press, op. 2008 (cit. on pp. 13, 15).

[106] Gregory P. Smith, David M. Golden, Michael Frenklach, Nigel W. Moriarty, Boris Eiteneer, Mikhail Goldenberg, C. Thomas Bowman, Ronald K. Hanson, Soonho Song, William C. Gardiner, Jr., Vitali V. Lissianski, and Zhiwei Qin: *GRI-Mech 3.0*. URL: http://www.me.berkeley.edu/gri_mech/ (cit. on pp. 14, 22, 112, 113).

[107] Efstathios Michaelides, Clayton T. Crowe, John D. Schwarzkopf: *Multiphase Flow Handbook*. 2 Aufl. Mechanical and Aerospace Engineering Series. [s.l.]: Taylor & Francis Inc, 2016 (cit. on pp. 15–17).

[108] Balachandar, S. and Eaton, J. K.: “Turbulent Dispersed Multiphase Flow.” In: *Annual Review of Fluid Mechanics* 42.1 (2010), pp. 111–133. DOI: 10.1146/annurev.fluid.010908.165243 (cit. on pp. 15–17).

[109] Farazi, S., Hinrichs, J., Davidovic, M., Falkenstein, T., Bode, M., Kang, S., Attili, A. and Pitsch, H.: “Numerical investigation of coal particle stream ignition in oxy-atmosphere.” In: *Fuel* 241 (2019), pp. 477–487. DOI: 10.1016/j.fuel.2018.11.108 (cit. on p. 16).

[110] Farmand, P., Nicolai, H., Schumann, C., Attili, A., Berger, L., Li, T., Geschwindner, C., Di Mare, F., Hasse, C., Böhm, B., Janicka, J. and Pitsch, H.: "Numerical investigation and assessment of flamelet-based models for the prediction of pulverized solid fuel homogeneous ignition and combustion." In: *Combustion and Flame* 235 (2022), p. 111693. DOI: 10.1016/j.combustflame.2021.111693 (cit. on p. 16).

[111] Nicolai, H.: "Towards Predictive Simulations of Low-Emission Reactive Solid Fuel Systems." In: (). DOI: 10.26083/tuprints-00021079 (cit. on p. 16).

[112] Elghobashi, S.: "On predicting particle-laden turbulent flows." In: *Applied Scientific Research* 52.4 (1994), pp. 309–329. DOI: 10.1007/BF00936835 (cit. on p. 16).

[113] Eaton, J. K. and Fessler, J. R.: "Preferential concentration of particles by turbulence." In: *International Journal of Multiphase Flow* 20 (1994), pp. 169–209. DOI: 10.1016/0301-9322(94)90072-8 (cit. on pp. 16, 17).

[114] Tropea, C., Yarin, A. and Foss, J. F.: *Springer handbook of experimental fluid mechanics*. Berlin: Springer, 2007 (cit. on p. 17).

[115] Subramaniam, S. and Balachandar, S.: *Modeling approaches and computational methods for particle-laden turbulent flows*. Computation and analysis of turbulent flows. London and San Diego, CA: Academic Press, an imprint of Elsevier, 2023 (cit. on p. 17).

[116] Spliethoff, H.: *Power Generation from Solid Fuels*. Berlin, Heidelberg: Springer Berlin Heidelberg, 2010. DOI: 10.1007/978-3-642-02856-4 (cit. on pp. 17–19).

[117] Kaltschmitt, M., Hartmann, H. and Hofbauer, H.: *Energie aus Biomasse*. Berlin, Heidelberg: Springer Berlin Heidelberg, 2016. DOI: 10.1007/978-3-662-47438-9 (cit. on p. 18).

[118] Pasangulapati, V., Ramachandriya, K. D., Kumar, A., Wilkins, M. R., Jones, C. L. and Huhnke, R. L.: "Effects of cellulose, hemicellulose and lignin on thermochemical conversion characteristics of the selected biomass." In: *Bioresource technology* 114 (2012), pp. 663–669. DOI: 10.1016/j.biortech.2012.03.036 (cit. on p. 18).

[119] Kicherer, A.: *Biomasseverbrennung in Staubfeuerungen: Technische Möglichkeiten und Schadstoffemissionen*. Als Ms. gedr. Vol. 344. Fortschritt-Berichte VDI Reihe 6, Energietechnik. Düsseldorf: VDI-Verl., 1996 (cit. on p. 18).

[120] van Krevelen, D. W.: *Coal: Typology - physics - chemistry - constitution*. Third, completely rev. ed. Amsterdam: Elsevier, 1993 (cit. on p. 18).

[121] Quaak, P., Knoef, H. and Stassen, H.: *Energy from biomass: A review of combustion and gasification technologies*. Washington: World Bank, 1999 (cit. on p. 19).

[122] Nunes, L. J. R., Matias, J. C. O., Loureiro, L. M. E. F., Sá, L. C. R., Silva, H. F. C., Rodrigues, A. M., Causer, T. P., DeVallance, D. B. and Ciolkosz, D. E.: "Evaluation of the Potential of Agricultural Waste Recovery: Energy Densification as a Factor for Residual Biomass Logistics Optimization." In: *Applied Sciences* 11.1 (2021), p. 20. DOI: 10.3390/app11010020 (cit. on p. 19).

[123] Zabrodiec Garcia, D. M.: *Experimentelle Untersuchung turbulenter partikelbeladener Strömungen unter Reaktiven Luft- und Oxyfuel-Bedingungen*. DOI: 10.18154/RWTH-2022-02974 (cit. on p. 19).

[124] Fletcher, T.: "Soot in coal combustion systems." In: *Progress in Energy and Combustion Science* 23.3 (1997), pp. 283–301. DOI: 10.1016/S0360-1285(97)00009-9 (cit. on pp. 20, 21, 92).

[125] Pielsticker, S., Gövert, B., Umeki, K. and Kneer, R.: "Flash Pyrolysis Kinetics of Extracted Lignocellulosic Biomass Components." In: *Frontiers in Energy Research* 9 (2021). DOI: 10.3389/fenrg.2021.737011 (cit. on p. 20).

[126] Gani, A. and Naruse, I.: "Effect of cellulose and lignin content on pyrolysis and combustion characteristics for several types of biomass." In: *Renewable Energy* 32.4 (2007), pp. 649–661. DOI: 10.1016/j.renene.2006.02.017 (cit. on p. 20).

[127] Richter, H. and Howard, J.: "Formation of polycyclic aromatic hydrocarbons and their growth to soot—a review of chemical reaction pathways." In: *Progress in Energy and Combustion Science* 26.4-6 (2000), pp. 565–608. DOI: 10.1016/S0360-1285(00)00009-5 (cit. on p. 21).

[128] You, X. F., Gorokhovski, M. A., Chinnayya, A., Chtab, A. and Cen, K. F.: "Experimental study and global model of PAH formation from coal combustion." In: *Journal of the Energy Institute* 80.1 (2007), pp. 12–21. DOI: 10.1179/174602207X171561 (cit. on p. 21).

[129] He, Q., Guo, Q., Umeki, K., Ding, L., Wang, F. and Yu, G.: "Soot formation during biomass gasification: A critical review." In: *Renewable and Sustainable Energy Reviews* 139 (2021), p. 110710. DOI: 10.1016/j.rser.2021.110710 (cit. on p. 21).

[130] Goodwin, D. G., Moffat, H. K., Schoegl, I., Speth, R. L. and Weber, B. W.: "Cantera: An Object-oriented Software Toolkit for Chemical Kinetics, Thermodynamics, and Transport Processes." In: (2022). DOI: 10.5281/ZENODO.6387882 (cit. on pp. 22, 46, 47, 112, 113, 115, 127).

[131] Law, C. K., Makino, A. and Lu, T. F.: *On the off-stoichiometric peaking of adiabatic flame temperature*. 2006. DOI: 10.1016/j.combustflame.2006.01.009 (cit. on p. 23).

[132] Hasegawa, T.: "Developments of Gas Turbine Combustors for Air-Blown and Oxygen-Blown IGCC." In: (). DOI: 10.5772/20215 (cit. on p. 23).

[133] Sattelmayer, T., Fiala, T. and Lauer, M.: "On Use of Chemiluminescence for Combustion Diagnostics." In: *Optical Diagnostics for Reacting and Non-Reacting Flows*. Ed. by Steinberg, Adam. Roy, Sukesh. American Institute of Aeronautics & Astronautics, 2023, pp. 931–1019 (cit. on pp. 23–25).

[134] Gaydon, A. G.: *The spectroscopy of flames*. London: Chapman and Hall, 1974 (cit. on p. 23).

[135] Herzberg, G.: *Molecular spectra and molecular structure*. Malabar, Fla.: Krieger, 1991 (cit. on p. 24).

[136] Kathrotia, T., Riedel, U., Seipel, A., Moshammer, K. and Brockhinke, A.: "Experimental and numerical study of chemiluminescent species in low-pressure flames." In: *Applied Physics B* 107.3 (2012), pp. 571–584. DOI: 10.1007/s00340-012-5002-0 (cit. on p. 24).

[137] Liu, C. and Xu, L.: "Laser absorption spectroscopy for combustion diagnosis in reactive flows: A review." In: *Applied Spectroscopy Reviews* 54.1 (2019), pp. 1–44. DOI: 10.1080/05704928.2018.1448854 (cit. on p. 25).

[138] Raffel, M., Willert, C. E. and Kompenhans, J.: *Particle image velocimetry*. Berlin [etc.]: Springer, 1998 (cit. on pp. 25, 26).

[139] Poelma, C., Westerweel, J. and Ooms, G.: "Turbulence statistics from optical whole-field measurements in particle-laden turbulence." In: *Experiments in Fluids* 40.3 (2006), pp. 347–363. DOI: 10.1007/s00348-005-0072-y (cit. on p. 26).

[140] Towers, D. P., Towers, C. E., Buckberry, C. H. and Reeves, M.: "A colour PIV system employing fluorescent particles for two-phase flow measurements." In: *Measurement Science and Technology* 10.9 (1999), pp. 824–830. DOI: 10.1088/0957-0233/10/9/309 (cit. on p. 26).

[141] Kosiwczuk, W., Cessou, A., Trinité, M. and Lecordier, B.: "Simultaneous velocity field measurements in two-phase flows for turbulent mixing of sprays by means of two-phase PIV." In: *Experiments in Fluids* 39.5 (2005), pp. 895–908. DOI: 10.1007/s00348-005-0027-3 (cit. on p. 26).

[142] Tóth, B., Anthoine, J. and Riethmuller, M. L.: "Two-phase PIV method using two excitation and two emission spectra." In: *Experiments in Fluids* 47.3 (2009), pp. 475–487. DOI: 10.1007/s00348-009-0674-x (cit. on p. 26).

[143] Bi, X., Sun, Z., Lau, T., Alwahabi, Z. and Nathan, G.: "Simultaneous imaging of two-phase velocities in particle-laden flows by two-color optical phase discrimination." In: *Optics letters* 46.16 (2021), pp. 3861–3864. DOI: 10.1364/OL.428357 (cit. on p. 26).

[144] Fan, L., McGrath, D., Chong, C. T., Mohd Jaafar, M. N., Zhong, H. and Hochgreb, S.: "Laser-induced incandescence particle image velocimetry (LII-PIV) for two-phase flow velocity measurement." In: *Experiments in Fluids* 59.10 (2018). DOI: 10.1007/s00348-018-2610-4 (cit. on p. 26).

[145] Fan, L., Chong, C. T., Tian, B., Zheng, Y., McGrath, D. and Hochgreb, S.: "Simultaneous two-phase flame velocity measurement using laser-induced incandescence particle image velocimetry (LII-PIV)." In: *Proceedings of the Combustion Institute* 38.1 (2021), pp. 1589–1597. DOI: 10.1016/j.proci.2020.07.010 (cit. on p. 26).

[146] Khalitov, D. A. and Longmire, E. K.: "Simultaneous two-phase PIV by two-parameter phase discrimination." In: *Experiments in Fluids* 32.2 (2002), pp. 252–268. DOI: 10.1007/s003480100356 (cit. on pp. 26, 60, 77).

[147] Zhang, W., Wang, Y. and Lee, S. J.: "Simultaneous PIV and PTV measurements of wind and sand particle velocities." In: *Experiments in Fluids* 45.2 (2008), pp. 241–256. DOI: 10.1007/s00348-008-0474-8 (cit. on p. 26).

[148] Muste, M., Yu, K., Fujita, I. and Ettema, R.: "Two-phase flow insights into open-channel flows with suspended particles of different densities." In: *Environmental Fluid Mechanics* 9.2 (2009), pp. 161–186. DOI: 10.1007/s10652-008-9102-7 (cit. on p. 26).

[149] Cheng, Y., Pothos, S. and Diez, F. J.: "Phase discrimination method for simultaneous two-phase separation in time-resolved stereo PIV measurements." In: *Experiments in Fluids* 49.6 (2010), pp. 1375–1391. DOI: 10.1007/s00348-010-0878-0 (cit. on p. 26).

[150] Becker, L. G.: "Untersuchung von gasassistierten Staubflammen mittels Lasermesstechnik: Dissertation." PhD thesis. Darmstadt: TU Darmstadt, 2019. URL: https://tuprints.ulb.tu-darmstadt.de/8727/ (cit. on pp. 26, 43, 60, 76).

[151] Diaz-Lopez, M. X., Rubio, J. S. and Ni, R.: "Simultaneous two-phase flow measurements in a high-speed particle-laden under-expanded jet." In: *14th International Symposium on Particle Image Velocimetry* 1.1 (2021). DOI: 10.18409/ispiv.v1i1.171 (cit. on p. 26).

[152] Kiger, K. T. and Pan, C.: "PIV Technique for the Simultaneous Measurement of Dilute Two-Phase Flows." In: *Journal of Fluids Engineering* 122.4 (2000), pp. 811–818. DOI: 10.1115/1.1314864 (cit. on p. 26).

[153] Pang, M. and Wei, J.: "Experimental investigation on the turbulence channel flow laden with small bubbles by PIV." In: *Chemical Engineering Science* 94 (2013), pp. 302–315. DOI: 10.1016/j.ces.2013.02.062 (cit. on p. 26).

[154] Carter, C. D. and Lee, T.: "LIF Theory and Practice." In: *Optical Diagnostics for Reacting and Non-Reacting Flows*. Ed. by Steinberg, Adam. Roy, Sukesh. American Institute of Aeronautics & Astronautics, 2023, pp. 181–253 (cit. on p. 27).

[155] Eckbreth, A.: *Laser Diagnostics for Combustion Temperature and Species*. Netherlands: Gordon and Breach Publishers, 1995 (cit. on pp. 27, 31, 32, 34, 35).

[156] Schulz, C. and Sick, V.: "Tracer-LIF diagnostics: quantitative measurement of fuel concentration, temperature and fuel/air ratio in practical combustion systems." In: *Progress in Energy and Combustion Science* 31.1 (2005), pp. 75–121. DOI: 10.1016/j.pecs.2004.08.002 (cit. on pp. 27–29).

[157] Czeslik, C., Seemann, H. and Winter, R.: *Basiswissen Physikalische Chemie*. 4., aktualisierte Aufl. Vieweg Studium. Wiesbaden: Vieweg + Teubner, 2010 (cit. on pp. 27–30).

[158] Matuszewska, A. and Czaja, M.: "The Use of Synchronous Fluorescence Technique in Environmental Investigations of Polycyclic Aromatic Hydrocarbons in Airborne Particulate Matter from an Industrial Region in Poland." In: (). DOI: 10.5772/intechopen.92402 (cit. on pp. 28, 29).

[159] Zhang, Y., Wang, L., Liu, P., Li, Y., Zhan, R., Huang, Z. and Lin, H.: "Measurement and extrapolation modeling of PAH laser-induced fluorescence spectra at elevated temperatures." In: *Applied Physics B* 125.1 (2019). DOI: 10.1007/s00340-018-7115-6 (cit. on pp. 28, 29, 81).

[160] Bejaoui, S., Mercier, X., Desgroux, P. and Therssen, E.: "Laser induced fluorescence spectroscopy of aromatic species produced in atmospheric sooting flames using UV and visible excitation wavelengths." In: *Combustion and Flame* 161.10 (2014), pp. 2479–2491. DOI: 10.1016/j.combustflame.2014.03.014 (cit. on pp. 29, 81).

[161] Fond, B., Böhm, B. and Beyrau, F.: "Phosphor Thermometry." In: *Optical Diagnostics for Reacting and Non-Reacting Flows*. Ed. by Steinberg, Adam. Roy, Sukesh. American Institute of Aeronautics & Astronautics, 2023, pp. 589–632 (cit. on pp. 29, 30).

[162] Totzauer, L. M.: "Analyse der Sauerstoffabhängigkeit von Leuchtstoffen auf Basis von Cer und Synthese von festen Lösungen mit Ce_2O_3." In: (2023). DOI: 10.26083/tuprints-00023367 (cit. on p. 30).

[163] Brübach, J., Pflitsch, C., Dreizler, A. and Atakan, B.: "On surface temperature measurements with thermographic phosphors: A review." In: *Progress in Energy and Combustion Science* 39.1 (2013), pp. 37–60. DOI: 10.1016/j.pecs.2012.06.001 (cit. on pp. 30, 31, 52, 55).

[164] Fuhrmann, N., Brübach, J. and Dreizler, A.: "On the mono-exponential fitting of phosphorescence decays." In: *Applied Physics B* 116.2 (2014), pp. 359–369. DOI: 10.1007/s00340-013-5700-2 (cit. on pp. 31, 52).

[165] Hahn, J. W. and Lee, E. S.: "Measurement of nonresonant third-order susceptibilities of various gases by the nonlinear interferometric technique." In: *Journal of the Optical Society of America B* 12.6 (1995), p. 1021. DOI: 10.1364/JOSAB.12.001021 (cit. on pp. 32, 114).

[166] Cutler, A. D., Gallo, E. C. A. and Cantu, L. M. L.: "WIDECARS spectra fitting in a premixed ethylene–air flame." In: *Journal of Raman Spectroscopy* 47.4 (2016), pp. 416–424. DOI: 10.1002/jrs.4829 (cit. on pp. 32, 34, 106, 109, 111, 112).

[167] Day, J. P. R., Domke, K. F., Rago, G., Kano, H., Hamaguchi, H.-o., Vartiainen, E. M. and Bonn, M.: "Quantitative coherent anti-Stokes Raman scattering (CARS) microscopy." In: *The journal of physical chemistry. B* 115.24 (2011), pp. 7713–7725. DOI: 10.1021/jp200606e (cit. on p. 33).

[168] Zentgraf, F.: "Investigation of Reaction and Transport Phenomena during Flame-Wall Interaction Using Laser Diagnostics." PhD thesis. Darmstadt: TU Darmstadt, 2022. DOI: 10.26083/tuprints-00021314. URL: https://tuprints.ulb.tu-darmstadt.de/id/eprint/21314 (cit. on pp. 33, 107, 111, 113).

[169] Magnotti, G. and Cutler, A. D.: "Dual-Pump CARS Development and Application to Supersonic Combustion." In: 2012 () (cit. on pp. 33, 108, 111).

[170] Hall, R. J. and Stufflebeam, J. H.: "Quantitative CARS spectroscopy of CO2 and N2O." In: *Applied optics* 23.23 (1984), pp. 4319–4327. DOI: 10.1364/AO.23.004319 (cit. on p. 35).

[171] Lucht, R. P.: "Three-laser coherent anti-Stokes Raman scattering measurements of two species." In: *Optics letters* 12.2 (1987), pp. 78–80. DOI: 10.1364/OL.12.000078 (cit. on p. 35).

[172] Farooq, A. and Alquaity, A. B. S.: "Laser Absorption." In: *Optical Diagnostics for Reacting and Non-Reacting Flows*. Ed. by Steinberg, Adam. Roy, Sukesh. American Institute of Aeronautics & Astronautics, 2023, pp. 431–475 (cit. on pp. 35, 36).

[173] Gordon, I. E., Rothman, L. S., Hargreaves, R. J., Hashemi, R., Karlovets, E. V., Skinner, F. M., Conway, E. K., Hill, C., Kochanov, R. V., Tan, Y., Wcisło, P., Finenko, A. A., Nelson, K., Bernath, P. F., Birk, M., Boudon, V., Campargue, A., Chance, K. V., Coustenis, A., Drouin, B. J., Flaud, J.-.-M., Gamache, R. R., Hodges, J. T., Jacquemart, D., Mlawer, E. J., Nikitin, A. V., Perevalov, V. I., Rotger, M., Tennyson, J., Toon, G. C., Tran, H., Tyuterev, V. G., Adkins, E. M., Baker, A., Barbe, A., Canè, E., Császár, A. G., Dudaryonok, A., Egorov, O., Fleisher, A. J., Fleurbaey, H., Foltynowicz, A., Furtenbacher, T., Harrison, J. J., Hartmann, J.-.-M., Horneman, V.-.-M., Huang, X., Karman, T., Karns, J., Kassi, S., Kleiner, I., Kofman, V., Kwabia–Tchana, F., Lavrentieva, N. N., Lee, T. J., Long, D. A., Lukashevskaya, A. A., Lyulin, O. M., Makhnev, V., Matt, W., Massie, S. T., Melosso, M., Mikhailenko, S. N., Mondelain, D., Müller, H., Naumenko, O. V., Perrin, A., Polyansky, O. L., Raddaoui, E., Raston, P. L., Reed, Z. D., Rey, M., Richard, C., Tóbiás, R., Sadiek, I., Schwenke, D. W., Starikova, E., Sung, K., Tamassia, F., Tashkun, S. A., Vander Auwera, J., Vasilenko, I. A., Vigasin, A. A., Villanueva, G. L., Vispoel, B., Wagner, G., Yachmenev, A. and Yurchenko, S. N.: "The HITRAN2020 molecular spectroscopic database." In: *Journal of Quantitative Spectroscopy and Radiative Transfer* 277 (2022), p. 107949. DOI: 10.1016/j.jqsrt.2021.107949 (cit. on pp. 36, 79).

[174] Rothman, L. S., Gordon, I. E., Barber, R. J., Dothe, H., Gamache, R. R., Goldman, A., Perevalov, V. I., Tashkun, S. A. and Tennyson, J.: "HITEMP, the high-temperature molecular spectroscopic database." In: *Journal of Quantitative Spectroscopy and Radiative Transfer* 111.15 (2010), pp. 2139–2150. DOI: 10.1016/j.jqsrt.2010.05.001 (cit. on p. 36).

[175] Liu, Y., Tan, J., Wang, H. and Lv, L.: "Characterization of heat release rate by OH* and CH* chemiluminescence." In: *Acta Astronautica* 154 (2019), pp. 44–51. DOI: 10.1016/j.actaastro.2018.10.022 (cit. on p. 36).

[176] Emmert, J.: "Spectrally Resolved Absorption Tomography for Reacting, Turbulent Gas Phase Systems: Theory and Application." In: (2022). DOI: 10.26083/tuprints-00020750 (cit. on pp. 36, 78).

[177] Magunov, A. N.: "Spectral pyrometry (Review)." In: *Instruments and Experimental Techniques* 52.4 (2009), pp. 451–472. DOI: 10.1134/S0020441209040010 (cit. on p. 36).

[178] Araújo, A.: "Multi-spectral pyrometry—a review." In: *Measurement Science and Technology* 28.8 (2017), p. 082002. DOI: 10.1088/1361-6501/aa7b4b (cit. on pp. 36, 37).

[179] Mitchell, R. E. and McLean, W. J.: "On the temperature and reaction rate of burning pulverized fuels." In: *Symposium (International) on Combustion* 19.1 (1982), pp. 1113–1122. DOI: 10.1016/S0082-078 4(82)80287-7 (cit. on p. 37).

[180] Schiemann, M., Vorobiev, N. and Scherer, V.: "Stereoscopic pyrometer for char combustion characterization." In: *Applied optics* 54.5 (2015), pp. 1097–1108. DOI: 10.1364/AO.54.001097 (cit. on pp. 37, 62).

[181] Michelsen, H. A., Schulz, C., Smallwood, G. J. and Will, S.: "Laser-induced incandescence: Particulate diagnostics for combustion, atmospheric, and industrial applications." In: *Progress in Energy and Combustion Science* 51 (2015), pp. 2–48. DOI: 10.1016/j.pecs.2015.07.001 (cit. on pp. 37–39, 81).

[182] Sipkens, T. A., Menser, J., Dreier, T., Schulz, C., Smallwood, G. J. and Daun, K. J.: "Laser-induced incandescence for non-soot nanoparticles: recent trends and current challenges." In: *Applied Physics B* 128.4 (2022), p. 72. DOI: 10.1007/s00340-022-07769-z (cit. on pp. 37, 39).

[183] Bladh, H. and Bengtsson, P.-E.: "Characteristics of laser-induced incandescence from soot in studies of a time-dependent heat- and mass-transfer model." In: *Applied Physics B* 78.2 (2004), pp. 241–248. DOI: 10.1007/s00340-003-1362-9 (cit. on p. 38).

[184] Bladh, H., Olofsson, N.-E., Mouton, T., Simonsson, J., Mercier, X., Faccinetto, A., Bengtsson, P.-E. and Desgroux, P.: "Probing the smallest soot particles in low-sooting premixed flames using laser-induced incandescence." In: *Proceedings of the Combustion Institute* 35.2 (2015), pp. 1843–1850. DOI: 10.1016/j.proci.2014.06.001 (cit. on p. 38).

[185] Doost, A. S., Ries, F., Becker, L. G., Bürkle, S., Wagner, S., Ebert, V., Dreizler, A., Di Mare, F., Sadiki, A. and Janicka, J.: "Residence time calculations for complex swirling flow in a combustion chamber using large-eddy simulations." In: *Chemical Engineering Science* 156 (2016), pp. 97–114. DOI: 10.1016/j.ces.2016.09.001 (cit. on p. 46).

[186] Pareja, J., Litterscheid, C., Molina, A., Albert, B., Kaiser, B. and Dreizler, A.: "Effects of doping concentration and co-doping with cerium on the luminescence properties of Gd3Ga5O12:Cr3+ for thermometry applications." In: *Optical Materials* 47 (2015), pp. 338–344. DOI: 10.1016/j.optmat.2015.05.052 (cit. on p. 52).

[187] Fuhrmann, N., Kissel, T., Dreizler, A. and Brübach, J.: "Gd 3 Ga 5 O 12 :Cr—a phosphor for two-dimensional thermometry in internal combustion engines." In: *Measurement Science and Technology* 22.4 (2011), p. 045301. DOI: 10.1088/0957-0233/22/4/045301 (cit. on p. 52).

[188] Fuhrmann, N., Schneider, M., Ding, C.-P., Brübach, J. and Dreizler, A.: "Two-dimensional surface temperature diagnostics in a full-metal engine using thermographic phosphors." In: *Measurement Science and Technology* 24.9 (2013), p. 095203. DOI: 10.1088/0957-0233/24/9/095203 (cit. on p. 52).

[189] Kosaka, H., Zentgraf, F., Scholtissek, A., Bischoff, L., Häber, T., Suntz, R., Albert, B., Hasse, C. and Dreizler, A.: "Wall heat fluxes and CO formation/oxidation during laminar and turbulent side-wall quenching of methane and DME flames." In: *International Journal of Heat and Fluid Flow* 70 (2018), pp. 181–192. DOI: 10.1016/j.ijheatfluidflow.2018.01.009 (cit. on p. 52).

[190] Brübach, J., Janicka, J. and Dreizler, A.: "An algorithm for the characterisation of multi-exponential decay curves." In: *Optics and Lasers in Engineering* 47.1 (2009), pp. 75–79. DOI: 10.1016/j.optlaseng.2008.07.015 (cit. on p. 53).

[191] Emmert, J., Grauer, S. J., Wagner, S. and Daun, K. J.: "Efficient Bayesian inference of absorbance spectra from transmitted intensity spectra." In: *Optics express* 27.19 (2019), pp. 26893–26909. DOI: 10.1364/OE.27.026893 (cit. on p. 79).

[192] Grauer, S. J., Emmert, J., Sanders, S. T., Wagner, S. and Daun, K. J.: "Multiparameter gas sensing with linear hyperspectral absorption tomography." In: *Measurement Science and Technology* 30.10 (2019), p. 105401. DOI: 10.1088/1361-6501/ab274b (cit. on p. 79).

[193] Desgroux, P., Mercier, X. and Thomson, K. A.: "Study of the formation of soot and its precursors in flames using optical diagnostics." In: *Proceedings of the Combustion Institute* 34.1 (2013), pp. 1713–1738. DOI: 10.1016/j.proci.2012.09.004 (cit. on pp. 81, 92).

[194] Subramaniam, Shankar and Balachandar, S.: *Modeling approaches and computational methods for particle-laden turbulent flows*. Computation and analysis of turbulent flows. London: Academic Press, 2023 (cit. on p. 91).

[195] Knowles, P. L. and Kiger, K. T.: "Quantification of dispersed phase concentration using light sheet imaging methods." In: *Experiments in Fluids* 52.3 (2012), pp. 697–708. DOI: 10.1007/s00348-011-1100-8 (cit. on p. 92).

[196] Wen, X., Ferraro, F., Nicolai, H., Hashimoto, N., Hayashi, J., Nakatsuka, N., Tainaka, K. and Hasse, C.: "Flamelet LES of a turbulent pulverized solid fuel flame using a detailed phenomenological soot model." In: *Proceedings of the Combustion Institute* 39.3 (2023), pp. 3429–3438. DOI: 10.1016/j.proci.2022.07.190 (cit. on p. 92).

[197] Kissel, T.: "Spektroskopische Methoden zur Charakterisierung wandnaher Verbrennungsprozesse. Technische Universität." PhD thesis. Darmstadt: TU Darmstadt, 2011. URL: https://tuprints.ulb.tu-darmstadt.de/id/eprint/2669 (cit. on p. 107).

[198] Ewart, P.: “A modeless, variable bandwidth, tunable laser.” In: *Optics Communications* 55.2 (1985), pp. 124–126. DOI: 10.1016/0030-4018(85)90314-1 (cit. on p. 107).

[199] Greifenstein, M.: “Experimental investigations of flame-cooling air interaction in an effusion cooled pressurized single sector model gas turbine combustor.” PhD thesis. Darmstadt: TU Darmstadt, 2021. DOI: 10.26083/tuprints-00019205 (cit. on p. 111).

[200] Jennings, D. E. and Brault, J. W.: “The ground state of molecular hydrogen.” In: *Journal of Molecular Spectroscopy* 102.2 (1983), pp. 265–272. DOI: 10.1016/0022-2852(83)90039-5 (cit. on p. 111).

[201] Mazza, F., Griffioen, N., Castellanos, L., Kliukin, D. and Bohlin, A.: “High-temperature rotational-vibrational O2CO2 coherent Raman spectroscopy with ultrabroadband femtosecond laser excitation generated in-situ.” In: *Combustion and Flame* 237 (2022), p. 111738. DOI: 10.1016/j.combustflame.2021.111738 (cit. on pp. 35, 112, 113).

[202] Zentgraf, F., Johe, P., Steinhausen, M., Hasse, C., Greifenstein, M., Cutler, A. D., Barlow, R. S. and Dreizler, A.: “Detailed assessment of the thermochemistry in a side-wall quenching burner by simultaneous quantitative measurement of CO 2 , CO and temperature using laser diagnostics.” In: *Combustion and Flame* 235 (2022), p. 111707. DOI: 10.1016/j.combustflame.2021.111707 (cit. on p. 112).

[203] Köser, J. C.: “Untersuchung der frühen Abbrandphase von Feststoffpartikeln mit optischer Diagnostik.” PhD thesis. Darmstadt: TU Darmstadt, 2020. DOI: 10.25534/tuprints-00013410 (cit. on p. 112).

A Detailed drawing of SFC burner

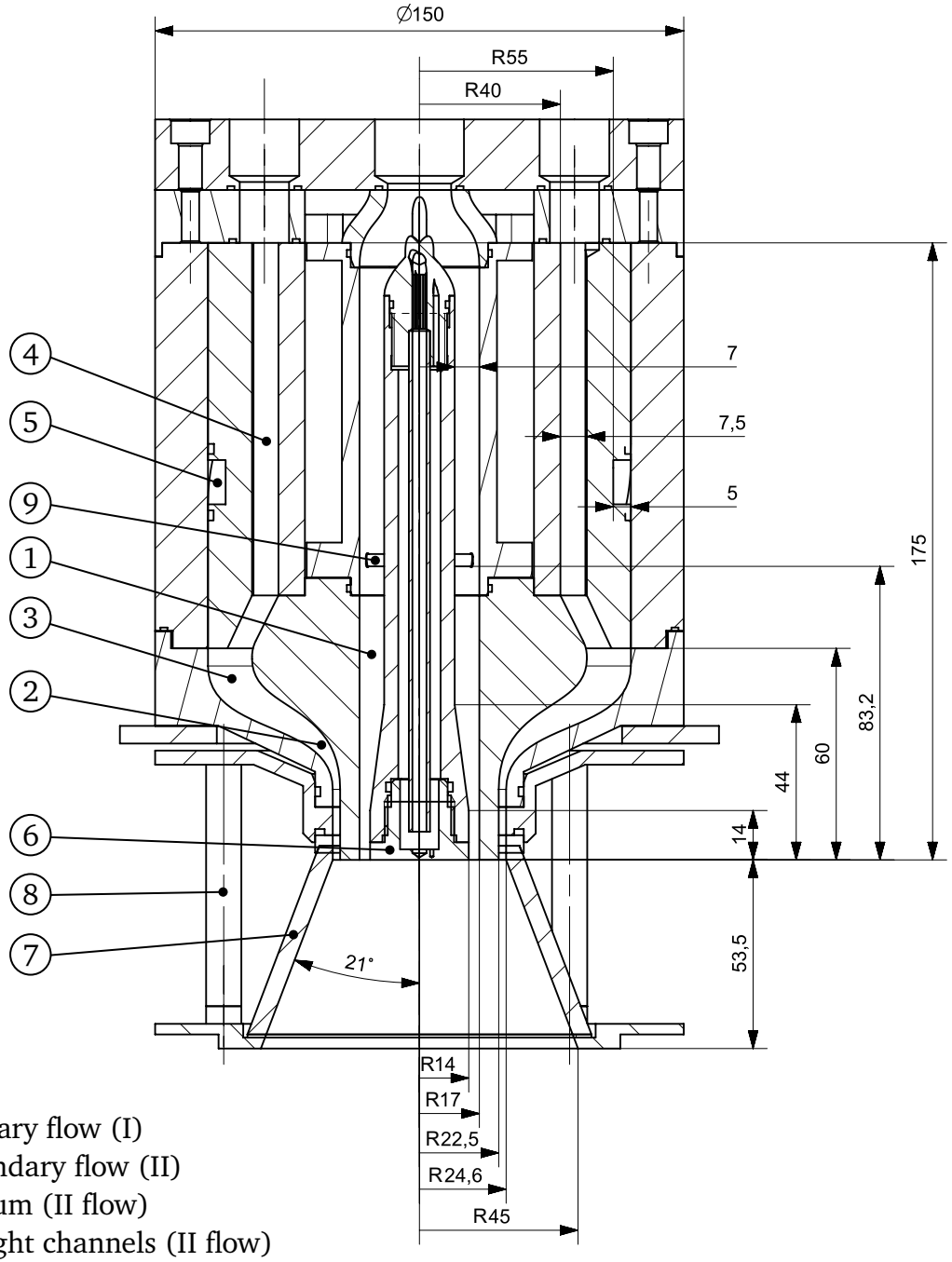

1 primary flow (I)
2 secondary flow (II)
3 plenum (II flow)
4 straight channels (II flow)
5 45° inclined channels (II flow)
6 bluff body
7 quartz glass diffusor
8 support structure diffusor
9 centering pin (NACA0030)

Figure A.1: SFC burner including quartz glass diffusor. Important components and dimensions are shown.

B Different designs of the tertiary flow for measurements inside the quarl and inside the combustion chamber

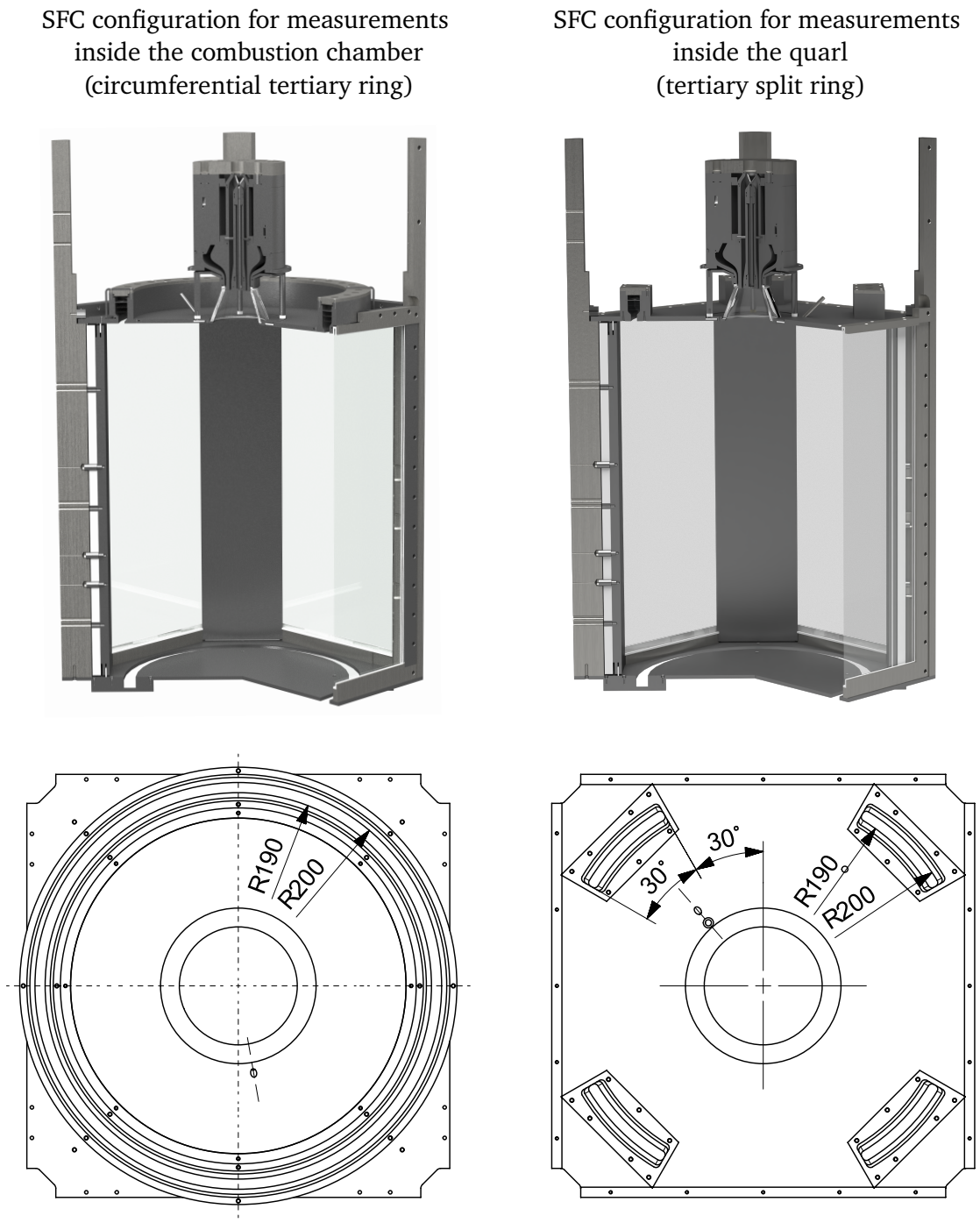

Figure B.1: Different configurations for the design of the tertiary flow of the SFC. Left: Design for measurements inside the combustion chamber. Right: Design for measurements inside the quarl. Illustrations of both configurations are shown on the top and the top view of the combustion chamber for both configurations is presented underneath.

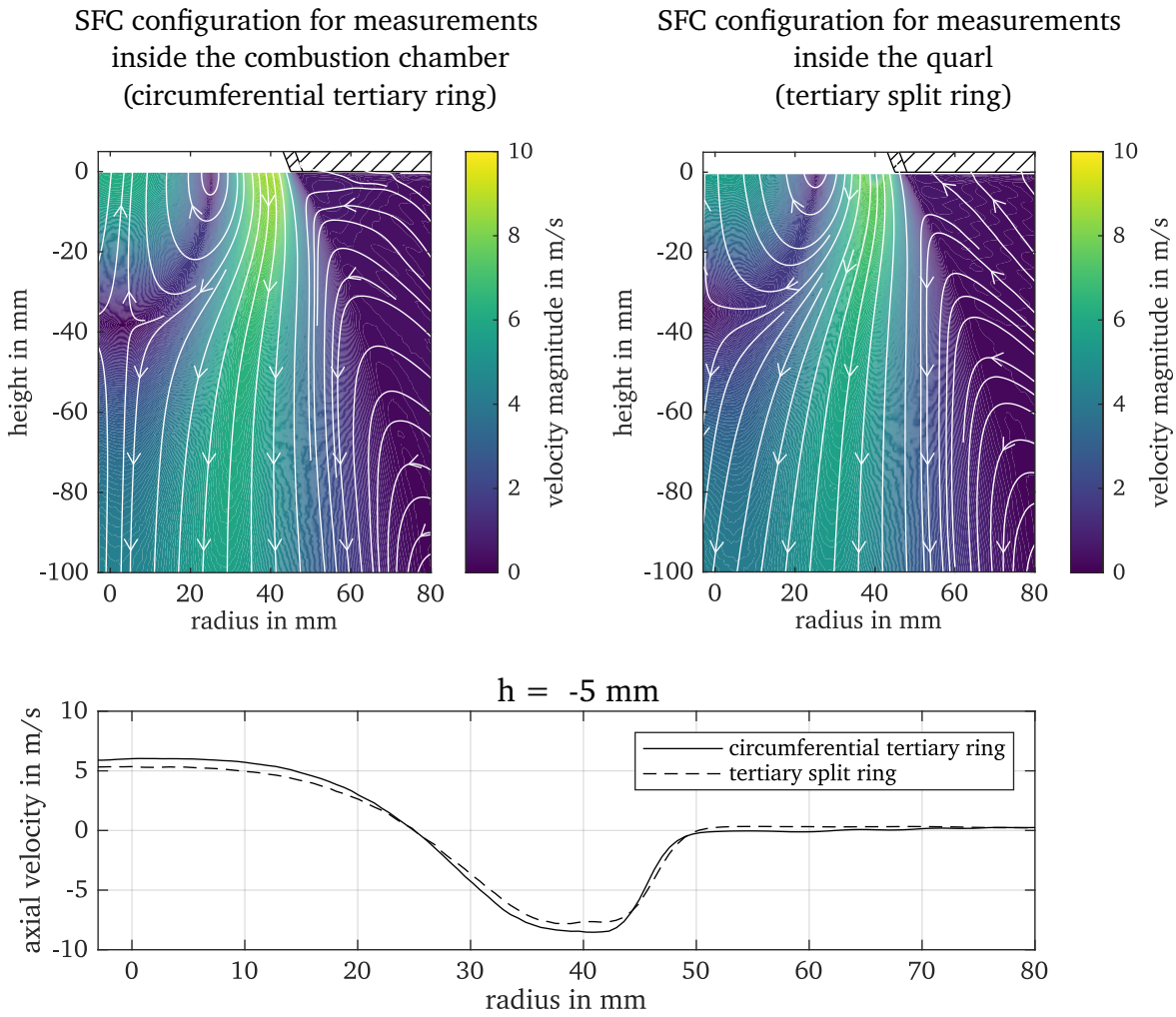

Figure B.2: Flow fields of operation condition OXY33-RL. Left: Flow field measured with SFC configuration for measurements inside the combustion chamber. Right: Flow field measured with SFC configuration for measurements inside the quarl. Bottom: Comparison of axial velocity profiles at $h = -5\ mm$ of both configurations.

C Declaration on the contribution to the publication ”Investigation on wall and gas temperatures inside a swirled oxy-fuel combustion chamber using thermographic phosphors, O2 rotational and vibrational CARS”.

Declaration on the contribution to the scientific publication

Erklärung zum Eigenanteil der wissenschaftlichen Veröffentlichung

Henrik Schneider, M.Sc.

Paper

Meißner, C., **Schneider, H.**, Sidiropoulos, E., Hölzer, J. I., Heckmann, T., Böhm, B., Dreizler, A. and Seeger, T.: "Investigation on wall and gas temperatures inside a swirled oxy-fuel combustion chamber using thermographic phosphors, O2 rotational and vibrational CARS." *In: Fuel 289 (2021), p. 119787.* https://doi.org/10.1016/j.fuel.2020.119787

Co-Authors

Christian Meißner, Dr.-Ing.
Evaggelos Sidiropoulos, M.Sc.
Jonas Immanuel Hölzer, M.Sc.
Tim Heckmann, B.Sc.
Benjamin Böhm, Dr.-Ing.
Andreas Dreizler, Prof. Dr. habil.
Thomas Seeger, Prof. Dr.-Ing.

Individual Contributions

- **Henrik Schneider**
  - Leading author for thermographic phosphor thermometry (TPT): Experimental setup, measurements, post-processing, analysis, visualization, and interpretation.
  - Operated the oxy-fuel combustion chamber for all measurements.
  - Conducted CARS experiments together with C. Meißner, E. Sidiropoulos, and J.I. Hölzer.
  - Interpretation of the recorded CARS data sets together with C. Meißner.
  - Main author of the test rig and TPT part of the paper and managed the review process together with C. Meißner.
- **Christian Meißner**
  - Leading author for Coherent anti-Stokes Raman spectroscopy (CARS): Experimental setup, measurements, post-processing, analysis, visualization, and interpretation.
  - Main author of the CARS part of the paper, performed literature research and managed the review process together with H. Schneider.
- **Evaggelos Sidiropoulos**
  - Designed CARS experimental setup together with C. Meißner.
  - Conducted CARS experiments together with C. Meißner, H. Schneider, and J.I. Hölzer.
  - CARS post-processing, analysis and interpretation of the recorded data sets together with C. Meißner.
  - Proofreading of the manuscript.
- **Jonas Immanuel Hölzer**
  - Conducted CARS experiments together with C. Meißner, H. Schneider, and E. Sidiropoulos.
  - Proofreading of the manuscript.
- **Tim Heckmann**
  - Conducted TPT experiments together with H. Schneider.
  - TPT post-processing, analysis and interpretation of the recorded data sets together with H. Schneider.
  - Proofreading of the manuscript.
- **Andreas Dreizler and Benjamin Böhm**
  - Support for interpretation and discussion of the results, proofreading of the manuscript.
- **Thomas Seeger**
  - Support for CARS measurements and CARS data processing.
  - Support for interpretation and discussion of the results, proofreading of the manuscript.

Overall Contribution of Henrik Schneider

A leading role in the conceptualization and conduction of the experiments, data analysis and main author of the manuscript together with C. Meißner. H. Schneider led the TPT measurements and was in charge of the test rig and test rig operation while C. Meißner led the CARS measurements.

Use of paper contents in other dissertations

This paper was part of the dissertation of Christian Meißner, who was leading the CARS experiments. He used the results from the CARS measurements in his dissertation. Other than the work of Dr.-Ing. Meißner, this publication is not the subject of any further ongoing or completed dissertation.

Signatures of all authors

[redacted]
Henrik Schneider

[redacted]
Tim Heckmann

[redacted]
Christian Meißner

[redacted]
Benjamin Böhm

[redacted]
Evaggelos Sidiropoulos

[redacted]
Andreas Dreizler

[redacted]
Jonas Immanuel Hölzer

[redacted]
Thomas Seeger

C Declaration on the contribution to the publication ”Investigation on wall and gas temperatures inside a swirled oxy-fuel combustion chamber using thermographic phosphors, O2 rotational and vibrational CARS”.

D Declaration on the contribution to the publication ”Investigation on flow dynamics and temperatures of solid fuel particles in a gas assisted oxy-fuel combustion chamber”.

Declaration on the contribution to the scientific publication

Erklärung zum Eigenanteil der wissenschaftlichen Veröffentlichung

Henrik Schneider, M.Sc.

Paper

Schneider, H., Valentiner, S., Vorobiev, N., Böhm, B., Schiemann, M., Scherer, V., Kneer, R. and Dreizler, A.: "Investigation on flow dynamics and temperatures of solid fuel particles in a gas-assisted oxy-fuel combustion chamber." *In: Fuel 286 (2021), p. 119424.* https://doi.org/10.1016/j.fuel.2020.119424

Co-Authors

Sarah Valentiner, M.Sc.
Nikita Vorobiev, Dr.-Ing.
Benjamin Böhm, Dr.-Ing.
Martin Schiemann, Dipl.-Phys. Dr. habil.
Viktor Scherer, Prof. Dr.-Ing.
Reinhold Kneer, Prof. Dr.-Ing.
Andreas Dreizler, Prof. Dr. habil.

Individual Contributions

- **Henrik Schneider**
  - Designed and conducted particle image velocimetry (PIV) and particle tracking velocimetry (PTV) measurements.
  - Operated the oxy-fuel combustion chamber for all measurements.
  - Post-processing, analysis, visualization, and interpretation of the recorded PIV and PTV data sets.
  - Interpretation of the recorded two-color pyrometry data sets together with S. Valentiner, N. Vorobiev, and M. Schiemann.
  - Main and corresponding author of the paper, performed literature research and managed the review process.
- **Sarah Valentiner**
  - Application of the two-color pyrometry experimental setup to the test rig together with N. Vorobiev.
  - Conducted two-color pyrometry experiments together with H. Schneider and N. Vorobiev.
  - Two-color pyrometry post-processing, analysis, visualization, and interpretation of the recorded data sets together with H. Schneider, N. Vorobiev, and M. Schiemann.
- **Nikita Vorobiev**
  - Support for two-color pyrometry measurements and post-processing.
  - Proofreading of the manuscript.
- **Martin Schiemann**
  - Author of the two-color pyrometry method section in the paper.
  - Support for interpretation and discussion of the results, proofreading of the manuscript.
- **Benjamin Böhm, Viktor Scherer, Reinhold Kneer, and Andreas Dreizler**
  - Support for interpretation and discussion of the results, proofreading of the manuscript.

Overall Contribution of Henrik Schneider

A leading role in the conceptualization and conduction of the experiments, data analysis and main author of the manuscript.

Use of paper contents in other dissertations

This publication is not the subject of any ongoing or completed dissertation.

Signatures of all authors

[redacted]

Henrik Schneider

[redacted]

Martin Schiemann

[redacted]

Sarah Valentiner

[redacted]

Viktor Scherer

[redacted]

Nikita Vorobiev

[redacted]

Reinhold Kneer

[redacted]

Benjamin Böhm

[redacted]

Andreas Dreizler

D Declaration on the contribution to the publication ”Investigation on flow dynamics and temperatures of solid fuel particles in a gas assisted oxy-fuel combustion chamber”.

E Declaration on the contribution to the publication ”Combined flow, temperature and soot investigation in oxy-fuel biomass combustion under varying oxygen concentrations using laser-optical diagnostics”.

Declaration on the contribution to the scientific publication

Erklärung zum Eigenanteil der wissenschaftlichen Veröffentlichung

Henrik Schneider, M.Sc.

Paper

Schneider, H., Bonarens, M., Hebel, J., Hardy, H., Emmert, J., Böhm, B., Wagner, S., Kneer, R. and Dreizler, A.: “Combined flow, temperature and soot investigation in oxy-fuel biomass combustion under varying oxygen concentrations using laser-optical diagnostics.” *In: Fuel 362 (2024), p. 130771.* https://doi.org/10.1016/j.fuel.2023.130771

Co-Authors

Matthias Bonarens, M.Sc.
Janik Hebel, M.Sc.
Hardy Hamel, M.Sc.
Johannes Emmert, Dr.-Ing.
Benjamin Böhm, Dr.-Ing.
Steven Wagner, Dr. rer. nat.
Reinhold Kneer, Prof. Dr.-Ing.
Andreas Dreizler, Prof. Dr. habil.

Individual Contributions

- **Henrik Schneider**
  - Designed and conducted chemiluminescence imaging (CL), particle image/tracking velocimetry (PIV/PTV), laser-induced incandescence (LII), and laser-induced fluorescence (LIF) measurements together with J. Hebel.
  - Operated the oxy-fuel combustion chamber for all measurements together with J. Hebel.
  - Post-processing, analysis, visualization, and interpretation of the recorded CL, PIV/PTV, LII, and LIF data sets.
  - Interpretation of the recorded tomographic absorption spectroscopy (TAS) data sets together with M. Bonarens, J. Emmert, and S. Wagner.
  - Main and corresponding author of the paper and performed the literature research.
- **Matthias Bonarens**
  - Conducted TAS experiments together with H. Schneider, J. Hebel, and H. Hamel.
  - TAS post-processing, analysis, and interpretation of the recorded data sets together with H. Schneider, J. Emmert, and S. Wagner.
  - Author of the TAS method section in the paper.
  - Proofreading of the manuscript.
- **Janik Hebel**
  - Conducted CL, PIV/PTV, LII, and LIF measurements together with H. Schneider.
  - Operated the oxy-fuel combustion chamber for all measurements together with H. Schneider.
  - Proofreading of the manuscript.
- **Hardy Hamel**
  - Conducted TAS experiments together with H. Schneider, M. Bonarens, and J. Hebel.
- **Johannes Emmert**
  - Support for TAS measurements and post-processing.
  - Proofreading of the manuscript.
- **Benjamin Böhm, Steven Wagner, Reinhold Kneer, and Andreas Dreizler**
  - Support for interpretation and discussion of the results, proofreading of the manuscript.

Overall Contribution of Henrik Schneider

A leading role in the conceptualization and conduction of the experiments, data analysis and main author of the manuscript.

Use of paper contents in other dissertations

This publication is not the subject of any ongoing or completed dissertation.

Signatures of all authors

[redacted]
Henrik Schneider

[redacted]
Benjamin Böhm

[redacted]
Matthias Bonarens

[redacted]
Steven Wagner

[redacted]
Janik Hebel

[redacted]
Reinhold Kneer

[redacted]
Hardy Hamel

[redacted]
Andreas Dreizler

[redacted]
Johannes Emmert

E Declaration on the contribution to the publication ”Combined flow, temperature and soot investigation in oxy-fuel biomass combustion under varying oxygen concentrations using laser-optical diagnostics”.

F Declaration on the contribution to the publication ”Rotational-vibrational O2-CO2 coherent anti-Stokes Raman spectroscopy for determination of thermochemical states in oxy-fuel biomass combustion”.

Declaration on the contribution to the scientific publication

Erklärung zum Eigenanteil der wissenschaftlichen Veröffentlichung

Henrik Schneider, M.Sc.

Paper

Schneider, H., Hebel, J., Böhm, B., Kneer, R. and Dreizler, A.: “Rotational-vibrational O_2-CO_2 coherent anti-Stokes Raman spectroscopy for determination of thermochemical states in oxy-fuel biomass combustion.” *In: Proceedings of the Combustion Institute, Volume 40, Issues 1-4 (2024), p.105457.* https://doi.org/10.1016/j.proci.2024.105457

Co-Authors

Janik Hebel, M.Sc.
Benjamin Böhm, Dr.-Ing.
Reinhold Kneer, Prof. Dr.-Ing.
Andreas Dreizler, Prof. Dr. habil.

Individual Contributions

- **Henrik Schneider**
  - Designed rotational-vibrational O_2-CO_2 coherent anti-Stokes Raman spectroscopy measurements.
  - Conducted rotational-vibrational O_2-CO_2 coherent anti-Stokes Raman spectroscopy measurements together with J. Hebel.
  - Operated the oxy-fuel combustion chamber for all measurements together with J. Hebel.
  - Post-processing, analysis, visualization, and interpretation of the recorded data sets.
  - Main and corresponding author of the paper and performed the literature research.
- **Janik Hebel**
  - Conducted rotational-vibrational O_2-CO_2 coherent anti-Stokes Raman spectroscopy measurements together with H. Schneider.
  - Operated the oxy-fuel combustion chamber for all measurements together with H. Schneider.
  - Proofreading of the manuscript.
- **Benjamin Böhm, Reinhold Kneer, and Andreas Dreizler**
  - Support for design of experiment, interpretation and discussion of the results, and proofreading of the manuscript.

Overall Contribution of Henrik Schneider

A leading role in the conceptualization and conduction of the experiments, data analysis and main author of the manuscript.

Use of paper contents in other dissertations

This publication is not the subject of any ongoing or completed dissertation.

Signatures of all authors

[redacted]

Henrik Schneider

[redacted]

Reinhold Kneer

[redacted]

Janik Hebel

[redacted]

Andreas Dreizler

[redacted]

Benjamin Böhm

F Declaration on the contribution to the publication ”Rotational-vibrational O2-CO2 coherent anti-Stokes Raman spectroscopy for determination of thermochemical states in oxy-fuel biomass combustion”.